

# UC Berkeley

## UC Berkeley Electronic Theses and Dissertations

### Title

Chemical Tools for Detecting Transition Metals for Biological and Environmental Applications

### Permalink

<https://escholarship.org/uc/item/7f0419hd>

### Author

Lee, Sumin

### Publication Date

2018

Peer reviewed|Thesis/dissertation

**Chemical Tools for Detecting Transition Metals for Biological and Environmental  
Applications**

By

Sumin Lee

A dissertation submitted in partial satisfaction of the

requirements for the degree of

Doctor of Philosophy

in

Chemistry

in the

Graduate Division

of the

University of California, Berkeley

Committee in charge:

Professor Christopher J. Chang, Chair

Professor Evan Miller

Professor Michelle C. Chang

Professor Seung-Wuk Lee

Summer 2018

Chemical Tools for Detecting Transition Metals for Biological and  
Environmental Applications

© 2018

by Sumin Lee

## **Abstract**

### **Chemical Tools for Detecting Transition Metals for Biological and Environmental Applications**

By Sumin Lee

Doctor of Philosophy in Chemistry

University of California, Berkeley

Professor Christopher J. Chang, Chair

Copper, iron and sodium are essential elements for life. The potent redox activity of copper and iron are essential to redox-dependent cellular processes, including respiration and biology spanning oxygen transport, nucleotide synthesis, and electron transfer. At the same time, however, mismanagement of copper and iron stores and subsequent oxidative stress and damaging events are implicated to many diseases such as Wilson's disease and neurodegenerative disorders. The non-redox active metal, sodium, has been recognized as regulating acid-base homeostasis and participating in maintaining membrane potential and triggering the activation of diverse signal transduction pathways. Therefore, we seek to develop new methods for monitoring copper, iron, and sodium in biological and environmental samples and in turn, to apply these chemical tools to help study the roles of these essential metals in healthy and disease states. The aims of my graduate research in Prof. Chris Chang's lab at UC Berkeley have been focused on developing new material-based binding platforms to enable monitoring of copper and iron levels in biological and environmental samples without complex and expensive instrumentation, designing novel imaging probes for copper based on protein tagging technique in living cells and in the neurons, and developing sodium fluorescent sensors based on a photoinduced electron transfer mechanism.

## Dedication

### The Lord's Prayer (NLT)

Our Father in heaven, may your name be honored.  
May your kingdom come soon. May your will be done here on earth, just as it is in heaven.  
Give us our food for today, and forgive us our sins, just as we have forgiven those who have  
sinned against us. And don't let us yield to temptation, but deliver us from the evil one.  
For yours is the kingdom, and the power, and the glory, forever, Amen.

Matt, 6:9-13

## Table of Contents

Acknowledgments		iii
Chapter 1	Development of Detection Platforms for Metal Ions as Biomedical Applications	4
Chapter 2	Copper Capture in a Thioether-Functionalized Porous Polymer Applied to the Detection of Wilson's Disease	24
Chapter 3	Iron Capture in a Functionalized Porous Polymer Applied to Remediation and Detection in Environmental Water Samples	58
Chapter 4	Ligand-Directed Acyl Imidazole Chemistry for Labeling Proteins in Copper-Rich Compartments in Cells and Neurons	92
Chapter 5	Development of Trappable Fluorescent Sodium Sensors for Imaging Sodium in Living Cells	119
Appendix 1	Functionalized Porous Aromatic Framework (PAFs)	143
Appendix 2	Modifying Electron Density of Tris(2-methylpyridine)amine (TPA)	158
Appendix 3	Identifying Active Methionine under Oxidative Stress	170
Appendix 4	Metalloproteomic Study with Episulfide Alkyne Probes	186

## Acknowledgments

Thanks God for all the time.

To my parents, for their prayer and support and overflowing love and I feel so blessed to have you as my parents and I wish I can do to my children as you have done to me.

Special thanks to Chris who accepted me in his group and all his guides for projects and for his patience and for all of his effort to teach me to be a scientist. Another big thank to Chris for having this wonderful lab. I would like to thank everyone one by one how you have influenced me and you've made my day since my first day in Berkeley. Every fun we had in the lab and outside of the lab, and some songs, it brings me smile and sometimes makes me outlaugh a little woman. But I really appreciate friendship and hope we can bump into somewhere.

Special thanks to Zeming who started the graduate school at the same time and worked on alkali metals fluorescent probes in this lab and for support and being good buddy. Hope your nanochemistry works smooth uphill and visit SF more often. Thanks to Kevin for inspiring me to draw portrait again and creating new Chewbacca language. Enjoy your formaldehyde world and hope you can start gym soon too. I am not talking that you are fat. And Tyler, thanks for every instrumental helps and mouse killing skill and bunch of a lot of songs that I might never listen again for my entire life. These three kids born in 1993 still gives me some concern about what had happened in 1993. And thanks to all of other lab members Allegra, Eva, Thom, Cheri, and Karla who have walked ahead of me and made the path smooth. Thanks for your friendship so I was able to settle down in Berkeley and feel like second home here. And also big thank to Lakshmi, Diana, and Joel for biology insight and all the help about protein works. Thank Tim, Marie, and a lot of mice that was sacrificed but Tim and Marie established good research based on your sacrifice so don't be sad that much. Song, you are doing extremely well and hope you can find some time to vent out all the stress but enjoy this moment. All of you are extremely supportive and intelligent, kind and generous, giving such a good example as 'perfect' postdoc so I will do my best to look after your examples. And rising babies; Audrey, Vanha, Hyojin and new postdocs; Dan, Jun, and Hide. It is unfortunate that I could not spend more time with you but please enjoy your research and time in the lab and also outside of the lab. Every one of you are really precious and 'influence' me to be a good scientist.

And also want to give thanks to all of my collaborators and their insight and help.

I want to give tons of blessing all of you wherever you are going and whoever you work with. Hope we can keep in touch forever. What I am now won't be possible if any of you aren't there.

I also want to thank my dear friends, Wendy, Eunice, Rani, and Robin who have hunted for hidden restaurants together and gobbling camping dinner and walked through all difficult time.

We will dig out another spots in Standford.

And also thanks to Solano Community Church where I found the home group and met another precious people there. I will miss you and also the K-1 kids and will check out how much they grow up.

Thank Rachmaninoff that I got enormous comfort from your great piece of art.

# Chapter 1

## **Development of Detection Platforms for Metal Ions as Biomedical Applications**

Portions of this work were published in the following scientific journal:

Ackerman, C. M.; Lee, S.; Chang, C. J. "Analytical Methods for Imaging Metals in Biology: From Transition Metal Metabolism to Transition Metal Signaling", *Anal. Chem.* **2017**, *89*, 22-41



## 1.1. Background and Motivation

Metals are necessary for sustaining all life and more than one third of the human proteome contains metal cations as cofactors at active-sites with catalytic functions or as structural cofactors.<sup>1,2</sup> Metals play roles in all aspects of biology such as interplaying between DNA to RNA to proteins<sup>3</sup> and mediating electron transfer,<sup>4</sup> transporting small-molecules, and acting as redox catalysts.<sup>5</sup> Over the past decades, a number of diseases have been reported to be related to metal imbalance in cells and tissues.<sup>6</sup> The discovery of Menkes and Wilson's diseases and their corresponding mutated genes provided a clear correlation between metal homeostasis and the developed symptoms.<sup>7</sup> Furthermore, Parkinson's and Alzheimer's diseases have been reported to show hyperaccumulation of transition metals in brain tissues.<sup>8</sup>

Traditionally, studies have mainly focused on the redox-inactive alkali metals, such as calcium, sodium, or potassium because of their abundance in biological systems and involvement in basic and complex biological processes. In contrast, the ability of redox-active transition metals like copper and iron in the cellular system has been relatively less explored. As these metals can generate reactive oxygen species (ROS) through Fenton chemistry,<sup>9</sup> numerous studies have reported that redox-active transition metals are involved in fundamental redox-dependent cellular processes including respiration, photosynthesis, and electron transfer and are required as cofactors within enzyme active sites and as signaling factors in the neuronal system.<sup>10-12</sup> Among these transition metals, I would like to focus on copper and iron as two of the most abundant transition metals in the human body and the environmental system as well.

Copper is an essential element for life, forming tight metal-ligand interactions as indicated by the natural order of stability for divalent metals, termed the Irving-Williams series,<sup>13</sup>. A catalogue of the principal types of enzymes that use each metal reveals that iron and copper are most commonly used as conduits for electrons in oxidoreductases.<sup>14</sup> Copper is not only an important cofactor for metalloproteins, but also its redox activity is utilized for fundamental redox-dependent cellular processes such as respiration and electron transfer (e.g., cytochrome c oxidase, azurin), pigmentation (tyrosinase), antioxidant defense (Cu/Zn superoxide dismutase)<sup>15</sup>, neurotransmitter synthesis (dopamine  $\beta$ -hydroxylase)<sup>16</sup>. Therefore, misregulation of copper homeostasis is related to development of many diseases, including cancer,<sup>2</sup> neurodegenerative Alzheimer's, Parkinson's, and Huntington's diseases,<sup>3</sup> and genetic disorders such as Menkes and Wilson's diseases.<sup>4</sup> However, the mechanisms of how copper causes such diseases remain unclear. To have a better understanding of the mechanism between copper misregulation and pathogenesis, appropriate detection tools for copper are highly necessary. These tools can help elucidate the mechanisms of metal acquisition and sequestration, which are vital for understanding the contribution of metals to healthy and disease states of human beings.

In addition to copper, iron is another biological metal of interest, being the fourth most abundant element in the earth's crust and the most abundant transition metal in the human body.<sup>17</sup> This metal is required for sustaining a range of physiological processes such as electron transfer, oxygen transport, respiration, and gene expression,<sup>18-21</sup> and iron deficiency leads to anemia, which can be associated with impairments such as cognitive development and immunity mechanisms.<sup>22</sup> At the same time, however, excess iron can increase production of reactive oxygen species, resulting in oxidative stress cascades that lead to lipid oxidation and DNA damage.<sup>19-21,23,24</sup> Indeed, aberrant iron accumulation is implicated in aging and in several diseases, including cardiovascular diseases, neurodegenerative diseases, and cancer.<sup>22,25-30</sup> For example, proliferating cancer cells accumulate elevated concentrations of labile iron compared to normal cells owing to their

increased metabolic activity, yet this expanded iron pool may also sensitize cancer cells to death by ferroptosis, a newly recognized iron-dependent cell-death pathway.<sup>31</sup> Due to its importance, iron homeostasis is precisely controlled from cellular to whole body level, with local and global overload and/or deficiency being detrimental.

Therefore, analytical techniques have been developed to trace copper and iron ions in cellular system and environmental systems. Over the past few decades, numerous techniques have been developed for characterizing the total metal ion pools to give spatial information, including laser ablation inductively coupled plasma mass spectrometry (LA-ICPMS), secondary ion mass spectrometry (SIMS), X-ray fluorescence microscopy (XFM), X-ray absorbance spectroscopy (XAS), particle-induced X-ray emission (PIXE), and various electron microscopy (EM) methods. Additionally, to image labile metal pools in the cellular system, fluorescent probes have been designed and utilized for specific organelles or animal studies by employing bioluminescence (Figure 1.1).<sup>32</sup>

Herein, I have developed new platforms for detecting copper and iron which can be applied in both living and environmental systems. These tools can monitor the copper and iron pools and their roles in biological and environmental samples, respectively. As a first platform for metal ion detection, I envisioned the application of solid-state frameworks, seeking to take advantage of their high surface area, well-defined porosity,<sup>33–35</sup> ease of processability,<sup>36</sup> and the diverse synthetic routes for functionalization.<sup>35,37–41</sup> Functional porous polymers have been shown to demonstrate efficient gas uptake and have been used in gas storage and separation and as catalysts for biomolecular immobilization.. (Figure 1.2)

As another platform for monitoring copper and iron, I would like to use a protein labeling strategy to monitor copper-related proteins. Over the last few decades, fluorescent probes have been reported as powerful tools to detect copper, demonstrating high sensitivity and high spatial and temporal resolution in living systems. The Chang lab has developed a series of copper(I) selective fluorescent probes for endogenous copper capture and targeting specific organelles, as well as bioluminescent probe for animal studies. (Figure 1.3) These studies have shown that labile copper is translocated upon copper influx and efflux which is triggered by mitochondrial redox signals, confirming that copper is involved in cellular signaling. However, we would like to address more specific questions regarding the proteins responsible for copper translocation and how they regulate redox-active copper in different physiological processes. Herein, we seek to address these questions by applying a protein labeling technology to stain cuproproteins upon formation of a covalent bond between a fluorophore and the protein, therefore providing a robust signal and enabling proteomic studies.

Towards this end, I have developed solid-state frameworks and protein labeling fluorescent probes for detecting copper and iron in biological and environmental systems. Additionally, I have also worked on developing probes for detecting sodium ions in the cells and using acyl imidazole-alkyne and episulfide-alkyne probes for identification of novel metalloproteins. This dissertation summarizes progress on the development of porous frameworks and fluorescent probes for transition metals and their application to detect transition metals in biomedical applications.

## **1.2. Polymer Platform to Detect Metal Ions**

### *1.2.1 Design and advantages of porous polymers*

Over the last few decades, numerous examples of inorganic–organic hybrid polymers have been reported. Porous polymer compounds with infinite structures have been intensively studied,

the natural and artificial zeolites serving as representative examples given their elaborate functions in molecular storage, recognition, separation, and catalytic activity. To improve their applicability, chemists have developed porous organic–inorganic hybrids and organic frameworks, supramolecules, and oligomers with a controlled functional pore to target specific analytes of interest in molecular separation, clean energy storage, photoelectric materials, molecular motors, and catalysis. As another direction of artificial porous polymer, compounds with backbones constructed from metal ions as connectors and ligands as linkers have been introduced as so-called coordination polymers or Metal Organic Frameworks (MOFs). The term ‘coordination polymer’ was first used by Y. Shibata in 1916 and the area was first reviewed in 1964.<sup>42</sup> Since the introduction of coordination polymers, covalent organic frameworks (COFs), polymers of intrinsic microporosity (PIMs), conjugated microporous polymers (CMPs), hyper-crosslinked polymers (HCPs), and porous aromatic frameworks (PAFs) have been prepared.. PAFs have attracted huge attention given the interest in creating nanometer-sized spaces and exploring novel phenomena within them. Their application has extended to gas separation, storage, and heterogeneous catalysis. In this thesis, we demonstrate the use of PAFs as backbone for detecting copper and iron ions.

### *1.2.2 Porous aromatic frameworks (PAF-1)*

In 2009, T. Ben, S. Qiu, and S. Zhu group developed a PAF based on diamond-topology. The original idea of PAF-1 comes from the structure and properties of diamond, in which each carbon atom is tetrahedrally connected to four neighboring atoms through covalent bonds. Breaking the C–C covalent bond of diamond and inserting rigid phenyl rings via a nickel(0)-catalyzed Yamamoto-type Ullmann cross-coupling should allow sufficient exposure of the faces and edges of phenyl rings with the expectation of increasing the internal surface area.<sup>35</sup> Indeed, PAF-1 displayed a record surface area of BET = 5640 m<sup>2</sup> g<sup>-1</sup> and exceptional physicochemical stability, being stable in acidic and basic conditions and at high temperatures (> 400 °C). Furthermore, PAF-1 also showed very high uptake of carbon dioxide (1.3 g g<sup>-1</sup> at 40 bar, 298 K). This new type of three-dimensional homogeneous, rigid, and open-network structure afforded a “new generation” PAF with several unusual, even peculiar properties. This example describes the significant progress in the development of PAFs, highlighting the relationship between structure design, synthetic method, and properties. The average pore size of PAF-1 is very small, resulting in broad reflection peaks in the powder X-ray diffraction (Figure 1.4). Most PAFs do not dissolve in organic solvents and the properties can be maintained in aqueous condition even in boiling water or cold acid or base solution. Based on their stability and high surface area, PAFs have been used as efficient gas storage, heterogenous catalysts, and selective uptake reagents in aqueous systems.

### *1.2.3 Applications of porous aromatic frameworks (PAFs)*

Compared with other ultrahigh surface area solids such as porous carbons, zeolites, (MOFs, and COFs, PAFs showed very high surface areas and excellent physicochemical stability. PAF-1 recorded surface area of 5640 m<sup>2</sup> g<sup>-1</sup> and based on this high surface area, PAFs appear to have high physicochemical stability which makes them unique ultrahigh surface area materials. Most PAFs have been reported to maintain their properties in boiling water and cold acid or base solution. This is due to their covalent bonding nature and crosslinked rigid biphenyl framework. High pressure hydrogen storage of PAF-1, PAF-3, and PAF-4 was determined at 77 K and the excess hydrogen uptake capacity

was found to be 7.0 wt% at 48 bar, 5.5 wt% at 60 bar, and 4.2 wt% at 60 bar for PAF-1, PAF-3, and PAF-4, respectively. The heat of adsorption related to hydrogen-adsorbent interactions were calculated from the hydrogen adsorption isotherms recorded at 77 K and 87 K, using the Clausius–Clapeyron equation, to afford values of 5.4 kJ mol<sup>-1</sup>, 6.6 kJ mol<sup>-1</sup>, and 6.3 kJ mol<sup>-1</sup> for PAF-1, PAF-3 and PAF-4 respectively. Accordingly, the pressure uptake of hydrogen by the corresponding PAFs were evaluated at 186 cm<sup>3</sup> g<sup>-1</sup>, 232 cm<sup>3</sup> g<sup>-1</sup>, and 169 cm<sup>3</sup> g<sup>-1</sup> for PAF-1, PAF-3, and PAF-4, respectively. A greater surface area means a greater volume of gas can be stored. However, in the case of low pressure gas storage, especially when ambient condition gas storage (1 bar, room temperature) was applied, both surface area and  $Q_{st}$  should be considered. Usually, the  $Q_{st}$  is more important and results often show higher gas uptake materials express higher  $Q_{st}$  at ambient conditions. PAFs not only have high surface areas and excellent physicochemical stabilities, but also exceptional selectivity for greenhouse gases such as CO<sub>2</sub> and methane.

In addition to their usage in gas storage, PAFs also show molecular recognition properties between organic molecules and water. PAF-5, PAF-11, and JUC-Z1 are hydrophobic materials with high organic small molecule uptake such as methanol and benzene against water, selectivity which could be used to eliminate harmful small organic molecules produced in industrial processes. PAF-2 shows high selectivity for adsorption of aromatic benzene as compared to aliphatic hexane. PAF-6 could uptake 0.35 g g<sup>-1</sup> of ibuprofen, with drug release occurring with a large initial burst within 10 h. PAF-15 exhibits high luminescence quenching ability of hazardous and explosive molecules, such as nitrobenzene, 2,4-dinitrotoluene (2,4-DNT), and 2,4,6-trinitrotoluene (TNT), and may serve as a new sensing material.<sup>43</sup> PAF-5 displays high stability and high surface area and exhibits excellent abilities to adsorb organic chemical pollutants at saturated vapor pressures and room temperature.<sup>44</sup> Combining the advantages of porous aromatic frameworks and ionic liquids, PAF/IL composite coated Solid Phase Microextraction (SPME) fibers exhibited a high adsorption capacity for organochlorine pesticides. Under optimized experimental conditions, enhancement factors of 247–1696 were obtained with good linearity in the range of 1–500 µg L<sup>-1</sup>. The detection and quantification limits were determined to be in the range of 0.11–0.29 µg L<sup>-1</sup> and 0.35–0.93 µg L<sup>-1</sup>.<sup>45</sup>

Functionalized PAFs have also been used for heavy metal ion capture, where a mercury ‘nano-trap’ was generated by functionalizing a high surface area and robust porous organic polymer with a high density of strong mercury chelating groups. The resultant porous organic polymer-based mercury ‘nano-trap’ exhibits a record-high saturation mercury uptake capacity of over 1,000 mg g<sup>-1</sup>, and can effectively reduce the mercury(II) concentration from 10 ppm to an extremely low level (less than 0.4 ppb).<sup>46</sup> T. Beng group present a study of the adsorption of selected metal ions, Sr<sup>2+</sup>, Fe<sup>3+</sup>, Nd<sup>3+</sup>, and Am<sup>3+</sup>, from aqueous solutions employing a carbon-based porous aromatic framework, BPP-7 (Berkeley Porous Polymer-7). This material displays high metal loading capacities together with excellent adsorption selectivity for neodymium over strontium.<sup>47</sup> Urea-functionalized PAF (Urea-MPN) has been applied to remove the perrhenate anion ReO<sub>4</sub><sup>-</sup> in a similar fashion to the mode of operation of the intractable anion radioactive pollutant TcO<sub>4</sub><sup>-</sup>.<sup>48</sup> These examples confirm that PAF-1 is a good backbone candidate for functionalization, allowing broad applications for absorption of analytes of interest. Furthermore, the unprecedented stability of PAFs enables their application in aqueous systems while still maintaining their properties. (Figure 1.5).

### 1.3. Fluorescence Platforms to Detect Metal Ions

#### 1.3.1 Approaches for designing transition metal-sensing fluorescent probes

One of the most remarkable scientific developments over the past decade is the ability to image individual biomolecules using optical microscopy techniques described as fluorescent single molecule detection which enables real-time, room temperature observations from cellular systems to animal studies. Single molecule fluorescent probes have allowed striking visualizations of single biomolecules at work.<sup>49,50</sup> Desirable properties of an effective fluorescent metal probe include (1) high selectivity for the metal of interest in the cellular media or upon local changes in pH, redox, and hydrophilicity/hydrophobicity and (2) high signal either from high turn-on or ratiometric shift to provide spatial information. There have been several turn-off fluorescent probes reported, however, these may provide false information because the absence of signal might result from turn-off upon interaction with the analytes of interest or due to the absence of the probe. The other important feature is (3) compatibility with common microscopy laser lines and/or filter sets with respect to excitation/emission wavelengths, being additionally desirable to have (4) visible, red-shifted spectral profiles to minimize sample photodamage and interference from native cellular autofluorescence when using blue wavelengths.

Based on these advantages of fluorescent probes, Chris Chang's group has developed several generations of fluorescent probes for labile copper pools that target Cu(I) and Cu(II). There are two strategies to access a fluorescent signal in correlation with the analytes of interest: "recognition" and "reactivity"-based fluorescence turn-on (Figure. 1.3). Recognition-based sensing utilizes a fluorophore attached to a metal receptor group that is not fluorescent in the absence of metal binding; however, upon metal coordination, the quenching mechanism is blocked and fluorescence is restored. A suitable receptor can often be designed based on coordination chemistry fundamentals, such as hard-soft acid-base theory, preferred coordination numbers, and ligand field geometries. In case of reactivity-based fluorescent probes, fluorescence turn-on occurs following a chemical reaction between the probe and metal of interest that causes the fluorophore to be uncaged. Because this approach most commonly makes use of an irreversible reaction, the fluorescent signal accumulates over time, generating high cell-retention species after the reaction. The Chang group has reported various types of copper fluorescent probes (Figure 1.6) and we would like to move to new generations of fluorescent copper probes built for protein labeling technologies.

Selective incorporation of a probe into a protein of interest (POI) usually requires several strategies.<sup>51,52</sup> (Figure 1.7) The most widely used probe is a fluorescent protein (FP), such as GFP (green fluorescent protein), which can be genetically encoded and facilitates the fluorescent monitoring of the behavior of a POI in live cells. Although such approach is quite powerful, the FP-fusion method is not applicable to natural (endogenous) proteins as it requires artificial expression of the FP-fused proteins. There are also concerns that the original properties of the POI are not retained in the FP-fused proteins as its bulky structure might interfere with the structure, function, and localization of the original proteins.<sup>53</sup> To overcome these shortcomings, the covalent labeling of proteins with synthetic small molecule probes has been developed. This strategy makes use of synthetic organic principles which has the advantages of flexible design of the probes that are amenable for NMR, IR, or Raman imaging and incorporate affinity tags or photo-crosslinking units.

There are two distinct strategies for the chemical labeling of a POI in live cells: (1) bioorthogonal chemical reactions and (2) a combination of molecular recognition and chemical reaction.<sup>54</sup> The first strategy relies completely on the selectivity of the chemical reaction. This method initially incorporates a noncanonical functional group (as a bioorthogonal reaction handle)

into a POI. The introduced reaction handle is subsequently modified using a corresponding reactant with high bioorthogonality (bioorthogonal reaction). In 2000, Bertozzi's group reported the modified Staudinger ligation between an azide and a phosphine.<sup>55</sup> Inspired by this bioorthogonality, Huisgen cycloadditions using azides/alkyne, transition metal-catalyzed bioorthogonal coupling reactions,<sup>56</sup> and inverse electron-demand Diels–Alder reactions of tetrazines with distorted alkenes/alkynes were developed.<sup>57</sup> Owing to the continuous development and improvement of such bioorthogonal reactions, the selective and efficient chemical modification of a POI in live cells has recently become possible.

The other approach other than blocking the active-site with bioorthogonal strategies has mainly been based on a proximity effect to enhance both the reaction kinetics and the selectivity. In this strategy, the proximity between a POI and a labeling reagent is mainly driven by molecular recognition by a specific recognition moiety. This recognition unit triggers a nucleophilic reaction to form a covalent bond to a POI. After forming the covalent bond between a POI and the probe, the recognition moiety can be released because it is not bound to the active sites of the enzymes or proteins. This strategy enables retention of the POI function while still providing robust information regarding metal-protein interactions..

### *1.3.2 Ligand-directed chemistry (LDAI)*

Even though the activity-based probes have advantages strategies are valuable for target identification and proteomics studies, these reagents cause the loss of the natural function of the proteins of interest. Permanent masking of the active site upon formation of a covalent bond ,results in the loss of unique structures and functions of the POI. Therefore, these methods are not appropriate to give spatial and temporal information in living systems. To preserve the functions of the POI, the Hamachi group has developed a new approach for endogenous protein labeling, termed ligand-directed (LD) chemistry.<sup>58</sup> LD chemistry is also facilitated through the proximity effect of protein–ligand recognition, with the ligand portion not being covalently linked to the POI owing to a cleavable electrophile moiety. The labeling proceeds in three steps: (1) recognition of the ligand moiety by the corresponding protein (micromolar to sub-micromolar dissociation constants are typically required); (2) the selective and accelerated reaction of the reactive electrophile on the reagent with a proximal nucleophilic amino acid on the surface of the POI; and (3) dissociation of the ligand from the labeled protein (Table 1). LD chemistry allows the activity and functions of the POI to be maintained after labeling. This is because the ligand moiety can protect nucleophiles at the active site of the POI from attacking the electrophile of the labeling reagent during labeling, and the cleaved ligand is removed from the POI after labeling. LD chemistry methods have been reported by Hamachi's group using tosyl (LDT), acyl imidazole (LDAI) and dibromophenyl benzoate (LDBB) as cleavable electrophiles. These methods exhibit distinct reactivity and amino acid selectivity. LDT chemistry employs a phenyl sulfonate (tosylate) group, which undergoes an S<sub>N</sub>2 reaction with nucleophilic amino acids, such as His, Tyr, Glu, Cys, and Asp. However, LDT chemistry has not given good results for membrane-protein labeling and sometimes suffers from slow reaction kinetics. LDAI and LDBB chemistry labels the POI through an acyl transfer reaction. LDAI chemistry showed a faster reaction rate than LDT chemistry, but it is applicable only to membrane-bound proteins. LDBB chemistry can be applied to intracellular proteins as well as cell surface membrane proteins; however, the reactive module is rather bulky and hydrophobic. Hamachi group developed a 'conditional proteomics' approach to identify proteins involved in zinc homeostasis based on a chemical proteomics strategy that utilizes designer zinc-responsive labeling reagents to tag such proteins and quantitative mass spectrometry for their

identification. Based on this LDAI chemistry, the Hamachi group applied this method to elucidate zinc dyshomeostasis, which can detect endogenous zinc induced by nitric-oxide in glioma cells, and monitored dynamic changes of the zinc-related proteome.

### **1.3. Dissertation Overview**

An interest in monitoring redox active metals in biology and environmental system led to the development of (1) solid-state frameworks for copper detection in biofluid samples applied as a Wilson's disease diagnostic tool; and (2) protein labeling fluorescent probes for monitoring cuproproteins. In addition to developing tools for redox-active metals, I have worked on preparing fluorescent probes for sodium ions and identifying methionines involved in MsrA/MsrB. Lastly, gel analysis of metalloprotein probes which is activated by metal coordination, followed by nucleophilic attack from amino acid on protein surface to identify metalloproteins. This dissertation focuses on the design, characterization, and application of two platforms for the detection of biological and environmental copper and iron for disease diagnostic tools and environmental indicators.

Chapter 2 presents the design, synthesis, characterization, and application of a copper specific porous aromatic framework (PAF-1-SMe). This chapter highlights the first use of this solid-state framework in biological systems to monitor the copper concentration in biofluid samples, with application in Wilson's disease diagnosis.

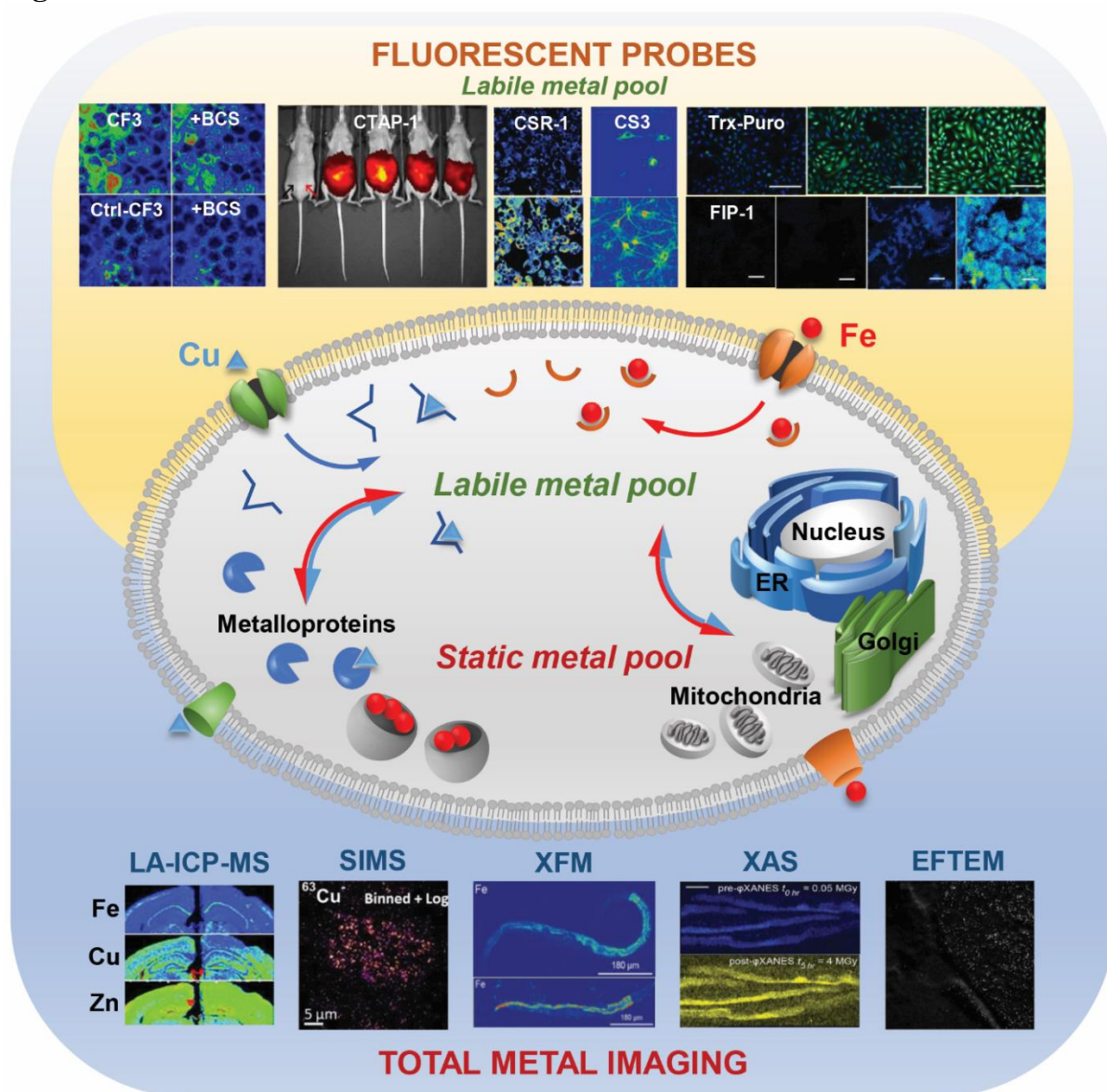
Chapter 3 presents the characterization and application of iron specific porous aromatic framework (PAF-1-ET). This chapter showed further application of a solid-state porous polymer in environmental systems to monitor iron in drinking water.

Chapter 4 discusses the labeling of copper-rich compartments in the cells and the neuronal system using LDAI chemistry. By covalently attaching Si-rhodamine to copper-rich proteins, this method provides stable information regarding the type of proteins responsible for copper efflux as well as the movement of copper within the neural system.

Chapter 5 presents several fluorescent sodium probes based on an aldehyde ether sodium receptor. This key intermediate was prepared and used to synthesize a BODIPY-based, rhodamine, and Tokyo-green fluorescent probes. We attempted to link an ester moiety to increase cell-retention and targetable moieties for mitochondria localization to visualize sodium ions in various cell lines.

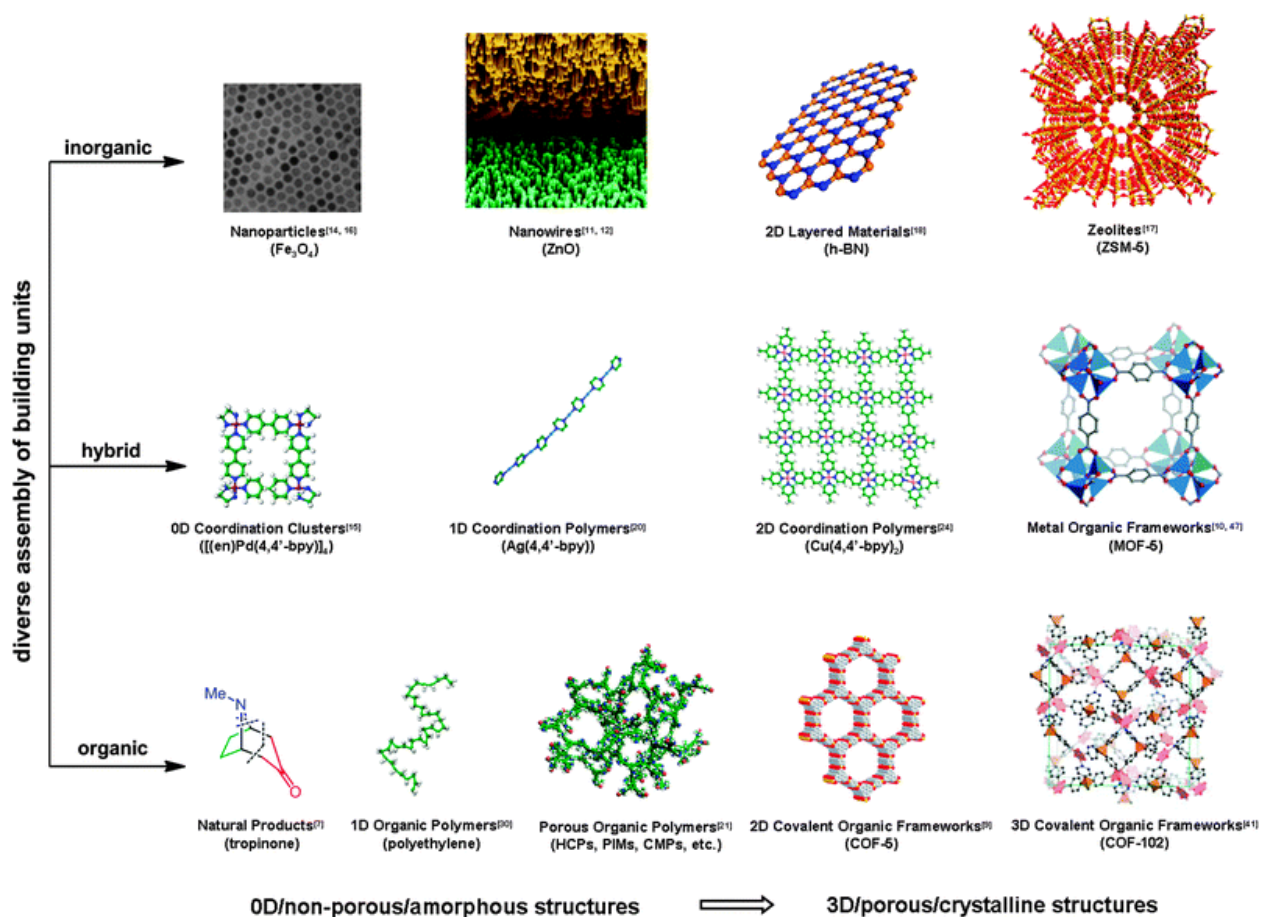
Appendices detail the development of other series of functionalized porous aromatic frameworks (Appendix 1), methionine sulfoxide profiling (Appendix 2), synthetic variation by linking electron withdrawing group to electron donating group on TPA to study Cu-triggered C-O bond cleavage (Appendix 3), and strategies for identification of novel metalloproteins using episulfide-alkyne probes. (Appendix 4).

## Figures

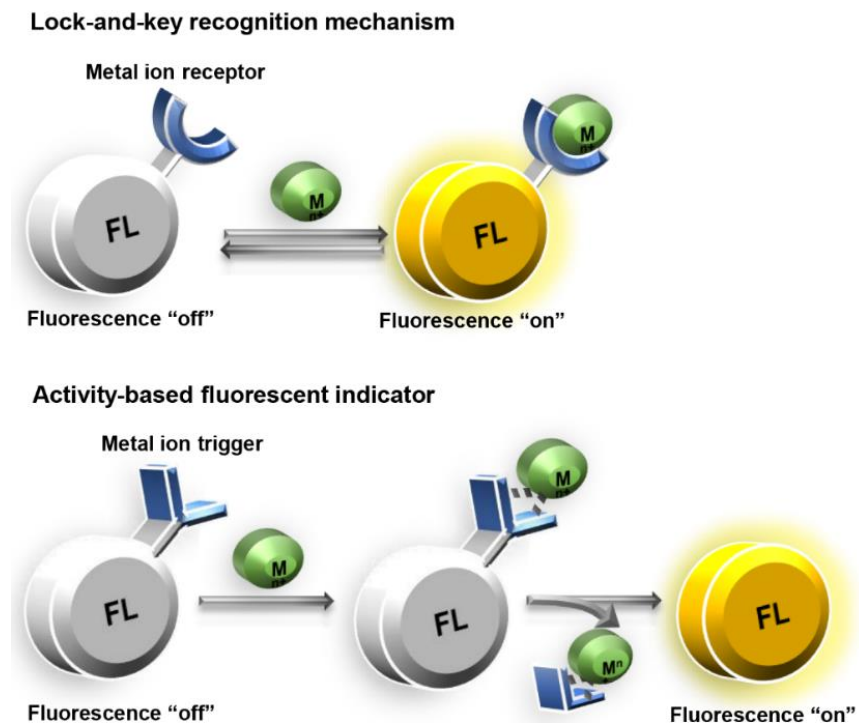


**Figure 1.1.** The total metal pool comprises the labile and static metal pools. Physical techniques that map the distribution of the total metal pool in cells, tissues, and organisms include technologies that measure atomic mass (LA-ICPMS and SIMS) and technologies that probe electronic structure (e.g., XFM, XAS, and EFTEM, among others). Fluorescent sensors map the labile metal pool. *Cited from Anal. Chem.* **2017**, *89*, 22–41

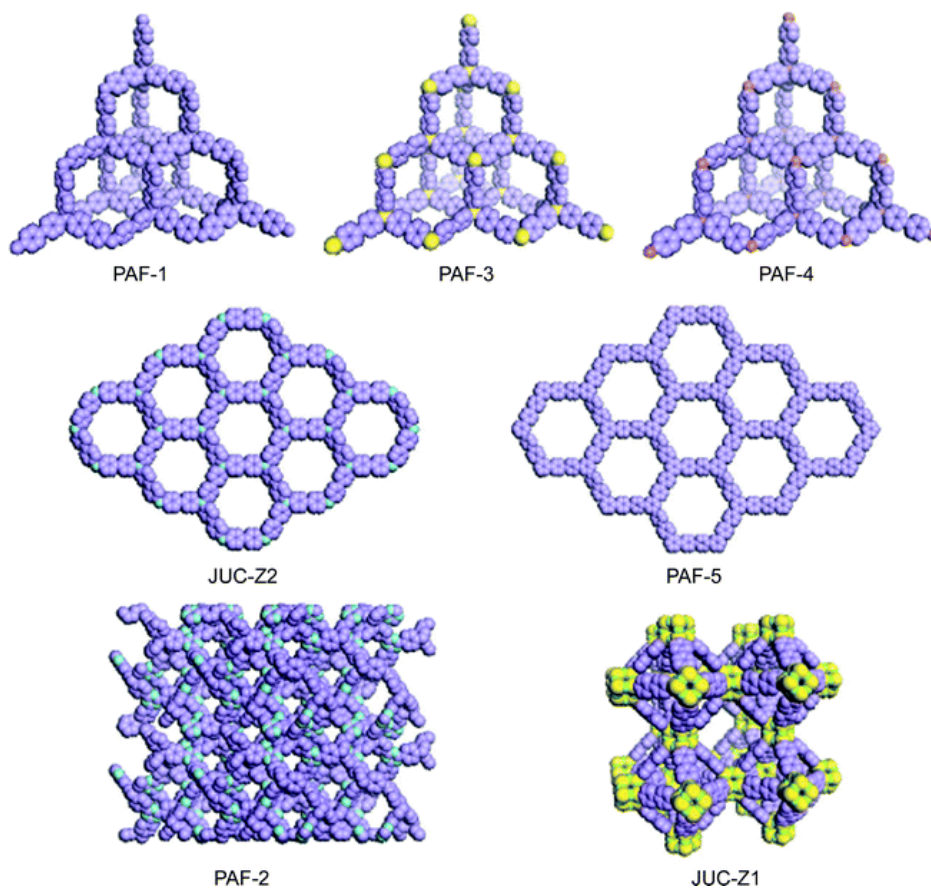




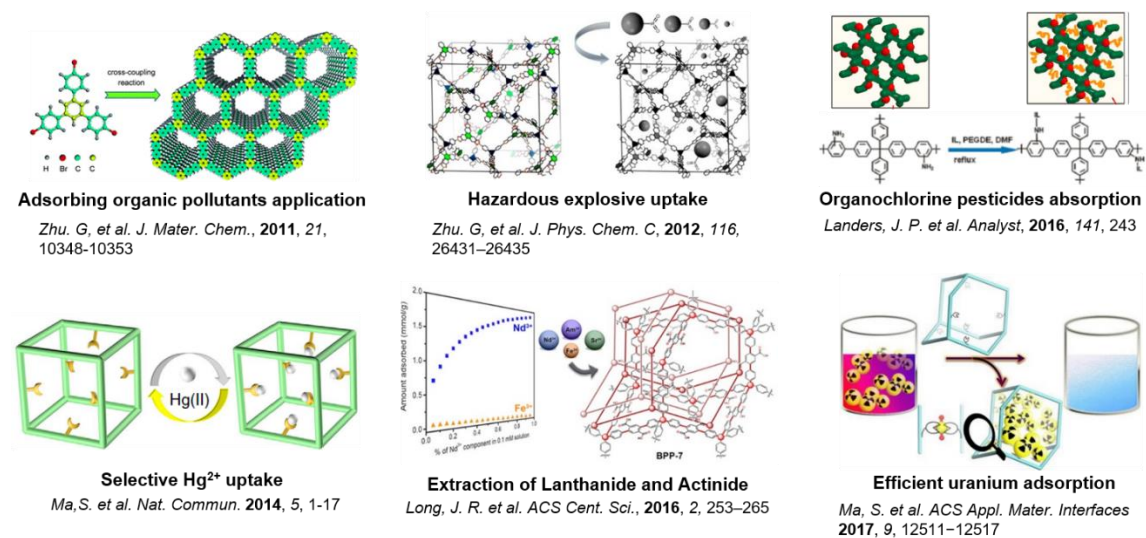
**Figure 1.2.** Selected examples for diverse assembly of building units to construct inorganic/hybrid/organic chemical architectures, ranging from the discrete 0D/non-porous/amorphous structures to the extended 3D/porous/crystalline structures. For clarity, many related systems, such as active carbons, mesoporous silicas, periodic mesoporous organosilicas, mesoporous carbons, and supermolecules, are not included herein. *Cited from Chem. Soc. Rev.*, **2013**, *42*, 548



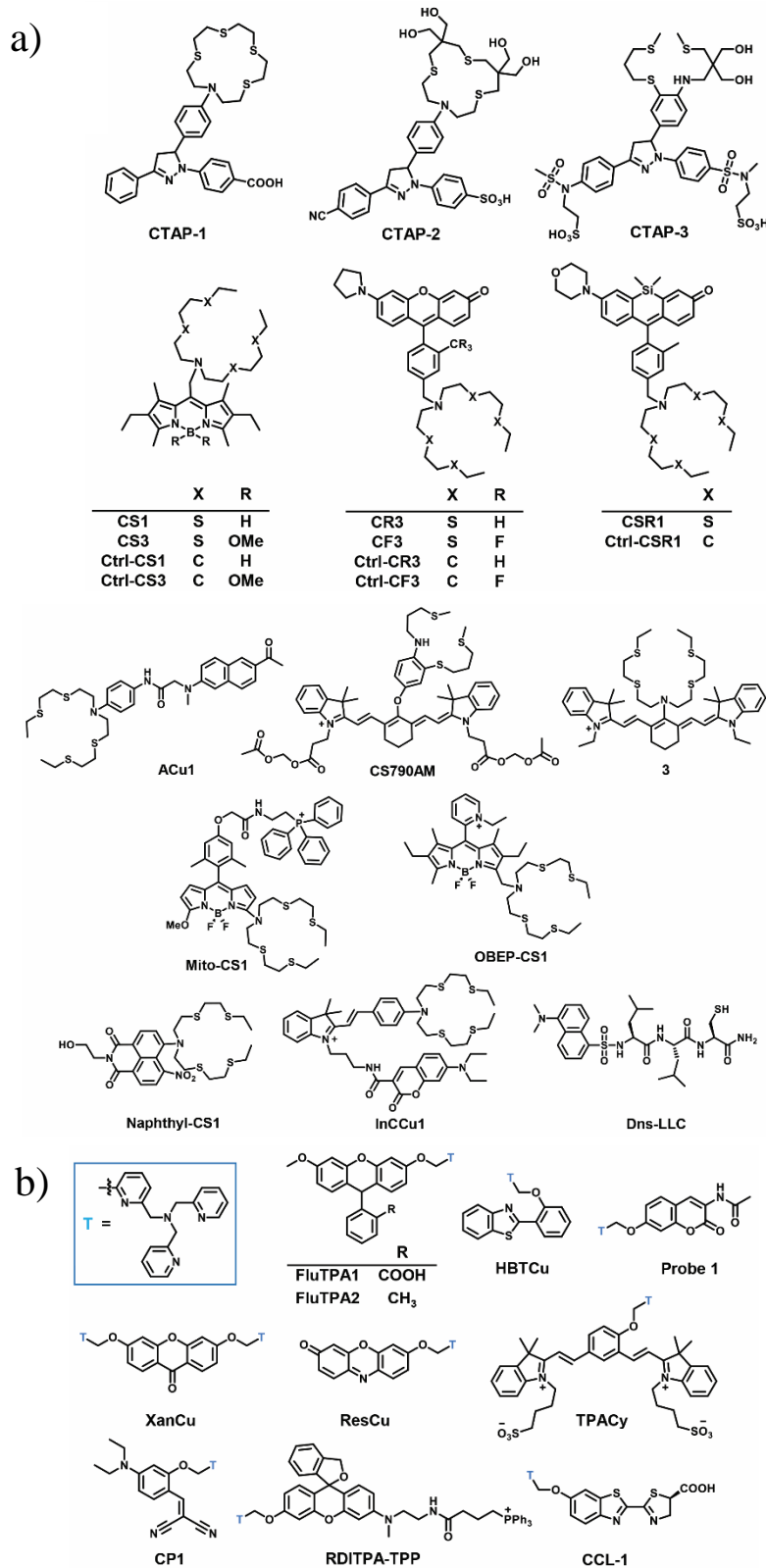
**Figure 1.5.** Illustration of recognition-based and reaction-based fluorescent sensors for metal ions. (Upper row) Recognition-based turn-on sensors fluoresce when the metal is bound; they are reversible, turning off when the metal is released. (Bottom row) Reaction-based indicators fluoresce after a metal-catalyzed, irreversible chemical event. The fluorophore does not remain associated with the metal after the reaction takes place. *Cited from Anal. Chem.* **2017**, *89*, 22–41



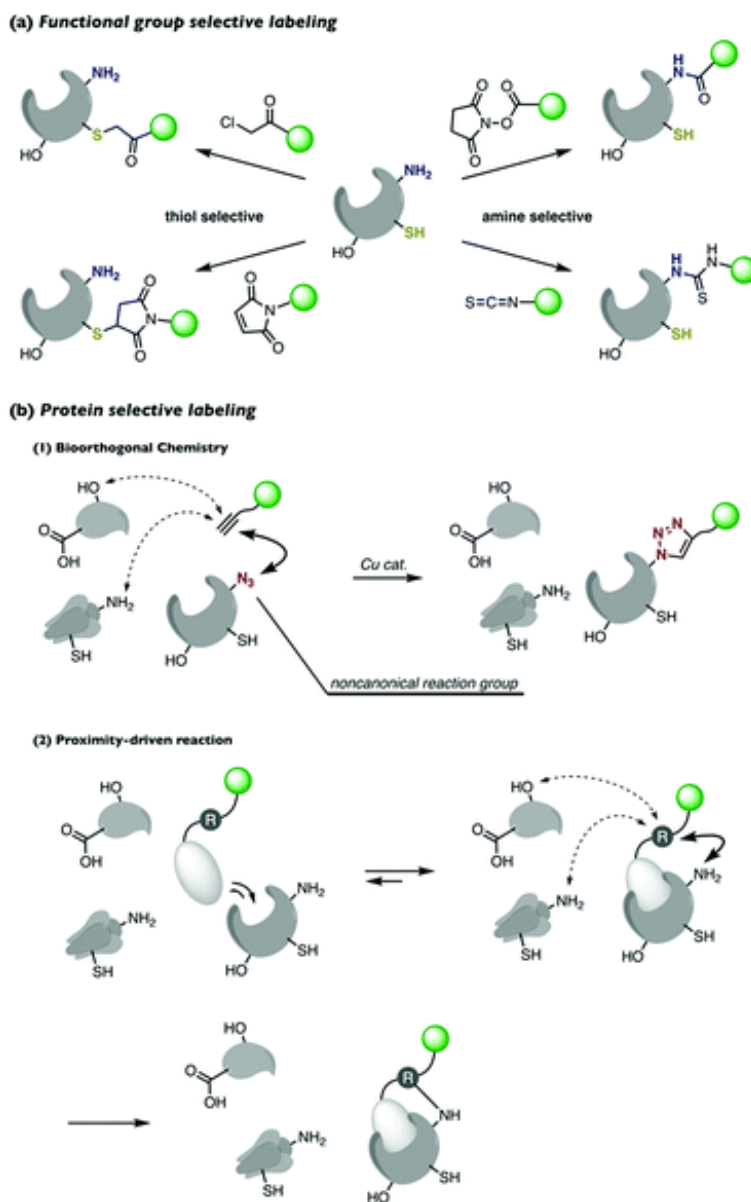
**Figure 1.4.** Structure model of synthesized and simulated PAF. (C, purple; N, blue; Si, yellow, O, green, Ge, brown). *Cited from CrystEngComm, 2013, 15, 17–26*



**Figure 1.5.** Examples of functionalized Porous Aromatic Framework (PAF) for organic molecules uptake (upper row) and heavy metal uptake (bottom row) in aqueous conditions.

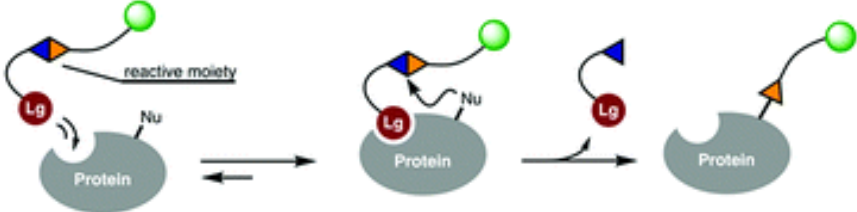


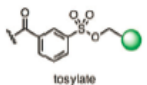
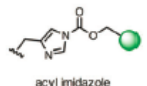
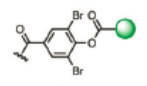
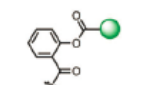
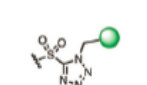
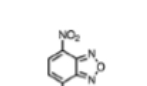
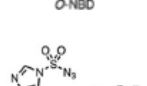
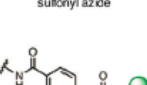
**Figure 1.6.** Fluorescent probes for copper (I): a) recognition based and b) reactivity based probes. Cited from *Anal. Chem.* **2017**, *89*, 22–41



**Figure 1.7.** Outline of protein labelling with synthetic small molecule probes: (a) functional group selective labeling (e.g. thiol or amine); (b) (1) bioorthogonal chemical reaction (e.g. Huisgen cycloaddition), (2) combination of molecular recognition and chemical reaction. *Cited from Chem. Commun., 2017, 53, 11972-11983*

**Table 1.1.** Protein labeling of LD chemistry



Reactive group	Modified proteins	Labeled amino acid	Binding affinity	Labeling time (h)	Condition
	hCAI, hCAII, FKBP12, Congerin II, Hsc70, SH2 domain, 14-3-3, HER2, NADH-quinone oxidoreductase	His, Tyr, Cys, Glu, Asp	$K_d < 43.5 \mu\text{M}$	> 10	Test tube, intracellular, tissue, <i>in vivo</i>
	FR, hCAII, hCAIX, hCAXII, B <sub>2</sub> R, NMDAR, AMPAR, GABAR, mGluR	Lys, Ser, Tyr	$K_d < 5.3 \mu\text{M}$	3–6	Test tube, cell surface, tissue
	hCAII, hCAXII, eDHFR	Lys, His	$K_i < 0.26 \mu\text{M}$	1–3	Test tube, cell surface, intracellular
	Actin	Lys	$K_d = 0.12 \mu\text{M}$	12	Test tube, intracellular
	Cyclophilin A	Not identified	$K_d = 36.8 \text{ nM}$	24	Cell lysate
	Avidin, VDAC	Lys	$K_d < 1.4 \text{ nM}$	1	Test tube, intracellular
	Streptavidin, avidin	Lys	$K_t < 0.3 \text{ nM}$	1	Cell lysate, cell surface
 + acidic and basic residues	hCAI, COX-1	Lys	$K_i < 3.4 \mu\text{M}$	48	Test tube, intracellular

**Table 1.1** Summary of the Ligand-Directed (LD) Chemistry. *Cited from Chem. Commun., 2017, 53, 11972-11983*

## 1.4. References

- (1) Li, Y.-F.; Chen, C.; Qu, Y.; Gao, Y.; Li, B.; Zhao, Y.; Chai, Z. Metallomics, Elementomics, and Analytical Techniques. *Pure Appl. Chem.* **2008**, *80* (12), 2577–2594.
- (2) Ascone, I.; Strange, R. Biological X-Ray Absorption Spectroscopy and Metalloproteomics. *J. Synchrotron Radiat.* **2009**, *16* (3), 413–421.
- (3) Finney, L. A.; O'Halloran, T. V. Transition Metal Speciation in the Cell: Insights from the Chemistry of Metal Ion Receptors. *Science* **2003**, *300* (5621), 931–936.
- (4) Gray, H. B.; Winkler, J. R. Electron Flow through Metalloproteins. *Biochim. Biophys. Acta BBA - Bioenerg.* **2010**, *1797* (9), 1563–1572.
- (5) Liu, J.; Chakraborty, S.; Hosseinzadeh, P.; Yu, Y.; Tian, S.; Petrik, I.; Bhagi, A.; Lu, Y. Metalloproteins Containing Cytochrome, Iron–Sulfur, or Copper Redox Centers. *Chem. Rev.* **2014**, *114* (8), 4366–4469.
- (6) McRae, R.; Bagchi, P.; Sumalekshmy, S.; Fahrni, C. J. In Situ Imaging of Metals in Cells and Tissues. *Chem. Rev.* **2009**, *109* (10), 4780–4827.
- (7) Dancis, A.; Yuan, D. S.; Haile, D.; Askwith, C.; Eide, D.; Moehle, C.; Kaplan, J.; Klausner, R. D. Molecular Characterization of a Copper Transport Protein in *S. Cerevisiae*: An Unexpected Role for Copper in Iron Transport. *Cell* **1994**, *76* (2), 393–402.
- (8) Bush, A. I. Metals and Neuroscience. *Curr. Opin. Chem. Biol.* **2000**, *4* (2), 184–191.
- (9) Vella, F. Principles of Bioinorganic Chemistry: By S J Lippard and J M Berg. Pp 411. University Science Books, Mill Valley, California. 1994. \$30 ISBN 0-935702-73-3 (Paper). *Biochem. Educ.* **1995**, *23* (2), 115–115.
- (10) Cvetkovic, A.; Menon, A. L.; Thorgersen, M. P.; Scott, J. W.; Ii, F. L. P.; Jr, F. E. J.; Lancaster, W. A.; Praissman, J. L.; Shanmukh, S.; Vaccaro, B. J.; et al. Microbial Metalloproteomes Are Largely Uncharacterized. *Nature* **2010**, *466* (7307), 779–782.
- (11) Yannone, S. M.; Hartung, S.; Menon, A. L.; Adams, M. W.; Tainer, J. A. Metals in Biology: Defining Metalloproteomes. *Curr. Opin. Biotechnol.* **2012**, *23* (1), 89–95.
- (12) Waldron, K. J.; Rutherford, J. C.; Ford, D.; Robinson, N. J. Metalloproteins and Metal Sensing. *Nature* **2009**, *460*, 823.
- (13) Irving, H.; Williams, R. J. P. Order of Stability of Metal Complexes. *Nature* **1948**, *162* (4123), 746–747.
- (14) Andreini, C.; Bertini, I.; Cavallaro, G.; Holliday, G. L.; Thornton, J. M. Metal Ions in Biological Catalysis: From Enzyme Databases to General Principles. *JBIC J. Biol. Inorg. Chem.* **2008**, *13* (8), 1205–1218.
- (15) Hart, P. J.; Balbirnie, M. M.; Ogihara, N. L.; Nersissian, A. M.; Weiss, M. S.; Valentine, J. S.; Eisenberg, D. A Structure-Based Mechanism for Copper–Zinc Superoxide Dismutase. *Biochemistry (Mosc.)* **1999**, *38* (7), 2167–2178.
- (16) Opazo, C. M.; Greenough, M. A.; Bush, A. I. Copper: From Neurotransmission to Neuroproteostasis. *Front. Aging Neurosci.* **2014**, *6*.
- (17) Weber, K. A.; Achenbach, L. A.; Coates, J. D. Microorganisms Pumping Iron: Anaerobic Microbial Iron Oxidation and Reduction. *Nat. Rev. Microbiol.* **2006**, *4* (10), 752–764.
- (18) Spangler, B.; Morgan, C. W.; Fontaine, S. D.; Vander Wal, M. N.; Chang, C. J.; Wells, J. A.; Renslo, A. R. A Reactivity-Based Probe of the Intracellular Labile Ferrous Iron Pool. *Nat. Chem. Biol.* **2016**, *12* (9), 680–685.
- (19) Hentze, M. W.; Muckenthaler, M. U.; Andrews, N. C. Balancing Acts. *Cell* **2004**, *117* (3), 285–297.



- (20) Dixon, S. J.; Stockwell, B. R. The Role of Iron and Reactive Oxygen Species in Cell Death. *Nat. Chem. Biol.* **2014**, *10* (1), 9–17.
- (21) Chang, C. J. Searching for Harmony in Transition-Metal Signaling. *Nat. Chem. Biol.* **2015**, *11* (10), 744–747.
- (22) Kew, M. C. Hepatic Iron Overload and Hepatocellular Carcinoma. *Liver Cancer* **2014**, *3* (1), 31–40.
- (23) Kurz, T.; Eaton, J. W.; Brunk, U. T. The Role of Lysosomes in Iron Metabolism and Recycling. *Int. J. Biochem. Cell Biol.* **2011**, *43* (12), 1686–1697.
- (24) Theil, E. C.; Goss, D. J. Living with Iron (and Oxygen): Questions and Answers about Iron Homeostasis. *Chem. Rev.* **2009**, *109* (10), 4568–4579.
- (25) Salonen, J. T.; Nyssönen, K.; Korpela, H.; Tuomilehto, J.; Seppänen, R.; Salonen, R. High Stored Iron Levels Are Associated with Excess Risk of Myocardial Infarction in Eastern Finnish Men. *Circulation* **1992**, *86* (3), 803–811.
- (26) Arezzini, B.; Lunghi, B.; Lungarella, G.; Gardi, C. Iron Overload Enhances the Development of Experimental Liver Cirrhosis in Mice. *Int. J. Biochem. Cell Biol.* **2003**, *35* (4), 486–495.
- (27) Carrier, J.; Aghdassi, E.; Cullen, J.; Allard, J. P. Iron Supplementation Increases Disease Activity and Vitamin E Ameliorates the Effect in Rats with Dextran Sulfate Sodium-Induced Colitis. *J. Nutr.* **2002**, *132* (10), 3146–3150.
- (28) Martins, S.; Logan, S.; Gilbert, R. E. Iron Therapy for Improving Psychomotor Development and Cognitive Function in Children under the Age of Three with Iron Deficiency Anaemia. In *Cochrane Database of Systematic Reviews*; The Cochrane Collaboration, Ed.; John Wiley & Sons, Ltd: Chichester, UK, 2001.
- (29) Brewer, G. J. Risks of Copper and Iron Toxicity during Aging in Humans. *Chem. Res. Toxicol.* **2010**, *23* (2), 319–326.
- (30) Hoffbrand, A. V.; Cohen, A.; Hershko, C. Role of Deferiprone in Chelation Therapy for Transfusional Iron Overload. *Blood* **2003**, *102* (1), 17–24.
- (31) Dixon, S. J.; Lemberg, K. M.; Lamprecht, M. R.; Skouta, R.; Zaitsev, E. M.; Gleason, C. E.; Patel, D. N.; Bauer, A. J.; Cantley, A. M.; Yang, W. S.; et al. Ferroptosis: An Iron-Dependent Form of Nonapoptotic Cell Death. *Cell* **2012**, *149* (5), 1060–1072.
- (32) Ackerman, C. M.; Lee, S.; Chang, C. J. Analytical Methods for Imaging Metals in Biology: From Transition Metal Metabolism to Transition Metal Signaling. *Anal. Chem.* **2017**, *89* (1), 22–41.
- (33) Jiang, J.-X.; Trewin, A.; Su, F.; Wood, C. D.; Niu, H.; Jones, J. T. A.; Khimyak, Y. Z.; Cooper, A. I. Microporous Poly(tri(4-Ethynylphenyl)amine) Networks: Synthesis, Properties, and Atomistic Simulation. *Macromolecules* **2009**, *42* (7), 2658–2666.
- (34) El-Kaderi, H. M.; Hunt, J. R.; Mendoza-Cortés, J. L.; Côté, A. P.; Taylor, R. E.; O’Keeffe, M.; Yaghi, O. M. Designed Synthesis of 3D Covalent Organic Frameworks. *Science* **2007**, *316* (5822), 268–272.
- (35) Ben, T.; Ren, H.; Ma, S.; Cao, D.; Lan, J.; Jing, X.; Wang, W.; Xu, J.; Deng, F.; Simmons, J. M.; et al. Targeted Synthesis of a Porous Aromatic Framework with High Stability and Exceptionally High Surface Area. *Angew. Chem. Int. Ed.* **2009**, *48* (50), 9457–9460.
- (36) Budd, P. M.; Ghanem, B. S.; Makhseed, S.; McKeown, N. B.; Msayib, K. J.; Tattershall, C. E. Polymers of Intrinsic Microporosity (PIMs): Robust, Solution-Processable, Organic Nanoporous Materials. *Chem. Commun.* **2004**, *0* (2), 230–231.

- (37) Sumida, K.; Rogow, D. L.; Mason, J. A.; McDonald, T. M.; Bloch, E. D.; Herm, Z. R.; Bae, T.-H.; Long, J. R. Carbon Dioxide Capture in Metal–Organic Frameworks. *Chem. Rev.* **2012**, *112* (2), 724–781.
- (38) Ding, S.-Y.; Wang, W. Covalent Organic Frameworks (COFs): From Design to Applications. *Chem. Soc. Rev.* **2013**, *42* (2), 548–568.
- (39) Feng, X.; Ding, X.; Jiang, D. Covalent Organic Frameworks. *Chem. Soc. Rev.* **2012**, *41* (18), 6010–6022.
- (40) Zhou, H.-C. “Joe”; Kitagawa, S. Metal–Organic Frameworks (MOFs). *Chem. Soc. Rev.* **2014**, *43* (16), 5415–5418.
- (41) Ben, T.; Qiu, S. Porous Aromatic Frameworks: Synthesis, Structure and Functions. *CrystEngComm* **2012**, *15* (1), 17–26.
- (42) Jolly, W. L. *Preparative Inorganic Reactions*; Interscience Publishers: New York, 1964.
- (43) Yuan, Y.; Ren, H.; Sun, F.; Jing, X.; Cai, K.; Zhao, X.; Wang, Y.; Wei, Y.; Zhu, G. Targeted Synthesis of a 3D Crystalline Porous Aromatic Framework with Luminescence Quenching Ability for Hazardous and Explosive Molecules. *J. Phys. Chem. C* **2012**, *116* (50), 26431–26435.
- (44) Ren, H.; Ben, T.; Sun, F.; Guo, M.; Jing, X.; Ma, H.; Cai, K.; Qiu, S.; Zhu, G. Synthesis of a Porous Aromatic Framework for Adsorbing Organic Pollutants Application. *J. Mater. Chem.* **2011**, *21* (28), 10348–10353.
- (45) Wu, M.; Chen, G.; Liu, P.; Zhou, W.; Jia, Q. Preparation of Porous Aromatic Framework/Ionic Liquid Hybrid Composite Coated Solid-Phase Microextraction Fibers and Their Application in the Determination of Organochlorine Pesticides Combined with GC-ECD Detection. *Analyst* **2015**, *141* (1), 243–250.
- (46) Li, B.; Zhang, Y.; Ma, D.; Shi, Z.; Ma, S. Mercury Nano-Trap for Effective and Efficient Removal of mercury(II) from Aqueous Solution. *Nat. Commun.* **2014**, *5*, ncomms6537.
- (47) Demir, S.; Brune, N. K.; Van Humbeck, J. F.; Mason, J. A.; Plakhova, T. V.; Wang, S.; Tian, G.; Minasian, S. G.; Tylliszczak, T.; Yaita, T.; et al. Extraction of Lanthanide and Actinide Ions from Aqueous Mixtures Using a Carboxylic Acid-Functionalized Porous Aromatic Framework. *ACS Cent. Sci.* **2016**, *2* (4), 253–265.
- (48) Shen, J.; Chai, W.; Wang, K.; Zhang, F. Efficient Removal of Anionic Radioactive Pollutant from Water Using Ordered Urea-Functionalized Mesoporous Polymeric Nanoparticle. *ACS Appl. Mater. Interfaces* **2017**, *9* (27), 22440–22448.
- (49) Tsien, R. Y. Fluorescent Probes of Cell Signaling. *Annu. Rev. Neurosci.* **1989**, *12* (1), 227–253.
- (50) Kapanidis, A. N.; Weiss, S. Fluorescent Probes and Bioconjugation Chemistries for Single-Molecule Fluorescence Analysis of Biomolecules. *J. Chem. Phys.* **2002**, *117* (24), 10953–10964.
- (51) Arnau, J.; Lauritzen, C.; Petersen, G. E.; Pedersen, J. Current Strategies for the Use of Affinity Tags and Tag Removal for the Purification of Recombinant Proteins. *Protein Expr. Purif.* **2006**, *48* (1), 1–13.
- (52) Day, R. N.; Davidson, M. W. The Fluorescent Protein Palette: Tools for Cellular Imaging. *Chem. Soc. Rev.* **2009**, *38* (10), 2887–2921.
- (53) Morin, X.; Daneman, R.; Zavortink, M.; Chia, W. A Protein Trap Strategy to Detect GFP-Tagged Proteins Expressed from Their Endogenous Loci in *Drosophila*. *Proc. Natl. Acad. Sci.* **2001**, *98* (26), 15050–15055.

- (54) Cravatt, B. F.; Wright, A. T.; Kozarich, J. W. Activity-Based Protein Profiling: From Enzyme Chemistry to Proteomic Chemistry. *Annu. Rev. Biochem.* **2008**, *77* (1), 383–414.
- (55) Saxon, E.; Bertozzi, C. R. Cell Surface Engineering by a Modified Staudinger Reaction. *Science* **2000**, *287* (5460), 2007–2010.
- (56) Yang, M.; Li, J.; Chen, P. R. Transition Metal-Mediated Bioorthogonal Protein Chemistry in Living Cells. *Chem. Soc. Rev.* **2014**, *43* (18), 6511–6526.
- (57) Sletten, E. M.; Bertozzi, C. R. Bioorthogonal Chemistry: Fishing for Selectivity in a Sea of Functionality. *Angew. Chem. Int. Ed.* **2009**, *48* (38), 6974–6998.
- (58) Matsuo, K.; Hamachi, I. Ligand-Directed Tosyl and Acyl Imidazole Chemistry. In *Chemoselective and Bioorthogonal Ligation Reactions*; Algar, W. R., Dawson, P. E., Medintz, I. L., Eds.; Wiley-VCH Verlag GmbH & Co. KGaA, 2017; pp 147–163.

## Chapter 2

### **Copper Capture in a Thioether-Functionalized Porous Polymer Applied to the Detection of Wilson's Disease**

Portions of this work were published in the following scientific journal:

Lee, S.; Barin, G.; Ackerman, C. M.; Muchenditsi, A.; Xu, J.; Reimer, J. A.; Lutsenko, S.; Long, J. R.; Chang, C. J. "Copper Capture in a Thioether-Functionalized Porous Polymer Applied to the Detection of Wilson's Disease", *J. Am. Chem. Soc.* **2016**, *138*, 7603-7609.

## Abstract

Copper is an essential nutrient for life, but at the same time hyperaccumulation of this redox-active metal in biological fluids and tissues is a hallmark of pathologies such as Wilson's and Menkes diseases, various neurodegenerative diseases, and toxic environmental exposure. Diseases characterized by copper hyperaccumulation are currently challenging to identify due to costly diagnostic tools that involve extensive technical workup. Motivated to create simple yet highly selective and sensitive diagnostic tools, we have initiated a program to develop new materials that can enable monitoring of copper levels in biological fluid samples without complex and expensive instrumentation. Herein, we report the design, synthesis, and properties of PAF-1-SMe, a robust diamondoid porous aromatic framework (PAF) densely functionalized with thioether groups for selective capture and concentration of copper from biofluids as well as aqueous samples. PAF-1-SMe exhibits a high selectivity for copper over other biologically-relevant metals, with a saturation capacity reaching over 600 mg/g. More-over, the combination of PAF-1-SMe as a material for concentration and capture of copper from biological samples with 8-hydroxyquinoline as a colorimetric indicator affords a method for identifying aberrant elevations of copper in urine samples from mice with Wilson's disease and also tracing exogenously added copper in serum. This divide-and-conquer sensing strategy, where functional and robust porous materials serve as molecular recognition elements that can be used to capture and concentrate analytes in conjunction with molecular indicators for signal readouts, establishes a valuable starting point for the use of porous polymer materials in non-invasive diagnostic applications.

## 2.1. Introduction

Copper is an essential element for human health,<sup>1</sup> and enzymes harness the redox activity of this metal to perform functions spanning energy generation, neurotransmitter and pigment synthesis, and epigenetic modification. On the other hand, misregulation of copper homeostasis is also connected to many diseases, including cancer,<sup>2</sup> neurodegenerative Alzheimer's, Parkinson's, and Huntington's diseases,<sup>3</sup> and genetic disorders such as Menkes and Wilson's diseases.<sup>4</sup> Technologies that can monitor copper homeostasis may therefore serve as valuable diagnostic tools for these diseases and related conditions. In one example of a copper-mediated disorder, Wilson's disease is caused by mutation of the gene that encodes the copper transporter ATP7B protein. Mutations in this protein may lead to hyperaccumulation of copper in the liver, brain, kidney, and cornea, which can result in lipid peroxidation and corresponding liver damage as well as neurologic and psychiatric abnormalities.<sup>4-6</sup> Patients suffering from Wilson's disease also exhibit high urinary copper levels (>100 mg/day, compared to 20-40 mg/day in healthy individuals) and increased serum free copper levels (>25  $\mu\text{g/dL}$ , compared to 11-25  $\mu\text{g/dL}$  in healthy individuals).<sup>4</sup> The source of this elevated copper is not sufficiently understood, but it is thought to derive from necrosis of damaged liver cells that are cleared through the blood stream.<sup>5</sup>

Wilson's disease is potentially fatal, although it is readily treated if diagnosed early in its development and before extensive tissue damage has occurred. Recognizing Wilson's disease is a challenge all its own, however, owing to a lack of targeted and readily implemented diagnostic tools. Magnetic resonance imaging (MRI) and electroencephalography (EEG) are two non-invasive techniques currently used to aid in Wilson's diagnosis; however, these techniques are not specific for Wilson's disease and instead serve primarily to identify secondary characteristics. While genetic tests can offer highly accurate diagnoses, over 300 different mutations for Wilson's

disease are listed in the Human Genome Organization database and only a few are fully characterized or widespread. Thus, genetic tests based on selected exons are not globally applicable.<sup>7</sup> In contrast, non-invasive tests on biofluids such as urine and blood can alternatively provide an accurate diagnosis, although these methods can require cumbersome extraction procedures that include the concentration of urine collected over 24 hours or acid digestion of serum. Expensive characterization methods such as inductively coupled plasma mass spectrometry (ICP-MS) or atomic absorption spectroscopy (AAS) are then used for direct copper detection.<sup>6-9</sup>

We therefore envisioned an alternative approach that would enable copper detection and readout of corresponding levels directly from biofluids as well as environmental samples in a colorimetric assay, thereby circumventing extensive sample processing. This strategy relies on the utilization of solid-state adsorbents to capture copper selectively and efficiently from the biosample of interest followed by treatment with a colorimetric agent to quantify copper levels. We anticipate that such a divide-and-conquer approach should be broadly applicable to detection of many biological and environmental analytes. In this context, porous polymers represent a promising class of such adsorbents for this purpose, owing to their high thermal and chemical stability, particularly to aqueous media, as well as high surface area, permanent porosity, and diversity of functional groups.<sup>10-15</sup> The canonical material porous aromatic framework (PAF)-1 in particular exhibits a high Brunauer-Emmett-Teller (BET) surface area (up to 5600 m<sup>2</sup>/g)<sup>14</sup> and is readily modified post-synthetically to introduce a variety of desired chemical functionalities in a dense and accessible manner.<sup>15</sup> Indeed, an elegant thiol (–SH) functionalized PAF-1 was recently reported as an effective and efficient platform for the capture of the toxic heavy metal mercury in water treatment.<sup>16</sup> We sought to prepare a new PAF-1 analog with copper-selective appendages to allow for specific and sensitive capture of this naturally occurring biological metal from biofluid samples. Inspection of copper binding sites in cytosolic metalloregulatory proteins show that they are dominated by histidine, cysteine, and methionine residues,<sup>17</sup> which feature –NH, –SH, and thioether (–SMe) functionalities, respectively. We reasoned that thioethers are less redox-active and pH-independent compared to their thiol counterparts and are also advantageous over nitrogen-containing binding moieties, such as histidine, to achieve high copper selectivity over other biologically relevant cations like Fe(II) and Zn(II). Indeed, our laboratory has previously reported synthetic fluorescent<sup>18,19</sup> and MRI copper probes<sup>20,21</sup> with thioether rich receptors, which revealed high selectivity towards copper ions in biological samples from cells to tissues to whole organisms. We now report the thioether-functionalized solid-state porous polymer PAF-1-SMe, an adsorbent that is selective for the capture and concentration of copper from complex biofluid samples. In conjunction with a colorimetric reagent for assessing copper levels, we further demonstrate that PAF-1-SMe can be used in an assay to selectively adsorb copper and detect elevated copper levels in biosamples (Scheme 2.1). This work establishes the potential utility of porous polymeric materials for non-invasive diagnostic applications, without the need for extensive sample processing or complex and expensive instrumentation.

## 2.2. Methods

### 2.2.1. General Method

Starting materials and reagents were purchased from Sigma-Aldrich and used as received without further purification. Tetrakis(4-bromophenyl)methane was prepared following the procedure reported in the literature.<sup>1</sup> All reactions were performed under a nitrogen or argon atmosphere and in dry solvents, unless otherwise stated

*Gas adsorption isotherms* were measured using a Micromeritics ASAP 2020 or 2040 instrument. Samples were transferred to a pre-weighed glass analysis tube, which was capped with a Transeal, and were evacuated on the ASAP until the outgas rate was less than 3  $\mu\text{bar}/\text{min}$ . Ultrahigh-purity grade (99.999%) nitrogen was used for gas adsorption measurements. Nitrogen isotherms were obtained using a 77 K liquid- $\text{N}_2$  bath and used to determine the surface areas and pore volumes using the Micromeritics software, assuming a value of  $16.2 \text{ \AA}^2$  for the molecular cross-sectional area of  $\text{N}_2$ . Pore-size distributions were calculated using the density functional theory method with a QSDFT adsorption branch model of  $\text{N}_2$  at 77 K adsorbed in carbon with slit/cylindrical/spherical pores, as implemented in the Quantachrome VersaWin software.

*Infrared spectra* were obtained on a Perkin-Elmer Spectrum 100 Optica FTIR spectrometer furnished with an attenuated total reflectance accessory.

*Thermal gravimetric analysis* (TGA) data was collected at ramp rates of  $5 \text{ }^\circ\text{C}/\text{min}$  under flowing nitrogen using a TA Instruments TGA Q5000.

*Diffraction data* were collected with  $0.2^\circ$  steps using a Bruker AXS D8 Advance diffractometer equipped with Cu- $\text{K}\alpha$  radiation ( $\lambda = 1.5418 \text{ \AA}$ ).

*Scanning electron microscopy* (SEM) samples of polymers were prepared by dispersing fine powders into methanol and drop casting onto a silicon chip. To dissipate charge, the samples were sputter coated with approximately 3 nm of Au (Denton Vacuum). Polymers were imaged at 5 keV and 12  $\mu\text{A}$  by field emission SEM (JEOL FSM6430).

*Carbon, hydrogen, nitrogen, and sulfur elemental analyses* were obtained from the Microanalytical Laboratory at the University of California, Berkeley. Elemental analysis for chlorine was performed at Galbraith Laboratories.

*Solid state NMR spectra*  $^1\text{H}$ - $^{13}\text{C}$  cross-polarization (CP) spectra were collected on a 7.05 Tesla magnet at  $^{13}\text{C}$  frequency of 75.5 MHz under 10 kHz magic-angle spinning (MAS) condition. A Chemagnetics 4 mm H/X probe and a Tecmag Discovery spectrometer were used. The Hartmann-Hahn condition for CP experiments was obtained on solid adamantane, which is also a secondary reference of  $^{13}\text{C}$  chemical shift (the methylene signal of adamantane was set to 38.48 ppm relative to TMS). Two pulse phase modulation (TPPM) proton decoupling scheme was used. The TPPM angle was 15 degree and the decoupling field strength was  $\sim 60 \text{ kHz}$ . A contact time of 10 ms and a pulse delay of 4 s were used in CP experiments.

*EPR* measurement were recorded at ambient temperature using an Active Spectrum X-band continuous wave spectrometer. The sweep was from 210 mT to 420 mT.

*UV-Vis spectroscopic measurements* were performed in 100 mM HEPES buffer (pH 6.7). Absorption spectra were recorded using a Varian Cary 50 spectrophotometer and samples for absorption measurements were prepared in  $1 \text{ cm} \times 0.5 \text{ cm}$  quartz cuvettes (1.4-mL volume, Starna).

*Inductively coupled plasma-mass spectrometry* (ICP-MS) was performed on samples that had been diluted into 2% nitric acid (made freshly from concentrated nitric acid (BDH Aristar Ultra) and MilliQ water) containing 20 ppb Ga internal standard (Inorganic Ventures, Christiansburg, VA). The samples were analyzed on a ThermoFisher iCAP-Qc ICP-MS in Kinetic Energy Discrimination (KED) mode against a calibration curve of known metal concentrations (made from CMS-5, Inorganic Ventures, Christiansburg, VA).

### 2.2.2. Synthesis of PAF-1-SMe

Anhydrous 1,5-cyclooctadiene (cod, 1.05 mL, 8.32 mmol, Aldrich) was added to a solution of bis(1,5-cyclooctadiene)nickel(0) (2.25 g, 8.18 mmol, Aldrich) and dried 2,2'-bipyridyl (1.28 g, 8.18 mmol, Aldrich) in distilled DMF (100 mL, Aldrich) in a dry box. The mixture was heated at 80 °C for 1 h. Tetrakis(4-bromophenyl)methane (1 g, 1.57 mmol) was added to the purple solution and the mixture was stirred at 80 °C overnight to obtain a deep purple suspension. After cooling to room temperature, concentrated HCl was added to the mixture. The residue was filtered with washing with warm THF (100 mL), H<sub>2</sub>O (100 mL), ethanol (100 mL), and CH<sub>3</sub>Cl (100 mL) respectively, and dried in vacuum oven (170 °C) to give PAF-1 as an off white powder. A pressure flask was charged with PAF-1 (200.0 mg), paraformaldehyde (1.0 g), glacial AcOH (6.0 ml), H<sub>3</sub>PO<sub>4</sub> (3.0 ml) and conc. HCl (20.0 ml). The flask was sealed and heated to 100 °C for 3 days. The resulting solid was filtered and washed with H<sub>2</sub>O (500 mL), THF (100 mL), ethanol (100 mL), and CH<sub>3</sub>Cl (100 mL) and then dried under vacuum oven (150 °C) to produce pale yellow solid of PAF-1-CH<sub>2</sub>Cl. Subsequently, PAF-1-CH<sub>2</sub>Cl was mixed with NaSCH<sub>3</sub> (1.2 g, 21.0 mmol, Aldrich) in 100 mL ethanol under N<sub>2</sub> and stirred at 70 °C for 3 days. The resulting solid was collected, washed with H<sub>2</sub>O (100 mL), THF (100 mL), ethanol (100 mL), and CH<sub>3</sub>Cl (100 mL), and then dried under vacuum oven (150 °C) to produce PAF-1-SMe as pale yellow powder. Elemental analysis found for PAF-1-SMe: 68.28% C, 5.68% H, 0.502% Cl, 9.60% S.

### 2.2.3. Determination of Distribution Coefficient ( $K_d$ ) for Copper Uptake

PAF-1-SMe (100.0 mg) was added to a column connected to a jar containing 1 L of 4.03 ppm CuCl<sub>2</sub> solution (100 mM HEPES buffer, pH 6.7). The copper solution was passed through PAF-1-SMe with flow rate of 0.5 mL/min. Subsequently, initial copper solution ( $C_i$ ) and filtrate ( $C_f$ ) were analyzed using ICP-MS ( $C_i = 4.03$  ppm;  $C_f = 0.283$  ppm) and used to determine the amount of copper captured by PAF-1-SMe. The amount of copper adsorbed by PAF-1-SMe was calculated by subtracting the residual copper concentration from the initial copper concentration. The following equation was used in order to determine the  $K_d$  value:

$$K_d = \frac{(C_i - C_f)}{C_f} \times \frac{V}{m}$$

Where  $C_i$  is the initial metal ion concentration,  $C_f$  is the final equilibrium metal ion concentration,  $V$  is the volume of the treated solution (mL) and  $m$  is the mass of sorbent used (g).<sup>2</sup>

### 2.2.4. Adsorption Kinetics for Copper and Iron Removal

A 10 mL aqueous CuCl<sub>2</sub> solution (10 ppm) or FeCl<sub>3</sub> solution (5 ppm in 100 mM HEPES buffer, pH 6.7) was added to an Erlenmeyer flask containing 2 mg of PAF-1-SMe. The mixture was stirred at room temperature for 8 h. During the stirring period, the mixture was filtered at intervals through a 0.45-mm membrane filter for all samples. The filtrates were analyzed using ICP-MS to determine the remaining copper concentration. The amount of copper adsorbed by PAF-1-SMe was calculated by subtracting the residual copper concentration from the initial copper concentration. The experimental data were fitted with a pseudo-second-order kinetic model using the following equation:



$$\frac{t}{q_t} = \frac{1}{k_2 q_e^2} + \frac{t}{q_e}$$

where  $k_2$  is the pseudo-second-order rate constant of adsorption (g/mg·min) and  $q_e$  is the amount of copper ion adsorbed at equilibrium (mg/g). The slope and intercept of the linear plot  $t/q_t$  vs  $t$  yielded the values of  $q_e$  and  $k_2$ , respectively.

### 2.2.5. Adsorption Isotherm

PAF-1-SMe (2.0 mg) was added to conical tubes containing 10 mL CuCl<sub>2</sub> solution (100 mM HEPES buffer, pH 6.7) with a wide range of copper concentrations. Each mixture was capped and stored in a shaker at room temperature overnight, and then filtered separately through a 0.45 mm membrane filter. The filtrates were analyzed by ICP-MS to determine the remaining copper content. The amount of copper adsorbed by PAF-1-SMe was calculated by subtracting the residual copper concentration from the initial copper concentration. The experimental copper uptake data were best fitted using a dual-site Langmuir model:

$$q_e = \frac{q_{sat,1} K_{L,1} C_e}{1 + K_{L,1} C_e} + \frac{q_{sat,2} K_{L,2} C_e}{1 + K_{L,2} C_e}$$

where  $q_e$  is the adsorption capacity (mmol/g),  $C_e$  is the equilibrium concentration of the metal ion (mg/L),  $q_{sat,1}$  and  $q_{sat,2}$  are saturation adsorption capacities (mmol/g) of two distinct adsorption sites, and  $K_{L,1}$  and  $K_{L,2}$  are the Langmuir constants (L/mg) that are related to the binding affinities of those adsorption sites. For comparison, the experimental data were also fitted using commonly employed single-site Langmuir and Freundlich models, top and bottom equations below, respectively:

$$q_e = \frac{q_{sat} K_L C_e}{1 + K_L C_e}$$

$$q_e = K_F C_e^{1/n}$$

where  $K_F$  is the binding energy constant (mg<sup>1-(1/n)</sup>·L<sup>1/n</sup>/g) and  $n$  is the Freundlich exponent. Overall, the dual-site Langmuir model provided a good description of the experimental data, particularly in the low concentration region. The fitting parameters and correlation coefficients are summarized in Table S1. Nonlinear regression was used in fitting all models.

### 2.2.6. Competitive assay

2 mg of PAF-1-SMe was added into separate conical tubes containing 10 mL aqueous solution of ZnCl<sub>2</sub>, CaCl<sub>2</sub>, MgCl<sub>2</sub>, NaCl, KCl, NiCl<sub>2</sub>, CoCl<sub>2</sub>, MnCl<sub>2</sub>, or NH<sub>4</sub>Fe(SO<sub>4</sub>)<sub>2</sub>·12H<sub>2</sub>O (10 ppm each in 100 mM HEPES buffer, pH 6.7). The slurry was stored in a shaker at room temperature overnight, and then was filtered through a 0.45 mm membrane filter. The filtrates were analyzed using ICP-MS to determine the concentration of remaining metal ions. The amount of metal ion

adsorbed by PAF-1-SMe was calculated by subtracting the residual copper concentration from the initial copper concentration.

### 2.2.7. Copper Uptake Studies in Biofluid Samples and Its Colorimetric Detection

*Urine collection.* To collect urine, 14-week-old Wilson's disease mice and controls from the background strain C57BL x129s6/svev were placed in Tecniplast metabolic cage systems for a period of 48 hours. During this period, the animals had access to water and food. The collected urine was centrifuged at 4,000 x g for 5 min at 4 °C to remove debris or food particles, and then stored at -80 °C until further analysis.

*Serum collection.* 2 L of porcine blood was purchased from Marin Sun Farm Inc. and was allowed to clot by leaving it undisturbed at room temperature for 30 minutes. The clot was removed by centrifuging at 3000 x g for 15 minutes in a refrigerated centrifuge, and the resulting supernatant was transferred to 6 mL tubes from Becton Dickinson (BD Vacutainer REF 367815 6.0 mL). The samples were stored at -20 °C and freshly thawed before each experiment.

*Copper uptake in biofluid samples.* A 1 mL sample of the urine of 14-week-old mice from a murine model of Wilson's disease or heterozygous type controls was added to a 1.5 mL tube containing 2 mg of PAF-1-SMe. In case of serum, additional copper salts (2, 5, 10 ppm) were added in 4 mL of serum to simulate Wilson's disease.<sup>3</sup> Moreover, as serum contains ca. 4-fold higher levels of iron compared to copper,<sup>4</sup> 1 mM acetohydroxyamic acid (AHA) as iron chelator was additionally added into serum.<sup>5</sup> PAF-1-SMe (2 mg) was added into each urine and serum sample, and biofluid samples with/without PAF-1-SMe were kept in a shaker at room temperature for overnight, filtered through 0.45 mm membrane filters, and analyzed by ICP-MS to determine remaining copper content. The amount of copper adsorbed by PAF-1-SMe was calculated by subtracting the residual copper concentration from the initial copper concentration.

*Colorimetric detection.* PAF-1-SMe applied to heterozygous and Wilson's disease urine specimens and serum samples was dried open to air overnight. Before treatment with 8-hydroxyquinoline (8-HQ), dried PAF-1-SMe was washed by adding 1 mL of DMSO and remove DMSO by immediate filtration. Subsequently, 1 mM 8-HQ in DMSO (1 mL) was added to the washed PAF-1-SMe and shaken three times. The liquid was filtered through a 0.45 mm membrane filter and transferred into 1 cm × 0.5 cm quartz cuvette (1.4-mL volume, Starna). The formation of complex between 8-HQ and copper extracted from PAF-1-SMe was monitored using a Varian Cary 50 spectrophotometer.

*Detection limit* of 8-HQ was measured in DMSO, in serum by adding external copper salt (1, 2, and 5 ppm of 1 mL of serum), and in urine by adding external copper salt (1.5, 3, and 5 ppm in 200 µL of urine sample). PAF-1-SMe (2 mg) was stored in each sample overnight in a shaker and dried after filtration. Dried PAF-1-SMe was washed by adding 1 mL of DMSO, and 1 mM 8-HQ in DMSO (1 mL) was added into washed PAF-1-SMe. The absorbance at 410 nm of each samples was plotted against initial copper concentrations. The detection limit of 8-HQ was calculated by the three-sigma method  $3\sigma/k$  as 186 ppb in DMSO, 756 ppb in serum samples, and 552 ppb for urine samples, respectively.

## 2.3. Result and discussion

The parent material PAF-1- was synthesized following a procedure reported in the literature<sup>14</sup> and chloromethylation of the phenyl rings of PAF-1<sup>16</sup> followed by treatment with NaSMe afforded the final PAF-1-SMe product (Scheme 2.2). Infrared spectroscopy revealed the successful formation of PAF-1-SMe as evidenced by the disappearance of C–H wagging of the –CH<sub>2</sub>Cl group at 1265 cm<sup>-1</sup> in PAF-1-CH<sub>2</sub>Cl (Figure 2.2). Elemental analysis also revealed a decrease in chlorine content from 13.6% in PAF-1-CH<sub>2</sub>Cl to 0.5% in the thioether-functionalized material, further supporting a successful transformation. The sulfur content in PAF-1-SMe was determined to be 9.6 ± 1.3% via elemental analysis, providing further evidence for efficient thioether formation from the chloromethyl starting material. Finally, solid-state <sup>1</sup>H–<sup>13</sup>C cross-polarization magic angle spinning (CP/MAS) NMR (Figure 2.1a) monitored distinct <sup>13</sup>C chemical shifts associated with the PAF-1-CH<sub>2</sub>Cl synthetic intermediate (43 ppm for –CH<sub>2</sub>Cl group) and the final PAF-1-SMe product (35 and 13 ppm for –CH<sub>2</sub>SCH<sub>3</sub> group), further confirming successful incorporation of –SMe groups.

In order to reveal the copper coordination in thioether groups, additional solid-state <sup>13</sup>C NMR experiments were performed. Indeed, we observed that addition of copper to the PAF-1-SMe material specifically broadened and decreased the intensities of peaks assigned to the thioether ligands and benzyl ring, which can be interpreted as copper being in proximity to these functionalities. Furthermore, data from EPR experiments provided a separate line of evidence for interaction between copper and thioether groups (Figure 2.3). N<sub>2</sub> adsorption isotherms collected at 77 K (Figure 2.4) revealed that PAF-1-SMe retained high permanent porosity with a BET surface area of 1075 m<sup>2</sup>/g, albeit smaller than the parent PAF-1 surface area of 3505 m<sup>2</sup>/g. The pore size distributions obtained from the adsorption isotherms were also in agreement with the incorporation of –CH<sub>2</sub>SMe groups. Indeed, while PAF-1 exhibited a uniform pore size distribution centered around 12 Å, PAF-1-SMe exhibited pore width maxima located at 6 Å and 9 Å (Figure 2.4d). To the best of our knowledge, PAF-1-SMe possesses the highest surface area of any thioether-modified porous material, including mesoporous materials (~979 m<sup>2</sup>/g),<sup>22</sup> organosilicas (15–260 m<sup>2</sup>/g),<sup>23</sup> metal-organic frameworks (~618 m<sup>2</sup>/g),<sup>24</sup> silsesquioxane aerogels (90–272 m<sup>2</sup>/g)<sup>25</sup>, and a thioether-based fluorescent covalent organic framework (454 m<sup>2</sup>/g).<sup>26</sup> Although we note elegant work that shows that high surface area is not a strict prerequisite for high performance<sup>27</sup>, the relatively high surface area and permanent porosity of PAF-1-SMe are both good indicators of the accessibility of the thioether groups within the polymeric network.

### 2.3.1. Copper Uptake, Kinetics, and Selectivity

After confirming the porosity and structural integrity of PAF-1-SMe upon post synthetic modification, we examined its ability to capture copper ions from aqueous solution. The distribution coefficient, *K<sub>d</sub>*, was measured with 4 ppm copper in HEPES buffer at pH = 6.7 and found 1.3 ± 0.2 × 10<sup>5</sup> mL/g, indicating a high copper selectivity and a more than 10-fold improvement over the best copper adsorbent materials reported to date (1.2 × 10<sup>4</sup> mL/g).<sup>28</sup> Time-course adsorption measurements further indicated that copper capture by PAF-1-SMe is kinetically efficient (Figure 2.9), with a pseudo-second order adsorption rate constant of 5.2 mg/mg·min that reaches equilibrium capacity within ~30 min. We assessed the overall capacity of PAF-1-SMe for copper from fitting of adsorption isotherms collected after equilibrating the polymer with a wide range of copper levels (1 ppb–800 ppm, Figure 2.8a). The best fit for the experimental data utilized a dual-site Langmuir model<sup>29</sup> with a strong adsorption site (saturation capacity of 67 mg/g) and a weak adsorption site (saturation capacity of 662 mg/g). The strong adsorption site was correlated

with the thioether groups within the framework, and this assignment is supported by comparing copper adsorption in PAF-1-CH<sub>2</sub>Cl and PAF-1-SMe up to ~10 ppm (Figure 2.8a, inset). For the low concentrations most relevant to diagnostic copper capture in biofluids, PAF-1-SMe displayed a much steeper uptake than PAF-1-CH<sub>2</sub>Cl, and this enhanced uptake notably persisted for higher copper concentrations (35 mg/g at 740 ppm). By comparison, PAF-1-CH<sub>2</sub>Cl showed higher uptake (~30-fold) in the range 3 ppb–740 ppm, providing evidence for the presence of copper ions trapped within the pores and/or adsorption at weaker binding sites in PAF-1-SMe. We note that the experimental saturation capacities for PAF-1-SMe were higher than predicted based on the calculated thioether density, and thus it is likely that each sulfur atom is capable of coordinating more than one copper ion. A similar observation was made with regard to sulfur-functionalized mesoporous carbons.<sup>30</sup> Notably, the total saturation capacity exhibited by PAF-1-SMe is higher than all previously reported copper adsorbents, including cellulose resin modified with sodium metaperiodate and hydroxamic acid groups (~246 mg/g),<sup>31</sup> zeolites, biomass and lignin-derived adsorbents (5.1-133.4 mg/g),<sup>32</sup> silica-polyamine composite resins (~80 mg/g),<sup>33</sup> and silica-based polymers (0.5-147 mg/g)<sup>34</sup>. More interestingly, the comparison of PAF-1-SMe to a commercially available thiol functionalized resin (Duolite GT-73) provided us valuable information on the highly accessible nature of –CH<sub>2</sub>SMe groups in PAF-1-SMe. This resin, featuring a higher loading of thiol groups (sulfur content of 16%) yet a much lower surface area (50 m<sup>2</sup>/g), was reported<sup>35</sup> to have a copper uptake of 25 mg/g at an equilibrium concentration of 160 ppm. Such a striking difference in uptake capacities underlines the importance of functional group accessibility which we believe is enabled by the highly porous nature of PAF-1-SMe.

Most importantly, PAF-1-SMe shows high selectivity for copper over other biologically relevant metal ions with minor background from only iron(II) (Figure 2.8b). Moreover, a direct competition assay revealed that PAF-1-SMe binds copper(II) much more tightly than iron(II) (Figure 2.10), suggesting its potential utility for selective copper capture in biological and environmental samples.

### 2.3.2. Copper Capture and Detection in Biofluids.

After demonstrating the ability of PAF-1-SMe to capture copper with good affinity and selectivity in aqueous buffer, we examined its performance in biofluid samples, with specific application as part of a potential diagnostic tool for Wilson's disease. Initial ICP-MS characterization of urine samples from 14-week old Wilson's disease and healthy heterozygous control mice revealed a much greater urine copper level for the disease model (1420 ppb versus 295 ppb Cu, respectively, Figure 2.11a).<sup>36</sup> The urine samples were accordingly treated with PAF-1-SMe, which resulted in successful capture of 1195 ppb copper from the Wilson's disease mice compared to 269 ppb for the control sample (capture efficiencies of 84% and 91%, respectively, Figure 2.11a). Thus, PAF-1-SMe is capable of extracting copper directly from biofluid samples and importantly distinguishing between healthy and diseased mouse models. As further improvement of this diagnostic, we sought to identify the adsorbed copper concentration using a colorimetric agent, thus obviating the need for expensive ICP-MS or related instrumentation. We chose to apply 8-hydroxyquinoline (8-HQ), which undergoes a distinct color change upon copper binding from colorless (315 nm absorption,  $\epsilon = 1.95 \times 10^3 \text{ M}^{-1} \text{ cm}^{-1}$ ) to green (410 nm absorption,  $\epsilon = 1.86 \times 10^3 \text{ M}^{-1} \text{ cm}^{-1}$ ) by formation of a Cu(II)-8-HQ complex.<sup>37</sup> To examine whether 8-HQ could bind copper captured within PAF-1-SMe, a solution of 8-HQ in DMSO was added to dried samples of PAF-1-SMe that had been exposed to urine from Wilson's disease or healthy control

mice. Indeed, PAF-1-SMe copper capture from unprocessed urine samples followed by treatment with 8-HQ led to a visible change in the absorbance at 410 nm for the Wilson's disease murine models, which was sufficient to distinguish them from the heterozygous mice. (Figure 2.11b). Calculation of the amount of copper adsorbed by PAF-1-SMe using the 410 nm absorbance peak as a standard also provided a good correlation with direct copper measurements by ICP-MS (Figure 2.11c). Furthermore, PAF-1-SMe adsorbed copper completely from the urine of heterozygous and Wilson's disease mice in ~30 min and showed substantially different uptake in as little as 1 min (Figure 2.11d), suggesting that these materials can be employed at shorter timescales.

Finally, we evaluated the performance of PAF-1-SMe for the detection of copper in serum, which is notably a more complex biofluid compared to urine with iron concentrations approximately 5 times greater than that of copper.<sup>38</sup> We used porcine serum sources owing to limitations in obtaining sufficient amounts of murine specimens required for this first-generation assay. Exogenous copper was added to the samples to simulate elevated serum free copper levels observed in patients with Wilson's disease.<sup>6,7</sup> Although we observed that PAF-1-SMe could preferentially bind copper over iron(II), it also absorbed a significant amount of iron in unprocessed serum. This iron uptake disturbed the subsequent colorimetric assay with 8-HQ due to an interfering signal from the 8-HQ-iron(II) complex (Figure 2.13). To reduce iron interference, we pre-treated the serum sample with acetohydroxamic acid (AHA), a high-affinity iron chelator that shows little interaction with copper.<sup>39</sup> Indeed, PAF-1-SMe shows dose-dependent copper capture for exogenous copper addition over a range of 0-10 ppm (Figures 2.12a, 2.12b). Analogous to the urine sample results, with AHA pretreatment 8-HQ can also serve as a colorimetric indicator when coupled with PAF-1-SMe for direct copper capture from serum and the 8-HQ assay revealed a positive linear dependence of the absorbance at 410 nm with increasing serum copper concentration (Figure 2.12c, inset). As also demonstrated for the urine samples, copper levels calculated from the 410 nm absorption was in good agreement with direct ICP-MS measurements (Figure 2.12d). Using a three-sigma method ( $3\sigma/k$ ), we determined that the detection limit for this PAF-1-SMe/8-HQ assay is 186 ppb in DMSO, 552 ppb in urine, and 756 ppb in serum (Figure 2.15). On balance, we note that AHA pretreatment does add an extra step to the protocol for serum compared to urine, but this methodology still avoids expensive instrumentation and sample processing. Indeed, this AHA pretreatment followed by application of PAF-1-SMe/8-HQ radically simplifies the traditional method to detect copper by ICP-MS, which includes boiling in nitric acid for digestion, centrifugation, and filtration.<sup>40</sup> Importantly PAF-1-SMe retained structure and porosity and maintained a high effective copper capture capacity after regeneration with 8-HQ (Figure 2.17 and Figure 2.18).

### 2.3.3. Conclusion

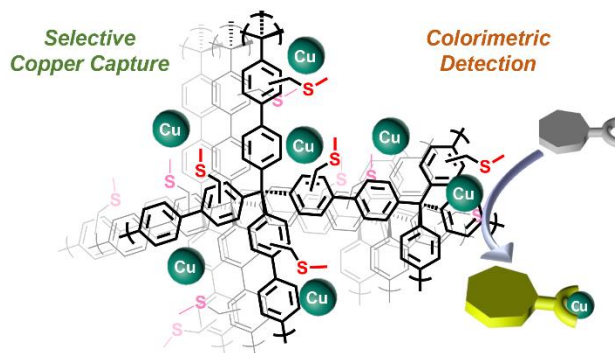
To close, we have demonstrated that the robust thi-oether-functionalized porous aromatic framework, PAF-1-SMe, accomplishes selective and efficient copper uptake from aqueous media, including from biofluid samples. Further, as demonstrated by the differentiation between urine samples of healthy and Wilson's disease mice, the combination of PAF-1-SMe with 8-HQ as a colorimetric indicator provides an efficient and accessible tool for metal detection directly from biological specimens with minimal processing and instrumentation needs. Our data provide a starting point for the use of functionalized porous materials in diagnostic or sensing applications for compatible biological, and perhaps environmental, field samples. In a broader sense, this divide-and-conquer strategy to indicator design, where one materials component is involved in

capture and concentration of analytes from samples with minimal processing, while the other molecular component offers a detection readout, is readily generalized and should offer a broad range of possibilities for mixing and matching different molecular, materials, and biological components for various sensing and imaging applications

## **2.4. Acknowledgments**

We thank the NIH under award GM79465 for support of synthesis and biological studies in the laboratory of C.J.C. Efforts for material characterization in the laboratories of J.A.R. and J.R.L. were supported by the Center for Gas Separations Relevant to Clean Energy Technologies, an Energy Frontier Research Center funded by the U.S. Department of Energy, Office of Science, Office of Basic Energy Sciences, under Award DE-SC0001015. C.J.C. is an Investigator at the Howard Hughes Medical Institute. G.B. thanks the Miller Institute for Basic Research in Science for a postdoctoral fellowship. C.M.A. is supported by a fellowship from the Fannie and John Hertz Foundation. We also thank K. Colwell for scanning electron microscopy (SEM) images and Dr. Katie R. Meihaus for editorial assistance.

## Figures



**Scheme 2.1.** Copper detection assay with PAF-1-SMe as a selective copper capture material coupled to a colorimetric indicator for detection and regeneration



**Scheme 2.2.** Synthesis of PAF-1-SMe.

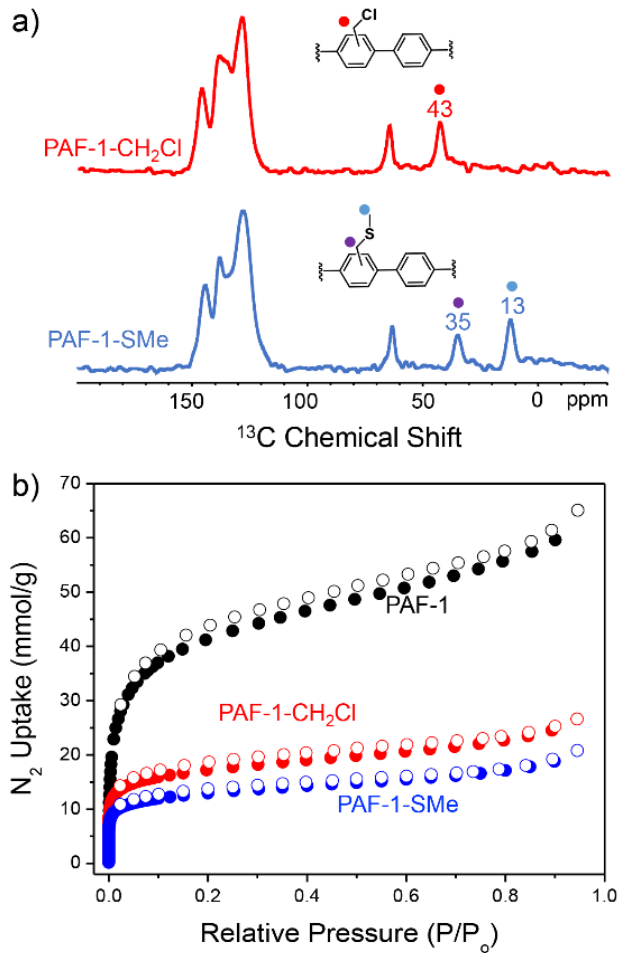


**Figure 2.1.** (a) Solid-state <sup>13</sup>C NMR spectra of PAF-1-CH<sub>2</sub>Cl and PAF-1-SMe (b) N<sub>2</sub> sorption isotherms of PAF-1, PAF-1-CH<sub>2</sub>Cl, and PAF-1-SMe at 77 K. Closed and open symbols represent adsorption and desorption branches, respectively.



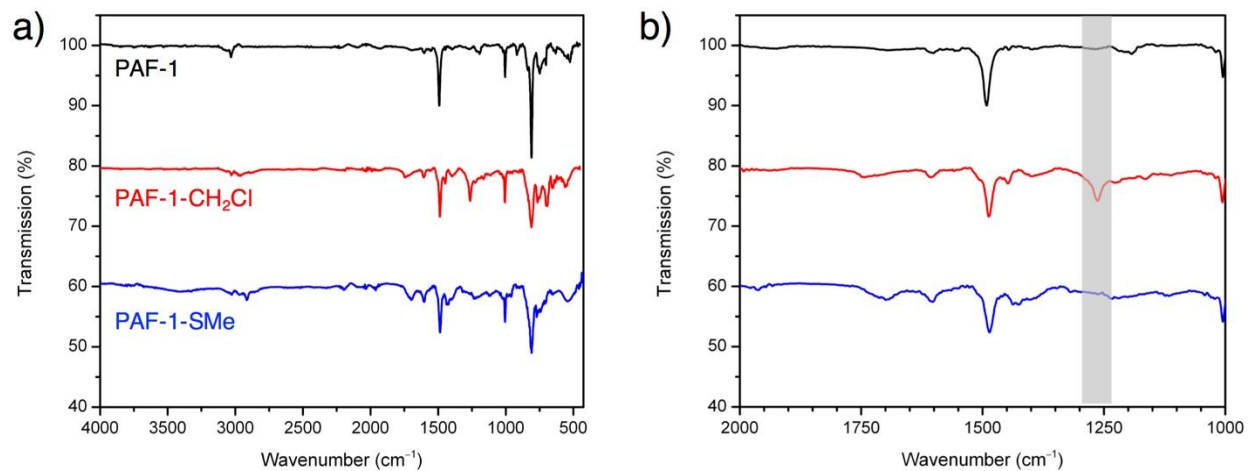


**Figure 2.2.** (a,b) FT-IR spectra of PAF-1, PAF-1-CH<sub>2</sub>Cl, and PAF-1-SMe.

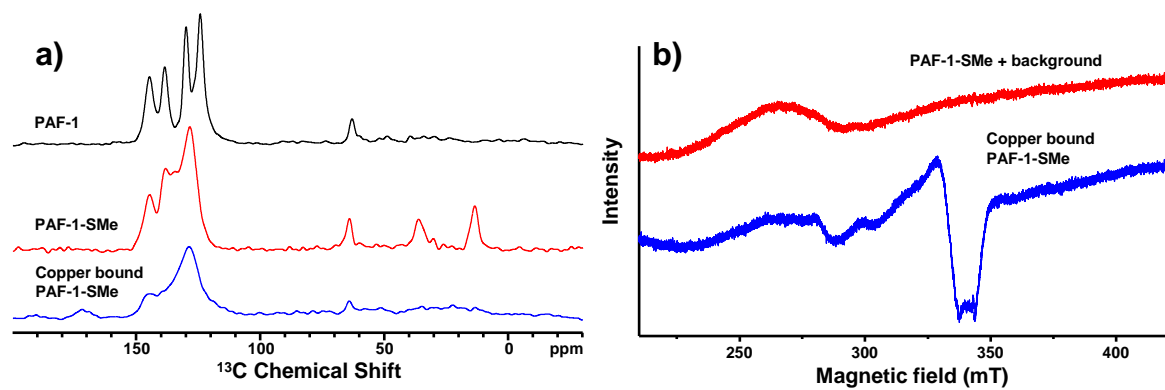


**Figure 2.3.** (a) Solid-state  $^{13}\text{C}$  NMR spectra of PAF-1 and PAF-1-SMe and copper bound PAF-1-SMe, (b) EPR spectra of PAF-1-SMe and copper bound PAF-1-SMe.

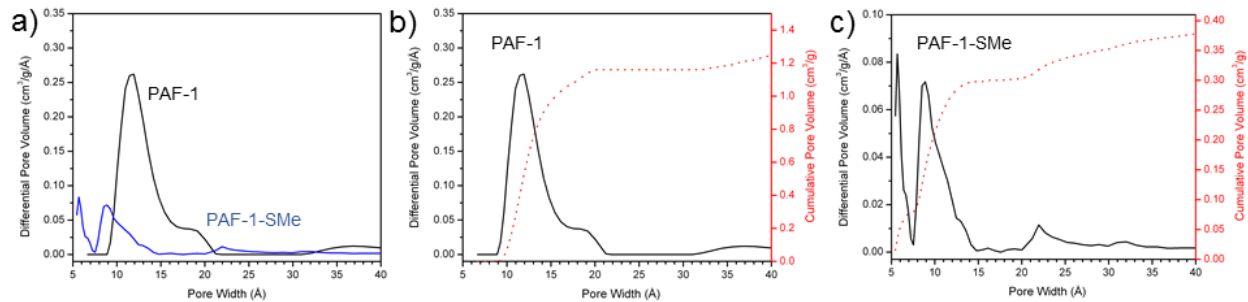


**Figure 2.4.** (a) Pore size distribution comparison of PAF-1 and PAF-1-SMe, (b) differential and cumulative pore volume graph of PAF-1, and (c) differential and cumulative pore volume graph of PAF-1-SMe

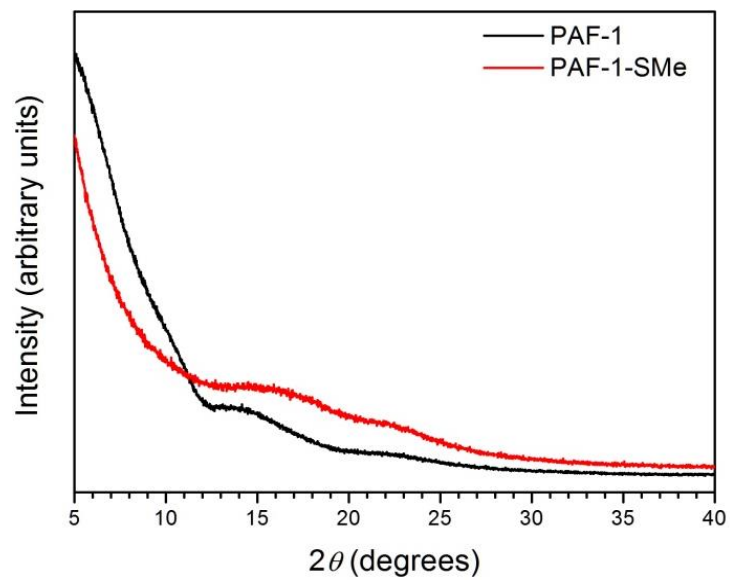


**Figure 2.5.** Powder X-ray diffraction patterns of PAF-1 and PAF-1-SMe, demonstrating the amorphous nature of both polymers.

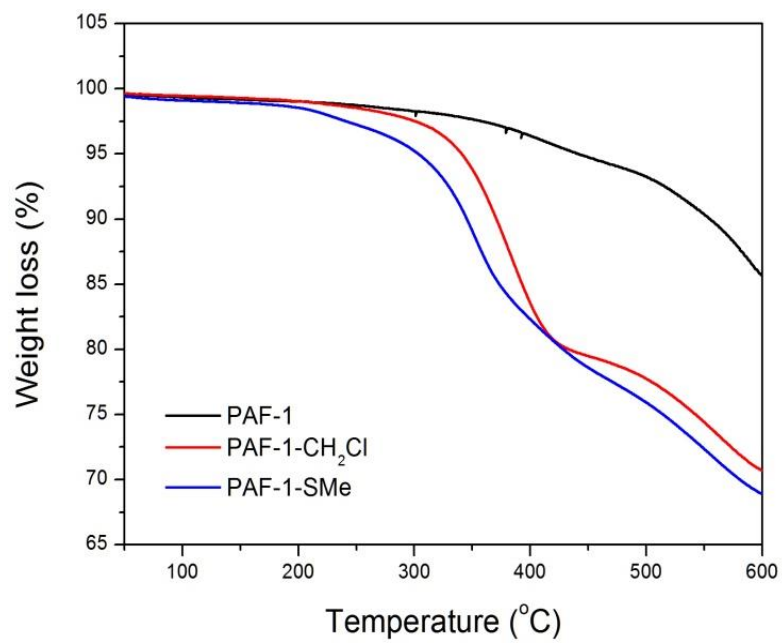


**Figure 2.6.** Thermogravimetric analysis of PAF-1, PAF-1-CH<sub>2</sub>Cl, and PAF-1-SMe.

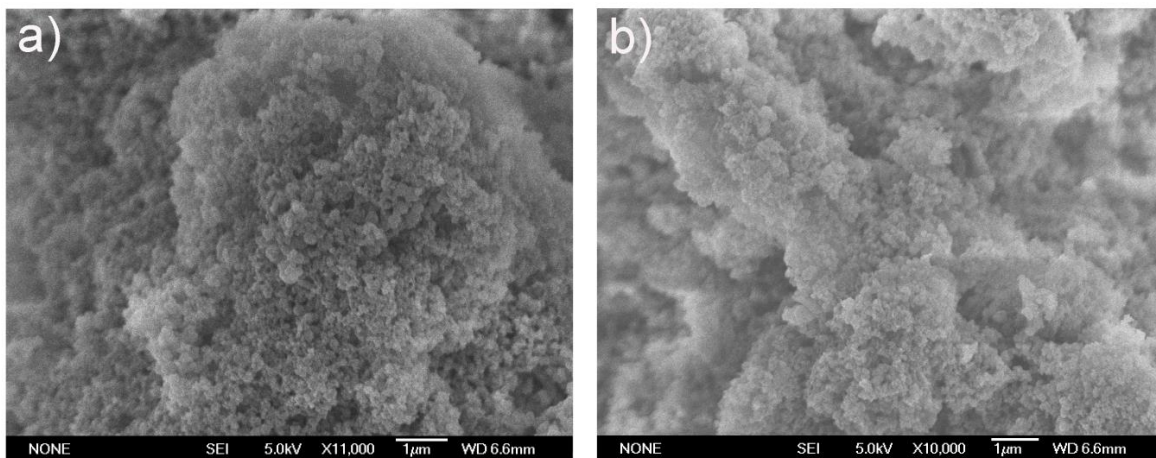


**Figure 2.7.** SEM images of (a) PAF-1 and (b) PAF-1-SMe.

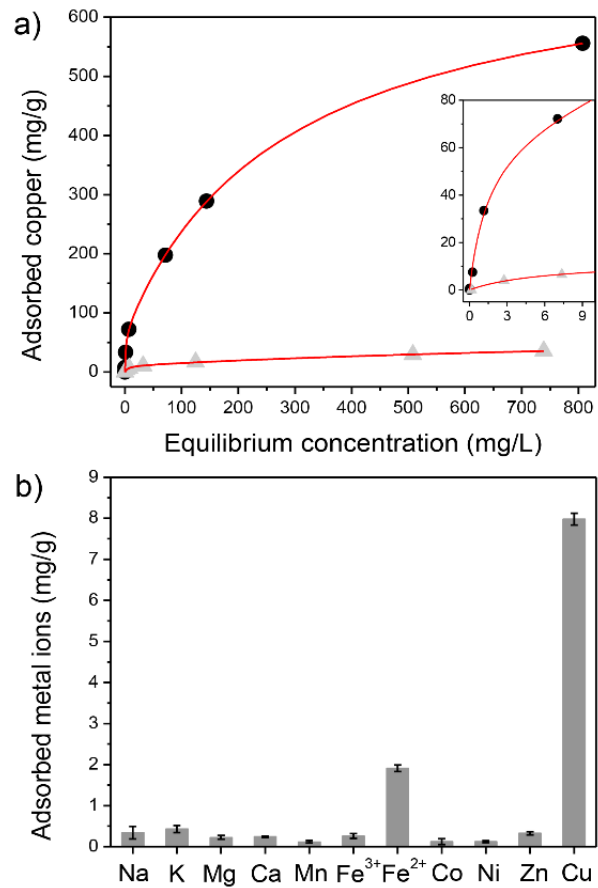


**Figure 2.8.** (a) Copper adsorption isotherm for PAF-1-SMe (black circles) and PAF-1-CH<sub>2</sub>Cl (gray triangle) fit using a dual-site Langmuir model (red line) The inset plot is magnified portion of initial equilibrium concentration range (0-10 mg/L) and absorbed amount of copper (mg/g) (b) PAF-1-SMe capture capacities of physiologically relevant metal ions (10 ppm). Data collected in 100 mM HEPES pH = 6.7.

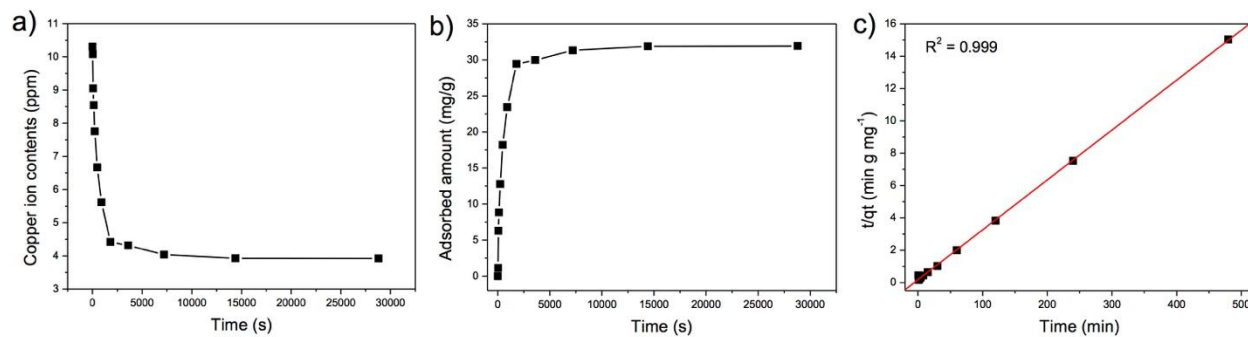


**Figure 2.9.** (a, b) Copper(II) adsorption kinetics of PAF-1-SMe using a copper(II) solution of 10 ppm (100 mM HEPES buffer, pH 6.7). (c) Pseudo-second order kinetic plot for copper(II) adsorption provided a high correlation coefficient and a rate constant  $k_2$  of 5.2 mg mg<sup>-1</sup> min<sup>-1</sup>.



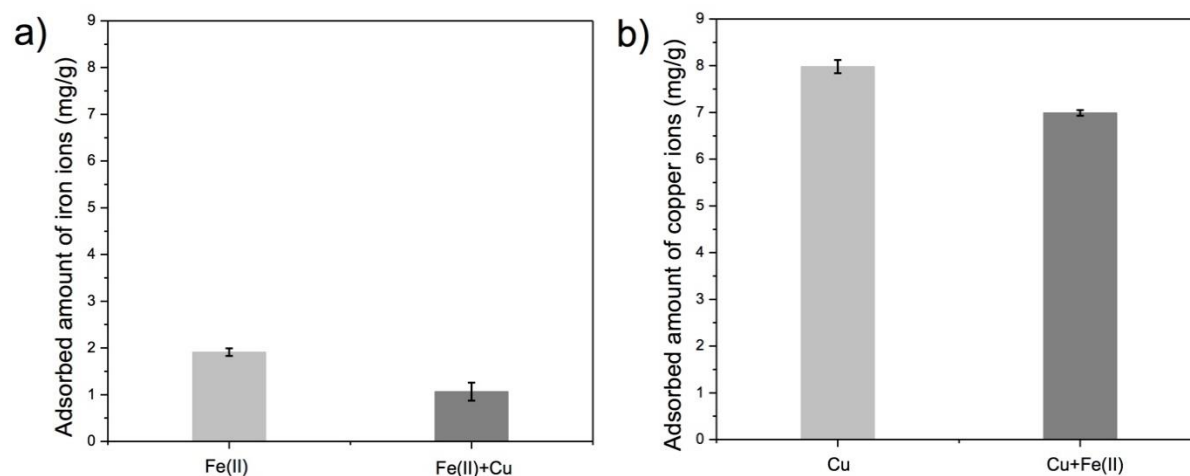


**Figure 2.10.** Competitive assay for iron and copper ion uptake. (a) Iron uptake (10 ppm in 100 mM HEPES buffer, pH 6.7, light gray bar) showed a decrease (dark gray bar) upon addition of copper ions (10 ppm). (b) Copper uptake (10 ppm, light gray bar) showed a slight decrease (dark gray bar) after adding additional iron ions (10 ppm).

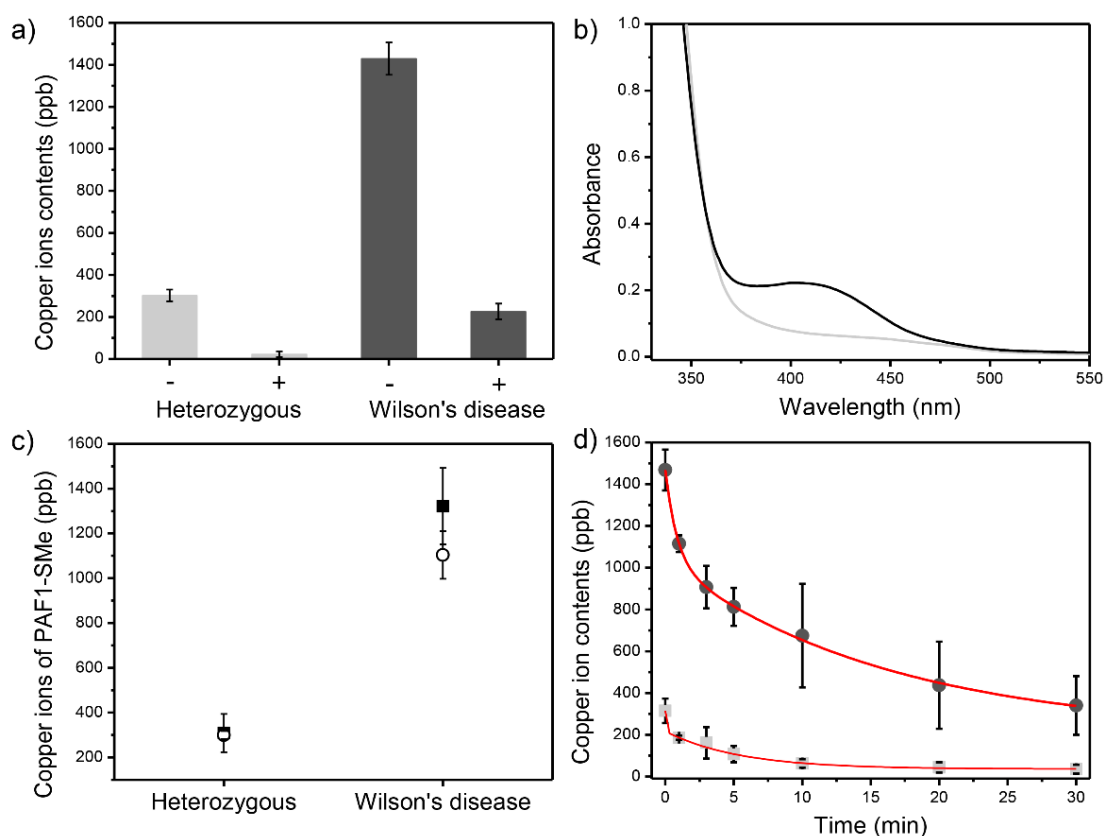


**Figure 2.11.** a) Urine samples (1 mL) from 14-week old heterozygous (light gray bars) and Wilson's disease (dark gray bars) mice analyzed by ICP-MS before (-) and after (+) exposure to 2 mg of PAF-1-SMe. (b) Absorption spectra after 8-hydroxyquinoline addition to dried PAF-1-SMe with DMSO washes applied to heterozygous (light gray) and Wilson's disease (dark gray) urine specimens. (c) Correlation between direct copper measurements by ICP-MS (open circles) versus calculated copper levels from 410-nm light absorption using 8-hydroxyquinoline as an indicator (black filled squares). (d) Real time copper uptake of PAF-1-SMe in the urine samples of heterozygous (light gray) and Wilson's disease mice (dark gray) measured at 1, 3, 5, 10, 20, and 30 min intervals and fitted with the double exponential decay model:  $y = A_1 \cdot \exp(-x/t_1) + A_2 \cdot \exp(-x/t_2)$ ;  $\langle \tau_{\text{Wilson's disease}} \rangle = 15.9 \text{ min}$  and  $\langle \tau_{\text{Heterozygous}} \rangle = 5.4 \text{ min}$  (red lines).

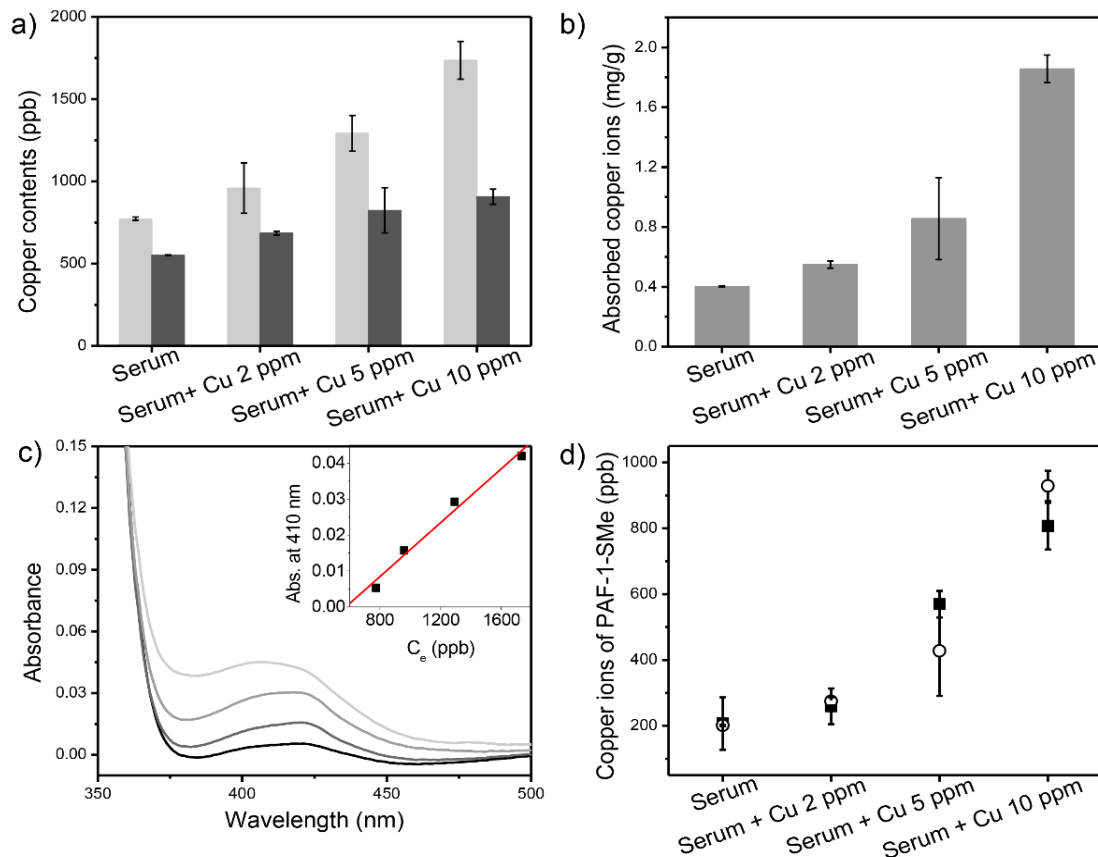


**Figure 2.12.** (a) Porcine serum samples (4 mL) with varying amounts of exogenous copper analyzed by ICP-MS before (light grey bars) and after (black bars) addition of PAF-1-SMe. (b) Dose-dependent adsorption of copper by PAF-1-SMe from serum samples. (c) Absorption spectra after addition of 8-hydroxyquinoline to dried PAF-1-SMe with one DMSO wash applied to serum specimens with 0, 2, 5, and 10 ppm of exogenous copper. (Inset) Calibration curve showing dependence of absorbance at 410 nm on initial copper concentration for each sample. (d) Comparison of direct copper measurements by ICP-MS (open circles) and calculated copper levels from absorbance at 410 nm using 8-hydroxyquinoline as an indicator (black filled squares).

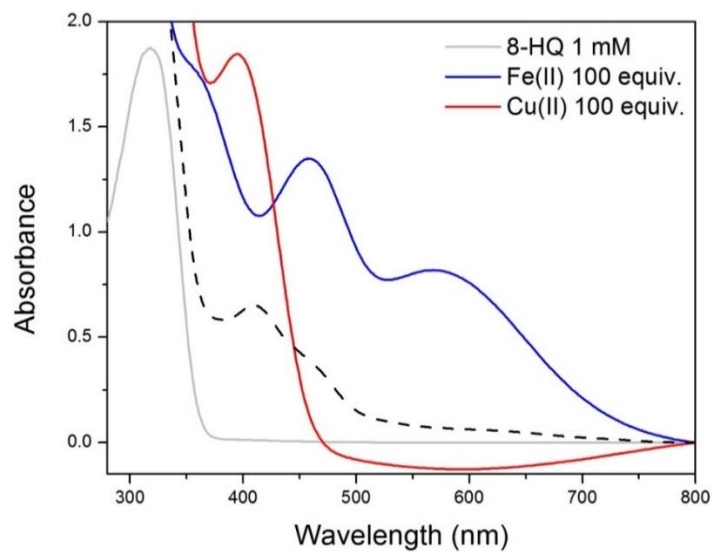


**Figure 2.13.** UV-Vis absorption spectra of 8-hydroxyquinoline with copper and iron ions (100 equiv. to 8-HQ in DMSO, red and blue, respectively) and spectra of 8-hydroxyquinoline (8-HQ) treated with PAF-1-SMe (2 mg) applied in serum without acetohydroxamic acid (AHA), which reveals absorption at 400 nm, 450 nm (sh) and 600 nm (sh) (dashed).

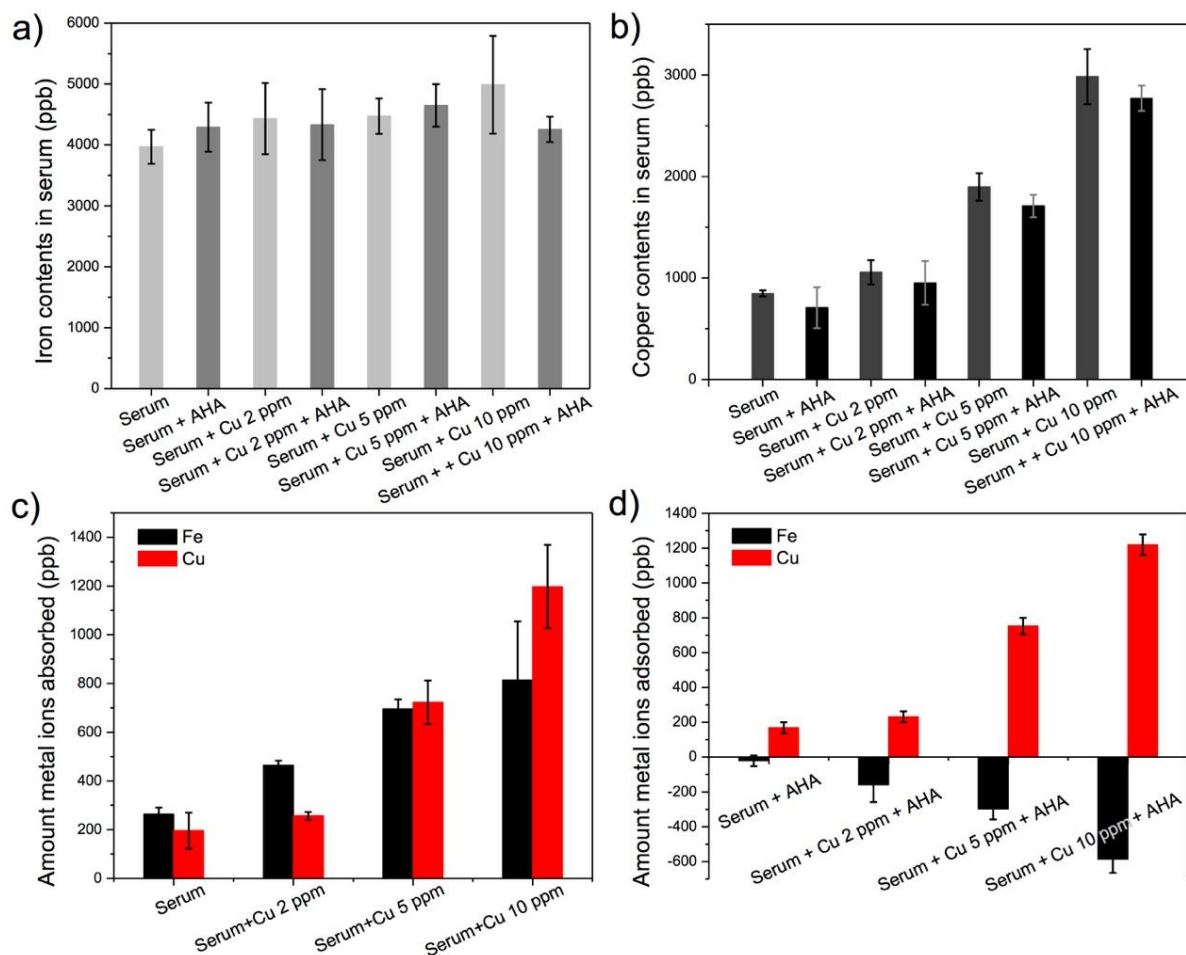


**Figure 2.14.** (a) Iron contents in serum (4 mL) in the absence (light gray bar) and presence (gray bar) of acetohydroxamic acid (AHA). (b) Copper contents in serum in the absence (dark gray bar) and presence (black bar) of acetohydroxamic acid (AHA). Adsorbed amount of iron and copper ions by PAF-1-SMe (2 mg) in the absence of AHA is shown in (c) and in presence of AHA is shown in (d).

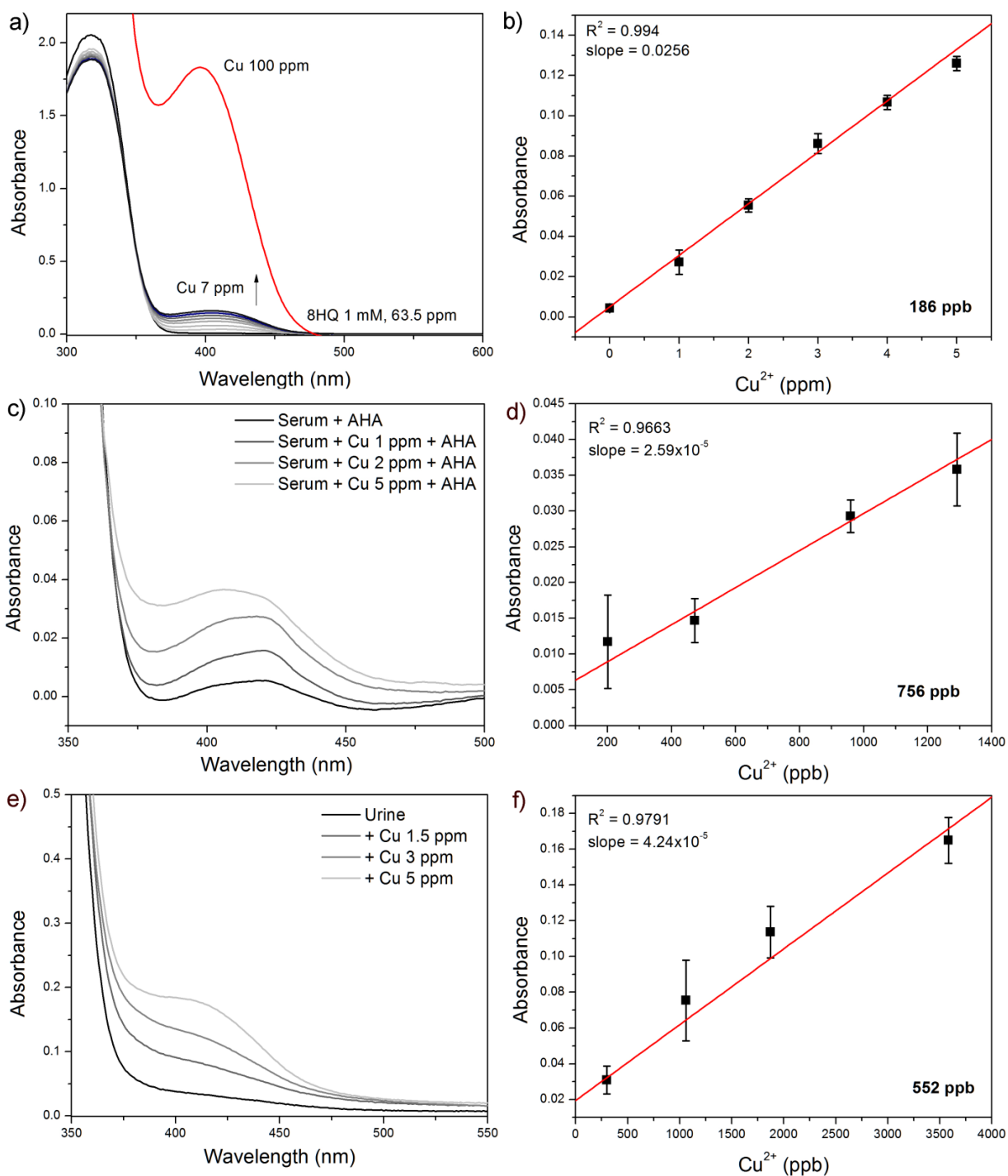


**Figure 2.15.** The detection limits (three-sigma method  $3\sigma/k$ ) of 8-hydroxyquinoline (1 mM) in DMSO (a and b), serum (c and d), and urine (e and f) were calculated to be 186, 756, and 552 ppb, respectively.

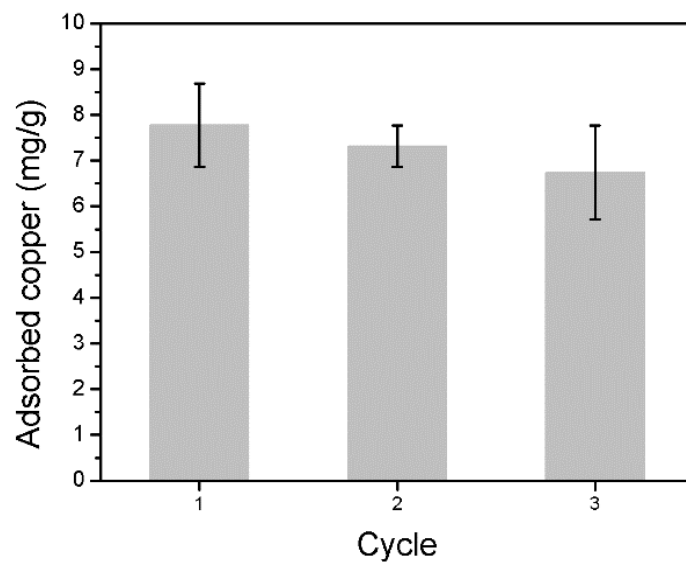


**Figure 2.16.** Comparison of copper uptake (10 ppm in 100 mM HEPES buffer, pH 6.7) by freshly synthesized PAF-1-SMe (cycle 1) with PAF-1-SMe regenerated twice by 8-hydroxyquinoline (1 mM) in DMSO (cycles 2 and 3).

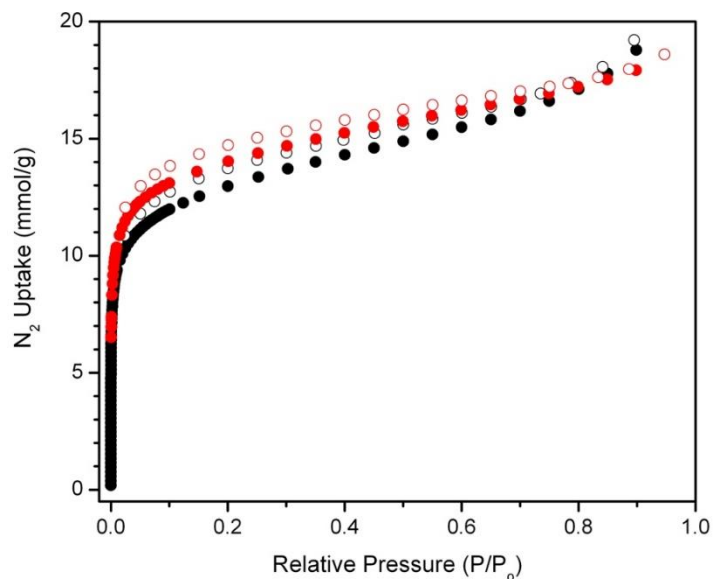


**Figure 2.17.** (a) N<sub>2</sub> sorption isotherms (77 K) of freshly synthesized PAF-1-SMe (black) and regenerated PAF-1-SMe (red) which was treated with biofluid and then followed by 8-HQ (100 mM) Closed and open symbols represent adsorption and desorption branches, respectively.



**Table 2.1.** Fitting parameters for three different models for the adsorption of copper(II) ions of PAF-1-SMe using nonlinear regression.

<i>Model</i>	Dual-site Langmuir	Single-site Langmuir	Freundlich
<i>Parameters</i>	$q_{sat,1} = 67$ $K_{L,1} = 0.68$ $q_{sat,2} = 662$ $K_{L,2} = 0.0035$	$q_{sat} = 682$ $K_L = 0.0054$	$K_F = 34.99$ $n = 2.42$
$R^2$	0.9999	0.9961	0.9981

## 2.5. References

1. Lippard, S. J.; Berg, J. M., *Principles of Bioinorganic Chemistry*. University Science Books: Mill Valley, CA; Mill Valley, CA, 1994.
2. Hentze, M. W.; Muckenthaler, M. U.; Andrews, N. C., Balancing acts: molecular control of mammalian iron metabolism. *Cell* **2004**, *117*, 285-297.
3. Theil, E. C.; Goss, D. J., Living with Iron (and Oxygen): Questions and Answers about Iron Homeostasis. *Chem. Rev.* **2009**, *109*, 4568-4579.
4. Aisen, P.; Enns, C.; Wessling-Resnick, M., Chemistry and biology of eukaryotic iron metabolism. *Int. J. Biochem. Cell Biol.* **2001**, *33* (10), 940-959.
5. Cammack, R.; Wrigglesworth, J. M.; Baum, H., *Transport and Storage*. CRC Press: 1989.
6. Johnson, D. C.; Dean, D. R.; Smith, A. D.; Johnson, M. K., Structure, function, and formation of biological iron-sulfur clusters. *Annu Rev Biochem* **2005**, *74*, 247-81.
7. Winterbourn, C. C., Toxicity of iron and hydrogen peroxide: the Fenton reaction. *Toxicol Lett.* **1995**, *82/83*, 969-74.
8. James, S. A.; Robert, B. R.; Hare, D. J.; de Jonge, M. D.; Birchall, I. E.; Jenkin, N. L.; Cherny, R. A.; Bush, A. I.; McColl, G., *Chem. Sci.* **2015**, *6*, 2952-2962.
9. von Haehling, S.; Jankowska, E. A.; van Veldhuisen, D. J.; Ponikowski, P.; Anker, S. D., Iron deficiency and cardiovascular disease. *Nat. Rev. Cardiol.* **2015**, *12*, 659-669.
10. Hare, D.; Ayton, S.; Bush, A.; Lei, P., A delicate balance: Iron metabolism and diseases of the brain. *Front Aging Neurosci* **2013**, *5*, 34.
11. Gerlach, M.; Ben-Shachar, D. B.; Riedere, P.; Youdim, M. B. H., Altered brain metabolism of iron as a cause of neurodegenerative diseases? *J. Neurochem.* **1994**, *63* (3), 793-807.
12. Torti, S. V.; Torti, F. M., Iron and cancer: more ore to be mined. *Nat Rev Cancer* **2013**, *13* (5), 342-355.
13. Wu, K. J.; Polack, A.; Dala-Favera, R., Coordinated regulation of iron-controlling genes, H-ferritin and IRP2, by c-MYC. *Science* **1999**, *283*, 676-9.
14. Pinnix, Z. K.; Miller, L. D.; Wang, W.; D'Agostino, R. J.; Kute, T.; Willingham, M. C.; Hatcher, H.; Tesfay, L.; Sui, G.; Di, X.; Torti, S. V.; Torti, F. M., *Sci. Transl. Med.* **2010**, *2* 43ra56.
15. Toyokuni, S., Role of iron in carcinogenesis: cancer as a ferrotoxic disease. *Cancer Sci.* **2009**, *100* (1), 9-16.
16. Carter, K. P.; Young, A. M.; Palmer, A. E., Fluorescent Sensors for Measuring Metal Ions in Living Systems *Chem. Rev.* **2014**, *114* (8), 4564-4601.
17. Domaille, D. W.; Que, E. L.; Chang, C. J., Synthetic Fluorescent Sensors for Studying to Cell Biology of Metals. *Nat. Chem. Biol.* **2008**, *4*, 168-175.
18. Irving, H.; Williams, R. J. P., The stability of transition-metal complexes. *J. Chem. Soc.* **1953**, 3192-3210.
19. Kemlo, J. A.; Shepherd, T. M., Quenching of Excited Singlet States by Metal Ions. *Chem. Phys. Lett.* **1977**, *47* (1), 158-162.
20. Varnes, A. W.; Dodson, R. B.; Wehry, E. L., Interactions of transition-metal ions with photoexcited states of flavines. Fluorescence quenching studies. *J. Am. Chem. Soc.* **1972**, *94* (3), 946-950.

21. Breuer, W.; Epsztejn, S.; Millgram, P.; Cabantchik, I. Z., Transport of iron and other transition metals into cells as revealed by a fluorescent probe. *J. Am. Phys. Soc.* **1995**, *268*, C1354-C1361.
22. Kakhlon, O.; Cabantchik, Z. I., The labile iron pool: characterization, measurement, and participation in cellular processes. *Free Radic. Biol. Med.* **2002**, *33*, 1037-1046.
23. Au-Yeung, H. Y.; Chan, J.; Chantarojsiri, T.; Chang, C. J., Molecular Imaging of Labile Iron(II) Pools in Living Cells with a Turn-On Fluorescent Probe. *J. Am. Chem. Soc.* **2013**, *135*, 15165-15173.
24. Hirayama, T.; Okuda, K.; Nagasawa, H., A highly selective turn-on fluorescent probe for iron(II) to visualize labile iron in living cells. *Chem. Sci.* **2013**, *4*, 1250-1256.
25. Niwa, M.; Hirayama, T.; Okuda, K.; Nagasawa, H., *Org. Biomol. Chem.* **2014**, *12*, 6590-6597.
26. Hirayama, T.; Tsuboi, H.; Niwa, M.; Miki, A.; Kadota, S.; Ikeshita, Y.; Okuda, K.; Nagasawa, H., A universal fluorogenic switch for Fe(II) ion based on N-oxide chemistry permits the visualization of intracellular redox equilibrium shift towards labile iron in hypoxic tumor cells. *Chem. Sci.* **2017**, *8* (7), 4858-4866.
27. Chan, J.; Dodani, S. C.; Chang, C. J., *Nat. Chem.* **2012**, *4*, 973-984.
28. Aron, A. T.; Ramos-Torres, K. M.; Cotruvo, J., J. A.; Chang, C. J., *Acc. Chem. Res.* **2015**, *48*, 2434-2442.
29. Chen, X.; Tian, X.; Shin, I.; Yoon, J., *Chem. Soc. Rev.* **2011**, *40*, 4783-4804.
30. Yang, Y.; Zhao, Q.; Feng, W.; Li, F., Luminescent chemodosimeters for bioimaging. *Chem Rev.* **2013**, *113*, 192-270.
31. Cho, D. G.; Sessler, J. L., *Chem. Soc. Rev.* **2009**, *38*, 1647-62.
32. Zlokarnik, G.; Negulescu, P. A.; Knapp, T. E.; Mere, L.; Burren, N.; Feng, L.; Whitney, M.; Roemer, K.; Tsein, R. Y., Quantitation of transcription and clonal selection of single living cells with beta-lactamase as reporter. *Science* **1998**, *279*, 84.
33. Lee, M. H.; Kim, J. S.; Sessler, J. L., Small molecule-based ratiometric fluorescence probes for cations, anions, and biomolecules. *Chem. Soc. Rev.* **2015**, *44*, 4185-4191.
34. Grynkiewicz, G.; Poenie, M.; Tsien, R. Y. J., A new generation of Ca<sup>2+</sup> indicators with greatly improved fluorescence properties. *Biol. Chem.* **1985**, *260*, 3440.
35. Harootunian, A. T.; Kao, J. P. Y.; Ecker, B. K.; Tsien, R. Y. J., Fluorescence ratio imaging of cytosolic free Na<sup>+</sup> in individual fibroblasts and lymphocytes. *Biol. Chem.* **1989**, *264*, 19458-19467.
36. Borstnik, K.; Paik, I. H.; Shapiro, T. A.; Posner, G. H., Antimalarial chemotherapeutic peroxides: artemisinin, yingzhaosu A and related compounds. *Int. J. Parasitol.* **2002**, *32* (13), 1661-1667.
37. Wang, X.; Creek, D. J.; Schiaffo, C. E.; Dong, Y.; Chollet, J.; Scheurer, C.; Wittlin, S.; Charman, S. A.; Dussault, P. H.; Wood, J. K.; Vennerstrom, J. L., Spiroadamantyl 1,2,4-trioxolane, 1,2,4-trioxane, and 1,2,4-trioxepane pairs: Relationship between peroxide bond iron(II) reactivity, heme alkylation efficiency, and antimalarial activity. *Bioorg & Med Chem Lett* **2009**, *19* (16), 4542-4545.
38. Deu, E.; Chen, I. T.; Lauterwasser, E. M.; Valderramos, J.; Li, H.; Edgington, L. E.; Renslo, A. R.; Bogoy, M., Ferrous iron-dependent drug delivery enables controlled and selective release of therapeutic agents in vivo. *Proc Natl Acad Sci USA* **2013**, *110* (45), 18244-18249.

39. Fontaine, S. D.; DiPasquale, A. G.; Renslo, A. R., Efficient and Stereocontrolled Synthesis of 1,2,4-Trioxolanes Useful for Ferrous Iron-Dependent Drug Delivery. *Org. Lett.* **2014**, *16* (16), 5776-9.
40. Fontaine, S. D.; Spangler, B.; Gut, J.; Lauterwasser, E. M. W.; Rosenthal, P. J.; Renslo, A. R., Drug Delivery to the Malaria Parasite Using an Arterolane-Like Scaffold. *ChemMedChem* **2015**, *10*, 47-51.
41. Abrams, R. P.; Carroll, W. L.; Woerpel, K. A., Five-Membered Ring Peroxide Selectively Initiates Ferroptosis in Cancer Cells. *ACS Chem Biol* *11*, 1305-1312.
42. Creek, D. J.; Charman, W. N.; Chiu, F. C.; Prankerd, R. J.; McCullough, K. J.; Dong, Y.; Vennerstrom, J. L.; Charman, S. A., Iron-mediated degradation kinetics of substituted dispiro-1,2,4-trioxolane antimalarials. *J. Pharm. Sci.* **2007**, *96* (11), 2945-2956.
43. Creek, D. J.; Charman, W. N.; Chiu, F. C.; Prankerd, R. J.; Dong, Y.; Vennerstrom, J. L.; Charman, S. A., Relationship between Antimalarial Activity and Heme Alkylation for Spiro- and Dispiro-1,2,4-Trioxolane Antimalarials. *Antimicrob. Agents Chemother.* **2008**, *52*, 1291-.
44. Tang, Y.; Dong, Y.; Wang, X.; Sriraghavan, K.; Wood, J. K.; Vennerstrom, J. L., Dispiro-1,2,4-trioxane Analogues of a Prototype Dispiro-1,2,4-trioxolane: Mechanistic Comparators for Artemisinin in the Context of Reaction Pathways with Iron(II). *J. Org. Chem.* **2005**, *70* (13), 5103-5110.
45. Chang, C. J., Searching for harmony in transition-metal signaling. *Nat. Chem. Biol.* **2015**, *11*, 744-747.
46. Dixon, S. J.; Patel, D. N.; Welsch, M.; Skouta, R.; Lee, E. D.; Hayano, M.; Thomas, A. G.; Gleason, C. E.; Tatonetti, N. P.; Slusher, B. S.; Stockwell, B. R., Pharmacological inhibition of cystine-glutamate exchange induces endoplasmic reticulum stress and ferroptosis. *eLife* **2014**, *3*, e02523.
47. Spangler, B.; Morgan, C. W.; Fontaine, S. D.; Vander Wal, M. N.; Chang, C. J.; Wells, J. A.; Renslo, A. R., A reactivity-based probe of the intracellular labile ferrous iron pool *Nat. Chem. Biol.* **2016**, *12*, 680-685.
48. Norman, D. G. G., R. J.; Uhrin, D.; Tilley, D. M. J., Location of Cyanine-3 on Double-Stranded DNA: Importance for Fluorescence Resonance Energy Transfer Studies. *Biochemistry* **2000**, *39*, 6317-6324.
49. Li, D.; Liu, L.; Li, W., Genetic Targeting of a Small Fluorescent Zinc Indicator to Cell Surface for Monitoring Zinc Secretion. *ACS Chem Biol* **2015**, *10* (4), 1054-1063.
50. Cerchiaro, G.; Manieri, T. M.; Bertuchi, F. R., Analytical methods for copper, zinc and iron quantification in mammalian cells. *Metallomics* **2013**, *5*, 1336-1345.
51. Epsztejn, S.; Kakhlon, O.; Glickstein, H.; Breuer, W.; Cabantchik, Z. I., Fluorescence Analysis of the Labile Iron Pool of Mammalian Cells. *Anal. Biochem.* **1997**, *248* (1), 31-40.
52. Ramos-Torres, K. M.; Koleman, S.; Chang, C. J., Thioether Coordination Chemistry for Molecular Imaging of Copper in Biological Systems. *Isr. J. Chem.* **2016**, *2016* (article ASAP).
53. Cotruvo, J., J. A.; Aron, A. T.; Ramos-Torres, K. M.; Chang, C. J., Synthetic fluorescent probes for studying copper in biological systems. *Chem. Soc. Rev.* **2015**, *44*, 4400-4414.
54. Rubino, J. T.; Franz, K. J., Coordination chemistry of copper proteins: How nature handles a toxic cargo for essential function. *J. Inorg. Biochem.* **2012**, *107* (1), 129-143.
55. Davis, A. V.; O'Halloran, T. V., A place for thioether chemistry in cellular copper ion recognition and trafficking. *Nat. Chem. Biol.* **2008**, *4*, 148-151.
56. Kim, B. E.; Nevitt, T.; Thiele, D. J., Mechanisms for copper acquisition, distribution and regulation. *Nat. Chem. Biol.* **2008**, *4*, 176-185.

57. Bogdan, A. R.; Miyazawa, M.; Hashimoto, K.; Tsuji, Y., Regulators of Iron Homeostasis: New Players in Metabolism, Cell Death, and Disease. *Trends Biochem Sci.* **2016**, *41* (3), 274-286.
58. V., T. S.; Torti, F. M., Ironing out cancer. *Cancer Res.* **2011**, *71*, 1511-4.
59. Dixon, S. J.; Lemberg, K. M.; Lamprecht, M. R.; Skouta, R.; Zaitsev, E. M.; Gleason, C. E.; Patel, D. N.; Bauer, A. J.; Cantley, A. M.; Yang, W. S.; Morrison, B. I.; Stockwell, B. R., *Cell* **2012**, *149* (1060-72).
60. Dixon, S. J.; Lemberg, K. M.; Lamprecht, M. R.; Skouta, R.; Zaitsev, E. M.; Gleason, C. E.; Patel, D. N.; Bauer, A. J.; Cantley, A. M.; Yang, W. S.; Morrison, B. I.; Stockwell, B. R., Ferroptosis: an iron-dependent form of nonapoptotic cell death. *Cell* **2012**, *149* (1060-1072).
61. Zhou, S.; Du, X.; Xie, J.; Wang, J., Interleukin-6 regulates iron-related proteins through c-Jun N-terminal kinase activation in BV2 microglial cell lines. *PLoS One* **2017**, *12* (7), e0180464.
62. Wang, B.; Zhang, J.; Song, F.; Tian, M.; Shi, B.; Jiang, H.; Xu, W.; Wang, H.; Zhou, M.; Pan, X.; Gu, J.; Yang, S.; Jiang, L.; Li, Z., EGFR regulates iron homeostasis to promote cancer growth through redistribution of transferrin receptor 1. *Cancer Lett.* **2016**, *381* (2), 331-340.
63. Seo, Y. A.; Kumara, R.; Wetli, H.; Wessling-Resnick, M., Regulation of divalent metal transporter-1 by serine phosphorylation. *Biochem. J.* **2016**, *473* (22), 4243-4254.
64. Cao, H.; Schroeder, B.; Chen, J.; Schott, M. B.; McNiven, M. A., The Endocytic Fate of the Transferrin Receptor Is Regulated by c-Abl Kinase. *J. Biol. Chem.* **2016**, *291* (32), 16424-16437.
65. Du, F.; Qian, C.; Qian, Z. M.; Wu, X. M.; Xie, H.; Yung, W. H.; Ke, Y., Hepcidin directly inhibits transferrin receptor 1 expression in astrocytes via a cyclic AMP-protein kinase A pathway. *Glia* **2011**, *59* (6), 936-945.
66. Poli, M.; Derosas, M.; Lusciati, S.; Cavadini, P.; Campanella, A.; Verardi, R.; Finazzi, D.; Arosio, P., Pantothenate kinase-2 (Pank2) silencing causes cell growth reduction, cell-specific ferroportin upregulation and iron deregulation. *Neurobiol Dis.* **2010**, *39* (2), 204-210.

## Chapter 3.

### **Iron Capture in a Functionalized Porous Polymer Applied to Remediation and Detection in Environmental Water Samples**

Portions of this work were published in the following scientific journal:

**S. Lee, M. K. Taylor K. Chakarawet, S. R. S. Bandaru, S. Gul, R. Chatterjee, C. M. Ackerman, J. Xu, J. A. Reimer, J. Yano, A. Gadgil, G. J. Long, F. Grandjean, J. R. Long and C. J. Chang** “Iron Capture in a Functionalized Porous Polymer Applied to Remediation and Detection in Environmental Water Samples”, *In preparation*

## Abstract

Iron is one of the most abundant elements in the environment and in the human body. Owing to its central role as an essential nutrient, iron homeostasis is tightly regulated and dysregulation of iron pools is implicated in numerous pathologies, including neurodegenerative diseases, atherosclerosis, and diabetes. Endogenous iron pool concentrations are directly linked to iron uptake from environmental sources such as drinking water and provide motivation for developing new technologies for assessing iron(II)&(III) levels. However, conventional methods for measuring iron(II)&(III) levels remain laborious and costly and require additional equipment and processing to remove iron(II)&(III) from the original environmental source. Herein, we report a simplified and accurate chemical platform to measure iron(II)&(III) concentrations in aqueous samples through a post-synthetically modified porous aromatic framework (PAF). The ether/thioether-functionalized PAF, termed PAF-1-ET, exhibits high selectivity for the uptake of iron(II)&(III) over other physiologically and environmentally relevant metal ions. Mössbauer spectroscopy, XANES, and EXAF measurements provide evidence to support iron(III) coordination within the PAF-1-ET. The iron-selective PAF-1-ET material was successfully employed to absorb and remove iron from groundwater, including field sources from West Bengal. Combined with the colorimetric sensor 8-hydroxyquinoline, PAF-1-ET enables direct readout of iron(II)&(III) concentrations from these same samples, providing a starting point to design and use molecularly-functionalized porous materials for potential dual remediation and detection applications.

### 3.1.1 Introduction

Iron is the fourth most abundant element in the earth's crust and the most abundant transition metal in the human body.<sup>1</sup> This metal is required for sustaining a range of physiological processes such as electron transfer, oxygen transport, respiration, and gene expression,<sup>2-5</sup> and iron deficiency leads to anemia.<sup>6</sup> At the same time, however, excess iron can increase production of reactive oxygen species, resulting in oxidative stress cascades that lead to lipid oxidation and DNA damage.<sup>3-5,7,8</sup> Indeed, aberrant iron accumulation is implicated in aging and in several diseases, including cardiovascular diseases, neurodegenerative diseases, and cancer.<sup>6,9-14</sup> In this context, chronic exposure to elevated iron levels is a potential contributor to abnormal iron accumulation and a common source of iron contamination is drinking water. The World Health Organization (WHO) recommends an upper limit of 0.3 ppm for iron in drinking water,<sup>15</sup> yet reported iron concentrations in water sources can vary over several orders of magnitude, ranging from 0.007 to 33.6 ppm in west Bengal<sup>16</sup> to undetectable amounts to 950 ppm based on Groundwater Ambient Monitoring and Assessment (GAMA) data from the San Francisco Bay (Supporting information). Because traditional methods for iron(II)&(III) detection require expensive instrumentation such as inductively coupled plasma mass spectrometry (ICP-MS) or atomic absorption spectroscopy,<sup>17,18</sup> it remains a challenge to rapidly and inexpensively screen the quality of drinking water in the context of iron and other metal contaminants, particularly in developing countries and other lower-resource environments.<sup>11,16,17,19-24</sup>

To meet this challenge, we sought to develop a chemical strategy that would enable simultaneous detection and removal of both ferrous and ferric iron from drinking water and other environmental and biomedical samples, with high selectivity over other metal competitors. In particular, we envisioned synthesizing a molecularly-tailored solid-state adsorbent that could

efficiently capture and remove iron(II)&(III) from a complex field specimen, allowing for simultaneous remediation of the sample and selective concentration of the metal analyte to facilitate its detection. We chose porous polymers as a materials chemistry platform for this dual remediation/detection function owing to their high chemical and thermal stability, particularly in aqueous and biological samples, as well as their ability to be functionalized in a molecular fashion.<sup>25–34</sup> Indeed, the parent porous aromatic framework, PAF-1, exhibits a high Brunauer-Emmett-Teller (BET) surface area (up to 5600 m<sup>2</sup>/g)<sup>35</sup> and is readily functionalized through post-synthetic modification.<sup>36–38</sup> We previously reported a thioether-functionalized variant of this porous polymer, PAF-1-SMe, as a platform for selective copper capture from biofluid samples as a diagnostic tool for Wilson's disease.<sup>36</sup> Herein, we present the development of an iron-selective PAF for dual remediation and detection of iron from environmental sources, including groundwater field samples. Specifically, ether-thioether (ET) functionalization of PAF-1 yields the material PAF-1-ET (Figure 1a), which exhibits highly selective iron uptake of both ferrous and ferric iron pools over other competing metals in laboratory and field water samples. Combining this molecular material for selective iron(II)&(III) capture and concentration from aqueous specimens with the dye 8-hydroxyquinoline enables the rapid and quantitative monitoring of iron levels in a simple and tunable colorimetric assay (Scheme 1). We highlight the potential utility of this method for remediation and screening of synthetic groundwater as well as field samples of drinking water sources collected from Bangladesh. This work provides a starting point for further applications of PAF-1-ET and development of new porous molecular materials for simplified, accurate, and rapid diagnostic and remediation applications without the need of bulky and expensive instrumentation.

### 3.1.2. Methods

#### 3.1.2.1. Synthesis of PAF-1-ET

Anhydrous 1,5-cyclooctadiene (cod, 1.05 mL, 8.32 mmol, Aldrich) was added to a solution of bis(1,5-cyclooctadiene)nickel(0) (2.25 g, 8.18 mmol, Aldrich) and dried 2,2'-bipyridyl (1.28 g, 8.18 mmol, Aldrich) in distilled DMF (100 mL, Aldrich) in a dry box. The mixture was heated at 80 °C for 1 h. Tetrakis(4-bromophenyl)methane (1.00 g, 1.57 mmol) was added to the purple solution and the mixture was stirred at 80 °C overnight to obtain a deep purple suspension. After cooling to room temperature, concentrated HCl was added to the mixture. The residue was filtered with washing with warm THF (100 mL), H<sub>2</sub>O (100 mL), ethanol (100 mL), and CH<sub>3</sub>Cl (100 mL) respectively, and dried in a vacuum oven at 170 °C to give PAF-1 as an off white powder. For PAF-1, % calc. for C<sub>24.5</sub>H<sub>16</sub>: C 94.80, H 5.20; observed. A pressure flask was charged with PAF-1 (0.20 g), paraformaldehyde (1.0 g), glacial AcOH (6.0 ml), H<sub>3</sub>PO<sub>4</sub> (3.0 ml), and conc. HCl (20.0 ml). The flask was sealed and heated to 90 °C for 3 days. The resulting solid was filtered and washed with H<sub>2</sub>O (500 mL), THF (100 mL), ethanol (100 mL), and CH<sub>3</sub>Cl (100 mL) to give PAF-1-CH<sub>2</sub>Cl. Elemental analysis found for PAF-1-CH<sub>2</sub>Cl, % calc. for C<sub>26.5</sub>H<sub>20</sub>Cl<sub>2</sub>: C 77.76, H 4.92, Cl 17.32; observed C 75.88, H 4.63, Cl 13.6. and then dried in vacuum oven at 150 °C to produce pale yellow solid of PAF-1-CH<sub>2</sub>Cl. Subsequently, PAF-1-CH<sub>2</sub>Cl was mixed with 2-(methylthio)ethan-1-ol (2.2 g, 0.021 mol, Aldrich) in 100 mL toluene in presence of 3 equivalents of NaH (1.5 g, 0.063 mol) under N<sub>2</sub> and stirred at 100 °C for 3 days. The resulting solid was collected, washed with H<sub>2</sub>O (100 mL), THF (100 mL), ethanol (100 mL), and CH<sub>3</sub>Cl (100 mL), and then dried under vacuum oven (150 °C) to produce PAF-1-ET as white powder. Elemental



analysis found for PAF-1.ET, % calc. for  $C_{32.5}H_{34}O_2S_2$ : C 74.96, H 6.58, O 6.14, S 12.31, Cl 0.00; observed C 74.89, H 5.08, O unmeasured, S 4.30, Cl 1.04.

Here the yield of substitution with 2-(methylthio)ethan-1-ol is 35% based on S elemental analysis of PAF-1-ET, which showed discrepancy of the decreased % of Cl. This might be attributed to high reactivity of sodium hydride with benzyl chloride to generate other side products.<sup>39</sup> Especially in case of 1,2-diphenylethane, estimated  $^{13}C$  NMR peak for bridge peak is reported to be 39 ppm in  $^{13}C$  NMR<sup>40,41</sup>, which might be responsible for the noise background in PAF-1-ET (Figure 1b)

### 3.1.2.2. Effect of Anion in Iron Uptake

Checked the anions effect of iron uptake using iron(III) chloride, iron(III) sulfate hydrate, ammonium iron(III) citrate. The metal stock concentration varied from 1~3 mg/L and from 21~30 mg/L and compared the iron uptake using 2 mg of PAF-1-ET. The mixture was stirred at room temperature for overnight. The mixture was filtered through a 0.45-mm membrane filter for all samples. The filtrates were analyzed using ICP-MS to determine the remaining iron concentration. The amount of iron adsorbed by PAF-1-ET was calculated by subtracting the residual iron concentration from the initial iron concentration:

### 3.1.2.3. Mössbauer Spectral Measurements.

$^{57}FeCl_3$  has been prepared by following a reported<sup>10</sup> procedure. A round bottom flask containing 50 mg of  $^{57}Fe$  oxide powder was fitted with a condenser and filled with an argon atmosphere. To this flask was added 1 mL of concentrated HCl which had been freeze-pump-thawed to remove any  $O_2$ . The solution was allowed to stir at reflux overnight until the evolution of  $H_2$  gas ceased and all of the  $^{57}Fe$  oxide had dissolved. The resulting yellow/green solution was heated under vacuum to remove excess HCl and water to make the  $^{57}FeCl_2$  dihydrate in a near quantitative 100 % yield. Storage in air lead to oxidation and a  $^{57}FeCl_3$  solution, to which ~50 mg of PAF-1-ET was added. The mixture was then stirred overnight at room temperature under  $N_2$ . PAF-1-ET with adsorbed iron(III) ions was collected, washed with 100 mL of warm  $H_2O$  and 100 mL of  $CH_3Cl$  and then dried in a vacuum oven at 150 °C to yield a white powder.

The  $^{57}Fe$  Mössbauer spectra of PAF-1-ET coordinated with  $^{57}Fe(III)$  have been obtained between 5 and 300 K with a SEE Co. Mössbauer spectrometer equipped with a Co-57 source in Rh matrix. The isomer shifts are given relative to  $\alpha$ -iron at 295 K. The spectral absorber was prepared under air by packing the sample into a 1.27 cm diameter Nylon washer before transferring to the spectrometer where the absorber was always maintained in a helium atmosphere.

The fits of all the 5 to 300 K Mössbauer spectra of PAF-1-ET used a Lorentzian line shape and involved two quadrupole doublets with a distribution of the local environments associated with the adsorbed iron(III) ions. Preliminary fits indicated that these two quadrupole doublets always had, within their experimental uncertainty, the same isomer shift and, in all subsequent fits, these two isomer shifts have been constrained to be equal. Further, the spectral area of these two components have been constrained to be equal because preliminary fits indicated a somewhat random temperature variation of their relative areas. The quadrupole splitting of the two doublets is found to be essentially independent of temperature. In addition a 9 percent by area high-spin

iron(II) component of unknown origin, but perhaps a residual from the preparation, was observed at all temperatures and is shown as the green component in Figures 4(a) and S7.

In addition to the two paramagnetic quadrupole doublets observed between 300 and 50 K, at 20, 10, and 5 K the spectra also exhibit additional components due to slow paramagnetic relaxation, on the Mössbauer timescale, components that have been fitted with the minimum number of broadened sextets needed to fit the spectral profile; as might be expected for a distribution of local iron(III) environments, quadrupole shifts of less than ca.  $\pm 0.3$  mm/s were associated with the iron(III) sextets.

A fit with the Debye model for a solid of the temperature dependence between 5 and 300 K of the isomer shift of the iron(III) adsorbed on PAF-1-ET, see the top of Figure 3.7, yields a Mössbauer temperature,  $\Theta_M$ , of 358(34) K. Further, a fit with the Debye model for a solid of the temperature dependence between 50 and 300 K of the logarithm of the spectral absorption area of PAF-1-ET, see the bottom of Figure 3.8, yields a Debye temperature,  $\Theta_D$ , of 141(3) K. The data points obtained at 5, 10, and 20 K have been excluded from this fit because of the extensive differences in the internal reabsorption of the Mössbauer  $\gamma$ -ray in the doublet and sextet portions of the spectra lead to larger than expected areas at these temperatures.

As is usually observed<sup>11,12</sup> the Mössbauer temperature is two to three times higher than the Debye temperature, because the two temperatures probe different portions of the phonon spectrum. Because the isomer shift depends on  $\langle v^2 \rangle$ , the mean-square velocity, and the absorption area depends on  $\langle x^2 \rangle$ , the mean-square displacement of the iron-57 nuclide, there is no model-independent relationship between these two temperatures. Generally, the isomer shift temperature dependence is more sensitive to high-energy phonons. Both these temperatures are relatively low and indicate the relative softness of the lattice around the iron(III) in PAF-1-ET. It is worth noting that the vibrations probed in the Mössbauer spectra are at lower energies than those probed in the FT-IR spectra shown in Figure 3.2 (b).

#### 3.1.2.4. X-ray absorption spectroscopy and EPR analysis

*X-ray Absorption Data collection.* X-ray absorption spectroscopy (XAS) data was collected at the Stanford Synchrotron Radiation Lightsource (SSRL) on beamline 9-3 (Storage ring conditions, 3.0 GeV, 500mA). Fe K-edge XAS spectra of porous aromatic framework (PAF) samples, packed in 0.5 mm thick aluminum sample holders with Kapton film windows on both sides, were recorded at room temperature. Reference compounds were used after diluting with boron nitride (1% w/w). Data were collected in transmission mode for reference compounds and as fluorescence excitation spectra for PAF samples using a 100-element Ge monolithic solid-state detector (Canberra). The incident radiation was monochromatized using a Si(220) double crystal monochromator which was detuned to 50% of flux maximum at Fe K-edge to minimize the higher harmonics and reduce x-ray flux. Harmonic rejection mirror was used to further reduce the contamination of higher harmonics radiation. The incident and transmitted X-ray intensities were monitored using N<sub>2</sub>-filled ion chambers. An iron foil spectrum was concomitantly recorded for energy calibration where the first inflection point was assigned to 7111.2 eV. Even at low X-ray flux, slight photoreduction of the PAF samples was observed after every 2 scans on the same spot. Therefore, data were collected at multiple spots of each sample and only first 2 scans from each spot were used for averaging the data.

*EXAFS Data Analysis.* XAS data reduction was done using program SamView (SixPack software, <http://www.sams-xrays.com/sixpack>). Athena software (Demeter version 0.9.25)<sup>45</sup> was used for data averaging and removal of pre-edge and post-edge backgrounds. A five-domain cubic spline was used to remove low-frequency background in  $k$ -space. The resulting  $k$ -space data,  $k^3\chi(k)$ , was then Fourier transformed into  $r$ -space using a  $k$  range of 3.46-10.52 Å<sup>-1</sup> (Figure 4b bottom) and used for extended X-ray absorption fine structure (EXAFS) refinement. EXAFS fitting was carried out using Artemis (Demeter software version 0.9.25)<sup>45</sup> with phase and amplitude functions obtained from FEFF, version 6.<sup>46</sup> The parameters  $R$  (average bond distance between Fe and scattering atom) and  $\sigma^2$  (mean square displacement of the bond distance) were allowed to vary, while  $N$ , the number of atoms in the shell, was systematically varied by integer steps. The value of  $E_0$  (the energy which represents the zero value of the photoelectron wave vector  $k$ ) was also varied but restricted to a common value for every shell in a given fit. The value for  $S_0^2$  (the amplitude reduction factor) was extracted from the fit to the data of Fe foil, and was fixed (0.95) during the fits. The best fit parameters for EXAFS curve fitting are listed in Table S1.

*EPR Analysis.* Low-temperature X-band EPR spectra were recorded using a Varian E109 EPR spectrometer equipped with a Model 102 Microwave bridge. Sample temperature was maintained at 8 K using an Air Products LTR liquid helium cryostat. The following spectrometer conditions were used: microwave frequency, 9.22 GHz; field modulation amplitude, 32 G at 100 kHz; microwave power, 20 mW. The data shown in Fig S8 shows a peak at  $g \sim 4.3$  that is expected for high spin ( $S = 5/2$ ) Fe<sup>III</sup> complexes

### 3.1.2.5. Iron Uptake Studies in Environmental Samples and Its Colorimetric Detection

*Genuine ground water collection.* Raw water samples were collected from the well head after approximately 5 min of continuous initial pumping to avoid bacterial contamination and oxygenated water. These samples were acidified immediately using HCl. As monitored by pH test strips (Merck,  $\pm 1$  pH unit), the pH of the samples of raw water, and those collected after electrolysis and settling, remained near pH 7. This result was consistent with beaker batch tests in synthetic Bangladesh groundwater and field tests of a 100 L ECAR reactor in West Bengal.<sup>47</sup>

*Synthetic Bengal Groundwater Preparation.* Concentrations of HCO<sub>3</sub><sup>-</sup>, Ca<sup>2+</sup>, Mg<sup>2+</sup>, Si, and P (8.2, 2.6, 1.9 mM, 1.3, and 0.16  $\mu$ M respectively) were prepared from reflected average levels in Bangladesh tube wells according to the British Geological Survey (BGS).<sup>48</sup> The target pH value (6.6 or 7.5) was maintained throughout the experiments by adding drops of 1.1 M HCl as needed. Initial concentrations of all ions varied by less than 10% in replicate batch experiments. The samples were stored at -20 °C and freshly thawed before each experiment.<sup>49</sup>

*Iron uptake in ground water samples.* A 5 mL sample of the synthetic ground water and genuine ground water samples was added to a 15 mL tube containing 2 mg of PAF-1-ET. To simulate different iron concentration in natural samples, ammonium iron(II) sulfate along with 1 equivalent of citric acid was added to synthetic ground water. In case of genuine ground water samples, 15-10 ppm of citric acid was added into samples before adding PAF-1-ET. Water samples with/without PAF-1-ET were kept in a shaker at room temperature overnight, filtered through 0.45  $\mu$ m membrane filters, and analyzed by ICP-MS to determine remaining iron content. The amount of iron adsorbed by PAF-1-ET was calculated by subtracting the residual iron concentration from the initial iron concentration.

*Colorimetric detection.* PAF-1-ET applied to water samples was dried open to air overnight. Subsequently, 1 mM 8-hydroxyquinoline, 8-HQ in DMSO (1 mL) was added to the PAF-1-ET, followed by being shaken three times. The liquid was filtered through a 0.45 mm membrane filter and transferred into 1 cm × 0.5 cm quartz cuvette (1.4-mL volume, Starna). The formation of complex between 8-HQ and iron extracted from PAF-1-ET was monitored using a Varian Cary 50 spectrophotometer.

*The Detection of limit* was based on the 3 sigma method ( $3\sigma/k$ ). Six replicates of dried PAF-1-ET which were applied in 133 ppb of Iron(III) stock solution as lowest sample point were measured in 1 mM of 8-HQ in DMSO. The standard deviation is calculated as  $\sigma$ . Subsequently, dried PAF-1-ET applied in the different iron(III) concentration from 190 to 1090 ppb were measured and 1 mM 8-HQ was added in dried PAFs and measured spectrum of each samples. The absorbance at 460 nm was plotted against the initial iron concentration and a linear regression curve was then fitted to give  $k$  the slope of the same line.<sup>50-54</sup> The detection of limit is calculated as 283 ppb.

### 3.1.2.6. Modeling study for iron coordination in PAF-1-ET

To determine the maximum number of ET functional groups that could feasibly coordinate the same iron atom based on geometric and steric constraints, a hypothetical PAF-1-ET with a single diamond net was generated using the program *Materials Studio 2017 R2*, and the geometry of the modeled structure was optimized with the *Forcite* module in *Materials Studio*. To build structures, we assume the following conditions.

- No S coordination to the iron ion due to the EXAFS data.
- To maintain charge balance, one monodentate sulfate anion is attached to the iron ion. The rest of the iron coordination sphere is filled with water molecules.

Considering the ET/Fe ratio of 2.9 for genuine groundwater samples (West Bengal, India), it is presumed that up to 3 oxygen atoms from the ET functional groups are coordinated to a single iron ion. Therefore, we first generated five feasible structures, where either 2 or 3 oxygen atoms from the ET functional group are coordinated to the iron atom. For easy understanding, a small portion of PAF-1-ET (a single tetra(biphenyl-yl)methane unit) is demonstrated in Figure 3.2.

For Figure 3.11a-c, an ET functional group is connected to each of two phenyl rings attached to the same tetrahedral carbon, and the oxygen atoms of each of these two ET functional groups are able to coordinate the same iron atom. Due to the flexibility of the ET functional groups, these functionalities can be located at either 2- or 3-position of the biphenyl moieties without disrupting their ability to coordinate the same iron atom. A third ET functional group can also coordinate the same iron atom when the three ET functionalities are located at the 2-, 2', and 3-positions of two biphenyl groups (Figure 3.11d). Furthermore, an iron ion can be coordinated by two functional groups at the 2- and 2'-positions of a single biphenyl moiety (Figure 3.11e). The wide range of possible ET/Fe coordination behaviors (as well as the random nature of ET functionalization throughout the PAF) would support the shift and broadening of <sup>13</sup>C NMR solid-state NMR spectra.

Because of the high porosity of pristine PAF-1, the actual framework can be partially interpenetrated. In this case, two or three ET functionalities from different nets can be coordinated to the same iron. As a typical example, the iron coordination environment of the interpenetrating

net is illustrated in Figure 3.11f. However, it was not possible to build a feasible structure with four ET functionalities coordinated to the same iron, due to congestion of the ET groups.

It should be noted that, in the case of maximum iron uptake, the ET/Fe ratio is estimated to be ca. 1.2. To provide a possible illustration of this lower ET/Fe ratio, another model structure was prepared in which the iron atom is coordinated by only one ET group (with the rest of the coordination sphere occupied by four water molecules and one sulfate anion). As a typical example, Figure 3.12a-b demonstrates the small portion of Fe-coordinated PAF-1-ET in different perspectives. In this structure, the ET functionality is attached to the 3-position of the tetra(biphenyl-yl)methane unit to minimize the interaction between the Fe ion and the tetrahedral carbon (because the solid-state NMR data implies the location of the iron ion should close to the benzene ring rather than the tetrahedral carbon). To stabilize the iron ions, the coordinated water molecule might weakly interact with a benzene ring (possibly weak CH- $\pi$  interaction), which may also related to the broadening of the signal in solid-state NMR spectra. However, we cannot fully exclude the possibility that the FeO<sub>6</sub> unit (i.e. Fe(SO<sub>4</sub>)(H<sub>2</sub>O)<sub>4</sub>(ET)) is stabilized at the corner created by the tetrahedral carbon.

Assuming that the structure of pristine PAF-1 is described as a single diamond net and half of the benzene rings are functionalized, four ET groups can be accommodated in each adamantane cage. This indicates that there is enough room to allow the guest diffusion even at the high Fe loading (Figure 3.12c).

### 3.1.2.7. Iron Uptake Studies in Environmental Samples and Its Colorimetric Detection

*Genuine ground water collection.* Raw water samples were collected from the well head after approximately 5 min of continuous initial pumping to avoid bacterial contamination and oxygenated water. These samples were acidified immediately using HCl. As monitored by pH test strips (Merck,  $\pm 1$  pH unit), the pH of the samples of raw water, and those collected after electrolysis and settling, remained near pH 7. This result was consistent with beaker batch tests in synthetic Bangladesh groundwater and field tests of a 100 L ECAR reactor in West Bengal.<sup>47</sup>

*Synthetic Bengal Groundwater Preparation.* Concentrations of HCO<sub>3</sub><sup>-</sup>, Ca<sup>2+</sup>, Mg<sup>2+</sup>, Si, and P (8.2, 2.6 1.9 mM, 1.3, and 0.16  $\mu$ M respectively) were prepared from reflected average levels in Bangladesh tube wells according to the British Geological Survey (BGS).<sup>48</sup> The target pH value (6.6 or 7.5) was maintained throughout the experiments by adding drops of 1.1 M HCl as needed. Initial concentrations of all ions varied by less than 10% in replicate batch experiments. The samples were stored at -20 °C and freshly thawed before each experiment.<sup>49</sup>

*Iron uptake in ground water samples.* A 5 mL sample of the synthetic ground water and genuine ground water samples was added to a 15 mL tube containing 2 mg of PAF-1-ET. To simulate different iron concentration in natural samples, ammonium iron(II) sulfate along with 1 equivalent of citric acid was added to synthetic ground water. In case of genuine ground water samples, 15-10 ppm of citric acid was added into samples before adding PAF-1-ET. Water samples with/without PAF-1-ET were kept in a shaker at room temperature overnight, filtered through 0.45 mm membrane filters, and analyzed by ICP-MS to determine remaining iron content. The amount of iron adsorbed by PAF-1-ET was calculated by subtracting the residual iron concentration from the initial iron concentration.

*Colorimetric detection.* PAF-1-ET applied to water samples was dried open to air overnight. Subsequently, 1 mM 8-hydroxyquinoline, 8-HQ in DMSO (1 mL) was added to the PAF-1-ET, followed by being shaken three times. The liquid was filtered through a 0.45 mm

membrane filter and transferred into 1 cm × 0.5 cm quartz cuvette (1.4-mL volume, Starna). The formation of complex between 8-HQ and iron extracted from PAF-1-ET was monitored using a Varian Cary 50 spectrophotometer.

*The Detection of limit* was based on the 3 sigma method ( $3\sigma/k$ ). Six replicates of dried PAF-1-ET which were applied in 133 ppb of Iron(III) stock solution as lowest sample point were measured in 1 mM of 8-HQ in DMSO. The standard deviation is calculated as  $\sigma$ . Subsequently, dried PAF-1-ET applied in the different iron(III) concentration from 190 to 1090 ppb were measured and 1 mM 8-HQ was added in dried PAFs and measured spectrum of each samples. The absorbance at 460 nm was plotted against the initial iron concentration and a linear regression curve was then fitted to give  $k$  the slope of the same line.<sup>50-54</sup> The detection of limit is calculated as 283 ppb.

### 3.1.3. Result and Discussion

#### 3.1.3.1. Synthesis and Characterization

Building on the design of PAF-1-SMe thioether for selective copper capture<sup>37</sup> as well as the related thiol material for mercury adsorption<sup>25</sup>. We synthesized a variety of PAF scaffolds and found that the derivative with an extended ether-thioether pendant, referred to here as PAF-1-ET, was an effective material for selective capture of both iron (II) and (III). The PAF-1-ET material was prepared in a three-step sequence based on reported procedures for the parent PAF-1 and PAF-1-CH<sub>2</sub>Cl,<sup>38</sup> followed by subsequent treatment with 2-(methylthio)ethan-1-ol to install the ether-thioether ligand (Figure 1a). Elemental analysis revealed that the chlorine content decreased from 13.6% in PAF-1-CH<sub>2</sub>Cl to 1.04% in PAF-1-ET while the sulfur content of the latter was found to be 4.30%, corresponding to grafting of 35% of the phenyl groups in PAF-1-ET. Infrared spectroscopy afforded further confirmation of the successful functionalization through the disappearance of a peak assigned to the C–H wagging mode of the –CH<sub>2</sub>Cl group at 1270 cm<sup>-1</sup> in PAF-1-CH<sub>2</sub>Cl (Figure 3.2a and b). It was also possible to monitor the successful functionalization by solid-state <sup>1</sup>H–<sup>13</sup>C cross-polarization magic angle spinning (CP/MAS) NMR spectroscopy and identification of <sup>13</sup>C new chemical shifts arising from the –CH<sub>2</sub>OCH<sub>2</sub>CH<sub>2</sub>SCH<sub>3</sub> group in PAF-1-ET (66, 53, 36, and 14 ppm) compared with a shift at 43 ppm for the -CH<sub>2</sub>Cl group in PAF-1-CH<sub>2</sub>Cl (Figure 1b). Nitrogen adsorption isotherms collected at 77 K revealed that PAF-1-ET retained permanent porosity with a high BET surface area of 1500 (±420) m<sup>2</sup>/g. The average pore size distribution obtained from the adsorption isotherms was smaller than the average value of 12 Å for PAF-1 and supporting incorporation of the ether-thioether groups (Figure 3.2).

#### 3.1.3.2. Kinetics and Selectivity of Iron Uptake.

After confirming the structural integrity and porosity of PAF-1-ET, we assessed its capacity for iron capture from aqueous solution by fitting of adsorption isotherms collected after equilibration with a wide range of iron levels (1 ppb to 300 ppm, Figure 2a). The best fit for the experimental data utilized a dual-site Langmuir model<sup>29</sup> encompassing a strong adsorption site correlated with the framework ether-thioether groups (saturation capacity of 16.3 mg/g) and a weak adsorption site associated with iron ions trapped and physisorbed in the pores<sup>37</sup> (saturation capacity of 98.0 mg/g) (Table S1). The strong adsorption site was correlated with the ether-thioether groups within the framework, and this assignment is supported by comparing copper adsorption in PAF-1-CH<sub>2</sub>Cl and PAF-1-ET up to ~10 mg/L (Figure 2a, inset). PAF-1-ET displayed

a much steeper up-take than PAF-1-CH<sub>2</sub>Cl, and this enhanced uptake notably persisted for higher iron concentrations. By comparison, PAF-1-CH<sub>2</sub>Cl showed higher uptake from 3.9 mg/g to 77 (~20-fold) in the range 2.6 mg/L–126 mg/L, providing evidence for the presence of iron(II) and (III) trapped within the pores and/or adsorption at weaker binding sites in PAF-1-ET. For the comparison, data collected on iron uptake by PAF-1-CH<sub>2</sub>Cl has been similarly fitted with a dual-site Langmuir model, albeit with lower saturation capacity (strong adsorption site saturation capacity of 6 mg/g and a weak adsorption site saturation capacity of 26 mg/g). Iron uptake by PAF-1-ET was also much steeper than PAF-1-CH<sub>2</sub>Cl over the entire range of iron solutions examined (7.6 mg/g for PAF-1-ET and PAF-1-CH<sub>2</sub>Cl 0.9 mg/g at 9.8 ppm, respectively). Most importantly, PAF-1-ET exhibited high selectivity for ferrous and ferric iron over other biologically-relevant metal ions (Na<sup>+</sup>, K<sup>+</sup>, Mg<sup>2+</sup>, Ca<sup>2+</sup>, Cu<sup>2+</sup>, and Zn<sup>2+</sup>) at 0.3, 2, and 20 ppm (Figure 2b). For example, the distribution coefficient,  $K_d$ , was found to be  $2.6 \pm 0.7 \times 10^4$  mL/g for 10 ppm ferrous iron in HEPES buffer at pH = 6.7 compared with  $K_d$  values of  $6.0 \times 10^2$ ,  $1.2 \times 10^2$ ,  $1.8 \times 10^2$ ,  $7.7 \times 10^2$ ,  $3.3 \times 10^3$ , and 38 mL/g for 10 ppm Na<sup>+</sup>, K<sup>+</sup>, Mg<sup>2+</sup>, Ca<sup>2+</sup>, Cu<sup>2+</sup>, and Zn<sup>2+</sup>, respectively, indicating most efficient uptake of iron in aqueous media. The concentration dependence of iron uptake by PAF-1-ET was also evaluated by examining various pH 6.7 aqueous solutions in HEPES buffer, and it was found that the amount of iron absorbed increases with its increasing concentration in solution (Figure 3a). In an effort to develop a colorimetric assay for the detection of iron(III) uptake by PAF-1-ET, we further evaluated the ability of 8-hydroxyquinoline (8-HQ) to bind iron captured within the framework. Upon binding iron, 8-HQ undergoes a distinct change from colorless (315 nm absorption,  $\epsilon = 1.95 \times 10^3 \text{ M}^{-1} \text{ cm}^{-1}$ ) to a blue-green color (460 and 560 nm absorption,  $\epsilon = 750 \text{ M}^{-1} \text{ cm}^{-1}$  at 460 nm) distinctive of a Fe–8-HQ complex.<sup>55–58</sup> Thus, the successful binding of captured iron(III) within PAF-1-ET by 8-HQ would allow for facile and quantitative determination of absorbed iron. To test for this capability, a 1 mM solution of 8-HQ in DMSO was added to dried samples of PAF-1-ET following their exposure to aqueous samples of iron (Figure 3a). Gratifyingly, in the presence of these iron-decorated samples the 8-HQ absorption spectra exhibited two new peaks at 460 and 560 nm (Figure 3b), indicative of iron(III) complex formation. The calculated amount of iron adsorbed by PAF-1-ET, based on the 460 nm absorbance peak for the highest sample concentration, correlated well with direct iron measurements by ICP-MS (Figure 3c).

To garner additional insight into the nature of the interaction of absorbed iron with the framework functional groups, <sup>57</sup>Fe Mössbauer data was collected between 5 and 300 K and the 100 and 5 K fitted spectra are shown in Figure 3.6. The complete set of fitted spectra are shown in Figure 3.7 and plots of the temperature dependence of the fitted hyperfine spectral parameters are shown in Figure 3.7 and given in Table 3.2. The details of the experimental measurements and the fitting procedure are given in the SI.

The spectral fits indicate that PAF-1-ET has adsorbed high-spin iron(III) ions that are completely paramagnetic; between 50 and 300 K the spectra are very similar and reveal a bimodal distribution of quadrupole splittings,  $\Delta E_Q$ , between ca. 0.6 and 1.0 mm/s, a distribution centered about a unique high-spin iron(III) isomer shift,  $\delta$ , of 0.385(2) mm/s at 300 K and 0.507(1) mm/s at 50 K. These values are all consistent with an iron(III) The spectral fits indicate that PAF-1-ET has adsorbed high-spin iron(III) ions that are completely paramagnetic; between 50 and 300 K the spectra are very similar and reveal a bimodal distribution of quadrupole splittings,  $\Delta E_Q$ , between ca. 0.6 and 1.0 mm/s, a distribution centered about a unique high-spin iron(III) isomer shift,  $\delta$ , of 0.385(2) mm/s at 300 K and 0.507(1) mm/s at 50 K. These values are all consistent with an iron(III) used to further investigate the nature and local coordination environment of iron within the

framework. X-ray absorption near edge structure (XANES) spectrum of iron(III) coordinated PAF-1-ET is presented in Figure 4b (top) along with some reference compounds. The rising edge energy of the sample aligns well with that of Fe<sub>2</sub>O<sub>3</sub> suggesting the existence iron as Fe<sup>+3</sup>. Figure 4b shows the *k*<sup>3</sup>-weighted Fe EXAFS data for iron(III) coordinated PAF-1-ET in *r*-space along with the best fit (see Table S3 for best fit parameters). The independent axis represents the apparent distance *R'*, which is shorter than the actual distance by ~0.5 Å due to a phase shift. For iron(III) coordinated PAF-1-ET<sup>59</sup>, the best two-shell fit was achieved with an immediate coordination environment of six oxygen at a distance of 2.00 ± 0.01 Å and 12 carbon at a distance of 3.06 ± 0.04 Å (Figure 4b, Table S3).

### 3.1.3.3. Iron Capture and Detection in Aqueous and Environmental Samples.

After demonstrating the ability of PAF-1-ET to absorb both iron(II) and (III) with high affinity and selectivity in aqueous buffer, we examined its performance in environmental samples. In particular, to verify its detection capability when exposed to various iron sources from different regions, synthetic ground water was prepared according to Gadgil group<sup>49</sup> with iron concentrations of 1.8, 4.7, 6.7, and 37 ppm. Furthermore, PAF-1-ET was also used to treat genuine ground water samples collected in West Bengal, which were reported to have 14 ppm of iron.<sup>16</sup> We found that PAF-1-ET adsorbed ca. 41 to 91 % of the iron(III) in the synthetic ground water samples depending on the solution concentration. In the presence of PAF-1-ET, the concentration of iron(III) in the genuine ground water decreases as indicated by the function,  $y = Ae^{-t/t_0} + C$ , where *y* is the detected amount of iron(III), *A* is a scale factor, *C* is a constant, *t*<sub>0</sub> is the decay time, and *t* is the elapsed time. The best fit shown in Figure 5 b corresponds to *A* = 10.0(4) mg/g, *C* = 4.1(1) mg/g, and *t*<sub>0</sub> = 12(1) min. In other words, within 24 min PAF-1-ET has captured 72 % of the iron(III) and is essentially saturated after ca. 36 minutes, so that the iron(III) concentration in the ground water remains constant (Figure 5b). Subsequent analysis of the PAF-1-ET samples using an 8-HQ assay revealed an increase in absorbance at 460 and 600 nm with increasing iron concentration in the original water samples (Figure 5c). As demonstrated for the aqueous buffer samples, the iron levels calculated from the absorption at 460 nm were in good agreement with those determined from direct ICP-MS measurements (Figure 5d). Using the three-sigma method (3σ/*k*)<sup>50–52,60</sup>, we determined that the detection limit for this PAF-1-ET/8-HQ assay is 283 ppb in aqueous solution (Figure 3.14). Importantly, PAF-1-ET retains crystallinity and porosity following regeneration with 8-HQ, and can be cycled three times without notable loss of iron absorption capacity (Figure 3.15).

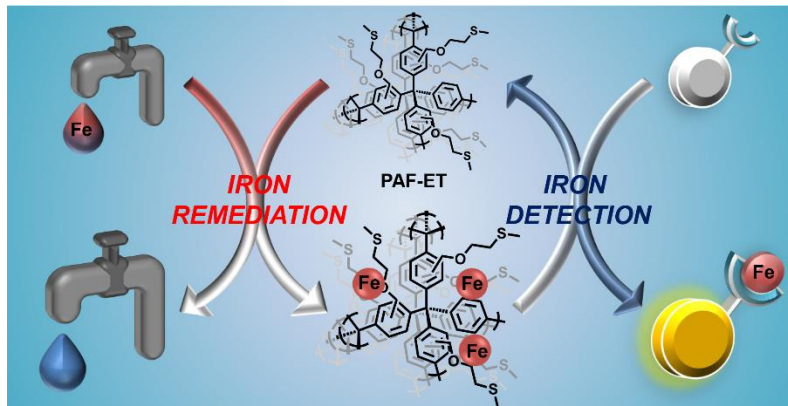
### 3.1.4 Conclusion

In conclusion, we have demonstrated that the ether-thioether-functionalized porous aromatic framework PAF-1-ET is capable of selective and efficient iron(II) and (III) uptake and removal from aqueous media and ground water. Following iron coordination, characterization of PAF-1-ET using Mössbauer spectroscopies and X-adsorption spectroscopy reveals that iron(III) is preferentially bound by oxygen in an octahedral environment. Thus it is the introduction of oxygen functionality within the framework that is responsible for the shift to iron selectivity from the previously reported thioether functionalized copper selective polymer<sup>36</sup>. Finally, the combination of PAF-1- ET with 8-HQ as a colorimetric indicator results in an efficient and accurate tool for determining iron ion concentration directly from ground water samples, with minimal processing and equipment needs.





## Figures



**Scheme 3.1.** Iron detection assay with PAF-1-ET as a selective iron capture and concentrator material for removal coupled to a colorimetric indicator for detection and regeneration.

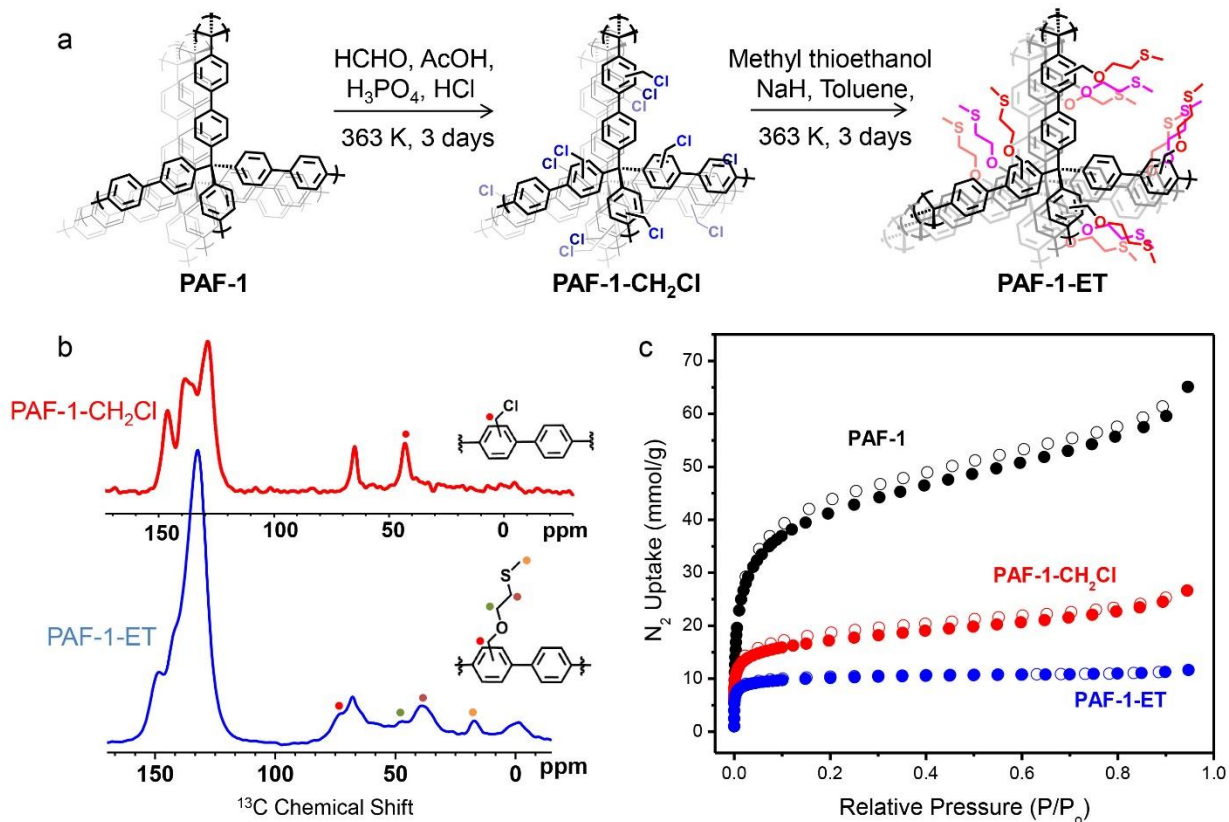


**Figure 3.1.** (a) Synthesis of PAF-1-ET. (b) Solid-state  $^{13}\text{C}$  NMR spectra of PAF-1- $\text{CH}_2\text{Cl}$  and PAF-1-ET (b)  $\text{N}_2$  absorption isotherms of PAF-1, PAF-1- $\text{CH}_2\text{Cl}$ , and PAF-1-ET at 77 K. Closed and open symbols represent adsorption and desorption branches, respectively.

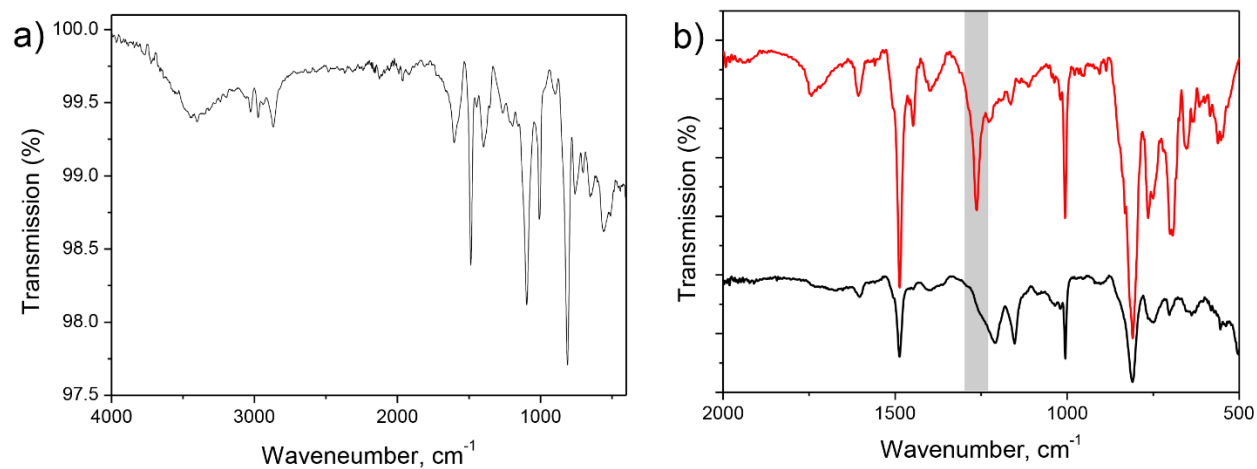


**Figure 3.2.** (a) FT-IR spectrum of PAF-1-ET and (b) a comparison of the 500-2000 cm<sup>-1</sup> spectral regions for PAF-1-CH<sub>2</sub>Cl (red) and PAF-1-ET (black). The grey band indicates the wagging mode of the -CH<sub>2</sub>Cl group.

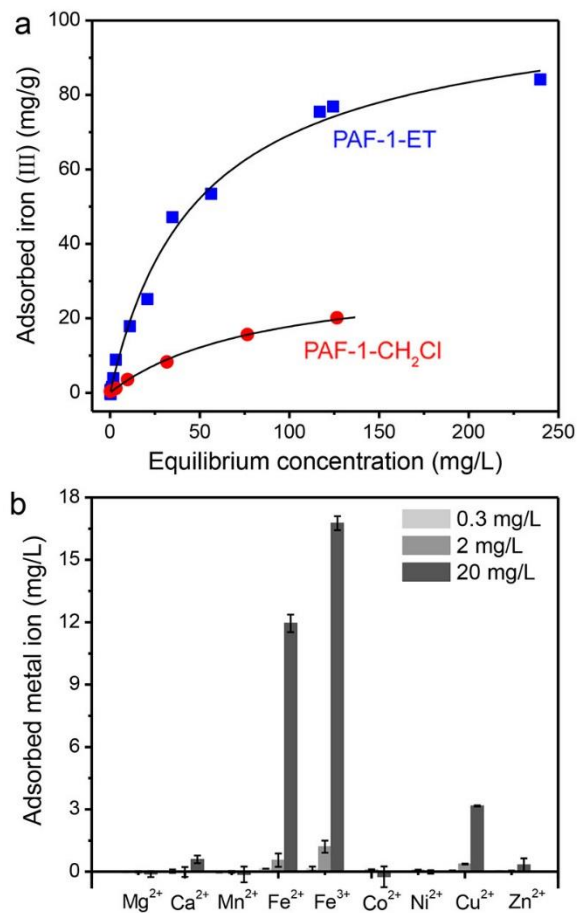


**Figure 3.3.** (a) Iron(III) adsorption isotherm in mg/g of PAF-1-ET (black squares) and PAF-1-CH<sub>2</sub>Cl (gray circles) fit obtained by using the dual-site Langmuir model (red lines) in different iron solution (1 ppb to 300 ppm using (NH<sub>4</sub>)<sub>2</sub>Fe(SO<sub>4</sub>)<sub>2</sub>·6H<sub>2</sub>O in a 100 mM HEPES buffer solution at pH = 6.7). Langmuir model (red line) discussed in the SI. The inset plot is a magnified portion of the initial equilibrium concentration range (0-10 mg/L) and the adsorbed amount of iron(III) (mg/g) (b) Capture capacities of PAF-1-ET in the presence of physiologically relevant metal ions (0.3, 2 and 20 ppm). In the case of the measurement with iron(III), one equivalent of citric acid was added. All data were collected in a 100 mM HEPES buffer solution at pH = 6.7.

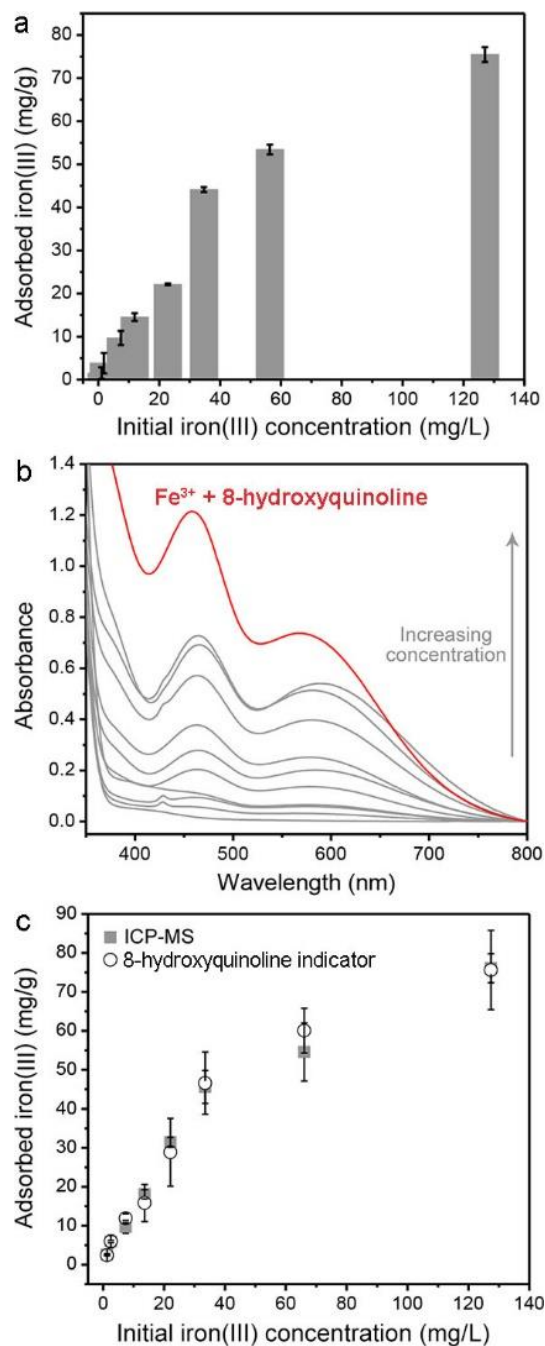


**Figure 3.4.** (a) Adsorbed iron(III) uptake of PAF-1-ET from the various initial iron(III) aqueous solutions in a 100 mM HEPES at pH 6.7. (b) Absorption spectra resulting from the addition of 1 mM aqueous solution of 8-hydroxy-quinoline(8-HQ) to dried PAF-1-ET obtained after their exposure to the iron(III) aqueous solutions shown in (a). The top red line corresponds to the absorption of a complex of iron(III) with 8-hydroxyquinoline(8-HQ) and the increase in the grey line absorbance at 460 nm correspond to the increase in initial concentrations of iron(III) in (a). (c) The good correlation between the iron(III) uptake measured by ICP-MS (gray filled squares) and the iron(III) uptake obtained from the absorbance at 460 nm in the presence of the 8-hydroxyquinoline indicator (open circles).

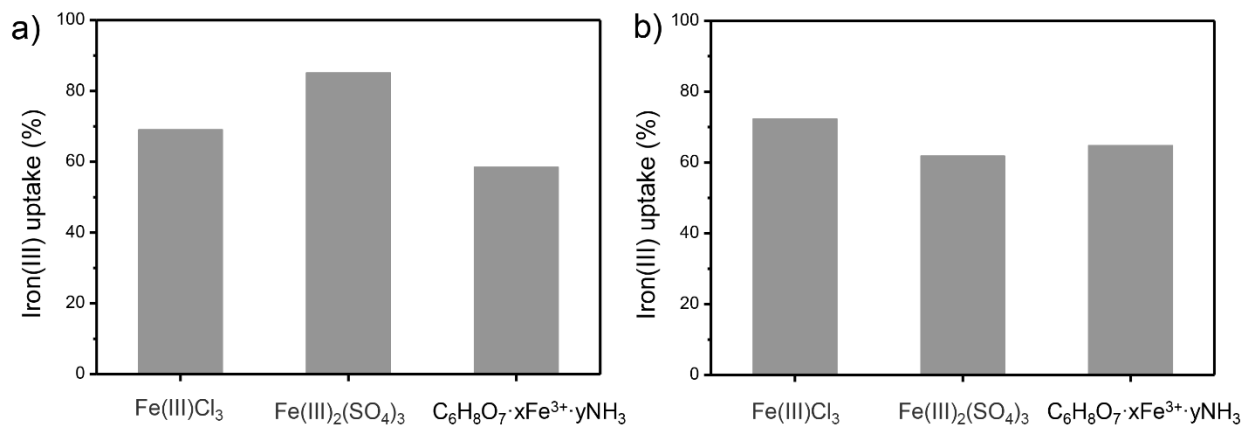


**Figure 3.5.** Comparison of the iron(III) uptake in the presence of chloride, sulfate, and citrate anions. The concentration of the initial PAF-1-ET aqueous solutions was 1 to 3 mg/L for (a) and 21 to 30 mg/L for (b).

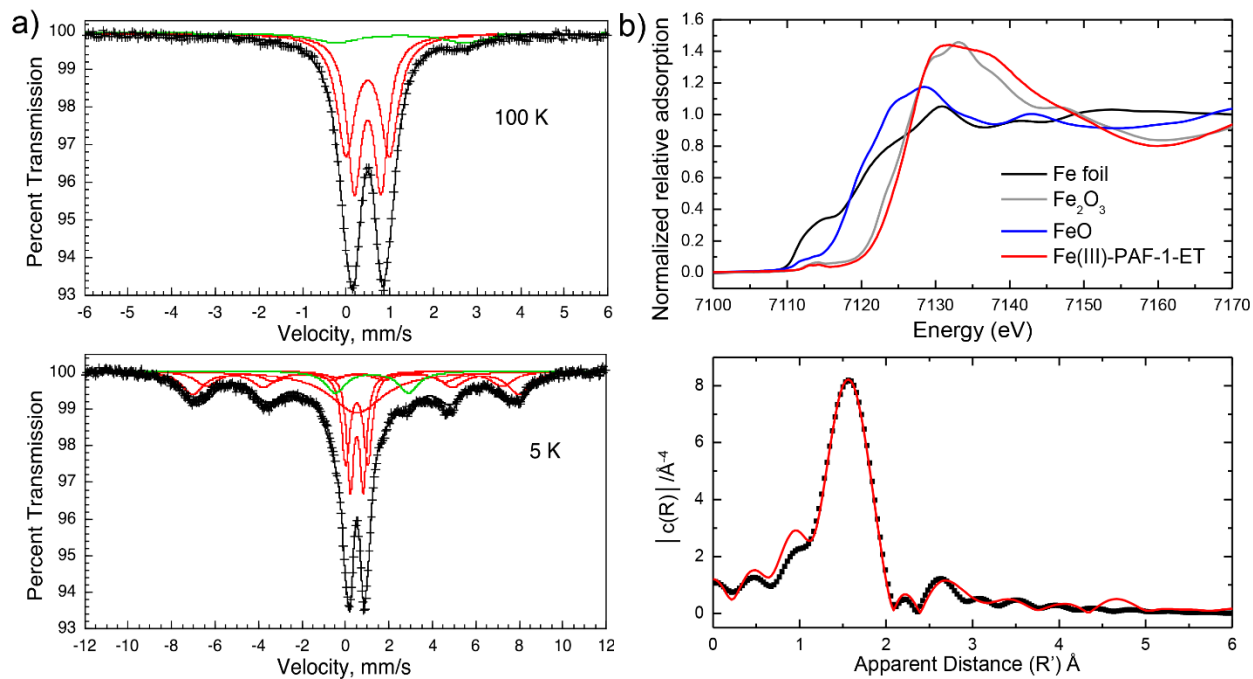


**Figure 3.6.** (a) The iron-57 Mössbauer spectra of PAF-1-ET obtained at 100 K (top) and 5 K (bottom). The red and green components in the fits are assigned to iron(III) and iron(II) ions, respectively. The total fit is shown in black. (b) The room temperature XANES spectra obtained at the Fe K-edge. (up) The Fourier transform of  $k^3$ -weighted Fe K-edge EXAFS data of Fe(III) adsorbed to PAF-1-ET and its fit shown in red.(bottom)



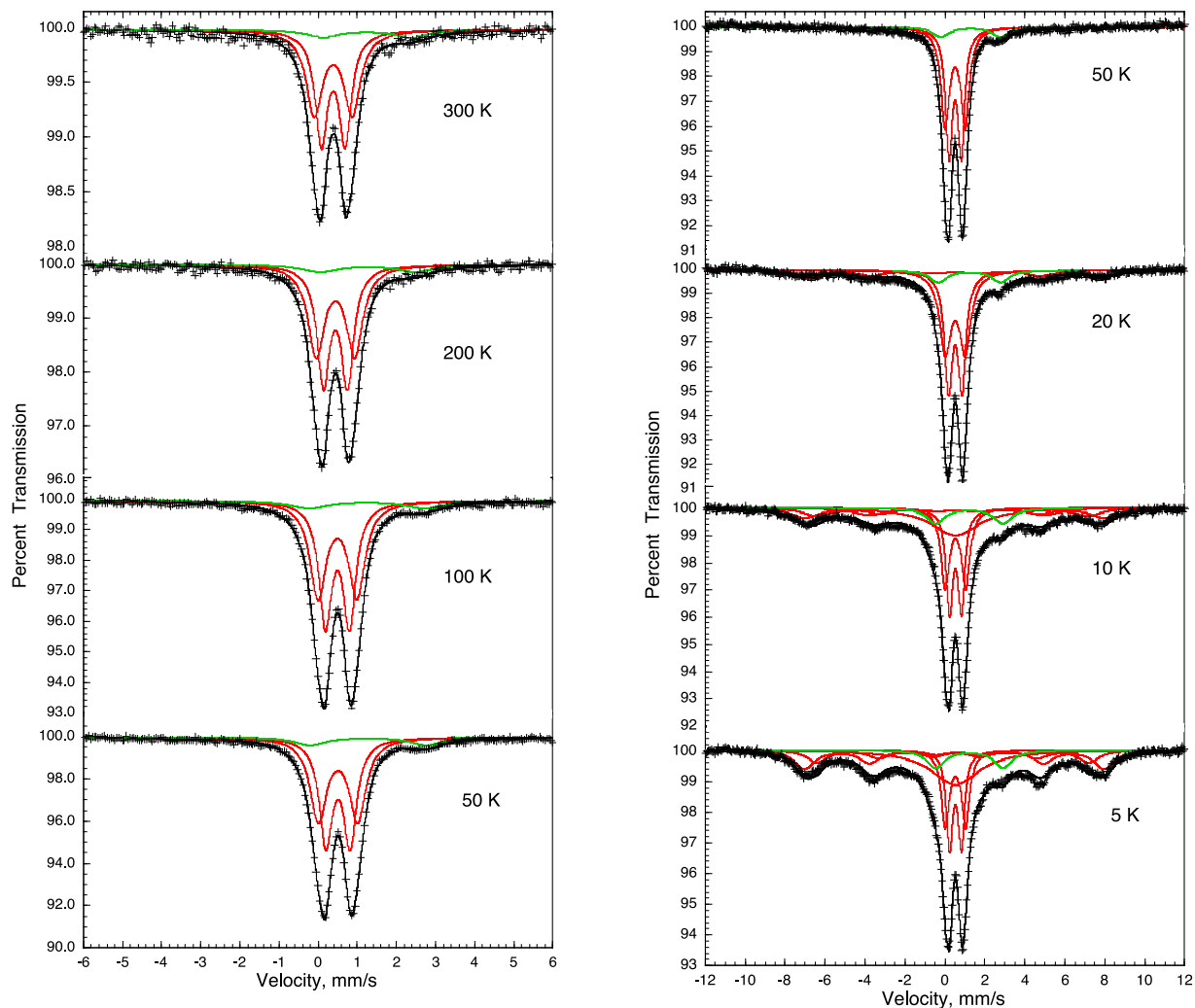


**Figure 3.7.** Mössbauer spectra of PAF-1-ET obtained at the indicated temperatures. The components assigned to iron(III) and iron(II) are shown in red and green, respectively. The total fit is shown in black.

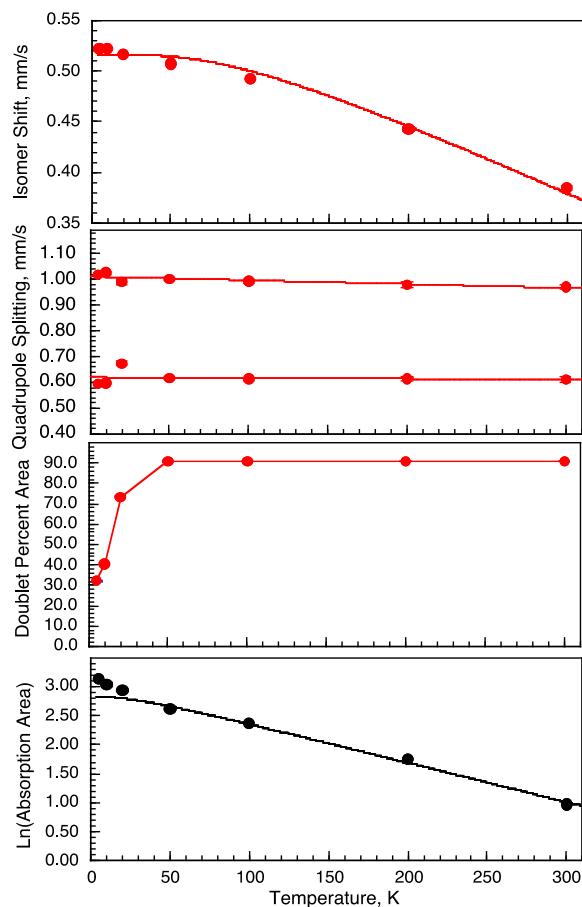


**Figure 3.8.** Top: the temperature dependence of the iron(III) isomer shift, with the Debye-model fit shown as the red line. Second: the temperature dependence of the iron(III) quadrupole splitting, with a linear fit shown. Third: the temperature dependence of the percent area of the two iron(III) quadrupole doublets. Bottom: the temperature dependence from 300 to 50 K of the logarithm of the spectral absorption area, expressed in  $(\% \epsilon)(\text{mm/s})$ , with the Debye-model fit shown as the black line. In all four plots the uncertainties are essentially the size of the symbols.

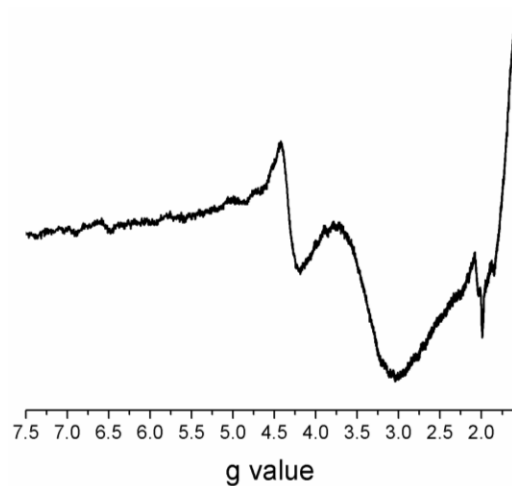


**Figure 3.9.** The derivative of the X-band of the electron paramagnetic resonance absorption spectrum of iron(III) adsorbed on PAF-1-ET measured at 8 K. The spectral absorption peak with a  $g$ -value of 4.3 is characteristic of high-spin iron(III).

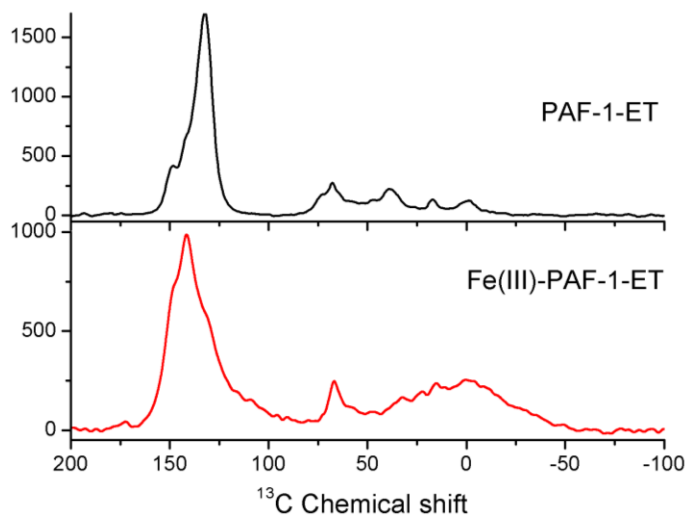


**Figure 3.10.** Solid-state  $^{13}\text{C}$  NMR comparison between PAF-1-ET (black) and Fe(III)-PAF-1-ET (red). For isotropic magnetic moments of paramagnetic iron, coordination results in a line broadening and overall shift. Benzene ring peaks of PAF-1-ET (148-132 ppm) shifted to 147-140 ppm of Fe(III)-PAF-1-ET and all ET functional group peaks of PAF-1-ET (73, 42, 39, and 17 ppm, refer to Figure 1b for assignment) to upfield in Fe(III)-PAF-1-ET. The quaternary carbon atom that is connected to four phenyl groups can be assigned to 67 ppm<sup>18</sup> and it was not affected by iron coordination. The peak at -1 ppm in PAF-1-ET is spinning sidebands.

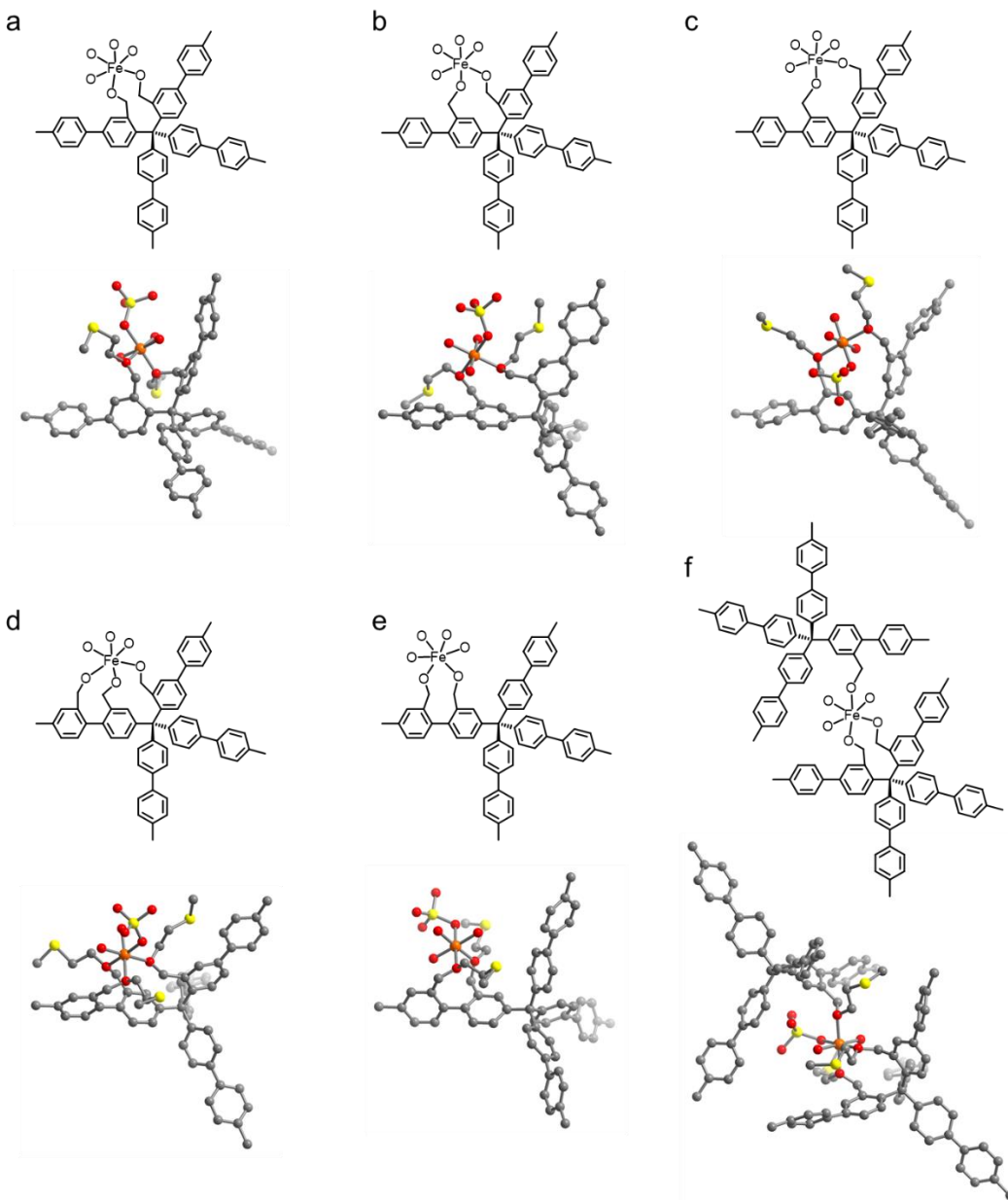


**Figure 3.11.** (Top) Illustration of the proposed local Fe coordination environment. (Bottom) Tetrahedral units extracted from the Fe-coordinated PAF-1-ET, where two (a-c, e) or three (d, f) ether oxygen atoms and a sulfate anion coordinate iron, along with two or one water molecules. Atom colors: C, O, S, and Fe atoms are gray, red, yellow, and orange, respectively. Hydrogen atoms and non-coordinated ET functional groups are omitted for clarity.

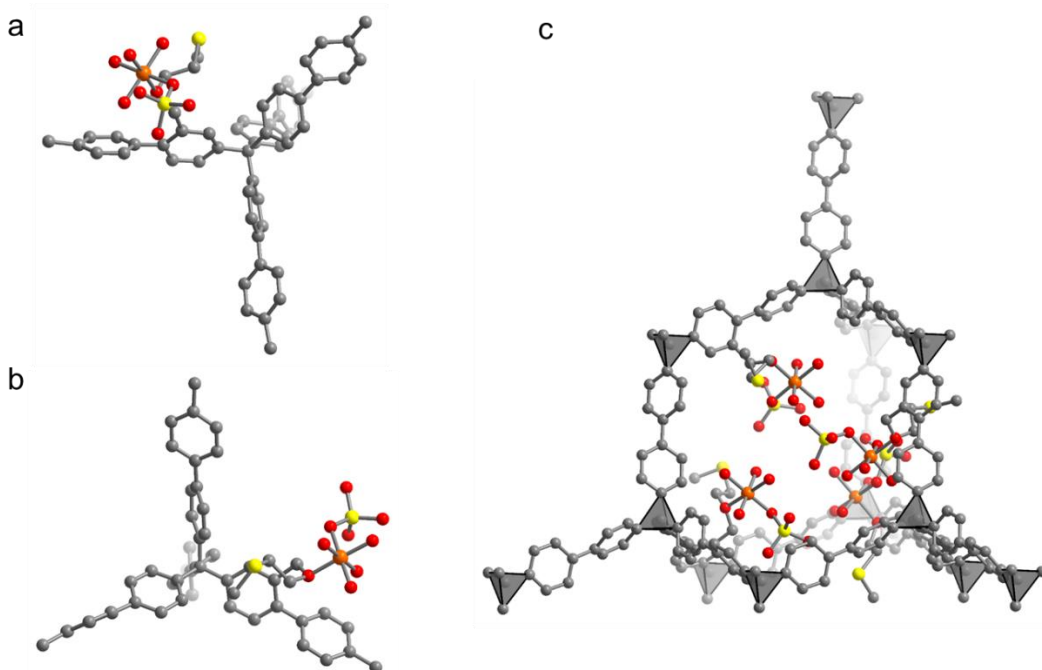


**Figure 3.12.** (a, b) Tetrahedral units extracted from the Fe-coordinated PAF-1-ET, where the ether oxygen atom coordinates with the central iron ion, along with a sulfate anion and four water molecules. The model is shown in two perspectives for clarity (a and b). (c) The adamantane cage of the same modeled structure. Four ET functionalities in the cage are shown for clarity. Atom colors are the same as those in Figure 3.11, while tetrahedral carbon (in the panel c) was shown in gray tetrahedra.

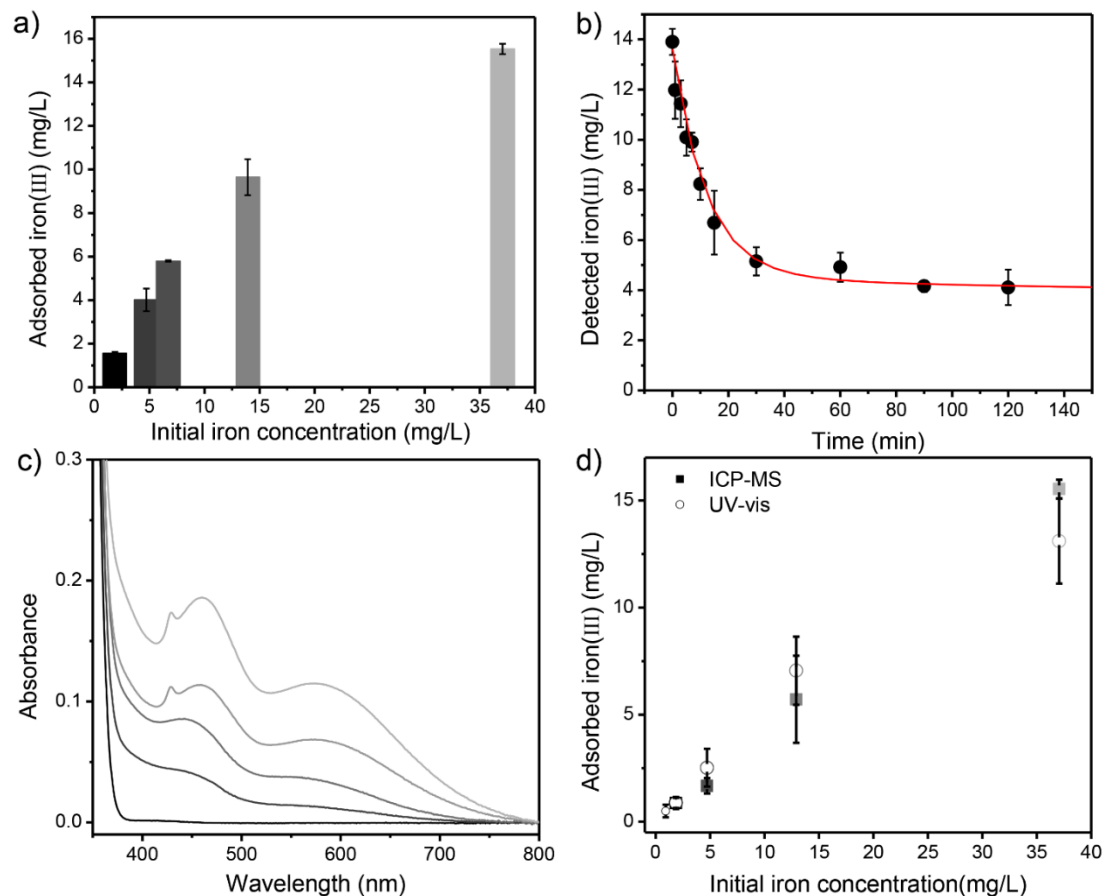


**Figure 3.13.** (a) Uptake by PAF-1-ET of iron(III) from synthetic ground water with initial iron(III) concentrations of 1.8, 4.7, 6.7, and 37 mg/L, and from ground water collected from West Bengal<sup>16</sup> with an initial iron(III) concentration of 14 ppm. (b) Real time iron(III) uptake of PAF-1-ET in the genuine ground water collected from West Bengal<sup>16</sup> and monitored from 1 to 720 min and fitted with the single exponential decay model:  $y = Ae^{(-t/t_0)} + C$ ;  $t = 11$  min (red line). (c) Absorption spectra after 8-hydroxyquinoline addition to dried PAF-1-ET applied in ground water shown in (a). Black as 1.8, charcoal gray as 4.7, middle gray as 6.7, gray as 14, and light gray as 37 mg/L. (d) Comparison of direct iron(III) measurements by ICP-MS (black filled squares) and calculated iron(III) levels from absorbance at 460 nm using 8-hydroxyquinoline as an indicator (open circles).

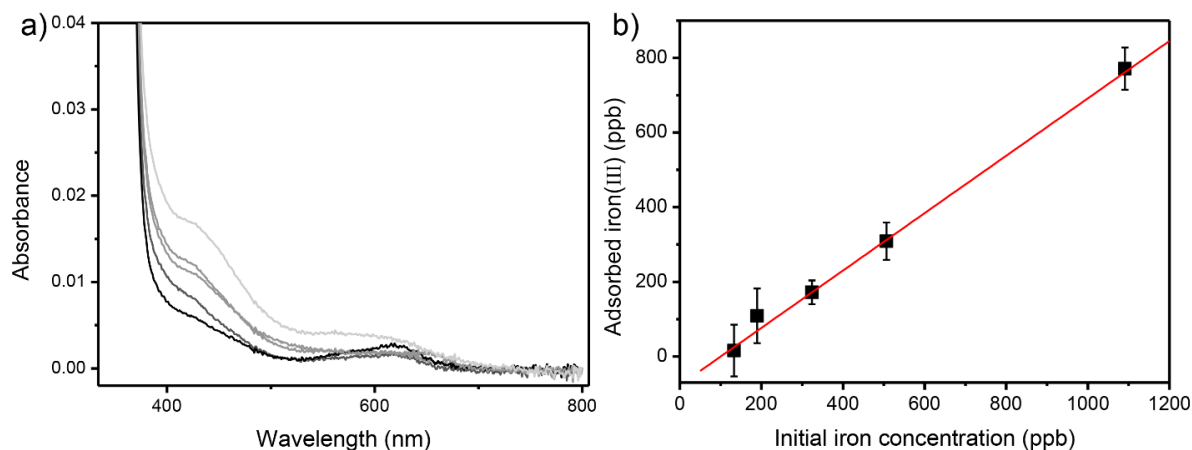


**Figure 3.14.** The detection limit was determined based on the 3 sigma method ( $3\sigma/k$ ). The colorimetric assay of 8-hydroxyquinoline (1 mM) in DMSO applied to dried PAF-1-ET in different iron(III) concentration (the lowest one is 133 ppb and upto 1090 ppb). a) The spectra from 1 mM 8-HQ in each iron(III) concentration and b) the plot of calculated capture iron(III) concentration based on 460 nm absorbance against the initial iron concentration. The detection of limit is calculated to be 283 ppb.



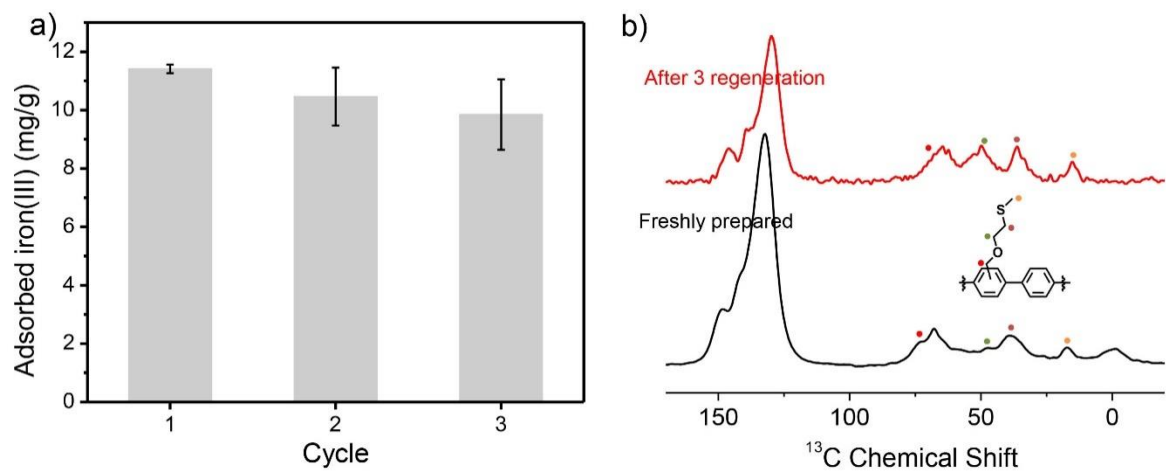


**Figure 3.15.** (a) Iron uptake comparison between freshly prepared PAF-1-ET, first regenerated polymer, and second regenerated polymer. (b) Solid-state  $^{13}\text{C}$  NMR comparison between freshly synthesized PAF-1-ET (black) and regenerated PAF-1-ET (red) that was treated in synthetic ground water samples followed by 8-hydroxyquinoline (100 mM).

**Table 3.1.** Fitting parameters for three different models for the adsorption of iron(III) ions of PAF-1-ET using nonlinear regression.

<i>Model</i>	Dual-site Langmuir
<i>Parameters</i>	$q_{sat,1} = 16.31$ $K_{L,1} = 0.0070$ $q_{sat,2} = 98.02$ $K_{L,2} = 5.56 \times 10^{-8}$
$R^2$	0.9934

**Table 3.2.** Iron-57 Mössbauer spectral parameters for the iron(III) quadrupole doublets in PAF-1-ET<sup>a</sup>

T, K	$\delta^b$	$\Delta E_{Q^1}$ , mm/s	$\Delta E_{Q^2}$ , mm/s	$\Delta E_{Q,ave}$ mm/s	$\Gamma,^{ave}$ mm/s	Area, %
300	0.385(2)	0.61(1)	0.97(1)	0.79(1)	0.45(2)	91
200	0.443(2)	0.614(8)	0.98(1)	0.80(1)	0.45(1)	91
100	0.492(1)	0.613(5)	0.999(3)	0.803(5)	0.45(1)	91
50	0.507(1)	0.617(5)	1.000(6)	0.809(6)	0.46(1)	91
20	0.516(1)	0.673(8)	0.99(1)	0.83(1)	0.58(2)	73.4(6)
10	0.522(1)	0.597(5)	1.025(6)	0.811(6)	0.45(1)	40.6(6)
5	0.522(1)	0.594(6)	1.019(7)	0.807(7)	0.43(1)	32.2(4)

<sup>a</sup>Statistical fitting uncertainties are given in parentheses. More realistic uncertainties are ca. two to three times larger. The absence of an uncertainty indicates that the parameter was constrained to the value given. <sup>b</sup>Referred to  $\alpha$ -iron at 295K.

**Table 3.3.** EXAFS fitting results for Fe K-edge.<sup>a</sup>

Sample	Path	R (Å)	N	$\sigma^2$ ( $10^{-3}$ Å <sup>2</sup> )	R-factor (%)	$\Delta E_0$ (eV)
Fe(III)@PAF-1-ET	Fe-O	2.00±0.01	6	5.98±0.59	0.65	-1.58±1.94
	Fe-C	3.06±0.04	12	16.6±5.11		

<sup>a</sup>Fitting for Fe(III)@PAF-1-ET sample was performed over the k-range  $3.46 \leq k(\text{Å}^{-1}) \leq 10.52$  and  $1.0 \leq R(\text{Å}) \leq 3.1$ .

### 3.1.4. References

- (1) Weber, K. A.; Achenbach, L. A.; Coates, J. D. Microorganisms Pumping Iron: Anaerobic Microbial Iron Oxidation and Reduction. *Nat. Rev. Microbiol.* **2006**, *4* (10), 752–764.
- (2) Spangler, B.; Morgan, C. W.; Fontaine, S. D.; Vander Wal, M. N.; Chang, C. J.; Wells, J. A.; Renslo, A. R. A Reactivity-Based Probe of the Intracellular Labile Ferrous Iron Pool. *Nat. Chem. Biol.* **2016**, *12* (9), 680–685.
- (3) Hentze, M. W.; Muckenthaler, M. U.; Andrews, N. C. Balancing Acts. *Cell* **2004**, *117* (3), 285–297.
- (4) Dixon, S. J.; Stockwell, B. R. The Role of Iron and Reactive Oxygen Species in Cell Death. *Nat. Chem. Biol.* **2014**, *10* (1), 9–17.
- (5) Chang, C. J. Searching for Harmony in Transition-Metal Signaling. *Nat. Chem. Biol.* **2015**, *11* (10), 744–747.
- (6) Kew, M. C. Hepatic Iron Overload and Hepatocellular Carcinoma. *Liver Cancer* **2014**, *3* (1), 31–40.
- (7) Kurz, T.; Eaton, J. W.; Brunk, U. T. The Role of Lysosomes in Iron Metabolism and Recycling. *Int. J. Biochem. Cell Biol.* **2011**, *43* (12), 1686–1697.
- (8) Theil, E. C.; Goss, D. J. Living with Iron (and Oxygen): Questions and Answers about Iron Homeostasis. *Chem. Rev.* **2009**, *109* (10), 4568–4579.
- (9) Salonen, J. T.; Nyssönen, K.; Korpela, H.; Tuomilehto, J.; Seppänen, R.; Salonen, R. High Stored Iron Levels Are Associated with Excess Risk of Myocardial Infarction in Eastern Finnish Men. *Circulation* **1992**, *86* (3), 803–811.
- (10) Arezzini, B.; Lunghi, B.; Lungarella, G.; Gardi, C. Iron Overload Enhances the Development of Experimental Liver Cirrhosis in Mice. *Int. J. Biochem. Cell Biol.* **2003**, *35* (4), 486–495.
- (11) Carrier, J.; Aghdassi, E.; Cullen, J.; Allard, J. P. Iron Supplementation Increases Disease Activity and Vitamin E Ameliorates the Effect in Rats with Dextran Sulfate Sodium-Induced Colitis. *J. Nutr.* **2002**, *132* (10), 3146–3150.
- (12) Martins, S.; Logan, S.; Gilbert, R. E. Iron Therapy for Improving Psychomotor Development and Cognitive Function in Children under the Age of Three with Iron Deficiency Anaemia. In *Cochrane Database of Systematic Reviews*; The Cochrane Collaboration, Ed.; John Wiley & Sons, Ltd: Chichester, UK, 2001.
- (13) Brewer, G. J. Risks of Copper and Iron Toxicity during Aging in Humans. *Chem. Res. Toxicol.* **2010**, *23* (2), 319–326.
- (14) Hoffbrand, A. V.; Cohen, A.; Hershko, C. Role of Deferiprone in Chelation Therapy for Transfusional Iron Overload. *Blood* **2003**, *102* (1), 17–24.
- (15) WHO. Iron in Drinking-Water Background Document for Development of WHO Guidelines for Drinking-Water Quality. *World Health Organ. Guidel.* **2003**, *2*, 1–9.
- (16) Amrose, S. E.; Bandaru, S. R. S.; Delaire, C.; van Genuchten, C. M.; Dutta, A.; DebSarkar, A.; Orr, C.; Roy, J.; Das, A.; Gadgil, A. J. Electro-Chemical Arsenic Remediation: Field Trials in West Bengal. *Sci. Total Environ.* **2014**, *488–489* (1), 539–546.
- (17) Ikem, A.; Egiebor, N. O.; Nyavor, K. Trace Elements In Water, Fish and Sediment from Tuskegee Lake, Southeastern Usa. *Water. Air. Soil Pollut.* **2003**, *149* (1–4), 51–75.
- (18) Majzlan, J.; Alpers, C. N.; Koch, C. B.; McCleskey, R. B.; Myneni, S. C. B.; Neil, J. M. Vibrational, X-Ray Absorption, and Mössbauer Spectra of Sulfate Minerals from the Weathered Massive Sulfide Deposit at Iron Mountain, California. *Chem. Geol.* **2011**, *284* (3), 296–305.

- (19) Karabulut, M.; Marasinghe, G. K.; Ray, C. S.; Day, D. E.; Waddill, G. D.; Booth, C. H.; Allen, P. G.; Bucher, J. J.; Caulder, D. L.; Shuh, D. K. An Investigation of the Local Iron Environment in Iron Phosphate Glasses Having Different Fe(II) Concentrations. *J. Non-Cryst. Solids* **2002**, *306* (2), 182–192.
- (20) Reimann, C.; Bjorvatn, K.; Frengstad, B.; Melaku, Z.; Tekle-Haimanot, R.; Siewers, U. Drinking Water Quality in the Ethiopian Section of the East African Rift Valley I—data and Health Aspects. *Sci. Total Environ.* **2003**, *311* (1), 65–80.
- (21) Challenges and opportunities in the use of iron in water and wastewater treatment | SpringerLink <https://link.springer.com/article/10.1023/A:1015131528247> (accessed Jul 7, 2017).
- (22) Berg, M.; Trang, P. T. K.; Stengel, C.; Buschmann, J.; Viet, P. H.; Van Dan, N.; Giger, W.; Stüben, D. Hydrological and Sedimentary Controls Leading to Arsenic Contamination of Groundwater in the Hanoi Area, Vietnam: The Impact of Iron-Arsenic Ratios, Peat, River Bank Deposits, and Excessive Groundwater Abstraction. *Chem. Geol.* **2008**, *249* (1), 91–112.
- (23) Buschmann, J.; Berg, M.; Stengel, C.; Winkel, L.; Sampson, M. L.; Trang, P. T. K.; Viet, P. H. Contamination of Drinking Water Resources in the Mekong Delta Floodplains: Arsenic and Other Trace Metals Pose Serious Health Risks to Population. *Environ. Int.* **2008**, *34* (6), 756–764.
- (24) Gyles, P. A.; Miller, A. Occurrence and Characteristics of Inorganic Ions and Microorganisms in Potable Water from Jamaica. *Environ. Earth Sci.* **2011**, *62* (7), 1431–1435.
- (25) Sapchenko, S. A.; Demakov, P. A.; Samsonenko, D. G.; Dybtsev, D. N.; Schröder, M.; Fedin, V. P. A Cryptand Metal–Organic Framework as a Platform for the Selective Uptake and Detection of Group I Metal Cations. *Chem. – Eur. J.* **2017**, *23* (10), 2286–2289.
- (26) Li, P.-Z.; Su, J.; Liang, J.; Liu, J.; Zhang, Y.; Chen, H.; Zhao, Y. A Highly Porous Metal–organic Framework for Large Organic Molecule Capture and Chromatographic Separation. *Chem. Commun.* **2017**, *53* (24), 3434–3437.
- (27) Wang, C.; Liu, X.; Demir, N. K.; Chen, J. P.; Li, K. Applications of Water Stable Metal–organic Frameworks. *Chem. Soc. Rev.* **2016**, *45* (18), 5107–5134.
- (28) Carboni, M.; W. Abney, C.; Liu, S.; Lin, W. Highly Porous and Stable Metal–organic Frameworks for Uranium Extraction. *Chem. Sci.* **2013**, *4* (6), 2396–2402.
- (29) Liu, X.; Demir, N. K.; Wu, Z.; Li, K. Highly Water-Stable Zirconium Metal–Organic Framework UiO-66 Membranes Supported on Alumina Hollow Fibers for Desalination. *J. Am. Chem. Soc.* **2015**, *137* (22), 6999–7002.
- (30) Adeyemo, A. A.; Adeoye, I. O.; Bello, O. S. Metal Organic Frameworks as Adsorbents for Dye Adsorption: Overview, Prospects and Future Challenges. *Toxicol. Environ. Chem.* **2012**, *94* (10), 1846–1863.
- (31) Bobbitt, N. S.; Mendonca, M. L.; Howarth, A. J.; Islamoglu, T.; Hupp, J. T.; Farha, O. K.; Snurr, R. Q. Metal–organic Frameworks for the Removal of Toxic Industrial Chemicals and Chemical Warfare Agents. *Chem. Soc. Rev.* **2017**, *46* (11), 3357–3385.
- (32) Zhang, Y.; Yuan, S.; Feng, X.; Li, H.; Zhou, J.; Wang, B. Preparation of Nanofibrous Metal–Organic Framework Filters for Efficient Air Pollution Control. *J. Am. Chem. Soc.* **2016**, *138* (18), 5785–5788.
- (33) Yaghi, O. M.; Li, G.; Li, H. Selective Binding and Removal of Guests in a Microporous Metal–organic Framework. *Nature* **1995**, *378* (6558), 703–706.
- (34) Ding, S.-Y.; Dong, M.; Wang, Y.-W.; Chen, Y.-T.; Wang, H.-Z.; Su, C.-Y.; Wang, W. Thioether-Based Fluorescent Covalent Organic Framework for Selective Detection and Facile Removal of Mercury(II). *J. Am. Chem. Soc.* **2016**, *138* (9), 3031–3037.

- (35) Ben, T.; Ren, H.; Shengqian, M.; Cao, D.; Lan, J.; Jing, X.; Wang, W.; Xu, J.; Deng, F.; Simmons, J. M.; et al. Targeted Synthesis of a Porous Aromatic Framework with High Stability and Exceptionally High Surface Area. *Angew. Chem. - Int. Ed.* **2009**, *48* (50), 9457–9460.
- (36) Lee, S.; Barin, G.; Ackerman, C. M.; Muchenditsi, A.; Xu, J.; Reimer, J. A.; Lutsenko, S.; Long, J. R.; Chang, C. J. Copper Capture in a Thioether-Functionalized Porous Polymer Applied to the Detection of Wilson's Disease. *J. Am. Chem. Soc.* **2016**, *138* (24), 7603–7609.
- (37) Demir, S.; Brune, N. K.; Van Humbeck, J. F.; Mason, J. A.; Plakhova, T. V.; Wang, S.; Tian, G.; Minasian, S. G.; Tylliszczak, T.; Yaita, T.; et al. Extraction of Lanthanide and Actinide Ions from Aqueous Mixtures Using a Carboxylic Acid-Functionalized Porous Aromatic Framework. *ACS Cent. Sci.* **2016**, acscentsci.6b00066.
- (38) Li, B.; Zhang, Y.; Ma, D.; Shi, Z.; Ma, S. Mercury Nano-Trap for Effective and Efficient Removal of mercury(II) from Aqueous Solution. *Nat. Commun.* **2014**, *5* (May), 5537.
- (39) Bank, S.; Prislowski, M. C. The High Reactivity of Radical-Anion-Prepared Sodium Hydride: Reaction with Benzyl Chloride. *J. Chem. Soc. Chem. Commun.* **1970**, *0* (23), 1624–1625.
- (40) Watkins, M. I.; Olah, G. A. Study of Increasingly Crowded Phenylethanes by Carbon-13 Spectroscopy and Molecular Mechanics Calculations. *J. Am. Chem. Soc.* **1981**, *103* (22), 6566–6574.
- (41) Yuan Yu; Bian Yubo. Efficient Homocoupling Reactions of Halide Compounds Catalyzed by Manganese (II) Chloride. *Appl. Organomet. Chem.* **2008**, *22* (1), 15–18.
- (42) Berto, T. C.; Hoffman, M. B.; Murata, Y.; Landenberger, K. B.; Alp, E. E.; Zhao, J.; Lehnert, N. Structural and Electronic Characterization of Non-Heme Fe(II)–Nitrosyls as Biomimetic Models of the FeB Center of Bacterial Nitric Oxide Reductase <https://pubs.acs.org/doi/abs/10.1021/ja111693f> (accessed Apr 10, 2018).
- (43) Owen, T.; Grandjean, F.; Long, G. J.; Domasevitch, K. V.; Gerasimchuk, N. Synthesis and Characterization of Two Intensely Colored Tris(benzoylcyanoxime)iron(II) Anionic Complexes <http://pubs.acs.org/doi/abs/10.1021/ic8004322> (accessed Feb 22, 2018).
- (44) Wagner, F. E.; Shenoy, G. K. Mössbauer Isomer Shifts. **1978**.
- (45) B. Ravel, M. N. ATHENA, ARTEMIS, HEPHAESTUS: Data Analysis for X-Ray Absorption Spectroscopy Using IFEFFIT. *J. SYNCHROTRON Radiat.* *12*, 537–541.
- (46) Zabinsky, S. I.; Rehr, J. J.; Ankudinov, A.; Albers, R. C.; Eller, M. J. Multiple-Scattering Calculations of X-Ray-Absorption Spectra. *Phys. Rev. B* **1995**, *52* (4), 2995–3009.
- (47) Electro-chemical arsenic remediation: Field trials in West Bengal - ScienceDirect <http://www.sciencedirect.com/science/article/pii/S0048969713013570> (accessed Jul 7, 2017).
- (48) Arsenic contamination of groundwater in Bangladesh: reports | British Geological Survey (BGS) <http://www.bgs.ac.uk/research/groundwater/health/arsenic/Bangladesh/reports.html> (accessed Jul 17, 2017).
- (49) Delaire, C.; van Genuchten, C. M.; Nelson, K. L.; Amrose, S. E.; Gadgil, A. J. Escherichia Coli Attenuation by Fe Electrocoagulation in Synthetic Bengal Groundwater: Effect of pH and Natural Organic Matter. *Environ. Sci. Technol.* **2015**, *49* (16), 9945–9953.
- (50) Zhu, D.; Xue, L.; Li, G.; Che, Y.; Jiang, H. A Turn-on Fluorescent Probe for Detection of Hydrogen Sulfide in Aqueous Solution and Living Cells. *Org. Chem. Front.* **2014**, *1* (5), 501–505.
- (51) Chen Yuncong; Zhu Chengcheng; Yang Zhenghao; Chen Junjie; He Yafeng; Jiao Yang; He Weijiang; Qiu Lin; Cen Jiajie; Guo Zijian. A Ratiometric Fluorescent Probe for Rapid

- Detection of Hydrogen Sulfide in Mitochondria. *Angew. Chem. Int. Ed.* **2013**, 52 (6), 1688–1691.
- (52) Holze R. C.M.A. Brett, A.M.O. Brett: *Electrochemistry — Principles, Methods and Applications*, Oxford University Press, Oxford, ISBN 0-19-855388-9, 1993, 427 Pages, £ 25.00. *Berichte Bunsenges. Für Phys. Chem.* **2010**, 98 (10), 1350–1350.
- (53) Šljukić Biljana; Compton Richard G. Manganese Dioxide Graphite Composite Electrodes Formed via a Low Temperature Method: Detection of Hydrogen Peroxide, Ascorbic Acid and Nitrite. *Electroanalysis* **2007**, 19 (12), 1275–1280.
- (54) He, G.; Liu, C.; Liu, X.; Wang, Q.; Fan, A.; Wang, S.; Qian, X. Design and Synthesis of a Fluorescent Probe Based on Naphthalene Anhydride and Its Detection of Copper Ions. *PLOS ONE* **2017**, 12 (10), e0186994.
- (55) Goswami, S.; Aich, K.; Kumar Das, A.; Manna, A.; Das, S. A Naphthalimide– Quinoline Based Probe for Selective, Fluorescence Ratiometric Sensing of Trivalent Ions. *RSC Adv.* **2013**, 3 (7), 2412–2416.
- (56) Yang, Y.; Ding, H.; Hao, S.; Zhang, Y.; Kan, Q. Iron(III), cobalt(II) and copper(II) Complexes Bearing 8-Quinolinol Encapsulated in zeolite for the Aerobic Oxidation of Styrene. *Appl. Organomet. Chem.* **2011**, 25 (4), 262–269.
- (57) Mladenova, R.; Ignatova, M.; Manolova, N.; Petrova, T.; Rashkov, I. Preparation, Characterization and Biological Activity of Schiff Base Compounds Derived from 8-Hydroxyquinoline-2-Carboxaldehyde and Jeffamines ED®. *Eur. Polym. J.* **2002**, 38 (5), 989–999.
- (58) Serratrice, G.; Boukhalifa, H.; Béguin, C.; Baret, P.; Caris, C.; Pierre, J.-L. O-TRENTOX, a New Tripodal Iron Chelator Based on 8-Hydroxyquinoline Subunits: Thermodynamic and Kinetic Studies. *Inorg. Chem.* **1997**, 36 (18), 3898–3910.
- (59) Teo, B. K. *EXAFS: Basic Principles and Data Analysis*; Inorganic Chemistry Concepts; Springer-Verlag: Berlin Heidelberg, 1986.
- (60) Ding Xiaojie; Qu Lingbo; Yang Ran; Zhou Yuchen; Li Jianjun. A Highly Selective and Simple Fluorescent Sensor for Mercury (II) Ion Detection Based on Cysteamine-capped CdTe Quantum Dots Synthesized by the Reflux Method. *Luminescence* **2014**, 30 (4), 465–471.

## Chapter 4.

### **Ligand-Directed Acyl Imidazole Chemistry for Labeling Proteins in Copper-Rich Compartments in Cells and Neurons**

Portions of this work were published in the following scientific journal:

Yuki Nishikawa in Itaru Hamachi lab in Kyoto University helped to synthesize Cu-DAI  
Pei Liu in Evan Miller lab in UC Berkeley prepared neurons and neuronal imaging.



## Abstract

Metals are key building blocks of life and essential for variety of important functions within living organisms, many of which involve proteins. As such, it is of importance to develop tools to investigate interactions between metals and proteins. As powerful tools for studying protein functions, labeling with chemical tags has been developed to facilitate tagging and enable analysis. Ligand-directed alkyloxyacyl imidazole (LDAI) chemistry has been reported to be cell-permeable and to undergo selective labeling to identify proteins that are spatially associated with given analytes in living cells. Herein, we envisioned that new chemical tagging probes, Cu-DAI, will enable us to study the dynamics of copper proteins with cellular activity. The Cu-DAI showed selective binding to copper even in the presence of other biologically relevant metals. We then applied the probe to living cells, showing 2-fold fluorescent enhancement by copper addition while significant diminishment in fluorescence was found upon addition of BCS which is a known copper chelator. To investigate the identity of labeled proteins, cells were transfected with ATP7a-Venus and a good co-localization of the fluorescence from probe-labeled proteins and ATP7a-Venus indicates that Cu-DAI is capable of tagging specific copper-rich compartments. With these promising results, we further utilized Cu-DAI for imaging copper-rich vesicles as well as copper fluxes in primary hippocampal neurons. The neurons were depolarized by chemo- or electrostimulation and triggered translocation of copper pools from soma to dendrites in neurons and Cu-DAI can follow these depolarization-induced copper fluxes, indicating Cu-DAI enables to follow and to unravel the importance of copper ion on neuron biology as well. We hope this project further elucidates the identity of copper rich compartments involved in biological signaling process in cells and neurons.

### 4.1.1 Introduction

Copper is an essential element for human health,<sup>1</sup> and enzymes harness the redox activity of copper to exploit functions spanning energy generation, pigment synthesis, and epigenetic modification. In addition, copper is found in high concentrations in the brain<sup>2,3</sup> and activation of neurons causes a marked redistribution of cellular copper and copper has been shown to affect the excitability of cultured neurons.<sup>4-6</sup> On the other hand, misregulation of copper homeostasis can lead to cellular malfunctions resulting from an aberrant increase of reactive oxygen species (ROS) and oxidative damages to proteins, lipids, and DNA/RNA,<sup>3,7</sup> and these are related to several diseases including cancer,<sup>8</sup> neurodegenerative diseases such as Alzheimer's, Parkinson's and Huntington's diseases,<sup>5</sup> and genetic disorders such as Menkes and Wilson's diseases.<sup>4</sup> However, the roles of copper in cellular and central nervous system remain poorly understood. A number of technologies have developed to monitor copper fluxes, and this includes synthetic fluorescent<sup>2,5,9-24</sup> and MRI copper probes<sup>25-29</sup> based on thioether-rich receptors which revealed high selectivity towards copper ions in intracellular system as well as whole organisms. Yet, they cannot be applied for specific labeling of copper-rich cellular compartments or proteins involved in copper fluxes, which are important for having better and more detailed understanding of how copper is regulated to fulfil fundamental physiological roles in live cells, tissues, and in vivo as well as the identification of copper-related proteins.

As powerful tools for studying cuproproteins, labeling with chemical tags has been developed to facilitate tagging and enable analysis. To date, the most widely used approach are genetically encodable protein-tag and tag-fused proteins, such as fluorescent proteins (FP; e.g. GFP) and SNAP/HALO-tag respectively.<sup>30-32</sup> Although they are widely used, the inherently large size and

innate differences between natural proteins and artificial proteins hinder them from being applied in metalloprotein identification. To minimize such perturbations, bioorthogonal chemistry has recently been developed by introducing reactive handles such as azide and alkyne groups onto target proteins by genetic methods. Like the protein tags, however, this strategy also demands genetic engineering for introduction of an appropriate reaction handle and thereby inapplicable to endogenously expressed (natural) proteins.<sup>33–37</sup> To minimize disturbing the natural cellular context, chemistry-based protein labeling techniques use a designed compound connecting a protein ligand and a probe through a cleavable reactive group, termed ligand-directed (LD) chemistry. In LD chemistry, the ligand part selectively recognizes and binds to the target protein, facilitating the chemical reaction of the reactive group with an amino acid located near the ligand-binding site through a proximity effect. Importantly, the ligand part can be removed after labeling using the cleavable linker of the LD reagents, so that the labeled protein retains its original function. This labeling mechanism permits biosensors to elucidate complicated cellular processes and allow visualization of various biological parameters, such as pH, ionic concentrations, metabolites, and protein activities.<sup>38–41</sup>

In particular, ligand-directed alkyloxyacyl imidazole (LDAI) chemistry has been reported to be cell-permeable and to undergo selective labeling to identify proteins that are spatially associated with given analytes in living cells.<sup>42–45</sup> Herein, we envisioned that new chemical tagging probes based on LDAI, Cu-DAI will enable us to study the dynamics of cuproproteins with cellular and neuronal activity. For copper selectivity, thioether-rich copper activator which is directly linked to acyl imidazole, allows selective labeling of amino acids on the proteins and/or copper rich compartments via acyl transfer reaction. As Cu-DAI contains a silicon-rhodamine (SiR) fluorophore which is linked to other side of acyl imidazole and known to have high photostability, low phototoxicity, and low background signal,<sup>46–50</sup> after acyl transfer reaction the proteins or copper-rich compartments can be labeled with SiR and hence they can be visualized by fluorescence microscopy. This Cu-DAI is robust in the aqueous condition and its selective binding and cleavage with copper is found over other biologically relevant metals. In cellular system, Cu-DAI shows copper-dependent fluorescent staining as indicated by treatment with copper ionophore Cu(gtsm) and copper chelator bathocuproine sulfonate (BCS), confirming the probe stains proteins with high local copper concentrations. (Scheme 4.1) Furthermore, the probe successfully labels copper rich compartments in neuronal system and reveals its capability to trace copper dynamics upon depolarization. We hope this project further elucidates the identity of copper rich compartments involved in biological signaling process in cells and neurons.

## 4.1.2. Methods

### 4.1.2.1. Synthesis of Cu-DAI

**Compound 1** (Bis((3-methyloxetan-3-yl)methyl) 4-bromoisophthalate) : To a solution of 3-methyl-3-oxetanemethanol (2.73 mL, 27.3 mmol) and pyridine (3.32 mL, 41.0 mmol) in CH<sub>2</sub>Cl<sub>2</sub> (25 mL), 2-bromobenzoyl chloride (3.00 g, 13.7 mmol) was added at 0 °C. The ice bath was removed, and the reaction was stirred at room temperature for 90 min. The solution was diluted with brine and extracted with CH<sub>2</sub>Cl<sub>2</sub>. The combined organics were washed with saturated NaHCO<sub>3</sub> and dried with MgSO<sub>4</sub>, and evaporated. Flash chromatography (10–30% EtOAc/hexanes) afforded the product as a colorless oil (3.74 g, 72%). <sup>1</sup>H NMR (CDCl<sub>3</sub>, 400 MHz) δ 7.85 – 7.80 (m, 1H), 7.69 – 7.65 (m, 1H), 7.41 – 7.36 (m, 1H), 7.36 – 7.32 (m, 1H), 4.64 (d, J = 6.1 Hz, 2H), 4.45 (d, J = 5.7 Hz, 2H), 4.44 (s, 2H), 1.44 (s, 3H); <sup>13</sup>C NMR (CDCl<sub>3</sub>, 500 MHz) δ

166.4 (C), 134.5 (CH), 132.9 (CH), 132.2 (C), 131.6 (CH), 127.4 (CH), 121.7 (C), 79.7 (CH<sub>2</sub>), 70.0 (CH<sub>2</sub>), 39.4 (C), 21.5 (CH<sub>3</sub>); HRMS (ESI) calcd for C<sub>12</sub>H<sub>14</sub>BrO<sub>3</sub> [M+H]<sup>+</sup> 285.0121, found 285.0125.

**Compound 2** (1,1'-(4-Bromo-1,3-phenylene)bis(4-methyl-2,6,7-trioxabicyclo[2.2.2]octane)) : A solution of **compound 1** (4.40 g, 10.6 mmol) in CH<sub>2</sub>Cl<sub>2</sub> was cooled to 0 °C under nitrogen, and BF<sub>3</sub>·OEt<sub>2</sub> (756 mg, 5.32 mmol, 0.5 eq) was added dropwise. The reaction was warm up to room temperature overnight while stirring (12 h). Anhydrous Et<sub>3</sub>N (3 mL) was added, and the resulting solution was stirred for 15 min at room temperature. It was then concentrated in vacuo and purified by flash chromatography (0–20% EtOAc/hexanes, with constant 40% v/v CH<sub>2</sub>Cl<sub>2</sub> additive) to provide 2.03 g (34%) as a white solid. <sup>1</sup>H NMR (DMSO-d<sub>6</sub>, 400 MHz) δ 7.81 (d, J = 2.2 Hz, 1H), 7.59 (d, J = 8.3 Hz, 1H), 7.34 (dd, J = 8.3, 2.3 Hz, 1H), 4.01 (s, 6H), 3.99 (s, 6H), 0.84 (s, 3H), 0.82 (s, 3H); <sup>13</sup>C NMR (DMSO-d<sub>6</sub>, 125 MHz) δ 136.6 (C), 135.5 (C), 133.9 (CH), 127.5 (CH), 125.7 (CH), 121.1 (C), 106.3 (C), 106.1 (C), 72.4 (CH<sub>2</sub>), 72.1 (CH<sub>2</sub>), 30.1 (C), 29.9 (C), 13.7 (CH<sub>3</sub>), 13.6 (CH<sub>3</sub>); HRMS (ESI) calcd for C<sub>18</sub>H<sub>25</sub>BrO<sub>8</sub>Na [M+2H<sub>2</sub>O+Na]<sup>+</sup> 471.0625, found 471.0611.

**The compound 3 and 4 were prepared according to reported procedure.**<sup>51</sup>

**Compound 3** (4,4'-methylenebis(3-bromo-N,N-dimethylaniline)) : Synthesis of 1 3-Bromo-N,N-dimethylaniline (5.00 g, 25.0 mmol) was dissolved in 37% formaldehyde solution (3.80 mL) and acetic acid (35.0 mL) and stirred at 60 °C for 2 h. After cooling, acetic acid was evaporated, then saturated NaHCO<sub>3</sub> aq. was added carefully. The aqueous phase was extracted with ethyl acetate (AcOEt), and the combined organic phase was washed with water and brine, dried over Na<sub>2</sub>SO<sub>4</sub>, filtered, and evaporated. The residue was purified by recrystallization (n-hexane/AcOEt) to obtain 1 as a white solid (4.20 g, 82%). <sup>1</sup>H NMR (400 MHz, CDCl<sub>3</sub>): δ 2.91 (s, 12H), 4.00 (s, 2H), 6.58 (dd, 2H, J = 2.4 Hz, 8.8 Hz), 6.84 (d, 2H, J = 8.8 Hz), 6.94 (d, 2H, J = 2.4 Hz). MS (ESI+ ) m/z: Calcd for [M+H]<sup>+</sup> 413.00, found 412.88.

**Compound 4** **Compound 3** (3.80 g, 9.22 mmol) was dissolved in dry tetrahydrofuran (THF) (100 mL) and stirred at -78 °C. sec-Butyllithium (s-BuLi) (1.4 M solution in n-hexane, 20.0 mL, 27.7 mmol) was slowly added for 30 min to the solution and stirred for further 2 h at the same temperature. SiMe<sub>2</sub>Cl<sub>2</sub> (2.20 mL, 18.4 mmol) was added to the reaction mixture and stirred at room temperature for 2 h. Then, 2 M HCl aq. was added carefully to neutralize the solution and THF was evaporated. The resulting aqueous solution was extracted with AcOEt, and the organic phase was washed with saturated NaHCO<sub>3</sub> aq., water, and brine, dried over Na<sub>2</sub>SO<sub>4</sub>, filtered, and evaporated to obtain the crude including 2, which was used for the next reaction immediately due to its high sensitivity toward oxygen. The residue was dissolved in acetone (50.0 mL) and stirred at -15 °C. KMnO<sub>4</sub> powder was added portion wise (6 × 600 mg) for 30 min, and stirring was continued for further 2 h at the same temperature. The purple suspension was filtered through a Celite pad, and the yellow filtrate was evaporated. The residue was purified by silica gel column chromatography to obtain 3 as a yellow solid (1.15 mg, 38%). <sup>1</sup>H NMR (400 MHz, CDCl<sub>3</sub>): δ 0.47 (s, 6H), 3.10 (s, 12H), 6.79 (d, 2H, J = 3.2 Hz), 6.84 (dd, 2H, J = 3.2 Hz, 8.8 Hz), 8.39 (d, 2H, J = 8.8 Hz). MS (ESI+ ) m/z: Calcd for [M+H]<sup>+</sup> 325.17, found 325.17.

**Compound 6** (3,7-bis(dimethylamino)-5,5-dimethyl-3'-oxo-3'H,5H-spiro[dibenzo[b,e]silole-10,1'-isobenzofuran]-5'-carboxylic acid) : A solution of **compound 2** (0.76 g, 1.85 mmol, 3 eq) in THF (70 mL) was cooled to -78 °C under nitrogen. *tert*-Butyllithium (1.7 M in pentane, 3.6 mL, 6.16 mmol, 10 eq) was added dropwise, and the reaction was stirred for 30 min at -78 °C. A solution of **compound 4** (200 mg, 0.616 mmol) in THF (10 mL) was then added dropwise. The reaction was allowed to slowly warm to room temperature and stirring for 5 h. It was subsequently

quenched with 1 N HCl (5 mL), which caused an immediate color change from pale orange to dark blue. After stirring for 10 min, the dark blue mixture was diluted with 15% *i*PrOH/CHCl<sub>3</sub> and brine (3×). The combined organic layers were dried with MgSO<sub>4</sub>, filtered, and concentrated *in vacuo*. Silica gel chromatography (0–20% MeOH/CH<sub>2</sub>Cl<sub>2</sub>, with constant 1% v/v AcOH additive) to provide the **compound 5** and proceed the deprotection in 6 N HCl with 2% (v/v) of CH<sub>3</sub>CN at 90 °C for overnight. The solution changed the color to yellowish orange and was concentrated *in vacuo*. The residual solution was diluted with 15% *i*PrOH/CHCl<sub>3</sub> and brine (3×). The combined organic layers were dried with MgSO<sub>4</sub>, filtered, and concentrated *in vacuo*. Silica gel chromatography (0–20% MeOH/CH<sub>2</sub>Cl<sub>2</sub>) to give the product with the yield of 16%. <sup>1</sup>H NMR (CDCl<sub>3</sub>, 400 MHz) δ 8.09 (d, *J* = 1.3 Hz, 1H), 7.35 (d, *J* = 1.2 Hz, 1H), 4.86 (s, 1H), 4.56–4.52 (m, 2H), 3.81–3.77 (m, 2H), 3.68 (s, 2H), 3.57 (t, *J* = 5.2 Hz, 2H), 3.33 (q, *J* = 5.5 Hz, 2H), 2.80–2.72 (m, 4H), 2.71–2.63 (m, 4H), 2.55 (q, *J* = 7.4 Hz, 4H), 1.44 (s, 9H), 1.25 (t, *J* = 7.4 Hz, 6H).

**Compound 7** (2,5-dioxopyrrolidin-1-yl 3,7-bis(dimethylamino)-5,5-dimethyl-3'-oxo-3'H,5H-spiro[dibenzo[b,e]siline-10,1'-isobenzofuran]-5'-carboxylate) : **Compound 6** (38 mg, 80 μmol), DMAP (4.0 mg, 32 μmol), and Et<sub>3</sub>N (67 μL, 0.48 mmol) were dissolved in dry DMF (3.0 mL). DSC (45 mg, 0.18 mmol) was added and the reaction was stirred at room temperature for 2 hour. It was subsequently diluted with 5% w/v citric acid and extracted with EtOAc (×2). The combined organic extracts were washed with brine, then dried over MgSO<sub>4</sub>, filtered and evaporated. The crude residue was purified by column chromatography on silica gel (50% EtOAc/hexane) to yield **Compound 7** (21 mg, 36 μmol, 45%), and used for the next step without further purification.

**Compound 8** (bis(2-(ethylthio)ethyl)amine) : Sodium cubes (500 mg, 22.4 mmol) were added into ethanol at 0 °C. After stirring for 10 min, ethanethiol (0.8 mL, 11.2 mmol) was added into the solution, followed by bis(2-chloroethyl)amine (1 g, 5.60 mmol) was added. The solution was stirring at room temperature for overnight and water (2 mL) was added carefully and residual ethanol was removed *in vacuo*. The solution is extracted with CH<sub>2</sub>Cl<sub>2</sub> and brine and organic layer was dried with MgSO<sub>4</sub> and concentration *in vacuo*. The crude product was purified by silica column in (Hexane: Ethyl acetate = 10:0 to 4:1) and the produce on TLC was stained by KMnO<sub>4</sub>, giving the colorless liquid with 26% yield. <sup>1</sup>H NMR (CDCl<sub>3</sub>, 400 MHz) δ 2.83 (t, *J* = 8 Hz, 4 H), 2.71 (t, *J* = 8 Hz, 4H), 2.56 (q, *J* = 8 Hz, 4H), 1.70 (s, broad, 1H), 1.27 (t, *J* = 8 Hz, 6H). <sup>13</sup>C NMR (CDCl<sub>3</sub>, 125 MHz) δ 48.3, 31.9, 25.8, 14.9.

**Compound 9** (*N*-((1H-imidazol-4-yl)methyl)-2-(ethylthio)-*N*-(2-(ethylthio)ethyl)ethan-1-amine) : 4-imidazole aldehyde (0.36 g, 3.74 mmol) was dissolved in 2 mL methanol. **Compound 8** (0.73 g, 3.74 mmol) in mixture of 10 mL methanol and acetic acid (10:1 v/v) was added dropwise into the solution. The solution was added sodium cyanoborohydride (0.38 g, 6.04 mmol) in 2 mL methanol and stirred at room temperature overnight. The solution was quenched by adding conc. HCl and remove the solvent by reduced pressure. The crude product was extracted with NaHCO<sub>3</sub> and ethyl acetate. The combined organic layer was dried with MgSO<sub>4</sub> ad purified with alumina column (CH<sub>2</sub>Cl<sub>2</sub> : CH<sub>3</sub>OH = 100:0 to 96:4) to give slight yellowish gel with 86% yield. <sup>1</sup>H NMR (CDCl<sub>3</sub>, 400 MHz) δ 7.60 (s, 1 H), 7.27 (s, 1H), 6.91 (s, 1H), 3.68 (s, 2H), 2.74 (t, *J* = 8 Hz, 4H), 2.64 (t, *J* = 8 Hz, 4H), 2.52 (q, *J* = 8 Hz, 4H), 1.23 (t, *J* = 8 Hz, 6H). <sup>13</sup>C NMR (CDCl<sub>3</sub>, 125 MHz) δ 135.0, 120.8, 53.4, 49.6, 29.6, 26.1, 14.9.

**Compound 10** (2-(2-((tert-butoxycarbonyl)amino)ethoxy)ethyl 4-((bis(2-(ethylthio)ethyl)amino)methyl)-1H-imidazole-1-carboxylate) : A solution of **compound 9** (48 mg, 0.18 mmol), tert-butyl (2-(2-(((2,5-dioxopyrrolidin-1-yl)oxy)carbonyl)oxy)ethoxy)ethyl)carbamate which was prepared following previous procedure<sup>52</sup> (51 mg, 0.15 mmol), and pyridine (35 μL, 0.44 mmol) in dry DMF (1.5 mL) was stirred at room

temperature for 12 hour under Ar atmosphere. It was subsequently diluted with EtOAc and washed with water ( $\times 2$ ) and brine, then dried over  $\text{Na}_2\text{SO}_4$ , filtered and evaporated. The crude residue was purified by column chromatography on silica gel (50–75% EtOAc/hexane, linear gradient) to yield **10** (28 mg, 55  $\mu\text{mol}$ , 37%) as a colorless oil.  $^1\text{H}$  NMR ( $\text{CDCl}_3$ , 400 MHz)  $\delta$  8.09 (d,  $J = 1.3$  Hz, 1H), 7.35 (d,  $J = 1.2$  Hz, 1H), 4.86 (s, 1H), 4.56–4.52 (m, 2H), 3.81–3.77 (m, 2H), 3.68 (s, 2H), 3.57 (t,  $J = 5.2$  Hz, 2H), 3.33 (q,  $J = 5.5$  Hz, 2H), 2.80–2.72 (m, 4H), 2.71–2.63 (m, 4H), 2.55 (q,  $J = 7.4$  Hz, 4H), 1.44 (s, 9H), 1.25 (t,  $J = 7.4$  Hz, 6H).

#### Synthesis of **Cu-DAI**

A solution of **compound 10** (11 mg, 21  $\mu\text{mol}$ ) in  $\text{CH}_2\text{Cl}_2$  (1 mL) / TFA (0.2 mL) was stirred at room temperature for 30 min. After removal of the solvent by evaporation, the residual TFA was further removed azeotropically with toluene ( $\times 2$ ) to give Boc-deprotected **10'**. The compound was used for the next step without further purification. A solution of **10'**, **7** (11 mg, 19  $\mu\text{mol}$ ), and  $\text{Et}_3\text{N}$  (26  $\mu\text{L}$ , 0.19 mmol) in dry DMF (1.0 mL) was stirred at room temperature for 1 hour. After removal of the solvent by evaporation, the residue was purified by RP-HPLC (ODS-A, preparative, A/B = 60/40 to 100/0 for 40 min, A =  $\text{CH}_3\text{CN}$ , B = 10 mM  $\text{NH}_4\text{OAc}$ ). The fraction was lyophilized to yield **Cu-DAI** (1.4 mg, 1.6  $\mu\text{mol}$ , 8.6%) as a blue film.  $^1\text{H}$  NMR ( $\text{CDCl}_3$ , 400 MHz)  $\delta$  8.34 (s, 1H), 8.24 (d,  $J = 7.9$  Hz, 1H), 8.13 (s, 1H), 7.39 (dd,  $J = 8.0, 0.7$  Hz, 1H), 6.97 (d,  $J = 2.9$  Hz, 2H), 6.72 (d,  $J = 8.9$  Hz, 2H), 6.52 (dd,  $J = 8.9, 2.9$  Hz, 2H), 4.63–4.57 (m, 2H), 3.89–3.82 (m, 2H), 3.78–3.68 (m, 4H), 2.97 (s, 12H), 2.94–2.82 (m, 4H), 2.82–2.68 (m, 4H), 2.53 (q,  $J = 7.4$  Hz, 4H), 1.22 (t,  $J = 7.4$  Hz, 6H), 0.64 (s, 3H), 0.60 (s, 3H). HR-ESI MS  $m/z$  calcd for  $[\text{M}+\text{H}]^+$  859.3702, found 859.3685

#### 4.1.2.2. Spectroscopic studies

**uHPLC** : The UHPLC in the facility is a Waters Acquity UHPLC-MS system. The analytical column is a Waters XBridge BEH C18, 3.5 $\mu\text{m}$ , 4.6 x 100 mm column. The catalysis facility is supported by Director, Office of Science, Office of Basic Energy Sciences, Chemical Sciences, Geosciences, & Biosciences Division, of the U.S. Department of Energy under Contract No. DE-AC02-05CH11231, FWP No. CH030201 (Catalysis Research Program).

**Spectroscopic methods and materials** All spectroscopic measurements were performed at 25  $^\circ\text{C}$  in PBS buffer (pH 7.4) purchased from. Absorption spectra were recorded using a Varian Cary 60 spectrophotometer and fluorescence spectra were recorded using a Photon Technology International Quanta Master 4 L-format scan spectrofluorometer equipped with an LPS-220B 75-W xenon lamp, A-1010B lamp housing with integrated igniter, switchable 814 photocounting/analog photomultiplier detection unit and MD5020 motor driver. Samples for absorption and emission measurements were contained in 0.35  $\times$  1 cm quartz cuvettes (1.4-mL volume; Starna). Excitation was at 633 nm. Stock solutions of  $\text{Cu}(\text{gtsm})^{53-55}$  in DMSO were used to provide  $\text{Cu}^{2+}$ . Metals used in the selectivity assays were derived from their chloride salts in PBS buffer.

**Cell fractionation and Inductively Coupled Plasma (ICP)-MS analysis** *Atp7a*<sup>-/-</sup> and matched control MEFs were fractionated using the NE-PER kit (Thermo Fisher). Extracts were digested by adding equal volumes of concentrated nitric acid, incubated overnight at room temperature on a rotator, and boiled for 2 hours at 95  $^\circ\text{C}$ . Digested extracts were diluted into 2% nitric acid with an internal standard and run on an iCAP-Q ICP-MS in KED mode. The level of each element found in the extraction reagent was subtracted from each measurement. The resulting values were normalized to protein concentration.

**Cell Culture Procedures.** Cells were maintained by the UC Berkeley Tissue Culture Facility. HEK293T cells were maintained as a monolayer in exponential growth at 37 °C in a 5% CO<sub>2</sub> atmosphere in Dulbecco's Modified Eagle Medium (DMEM, Gibco) supplemented with 10% fetal bovine serum (FBS, Seradigm), 1% glutamax (Gibco), and 1% non-essential amino acids (NEAA, Gibco). MEF ATP7a KO and WT cells were maintained as a monolayer in exponential growth at 37 °C in a 5% CO<sub>2</sub> atmosphere in DMEM supplemented with 10% FBS. One day before imaging, **Neuron cultures:** Hippocampi were dissected from embryonic day 18 Sprague Dawley rats (Charles River Laboratory) in cold sterile HBSS (zero Ca<sup>2+</sup>, zero Mg<sup>2+</sup>). All dissection products were supplied by Invitrogen, unless otherwise stated. Hippocampal tissue was treated with trypsin (2.5%) for 15 min at 37 °C. The tissue was triturated using fire polished Pasteur pipettes, in minimum essential media (MEM) supplemented with 5% fetal bovine serum (FBS; Thermo Scientific), 2% B-27, 2% 1M D-glucose (Fisher Scientific) and 1% glutamax. The dissociated cells were plated onto 12 mm diameter coverslips (Fisher Scientific) pre-treated with PDL at a density of 30-40,000 cells per coverslip in MEM supplemented media (as above). Neurons were maintained at 37 °C in a humidified incubator with 5 % CO<sub>2</sub>. At 3 days in vitro (DIV) half of the MEM supplemented media was removed and replaced with Neurobasal media containing 2% B-27 supplement and 1% glutamax.

**Confocal Fluorescence Imaging Experiments.** Confocal fluorescence imaging studies were performed with a Zeiss laser scanning microscope 710 with a 20x or 63x oil immersion objective lens using Zen 2009 software (Carl Zeiss). Cu-DAI were excited using 633 nm diode laser and emission was collected using a META detector between 650 to 750 nm. The cells were incubated with 1 μM Cu-DAI in HBSS (0.9 mM MgCl<sub>2</sub>) and imaged at 37 °C throughout the course of the experiment. Image analysis and quantification was performed using ImageJ (National Institutes of Health).

**Image analysis and quantification** ImageJ (National Institutes of Health) was used for image analysis. For quantification of fluorescence intensity, each image was set to 8-bit greyscale and inverted. The fluorescence intensity was estimated using non-calibrated OD function. The area of stained cells was selected by setting appropriate threshold ( $\geq 0.025$ ). The statistics of the image was then measured by the "Measure" function and the average fluorescence intensity was obtained by dividing the integrated density (IntDen) over area. For each condition, four images of different fields of cells from each biological replicate were analyzed using this process and the values were combined for statistical analysis.

**For dot blots,** HEK 293T cell (1 mg/mL, concentration was determined by BCA assay) was homogenized in PBS buffer. Cleared lysates were quantified and spotted on a nitrocellulose membrane at protein content of 2 μg. After blocking, the membrane was visualized on with excitation of 633 nm channel. ImageJ was used for blot quantification.

**Transfection in hippocampus neurons:** Before siRNA transfection, the neurons were first placed in an incubator containing 5% CO<sub>2</sub> at 37 °C for 24 h. Transfection was carried out using Lipofectamine 2000 (Invitrogen, USA) following the manufacturer's instructions. 5 μg of siDNA was dissolved in 50 μL of serum-free NB medium (solution A) and incubated at room temperature (RT) for 5 min. Then, 3 μL of Lipofectamine 2000 was added to 50 μL of a serum-free NB medium (solution B) and incubated at RT for 5 min. The two solutions were mixed together and incubated at RT for 30 min. Finally, the mixture was added to the cells dropwise followed by incubation under an atmosphere of CO<sub>2</sub>. After 48 h incubation, the cells were obtained for transfection efficacy identification.

**Extracellular field stimulation:** Extracellular field stimulation was delivered by a Grass Stimulator connected to a recording chamber containing two platinum electrodes (Warner), with triggering provided through a Digidata 1332A digitizer and pCLAMP 10 software (Molecular Devices). Action potentials were triggered by 1 ms 80 V field potentials delivered at 5 Hz. To prevent recurrent activity the HBS bath solution was supplemented with synaptic blockers 10  $\mu$ M 2,3-Dioxo-6-nitro-1,2,3,4-tetrahydrobenzo[f]quinoxaline-7-sulfonamide (NBQX; Santa Cruz Biotechnology) and 25  $\mu$ M DL-2-Amino-5-phosphonopentanoic acid (APV; Sigma-Aldrich).

### 4.1.3. Result and Discussion

#### 4.1.3.1. Design of Cu-DAI and Characterization.

To develop cuproprotein labeling probe, thioether-rich copper receptor (**compound 8** in Figure 4.1), with reference to previous copper selective fluorescent probes,<sup>2,5,9-24</sup> was synthesized in three steps. Dicarboxylic acid silicon-rhodamine, SirR, was prepared according to reported procedure.<sup>46</sup> Two pieces were linked by amide coupling to give Cu-DAI. The probe is cell-permeable and selectively binds to copper which can activate the carbamate unit of AI, resulting in the formation of covalent linkage to the cuproprotein surface through acyl transfer reaction.

Coordination of copper to the thioether-rich activator facilitates the reactivity of the carbamate unit of acyl imidazole, which is supported by changes of HPLC traces shown in the Figure 4.1. LC chromatograms of the reaction between 5  $\mu$ M Cu-DAI in the presence of 5 molar equivalent of methyl ester serine and 2 molar equivalent of Cu<sup>+</sup> in PBS with 2 mM GSH showed conversion to copper-bound species and/or copper-induced acyl transfer reaction product. No significant reaction was found in the absence of the amino acid (Figure 4.1a and Figure 4.2), suggesting minimal hydrolysis and hence good stability of the probe in aqueous solution. Especially, after 1 hour incubation of Cu-DAI with Cu<sup>+</sup> and methyl ester serine, the copper-bound intermediate with MS at 1042 m/z was detected at the LC chromatogram of the reaction mixture at retention time of 7.4 min, confirming Cu-DAI is following LDAI chemistry. To examine the effect of amino acid in the activation of acyl imidazole, 5 different amino acids were incubated with 5  $\mu$ M Cu-DAI and compared the traces after 30 min incubation. Most of the Cu-DAI was found to remain intact in the presence of Cu<sup>+</sup> but no amino acid in 2 mM GSH/PBS buffer, as well as in the presence of the amino acid but no Cu<sup>+</sup>. Interestingly, almost complete conversion of Cu-DAI was found in the presence of both Cu<sup>+</sup> and amino acid, suggesting acyl transfer reaction occurred through activation of the acyl imidazole by copper ion and nucleophilic attack by amino acids.

Furthermore, the labeling of Cu-DAI showed good selectivity for copper(II) over copper(I) and other biologically relevant metals ions by HPLC (Figure 4.1 c) and dot blots imaging (Figure 4.2), where the latter showed remarkable increase in fluorescence from labeled cell lysates only in the presence of copper. The specificity toward copper was further supported by diminishment of the Cu-induced fluorescent enhancement of the cell lysates by copper chelator BCS (Figure 4.2). To evaluate the copper binding constant by Cu-DAI, coumarin analog of Cu-DAI, Cu-DAI-Dc, was employed for this study instead of the SiR one because of possible emission overlap between SiR and the reported copper fluorescent probe CSR1.<sup>56,57</sup> The competitive assay can help to deduce the range of binding constant of Cu-DAI-Dc in comparison with the previously reported copper fluorescent probe. In this study, Cu-DAI-Dc (0–5 equiv) was continuously added to a pH 7.0 buffer solution (25 mM HEPES) containing CuCl<sub>2</sub> (2 equiv) and a fluorescence turn-on copper sensor, CSR1 (2  $\mu$ M), which is reported to have dissociation constant ( $K_d$ ) with Cu<sup>2+</sup> of  $2 \times 10^{-13}$  M.<sup>58</sup> The

solution containing probes was excited at 608 nm where Cu-DAI-Dc does not absorb but CSR1 and its copper-bound complex do. If Cu-DAI-Dc has smaller dissociation constant, free Cu-DAI-Dc can displace copper ion from CSR1, resulting in decrease in fluorescence from CSR1. It was found that the addition of Cu-DAI-Dc to the solution mixture revealed significant decrease in fluorescence intensity of CSR1, which confirmed that Cu-DAI-Dc has comparable and probably smaller dissociation constant than CSR1 ( $2 \times 10^{-13}$  M; Figure 4.3) This value is promising as it is in similar range as the dissociation constants of copper-binding proteins or copper ligands in living system.<sup>59</sup>

#### *4.1.3.2. Live-Cell Imaging of Changes in Labile Copper Pools in HEK 293T and MEF ATP7A KO/WT*

Having established the ability of Cu-DAI to respond selectively to copper levels in aqueous buffer system, we next explored its ability to respond to changes in copper(II) levels in living cells. The data established that Cu-DAI is capable of visualizing increases in intracellular copper levels in HEK 293T cells which are pre-incubated with copper ionophore Cu(gtsm) ( $2 \mu\text{M}$ )<sup>53-55</sup> for 2 hours. An overall 2-fold increase in fluorescent intensity in cytosol was found as compared to control which showed punctate pattern along some specific compartments. In contrast, HEK 293T cells pretreated with  $200 \mu\text{M}$  BCS as copper chelator for 10 h then stained with Cu-DAI for 15 min exhibited a significant decrease in fluorescent intensity as compared to control cells (Figure 4.5), supporting that Cu-DAI can monitor dynamic changes in intracellular copper level.

Next, we sought to explore its applicability to assay Cu levels in different cell types, particularly those with different expression levels of ATP7A as mutations in the copper transporters (ATP7A and ATP7B) are the main causes of disorders in copper metabolism and homeostasis,<sup>60,61</sup> and the mutation in the ATP7A/ATP7B gene can cause dislocation of copper excretion, resulting in toxic accumulation of Cu in the liver and, as a consequence, development of Wilson disease.<sup>62,63</sup> Cu-DAI stained-ATP7A KO cells were found to show brighter fluorescence compared with ATP7A WT cells, revealing that Cu-DAI can detect higher basal copper level in ATP7A KO cells, probably due to the deficiency in cellular copper export. Furthermore, both WT and KO cells showed fluorescent increase with Cu(gtsm) in time- and concentration-dependent manner and fluorescent decrease in the presence of  $200 \mu\text{M}$  BCS, respectively (Figure 4.6). These validates that Cu-DAI can detect changes in copper levels in the ATP7A WT and KO cells.

#### *4.1.3.3. Neuron Imaging, Transfection and Electrostimulation*

We moved on to neuron imaging with Cu-DAI to visualize copper-rich compartments. Cu-DAI was incubated in cultured hippocampal neurons and showed punctate staining in the resting states. (Figure 4.7, red channel) One of the benefits of copper protein labeling probe in the far-red to NIR window is that these new tools can be interfaced with a wide variety of blue, green, and red optical tools, i.e. capable for multicolor imaging of multi-analytes simultaneously. Of particular interests are the genetically encoded optical tools such as GFP, since these fluorescent proteins are more widely used and exhibit more predictable cellular and photophysical behavior than their red fluorescent counterparts.<sup>64</sup> Based on these benefits, multicolor imaging by Cu-DAI and fluorescence protein fused with different cellular proteins, including mitochondria, vesicle-associated membrane protein: VAMP, and copper trafficking proteins: ATP7a, were conducted in order to identify the proteins or compartments labeled by Cu-DAI. We performed simultaneous co-staining experiments on neurons with Cu-DAI (Figure 4.7 Red channel), mitochondria (Figure



4.7a)), vesicle-associated membrane protein (VAMP2) (Figure 4.7 b)), and ATP7a (Figure 4.7 c)). Under these conditions distinct cellular components were clearly visible in different colors, establishing the utility of Cu-DAI as multicolor imaging probe as well as its ability for providing robust signal anchored in cuproproteins. Colocalization between organelle markers and Cu-DAI labeling revealed that ATP7A is one of the predominant proteins labeled by Cu-DAI but not with mitochondria and VAMP2. (Figure 4.7)

Herein, we moved on to characterize the distribution of labile copper pools in activated neuronal cells. Depolarization of neurons induced by KCl (50 mM),<sup>19</sup> Glu/Gly (50  $\mu$ M/ 5  $\mu$ M),<sup>6</sup> and electrostimulation<sup>65,66</sup> followed by staining with Cu-DAI revealed significant different staining patterns as compared to the control neurons in resting state. The fluorescence puncta in chemically and electrically stimulated neurons labeled with 1  $\mu$ M Cu-DAI are more diffuse than those in control neurons, suggesting that copper-rich compartments mainly localized in the cell body of the resting neurons while copper-rich compartments moved from their somatic cell bodies to peripheral processes, i.e. copper fluxes, upon depolarization and Cu-DAI can detect distributed copper-proteins in the neurons. (Figure 4.8)

In Figure 4.9, the number of stained neurons with Cu-DAI fluorescence puncta which were located at 1 cell body away from the center of neuron was counted and 2-fold increase was found in electrostimulated neurons than those in resting states, clearly displaying that Cu-DAI can visualize changes in copper location in neurons under resting state and after electrostimulation. To further identify proteins or organelles which are involved in copper movements throughout depolarization, we imaged depolarization in neuronal cultures expressing fluorescent proteins fused with different cellular proteins and labeled with Cu-DAI. Upon electrostimulation at 3000 AP at 20 Hz, we could clearly observe copper-rich compartments stained with Cu-DAI moved away from cell body to dendrites. Mitochondria and VAMP2 showed more punctate staining in the dendrites as compared to the control neurons, however, still their GFP fluorescence did not match with the stained Cu-DAI signal. On the other hand, in case of ATP7a, its Venus fluorescence showed more puncta in dendrites of electrostimulated neurons, as compared to control resting neurons, and the staining pattern matches well with the red signal from Cu-DAI labeled proteins. Taken together, these experiments demonstrate the ability of Cu-DAI as probe for multichannel co-staining experiments and to help elucidate the identity of copper-rich compartments and organelles as well as their roles on neuronal activities.

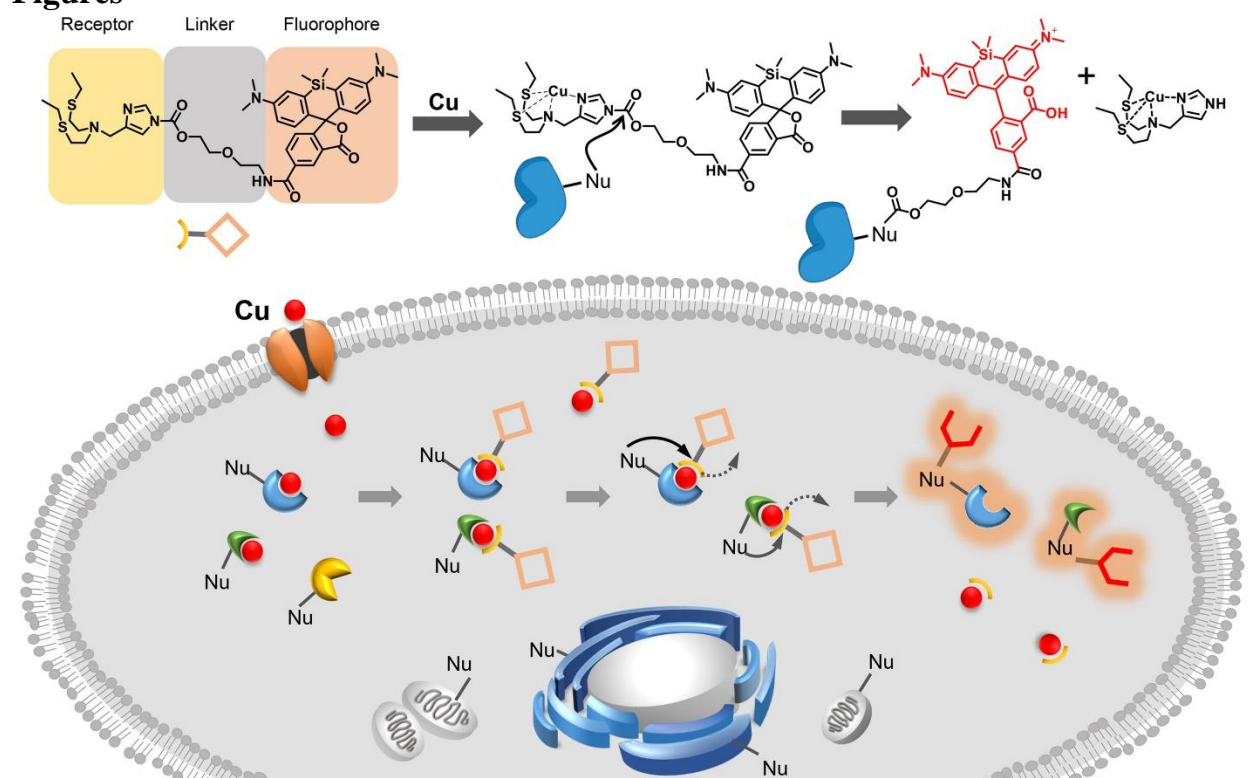
#### **4.1.4. Conclusion**

We have described the design, synthesis, and characterization of a new protein labeling reagent, Cu-DAI as a stable and selective probe toward copper over biologically relevant metal ions. Copper promoted protein labeling was evaluated on fluorescence imaging of HEK293T cells, showing fluorescent increase by Cu(gtsm) treatment and decrease by BCS. It could also detect endogenous copper accumulation caused by ATP7A mutation in MEF cells.

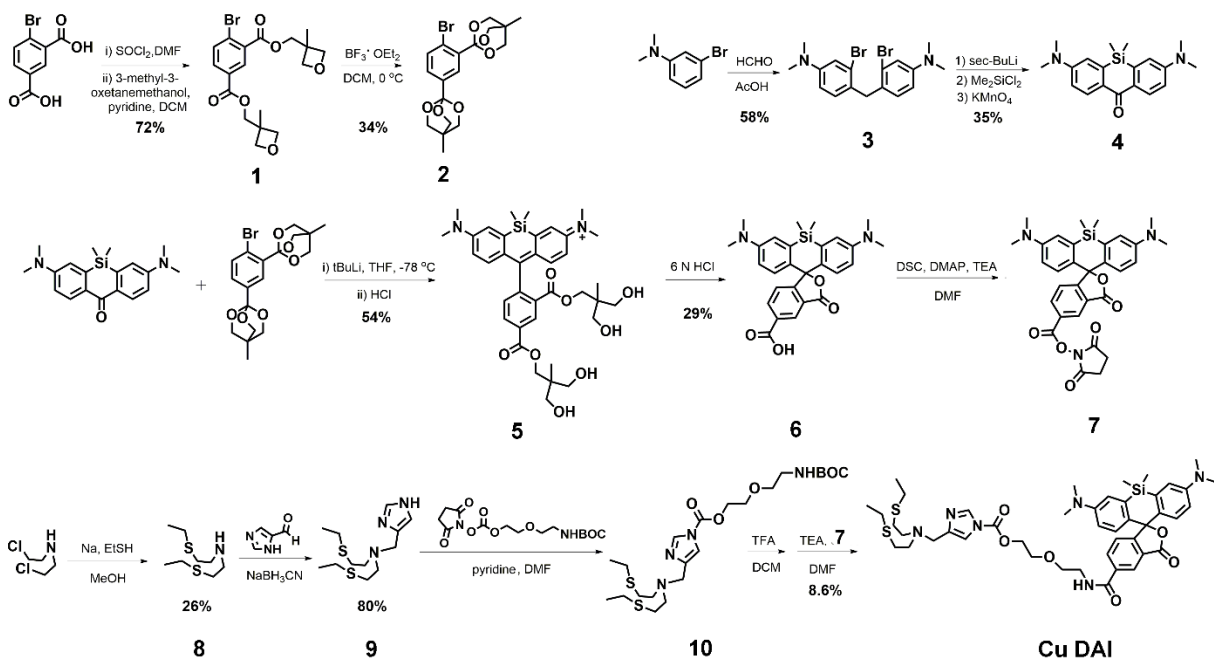
Furthermore, we applied this copper protein labeling reagent in cultured hippocampal neurons and Cu-DAI readily stained proteins with punctate labeling in resting state. Through colocalization imaging with Cu-DAI and molecular markers for cellular organelles and protein, copper trafficking protein, ATP7A was found to be one of the predominantly labeled proteins by Cu-DAI, but not mitochondria and VAMP2. We triggered depolarization-induced copper movement from soma to dendrites by chemical and electrical depolarization, followed by staining with Cu-DAI. The reagent successfully labeled copper-rich compartments and revealed more diffused copper loci,

which spread from soma to peripheral processes of neurons, after electrostimulation. To identify proteins or organelles which are involved in copper movements during depolarization, constructs of fluorescence proteins fused with different cellular proteins were expressed in neurons, and changes in fluorescence pattern of these constructs throughout depolarization processes were investigated and compared to the fluorescence of Cu-DAI-labeled proteins by co-staining experiments. It was found that fluorescence from fluorescence proteins fused with ATP7A overlapped well with the staining by Cu-DAI but neither for fluorescence proteins fused with mitochondria or VAMP2. To conclude, we have established a new copper-rich protein labeling reagent with red emission which can show robust performance on imaging copper ion in live cells and neurons with high selectivity. We anticipate that Cu-DAI will prove to be a valuable tool in efforts to map protein involvement in cellular dynamics in a variety of systems.

## Figures



**Scheme 4.1.** Workflow of conditional labeling of Cu-DAI on cellular proteins with high local Cu levels



**Scheme 4.2.** Synthetic route of Cu-DAI

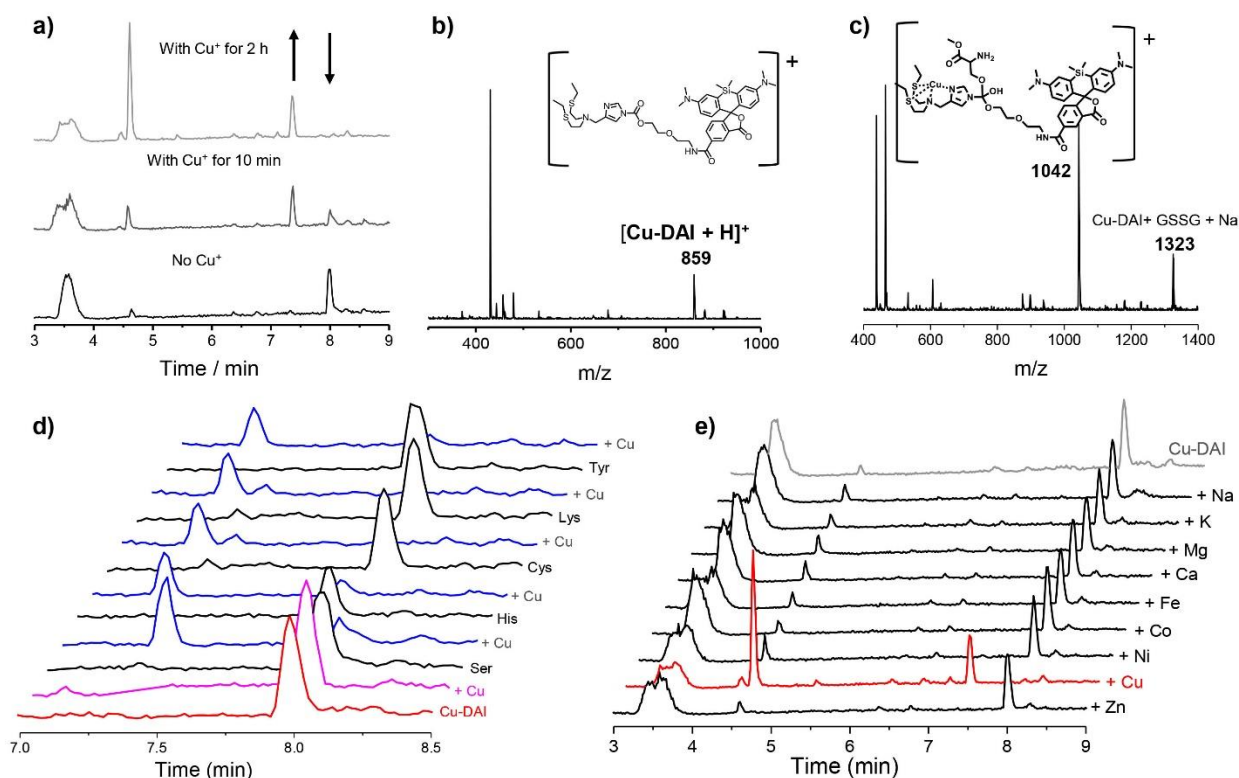


**Figure 4.1.** a) LC chromatograms of the reaction between 5  $\mu\text{M}$  Cu-DAI and 2 equivalent of  $\text{Cu}^+$  in 2 mM GSH in PBS. b) MS of the peak with retention time at 8.0 min, confirming the presence of the probe. c) MS of the peak with retention time 7.4 min, confirming formation of product from the probe,  $\text{Cu}^+$  and methyl ester serine. d) Metal selectivity test with biologically relevant metals including 2 mM for  $\text{Na}^+$ ,  $\text{K}^+$ ,  $\text{Mg}^{2+}$ ,  $\text{Ca}^{2+}$ , and 10  $\mu\text{M}$  for other metals such as  $\text{Fe}^{2+}$ ,  $\text{Co}^{2+}$ ,  $\text{Ni}^{2+}$ ,  $\text{Cu}^{2+}$ , and  $\text{Zn}^{2+}$ . 5 molar equivalent of methyl ester serine was incubated with 5  $\mu\text{M}$  Cu-DAI for 15 min, followed by further incubation with the metal ions for 15 min and recorded the LC chromatograms of the solution mixture. e) LC chromatograms of 5  $\mu\text{M}$  Cu-DAI (red), 5  $\mu\text{M}$  Cu-DAI incubated with 10  $\mu\text{M}$   $\text{Cu}^+$  (pink), and 5  $\mu\text{M}$  Cu-DAI incubated with different amino acids (25  $\mu\text{M}$ ) for 30 min, followed by further incubation with 10  $\mu\text{M}$   $\text{Cu}^+$  for 30 min.

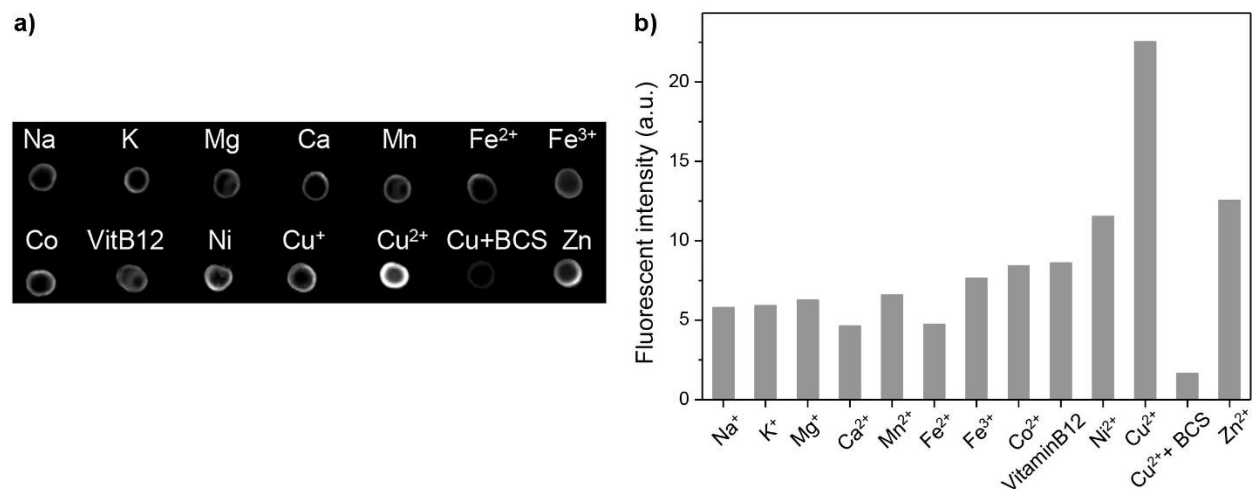


**Figure 4.2.** a) Dot blot of HEK 293T cell lysate (1 mg/mL measured by BCA assay) incubated with 50  $\mu$ M Cu-DAI and 2 mM Na<sup>+</sup>, K<sup>+</sup>, Mg<sup>2+</sup>, Ca<sup>2+</sup> and 50  $\mu$ M Mn<sup>2+</sup>, Fe<sup>2+</sup>, Fe<sup>3+</sup>, Co<sup>2+</sup>, vitamin B, Ni<sup>2+</sup>, Cu<sup>+</sup>, Cu<sup>2+</sup>, Cu<sup>2+</sup> with pre-incubation with 5 molar equivalent of BCS, Zn<sup>2+</sup>. In case of Cu<sup>+</sup> and Fe<sup>2+</sup>, protein pellets were brought inside glovebox, and metal stock solution were prepared and added to the pellets with Cu-DAI-Dc for 1 hr incubation inside the glovebox. b) Integrated fluorescent intensity of each dot blot showing Cu-DAI showed strongest fluorescence in the presence of Cu<sup>2+</sup>.

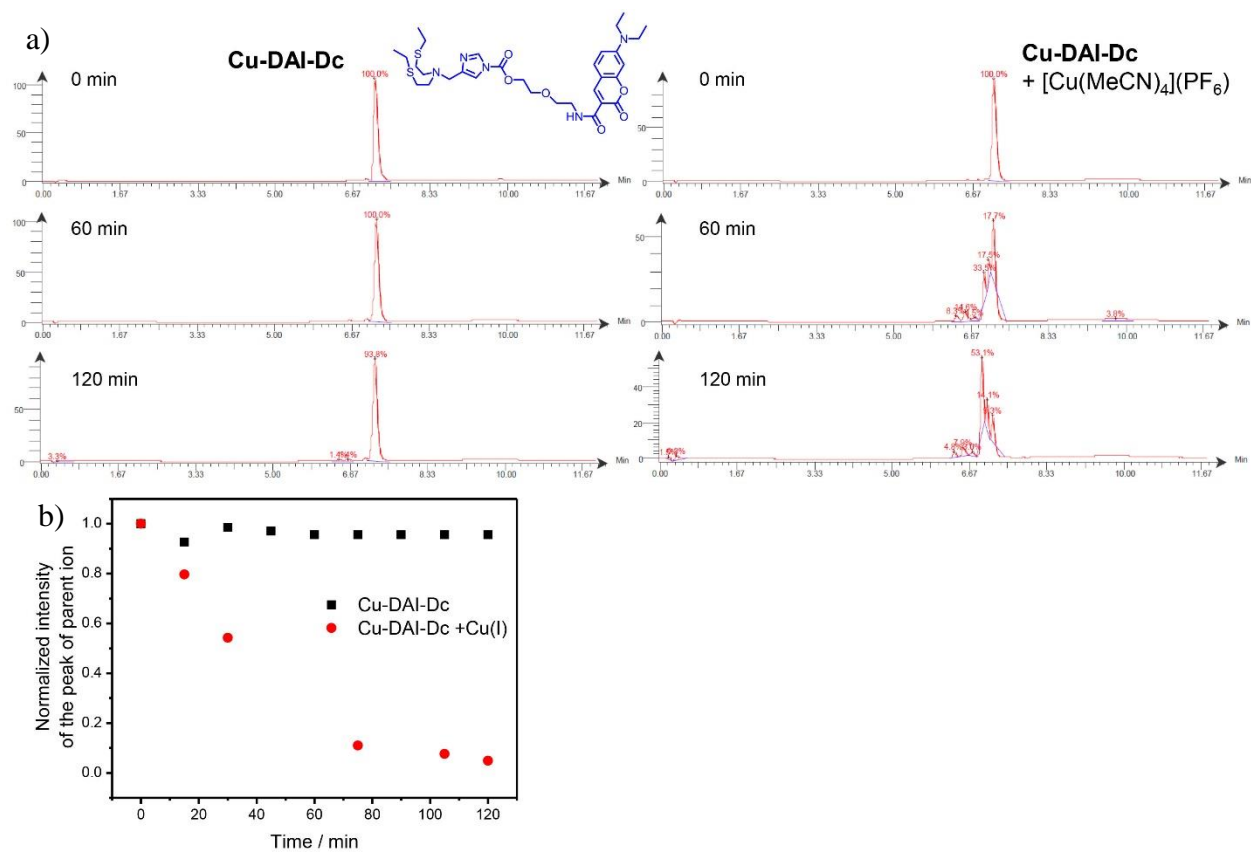


**Figure 4.3.** a) LC chromatograms of the reaction between 5  $\mu\text{M}$  Cu-DAI and 2 equivalent of  $\text{Cu}^+$  in 2 mM GSH in PBS. b) Normalized intensity of the peak of parent ion over time upto 120 min.

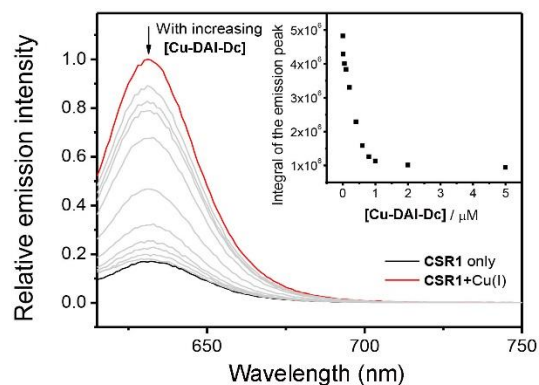
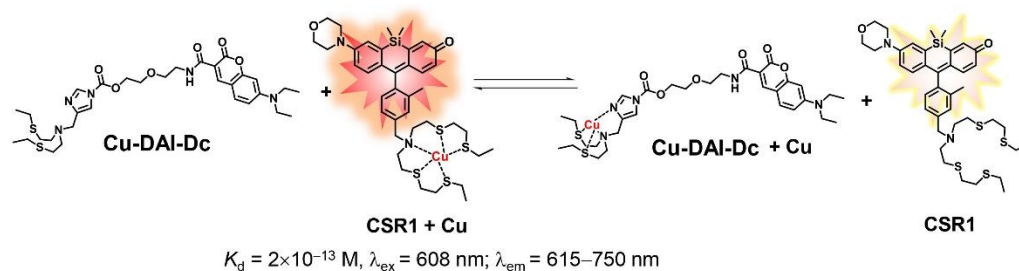


**Figure 4.4.** a) Competitive binding of copper ion between Cu-DAI-Dc and CSR1, a reported fluorescent copper probe (CSR1)<sup>58</sup>. Increasing concentration of Cu-DAI-Dc resulted in a significant decrease in fluorescence of CSR1, suggesting displacement of bound copper ion from CSR1 and hence strong binding affinity on copper ion by Cu-DAI-Dc.



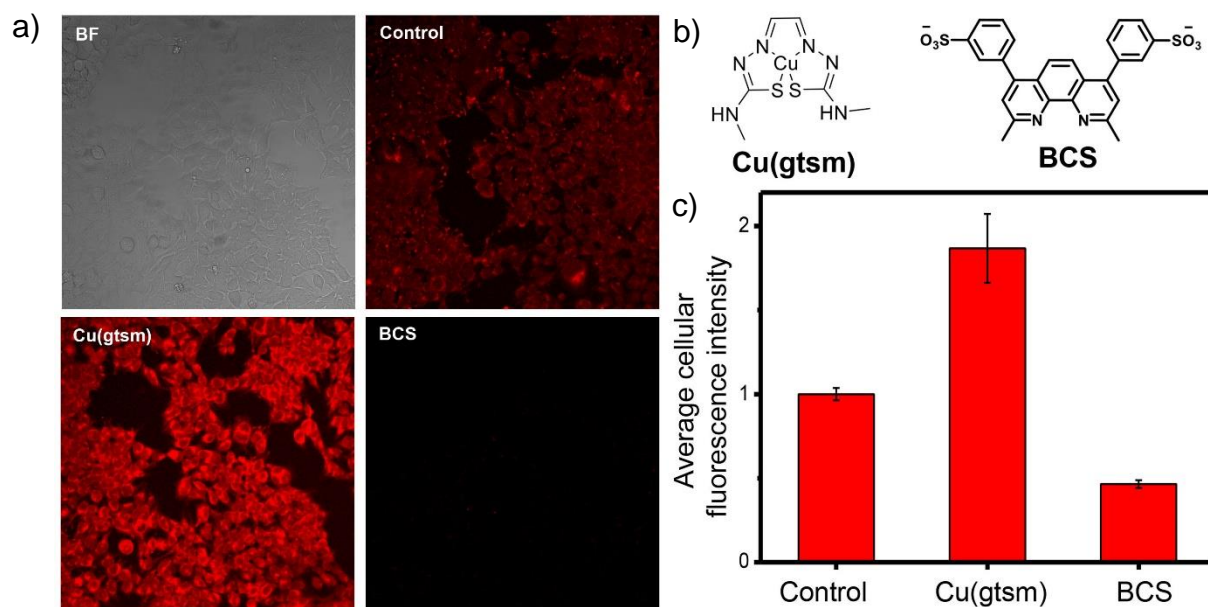


**Figure 4.5.** a) Confocal fluorescence microscopic images of HEK 293T cells treated with 1  $\mu$ M Cu-DAI, Cu(gtsm), and BCS. The cells were incubated with 2  $\mu$ M Cu(gtsm) for 2 hrs or 200  $\mu$ M BCS in DMEM/10% FBS medium overnight and washed with DMEM/10% FBS and PBS, followed by incubation with 1  $\mu$ M Cu-DAI in DPBS solution and then imaged after 15 min. b) The chemical structures of Cu(gtsm) and BCS. c) Normalized cellular fluorescence intensities of the HEK 293T cells as determined by ImageJ, showing 2-fold turn on and fluorescent turn off in presence of BCS. Error bars denote standard derivation (SD; n = 3).

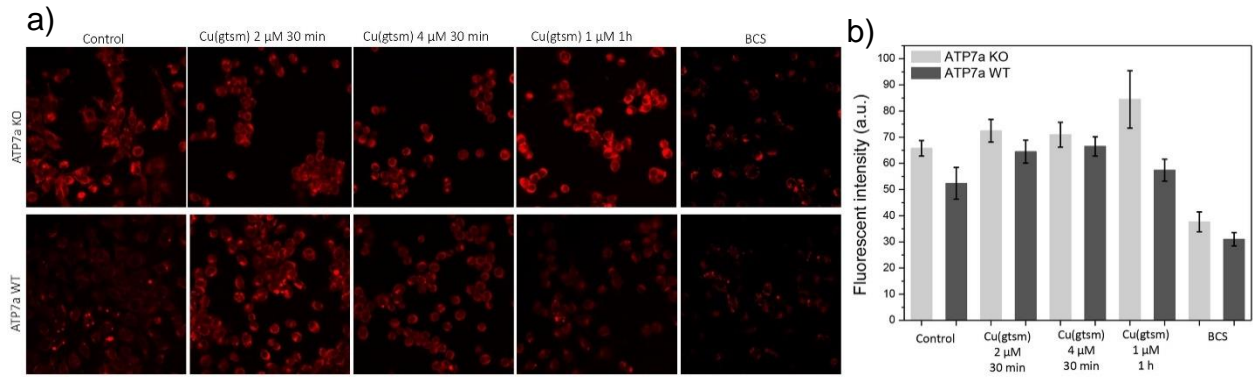


**Figure 4.6.** a) Confocal fluorescence microscopic images of MEF ATP7a WT or KO cells treated with 1  $\mu$ M Cu-DAI, Cu(gtsm), and BCS. The cells were incubated with 2  $\mu$ M Cu(gtsm) for 30 min, 4  $\mu$ M Cu(gtsm) for 30 min, 1  $\mu$ M Cu(gtsm) for 60 min or 200  $\mu$ M BCS in DMEM/10% FBS for overnight and washed with DMEM/10% FBS and PBS, followed by incubation with 1  $\mu$ M Cu-DAI in DPBS and then imaged after 15 min. b) Fluorescence intensities of the MEF cells as determined by ImageJ. Error bars denote standard derivation (SD; n = 3).

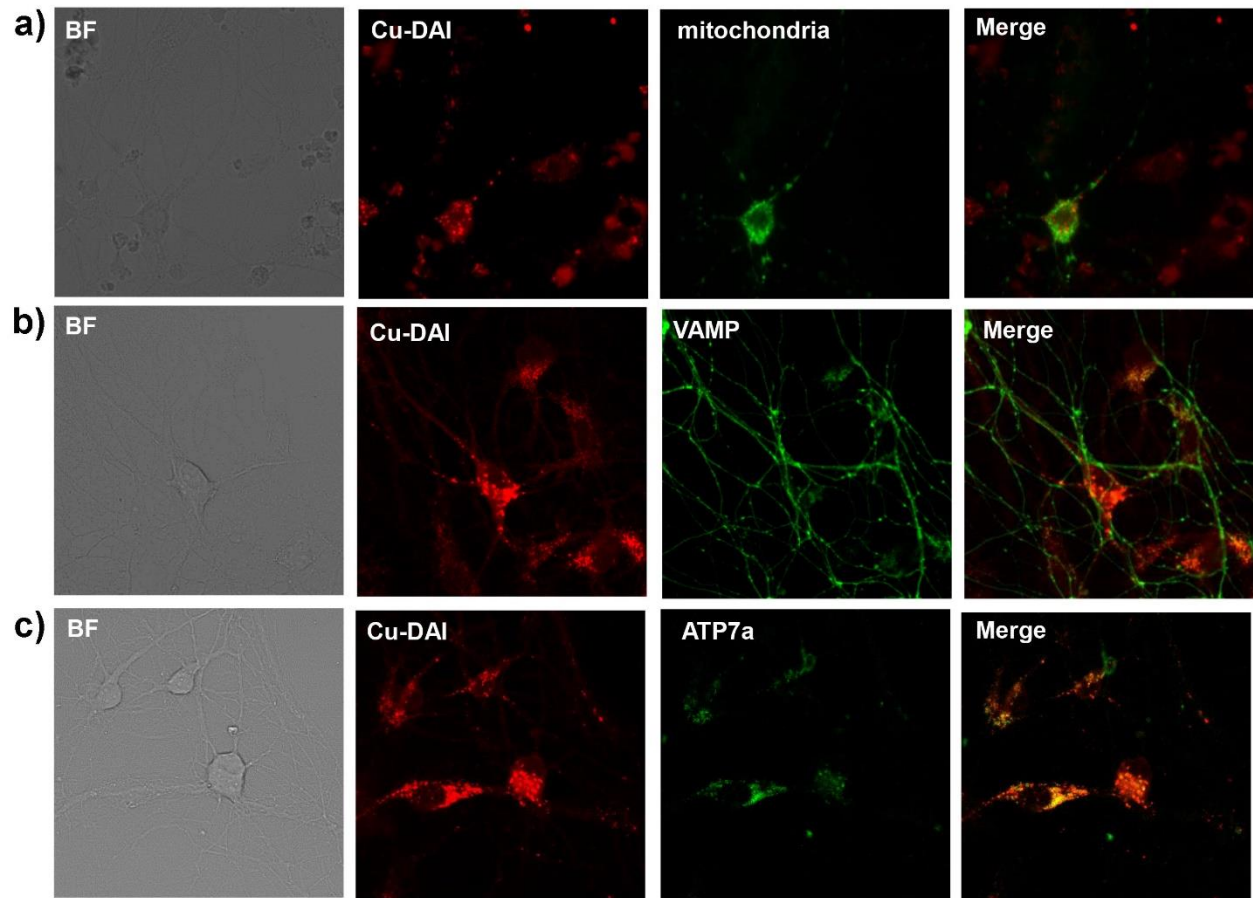


**Figure 4.7.** Primary hippocampal neurons transfected with (a) mitochondria-GFP, (b) VMAP-GFP (c) ATP7a-Venus and co-incubated with 1  $\mu$ M Cu-DAI. The green channel shows fluorescence from GFP or Venus and the red channel shows fluorescence from Cu-DAI.

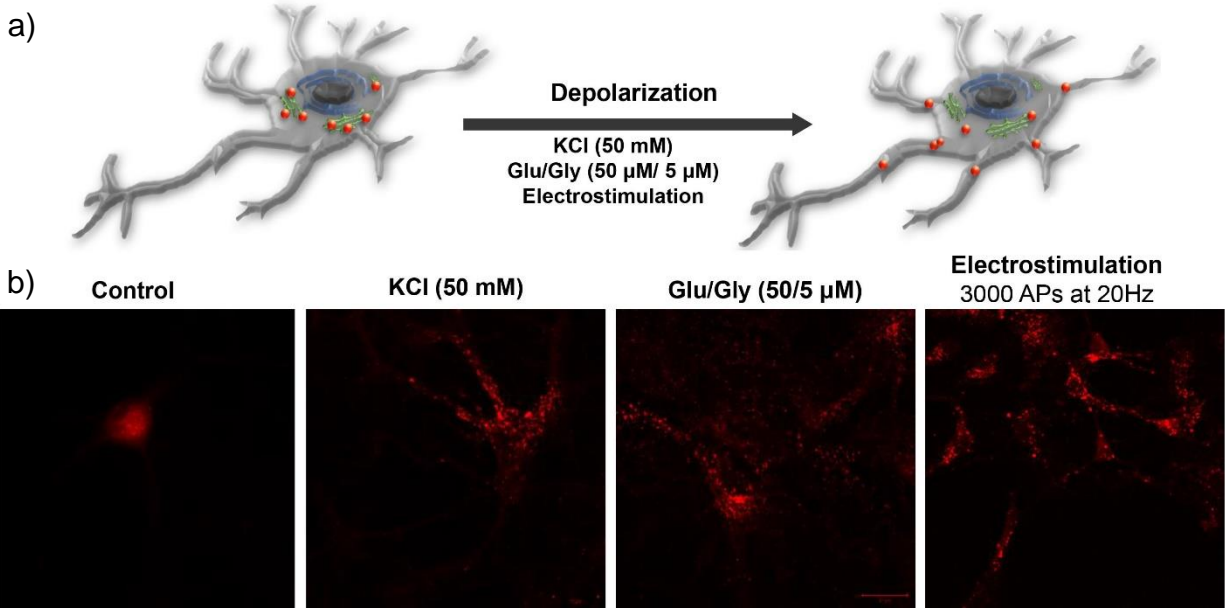


**Figure 4.8.** a) Illustration of neurons showing copper flux in primary hippocampal neurons from soma to dendrites upon by KCl (2 mM), Glu/Gly (50  $\mu$ M/ 5  $\mu$ M), and electrostimulation. b) Primary hippocampal neurons in resting state or after stimulation by KCl, Glu/Gly or electrical pulses were stained by 1  $\mu$ M Cu-DAI in HBSS for 15 min and then imaged by confocal microscopy, showing significant changes in distribution of copper-rich compartments

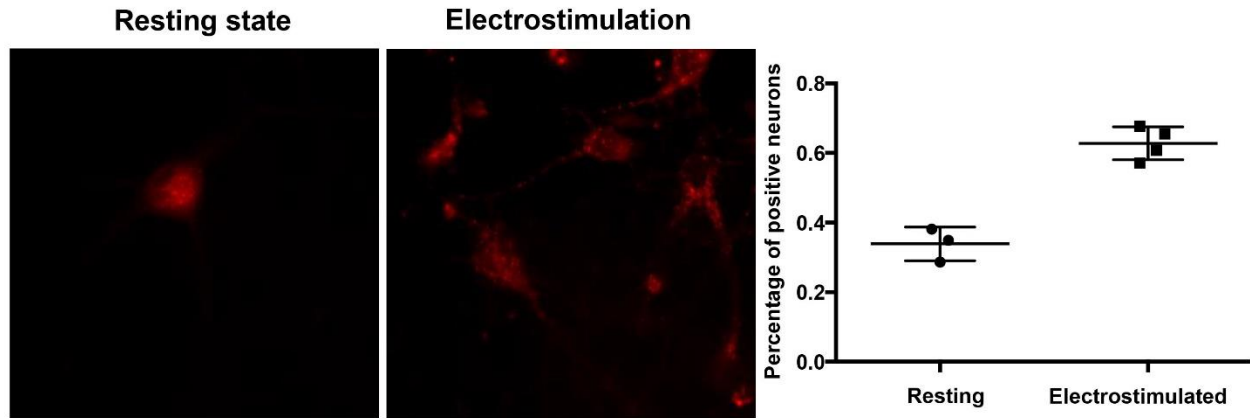


**Figure 4.9.** Primary hippocampal neuron images in resting state and depolarized state upon electrostimulation. Percentage of the number of neurons showing at least one body away from soma to dendrite away increases as double after depolarization.

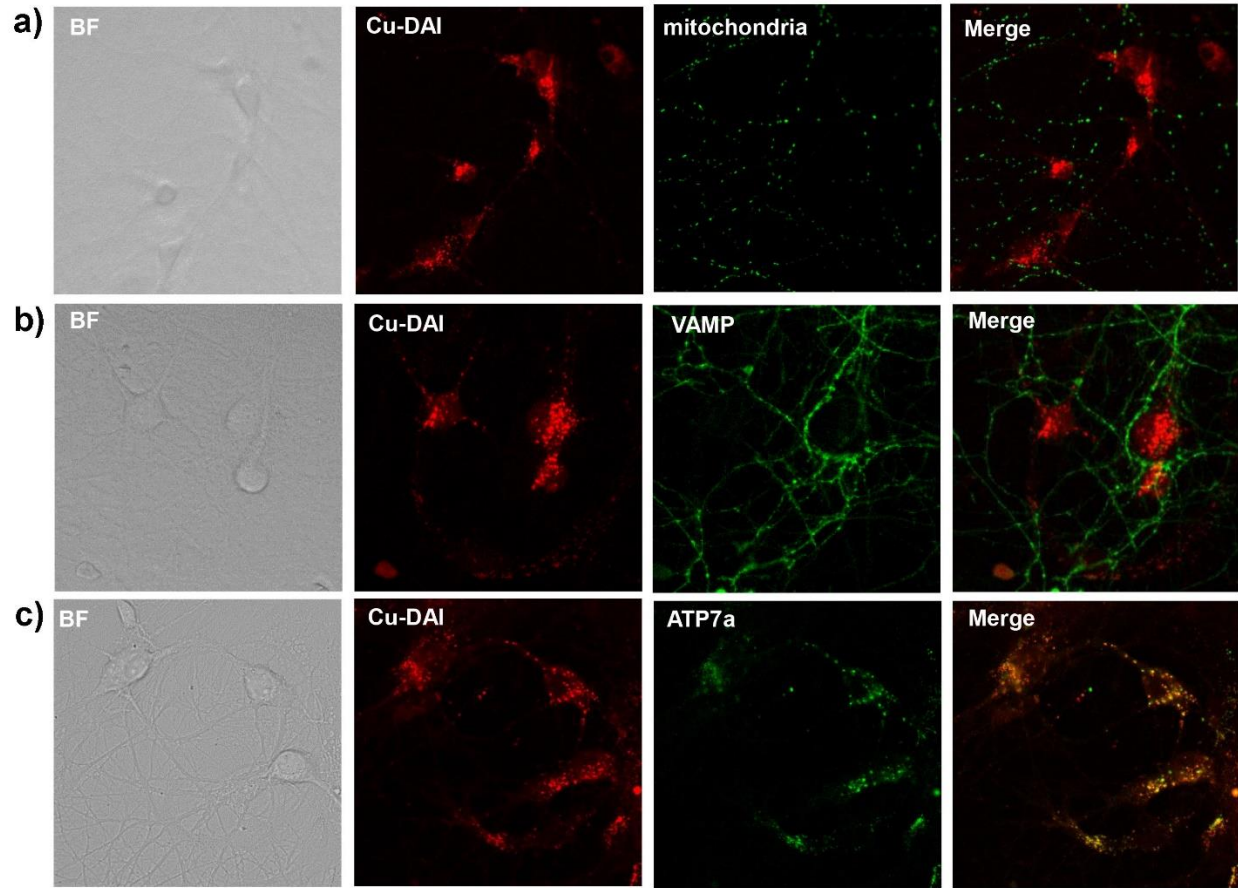


**Figure 4.10.** Electrostimulation triggered depolarization of primary hippocampal neurons transfected with (a) mitochondria-GFP, (b) VMAP-GFP (c) ATP7a-Venus and co-incubated with 1  $\mu$ M Cu-DAI. The neurons images were observed by confocal microscopy. The green channel shows fluorescence from GFP or Venus and the red channel shows fluorescence from Cu-DAI.

#### 4.1.5. References

- (1) Vella, F. Principles of Bioinorganic Chemistry: By S J Lippard and J M Berg. Pp 411. University Science Books, Mill Valley, California. 1994. \$30 ISBN 0-935702-73-3 (Paper). *Biochem. Educ.* **1995**, *23* (2), 115–115.
- (2) Dodani, S. C.; Firl, A.; Chan, J.; Nam, C. I.; Aron, A. T.; Onak, C. S.; Ramos-Torres, K. M.; Paek, J.; Webster, C. M.; Feller, M. B.; et al. Copper Is an Endogenous Modulator of Neural Circuit Spontaneous Activity. *Proc. Natl. Acad. Sci.* **2014**, *111* (46), 16280–16285.
- (3) Gaetke, L. M.; Chow, C. K. Copper Toxicity, Oxidative Stress, and Antioxidant Nutrients. *Toxicology* **2003**, *189* (1), 147–163.
- (4) Barnham, K. J.; Bush, A. I. Biological Metals and Metal-Targeting Compounds in Major Neurodegenerative Diseases. *Chem. Soc. Rev.* **2014**, *43* (19), 6727–6749.
- (5) Que, E. L.; Domaille, D. W.; Chang, C. J. Metals in Neurobiology: Probing Their Chemistry and Biology with Molecular Imaging. *Chem. Rev.* **2008**, *108* (5), 1517–1549.
- (6) Schlieff, M. L. NMDA Receptor Activation Mediates Copper Homeostasis in Hippocampal Neurons. *J. Neurosci.* **2005**, *25* (1), 239–246.
- (7) Halliwell, B.; Gutteridge, J. M. C. [1] Role of Free Radicals and Catalytic Metal Ions in Human Disease: An Overview. In *Methods in Enzymology; Oxygen Radicals in Biological Systems Part B: Oxygen Radicals and Antioxidants*; Academic Press, 1990; Vol. 186, pp 1–85.
- (8) Brady, D. C.; Crowe, M. S.; Turski, M. L.; Hobbs, G. A.; Yao, X.; Chaikuad, A.; Knapp, S.; Xiao, K.; Campbell, S. L.; Thiele, D. J.; et al. Copper Is Required for Oncogenic BRAF Signalling and Tumorigenesis. *Nature* **2014**, *509* (7501), 492–496.
- (9) Chang, C. J. Searching for Harmony in Transition-Metal Signaling. *Nat. Chem. Biol.* **2015**, *11* (10), 744–747.
- (10) Chang, C. J. Bioinorganic Life and Neural Activity: Toward a Chemistry of Consciousness? *Acc. Chem. Res.* **2017**, *50* (3), 535–538.
- (11) Carter, K. P.; Young, A. M.; Palmer, A. E. Fluorescent Sensors for Measuring Metal Ions in Living Systems. *Chem. Rev.* **2014**, *114* (8), 4564–4601.
- (12) Palmer, A. E.; Tsien, R. Y. Measuring Calcium Signaling Using Genetically Targetable Fluorescent Indicators. *Nat. Protoc.* **2006**, *1* (3), 1057–1065.
- (13) Aron, A. T.; Ramos-Torres, K. M.; Cotruvo, J. A.; Chang, C. J. Recognition- and Reactivity-Based Fluorescent Probes for Studying Transition Metal Signaling in Living Systems. *Acc. Chem. Res.* **2015**, *48* (8), 2434–2442.
- (14) Nolan, E. M.; Lippard, S. J. Small-Molecule Fluorescent Sensors for Investigating Zinc Metalloneurochemistry. *Acc. Chem. Res.* **2009**, *42* (1), 193–203.
- (15) Domaille, D. W.; Que, E. L.; Chang, C. J. Synthetic Fluorescent Sensors for Studying the Cell Biology of Metals. *Nat. Chem. Biol.* **2008**, *4* (3), 168–175.
- (16) Dean, K. M.; Qin, Y.; Palmer, A. E. Visualizing Metal Ions in Cells: An Overview of Analytical Techniques, Approaches, and Probes. *Biochim. Biophys. Acta BBA - Mol. Cell Res.* **2012**, *1823* (9), 1406–1415.
- (17) Zeng, L.; Miller, E. W.; Pralle, A.; Isacoff, E. Y.; Chang, C. J. A Selective Turn-On Fluorescent Sensor for Imaging Copper in Living Cells. *J. Am. Chem. Soc.* **2006**, *128* (1), 10–11.
- (18) Dodani, S. C.; Leary, S. C.; Cobine, P. A.; Winge, D. R.; Chang, C. J. A Targetable Fluorescent Sensor Reveals That Copper-Deficient SCO1 and SCO2 Patient Cells Prioritize Mitochondrial Copper Homeostasis. *J. Am. Chem. Soc.* **2011**, *133* (22), 8606–8616.
- (19) Dodani, S. C.; Domaille, D. W.; Nam, C. I.; Miller, E. W.; Finney, L. A.; Vogt, S.; Chang, C. J. Calcium-Dependent Copper Redistributions in Neuronal Cells Revealed by a

- Fluorescent Copper Sensor and X-Ray Fluorescence Microscopy. *Proc. Natl. Acad. Sci.* **2011**, *108* (15), 5980–5985.
- (20) Hirayama, T.; Bittner, G. C. V. de; Gray, L. W.; Lutsenko, S.; Chang, C. J. Near-Infrared Fluorescent Sensor for in Vivo Copper Imaging in a Murine Wilson Disease Model. *Proc. Natl. Acad. Sci.* **2012**, *109* (7), 2228–2233.
- (21) Miller, E. W.; Zeng, L.; Domaille, D. W.; Chang, C. J. Preparation and Use of Coppersensor-1, a Synthetic Fluorophore for Live-Cell Copper Imaging. *Nat. Protoc.* **2006**, *1* (2), 824–827.
- (22) Hong-Hermesdorf, A.; Miethke, M.; Gallaher, S. D.; Kropat, J.; Dodani, S. C.; Chan, J.; Barupala, D.; Domaille, D. W.; Shirasaki, D. I.; Loo, J. A.; et al. Subcellular Metal Imaging Identifies Dynamic Sites of Cu Accumulation in *Chlamydomonas*. *Nat. Chem. Biol.* **2014**, *10* (12), 1034–1042.
- (23) Domaille, D. W.; Zeng, L.; Chang, C. J. Visualizing Ascorbate-Triggered Release of Labile Copper within Living Cells Using a Ratiometric Fluorescent Sensor. *J. Am. Chem. Soc.* **2010**, *132* (4), 1194–1195.
- (24) Jia, S.; Ramos-Torres, K. M.; Kolemen, S.; Ackerman, C. M.; Chang, C. J. Tuning the Color Palette of Fluorescent Copper Sensors through Systematic Heteroatom Substitution at Rhodol Cores. *ACS Chem. Biol.* **2017**.
- (25) Que, E. L.; New, E. J.; Chang, C. J. A Cell-Permeable Gadolinium Contrast Agent for Magnetic Resonance Imaging of Copper in a Menkes Disease Model. *Chem. Sci.* **2012**, *3* (6), 1829–1834.
- (26) Que, E. L.; Gianolio, E.; Baker, S. L.; Aime, S.; Chang, C. J. A Copper-Activated Magnetic Resonance Imaging Contrast Agent with Improved Turn-on Relaxivity Response and Anion Compatibility. *Dalton Trans.* **2009**, *39* (2), 469–476.
- (27) Que, E. L.; Chang, C. J. A Smart Magnetic Resonance Contrast Agent for Selective Copper Sensing. *J. Am. Chem. Soc.* **2006**, *128* (50), 15942–15943.
- (28) Que, E. L.; Gianolio, E.; Baker, S. L.; Wong, A. P.; Aime, S.; Chang, C. J. Copper-Responsive Magnetic Resonance Imaging Contrast Agents. *J. Am. Chem. Soc.* **2009**, *131* (24), 8527–8536.
- (29) Que, E. L.; Chang, C. J. Responsive Magnetic Resonance Imaging Contrast Agents as Chemical Sensors for Metals in Biology and Medicine. *Chem. Soc. Rev.* **2009**, *39* (1), 51–60.
- (30) Tsien, R. Y. The Green Fluorescent Protein. *Annu. Rev. Biochem.* **1998**, *67* (1), 509–544.
- (31) Gautier, A.; Juillerat, A.; Heinis, C.; Corrêa, I. R.; Kindermann, M.; Beaufils, F.; Johnsson, K. An Engineered Protein Tag for Multiprotein Labeling in Living Cells. *Chem. Biol.* **2008**, *15* (2), 128–136.
- (32) Day, R. N.; Davidson, M. W. The Fluorescent Protein Palette: Tools for Cellular Imaging. *Chem. Soc. Rev.* **2009**, *38* (10), 2887–2921.
- (33) Saxon, E.; Bertozzi, C. R. Cell Surface Engineering by a Modified Staudinger Reaction. *Science* **2000**, *287* (5460), 2007–2010.
- (34) Arnau, J.; Lauritzen, C.; Petersen, G. E.; Pedersen, J. Current Strategies for the Use of Affinity Tags and Tag Removal for the Purification of Recombinant Proteins. *Protein Expr. Purif.* **2006**, *48* (1), 1–13.
- (35) Sletten, E. M.; Bertozzi, C. R. Bioorthogonal Chemistry: Fishing for Selectivity in a Sea of Functionality. *Angew. Chem. Int. Ed.* **2009**, *48* (38), 6974–6998.
- (36) Yang, M.; Li, J.; Chen, P. R. Transition Metal-Mediated Bioorthogonal Protein Chemistry in Living Cells. *Chem. Soc. Rev.* **2014**, *43* (18), 6511–6526.



- (37) Murrey, H. E.; Judkins, J. C.; am Ende, C. W.; Ballard, T. E.; Fang, Y.; Riccardi, K.; Di, L.; Guilmette, E. R.; Schwartz, J. W.; Fox, J. M.; et al. Systematic Evaluation of Bioorthogonal Reactions in Live Cells with Clickable HaloTag Ligands: Implications for Intracellular Imaging. *J. Am. Chem. Soc.* **2015**, *137* (35), 11461–11475.
- (38) Berger, A. B.; Vitorino, P. M.; Bogyo, M. Activity-Based Protein Profiling. *Am. J. Pharmacogenomics* **2004**, *4* (6), 371–381.
- (39) Cravatt, B. F.; Wright, A. T.; Kozarich, J. W. Activity-Based Protein Profiling: From Enzyme Chemistry to Proteomic Chemistry. *Annu. Rev. Biochem.* **2008**, *77* (1), 383–414.
- (40) Liu, Y.; Patricelli, M. P.; Cravatt, B. F. Activity-Based Protein Profiling: The Serine Hydrolases. *Proc. Natl. Acad. Sci.* **1999**, *96* (26), 14694–14699.
- (41) Weerapana, E.; Wang, C.; Simon, G. M.; Richter, F.; Khare, S.; Dillon, M. B. D.; Bachovchin, D. A.; Mowen, K.; Baker, D.; Cravatt, B. F. Quantitative Reactivity Profiling Predicts Functional Cysteines in Proteomes. *Nature* **2010**, *468* (7325), 790–795.
- (42) Miki, T.; Awa, M.; Nishikawa, Y.; Kiyonaka, S.; Wakabayashi, M.; Ishihama, Y.; Hamachi, I. A Conditional Proteomics Approach to Identify Proteins Involved in Zinc Homeostasis. *Nat. Methods* **2016**, *13* (11), 931–937.
- (43) Amaike, K.; Tamura, T.; Hamachi, I. Recognition-Driven Chemical Labeling of Endogenous Proteins in Multi-Molecular Crowding in Live Cells. *Chem. Commun.* **2017**, *53* (88), 11972–11983.
- (44) Ueda, T.; Tamura, T.; Hamachi, I. In Situ Construction of Protein-Based Semisynthetic Biosensors. *ACS Sens.* **2018**, *3* (3), 527–539.
- (45) Matsuo, K.; Hamachi, I. Ligand-Directed Tosyl and Acyl Imidazole Chemistry. In *Chemoselective and Bioorthogonal Ligation Reactions*; Algar, W. R., Dawson, P. E., Medintz, I. L., Eds.; Wiley-VCH Verlag GmbH & Co. KGaA, 2017; pp 147–163.
- (46) Lukinavičius, G.; Umezawa, K.; Olivier, N.; Honigsmann, A.; Yang, G.; Plass, T.; Mueller, V.; Reymond, L.; Jr, I. R. C.; Luo, Z.-G.; et al. A near-Infrared Fluorophore for Live-Cell Super-Resolution Microscopy of Cellular Proteins. *Nat. Chem.* **2013**, *5* (2), 132.
- (47) Egawa, T.; Hanaoka, K.; Koide, Y.; Ujita, S.; Takahashi, N.; Ikegaya, Y.; Matsuki, N.; Terai, T.; Ueno, T.; Komatsu, T.; et al. Development of a Far-Red to Near-Infrared Fluorescence Probe for Calcium Ion and Its Application to Multicolor Neuronal Imaging. *J. Am. Chem. Soc.* **2011**, *133* (36), 14157–14159.
- (48) Koide, Y.; Urano, Y.; Hanaoka, K.; Terai, T.; Nagano, T. Development of an Si-Rhodamine-Based Far-Red to Near-Infrared Fluorescence Probe Selective for Hypochlorous Acid and Its Applications for Biological Imaging. *J. Am. Chem. Soc.* **2011**, *133* (15), 5680–5682.
- (49) Koide, Y.; Urano, Y.; Hanaoka, K.; Terai, T.; Nagano, T. Evolution of Group 14 Rhodamines as Platforms for Near-Infrared Fluorescence Probes Utilizing Photoinduced Electron Transfer. *ACS Chem. Biol.* **2011**, *6* (6), 600–608.
- (50) Guo, Z.; Park, S.; Yoon, J.; Shin, I. Recent Progress in the Development of near-Infrared Fluorescent Probes for Bioimaging Applications. *Chem. Soc. Rev.* **2013**, *43* (1), 16–29.
- (51) Sato, R.; Kozuka, J.; Ueda, M.; Mishima, R.; Kumagai, Y.; Yoshimura, A.; Minoshima, M.; Mizukami, S.; Kikuchi, K. Intracellular Protein-Labeling Probes for Multicolor Single-Molecule Imaging of Immune Receptor–Adaptor Molecular Dynamics. *J. Am. Chem. Soc.* **2017**, *139* (48), 17397–17404.
- (52) Fujishima, S.; Yasui, R.; Miki, T.; Ojida, A.; Hamachi, I. Ligand-Directed Acyl Imidazole Chemistry for Labeling of Membrane-Bound Proteins on Live Cells. *J. Am. Chem. Soc.* **2012**, *134* (9), 3961–3964.

- (53) Xiao, Z.; Donnelly, P. S.; Zimmermann, M.; Wedd, A. G. Transfer of Copper between Bis(thiosemicarbazone) Ligands and Intracellular Copper-Binding Proteins. Insights into Mechanisms of Copper Uptake and Hypoxia Selectivity. *Inorg. Chem.* **2008**, *47* (10), 4338–4347.
- (54) Djoko, K. Y.; Paterson, B. M.; Donnelly, P. S.; McEwan, A. G. Antimicrobial Effects of copper(II) Bis(thiosemicarbazonato) Complexes Provide New Insight into Their Biochemical Mode of Action. *Metallomics* **2014**, *6* (4), 854–863.
- (55) Acevedo, K. M.; Hayne, D. J.; McInnes, L. E.; Noor, A.; Duncan, C.; Moujalled, D.; Volitakis, I.; Rigopoulos, A.; Barnham, K. J.; Villemagne, V. L.; et al. Effect of Structural Modifications to Glyoxal-bis(thiosemicarbazonato)copper(II) Complexes on Cellular Copper Uptake, Copper-Mediated ATP7A Trafficking, and P-Glycoprotein Mediated Efflux. *J. Med. Chem.* **2018**, *61* (3), 711–723.
- (56) Wagner, B. D. The Use of Coumarins as Environmentally-Sensitive Fluorescent Probes of Heterogeneous Inclusion Systems. *Mol.* **2009** 210–237.
- (57) Castner, E. W.; Kennedy, D.; Cave, R. J. Solvent as Electron Donor: Donor/Acceptor Electronic Coupling Is a Dynamical Variable. *J. Phys. Chem. A* **2000**, *104* (13), 2869–2885.
- (58) Krishnamoorthy, L.; Jr, J. A. C.; Chan, J.; Kaluarachchi, H.; Muchenditsi, A.; Pendyala, V. S.; Jia, S.; Aron, A. T.; Ackerman, C. M.; Wal, M. N. V.; et al. Copper Regulates Cyclic-AMP-Dependent Lipolysis. *Nat. Chem. Biol.* **2016**, *12* (8), 586–592.
- (59) Joseph A. Cotruvo, J.; Aron, A. T.; Ramos-Torres, K. M.; Chang, C. J. Synthetic Fluorescent Probes for Studying Copper in Biological Systems. *Chem. Soc. Rev.* **2015**, *44* (13), 4400–4414.
- (60) Wang, Y.; Hodgkinson, V.; Zhu, S.; Weisman, G. A.; Petris, M. J. Advances in the Understanding of Mammalian Copper Transporters. *Adv. Nutr.* **2011**, *2* (2), 129–137.
- (61) Linz, R.; Lutsenko, S. Copper-Transporting ATPases ATP7A and ATP7B: Cousins, Not Twins. *J. Bioenerg. Biomembr.* **2007**, *39* (5–6), 403–407.
- (62) Gupta, A.; Lutsenko, S. Human Copper Transporters: Mechanism, Role in Human Diseases and Therapeutic Potential. *Future Med. Chem.* **2009**, *1* (6), 1125–1142.
- (63) Polishchuk, E. V.; Concilli, M.; Iacobacci, S.; Chesi, G.; Pastore, N.; Piccolo, P.; Paladino, S.; Baldantoni, D.; van IJzendoorn, S. C. D.; Chan, J.; et al. Wilson Disease Protein ATP7B Utilizes Lysosomal Exocytosis to Maintain Copper Homeostasis. *Dev. Cell* **2014**, *29* (6), 686–700.
- (64) Morin, X.; Daneman, R.; Zavortink, M.; Chia, W. A Protein Trap Strategy to Detect GFP-Tagged Proteins Expressed from Their Endogenous Loci in *Drosophila*. *Proc. Natl. Acad. Sci.* **2001**, *98* (26), 15050–15055.
- (65) Brosenitsch, T. A.; Katz, D. M. Physiological Patterns of Electrical Stimulation Can Induce Neuronal Gene Expression by Activating N-Type Calcium Channels. *J. Neurosci.* **2001**, *21* (8), 2571–2579.
- (66) Ghasemi-Mobarakeh, L.; Prabhakaran, M. P.; Morshed, M.; Nasr-Esfahani, M. H.; Baharvand, H.; Kiani, S.; Al-Deyab, S. S.; Ramakrishna, S. Application of Conductive Polymers, Scaffolds and Electrical Stimulation for Nerve Tissue Engineering. *J. Tissue Eng. Regen. Med.* **5** (4), e17–e35.

## Chapter 5.

### **Development of Trappable Fluorescent Sodium Sensors for Imaging Sodium in Living Cells**

### 5.1.1 Introduction

Sodium is the most abundant metal ion in the human body and is involved in many physiological and pathological processes. Sodium concentration is regulated by various exchangers and transporters to maintain intracellular  $\text{Na}^+$  concentrations in the 50 mM range while extracellular sodium is typically in the 100 mM range and higher.<sup>1,2</sup> This  $\text{Na}^+$  gradient across the cell membrane is a major source of energy for most transport systems.<sup>3-5</sup>

Additionally, abnormal levels of  $\text{Na}^+$  in tissues and misregulation of  $\text{Na}^+$  influx may be critical indicators for pathological human states such as neurodegeneration and heart disease. Thus, detecting fluctuations in sodium ion concentrations would be highly useful.<sup>6-9</sup> For example, inhibitors of oxidative phosphorylation or of the  $\text{Na}^+/\text{K}^+$  pump can lead to aberrant neurotoxic effects of the endogenous neurotransmitters NMDA or glutamate. Reduced ATP levels depolarize cell membranes and permit intracellular accumulation of sodium.<sup>10</sup> The ability to trace sodium influxes in cells, along with an understanding of the corresponding metabolism, can help us to better understand human disease.

To understand the role of sodium, various methods have been utilized; for example, flame photometry,  $^{22}\text{Na}$  tracer experiments and electron microprobe analysis. However, these destructive techniques only measure total  $\text{Na}^+$  concentration but not labile  $\text{Na}^+$  as well as causing the loss of spatial information of  $\text{Na}^+$ .<sup>11</sup> Additionally, nuclear magnetic resonance of  $^{23}\text{Na}$  can detect the  $\text{Na}^+$  in non-destructive way but requires a large quantity of tissues and expensive instrumentation. Lastly, Na-sensitive microelectrodes can also be used but are limited to relatively large cells.<sup>12</sup>

One of the most promising ways to detect the  $\text{Na}^+$  is the use of fluorescent sensors. These chemical probes have many advantages, such as high signal to noise ratio, detection limits in the millimolar range, spatial and temporal resolution and real time detection of sodium ions. Several fluorescent sodium sensors have been reported, including commercially available probes such as SBFI and Sodium Green.<sup>13</sup> These probes display ratiometric signal and have high turn-on in the presence of sodium ions, respectively. However, both dyes are too bulky to load into live cells as the cellular environment induces their aggregation within the cell. Other related sensors still require further optimization, since their  $K_d$  values are not appropriate for applications in biological systems and some have low selectivity over  $\text{K}^+$  ions, which limits their usage.<sup>13</sup>

Therefore, the principles that should be considered in designing improved fluorescent sodium sensors are 1) fluorophores with excitation in the visible range, 2) reasonable  $K_d$  values for intracellular sodium as 2~30 mM, 3) high selectivity over  $\text{K}^+$  ion, 4) solubility, and 5) permeability and trappability in live cells.

## 5.1.2. Experiment

### 5.1.2.1. Materials and physical methods.

All reactions utilizing air- or moisture-sensitive reagents were performed in flame-dried glassware under a dry N<sub>2</sub> atmosphere. All other reagents were purchased from Aldrich, Oakwood, AK Scientific, or Fisher Scientific and used as received without further purification. Silica gel P60 (SiliCycle) and Brockmann basic aluminum oxide (Sigma-Aldrich) were used for column chromatography. 3,6-bis((tert-butyldimethylsilyloxy)-9H-xanthen-9-one (**compound 18**) were prepared as reported previously.<sup>14</sup> <sup>1</sup>H and <sup>13</sup>C NMR spectra of new compounds were collected in either CDCl<sub>3</sub> or CD<sub>3</sub>OD (Cambridge Isotope Laboratories) at 25 °C at the reported frequency at the College of Chemistry NMR Facility at the University of California, Berkeley unless otherwise specified. All chemical shifts were referenced to the residual solvent peak from chloroform at 7.26 ppm. Fluorometry measurements were performed on a Quanta Master 4 L-format scanning spectrofluorometer equipped with an LPS-220B 75 W xenon lamp and power supply, A-1010B lamp housing with an integrated igniter, switchable 814 photon-counting/analog photomultiplier detection unit, and MD5020 motor driver (Photon Technology International). Preparatory HPLC purification was performed on an Agilent 1260 Infinity HPLC with an Agilent Zorbax-Extend C18 column (particle size 5 μm, 5 mm × 250 mm) and a flow rate of 10 mL/min. UV spectra were acquired using a Cary Bio50 spectrophotometer (Varian). Samples for both fluorometry and UV-visible spectroscopy were prepared in a 1 cm × 0.1 cm quartz cuvette (Starna).

### 5.1.2.2. Synthesis

**3-methoxy-4-nitrobenzaldehyde (1)** : 3-hydroxy-4-nitrobenzaldehyde (18 g, 106 mmol, 1 equiv.) and methyl iodide (20 mL, 3 equiv.) were dissolved in 200 mL CH<sub>3</sub>CN. The reaction was stirred for 4 hours at room temperature and extracted with brine and dichloromethane. The solvent was removed by rotary evaporation to give the **1** (18 g, 95%) <sup>1</sup>H NMR (400 MHz, CDCl<sub>3</sub>) δ 9.69 (s, 1H), 7.57 (d, *J* = 8.0 Hz, 1H), 7.18 (d, *J* = 8.0 Hz, 1H), 6.89 (s, 1H), 3.68 (s, 3H). <sup>13</sup>C NMR (100 MHz, CDCl<sub>3</sub>) δ 190.21, 152.99, 139.63, 125.91, 122.59, 112.49, 56.78.

**2-(3-methoxy-4-nitrophenyl)-5,5-dimethyl-1,3-dioxane (2)** : **Compound 1** (20 g, 110 mmol, 1 equiv.), 2,2-dimethylpropane-1,3-diol (34 g, 330 mmol, 3 equiv.) and 2 mL H<sub>2</sub>SO<sub>4</sub> were dissolved in 200 mL anhydrous benzene. The reaction was stirred for overnight at 120 °C and cooled to room temperature. The mixture was extracted with brine and dichloromethane and dried over Na<sub>2</sub>SO<sub>4</sub>. The combined organic layer was condensed to give the **2** (32 g, 100%) <sup>1</sup>H NMR (400 MHz, CDCl<sub>3</sub>) δ 7.83 (d, *J* = 8.4 Hz, 1H), 7.24 (s, 1H), 7.13 (d, *J* = 8.4 Hz, 1H), 5.38 (s, 1H), 3.96 (s, 3H), 3.77 (d, *J* = 11.2 Hz, 2H), 3.64 (d, *J* = 11.2 Hz, 2H), 1.24 (s, 3H) 0.80 (s, 3H). <sup>13</sup>C NMR (100 MHz, CDCl<sub>3</sub>) δ 144.75, 128.92, 125.67, 118.09, 111.27, 99.92, 56.50, 30.26, 22.98, 21.78.

**4-(5,5-dimethyl-1,3-dioxan-2-yl)-2-methoxyaniline (3)** : **Compound 2** (25 g, 112 mmol, 1 equiv.) and raney nickel (catalytic amount, about 3 mL) were added into methanol in the water bath (30- 40 °C). sodium borohydride (10 g, 280 mmol, 2.5 equiv.) were slowly added into the solution. The reaction stirred for 20 minutes and celite filtration removed the raney nickel and filtrate was concentrated to yield the **3** (19 g, 85%) <sup>1</sup>H NMR (400 MHz, CDCl<sub>3</sub>) δ 6.95 (s, 1H), 6.89 (d, *J* = 8.0 Hz, 1H), 6.66 (d, *J* = 8.0 Hz, 1H), 5.28 (s, 1H), 3.86 (s, 3H), 3.73 (d, *J* = 11.2 Hz, 2H),

3.61 (d,  $J = 11.2$  Hz, 2H), 1.28 (s, 3H), 0.77 (s, 3H).  $^{13}\text{C}$  NMR (100 MHz,  $\text{CDCl}_3$ )  $\delta$  136.77, 129.02, 119.13, 114.37, 108.06, 102.19, 55.47, 30.21, 23.15, 21.94

***N*-(4-(5,5-dimethyl-1,3-dioxan-2-yl)-2-methoxyphenyl)-4-nitrobenzenesulfonamide (4)**

***N*-(2-methoxyphenyl)-4-nitrobenzenesulfonamide (6 a), *N*-(4-bromo-2-methoxyphenyl)-4-nitrobenzenesulfonamide (6 b).** : **Compound 4 a** (19 g, 80 mmol, 1.0 equiv.) and pyridine (50 mL) were dissolved in 100 mL dichloromethane. Nosyl chloride (26.6 g, 120 mmol, 1.5 equiv.) dissolved in 100 mL dichloromethane was then added into the reaction mixture dropwise over 30 minutes at room temperature. The reaction mixture was stirred for 3 hours at room temperature and washed with brine and dried over  $\text{Na}_2\text{SO}_4$ . The solvent was removed by rotary evaporation and purified by flash column chromatography (silica gel, 75% dichloromethane/hexanes) gave **4** as a yellow solid (20.1 g, 65% yield).  $^1\text{H}$  NMR (300 MHz,  $\text{CDCl}_3$ )  $\delta$  8.21 (d,  $J = 8.8$  Hz, 2H), 7.90 (d,  $J = 8.8$  Hz, 2H), 7.55 (d,  $J = 8.0$  Hz, 1H), 7.04 (s, 2H), 6.92 (s, 1H), 5.28 (s, 1H), 3.72 (d,  $J = 11.2$  Hz, 2H), 3.67 (s, 3H), 3.60 (d,  $J = 11.2$  Hz, 2H), 1.24 (s, 3H), 0.77 (s, 3H).  $^{13}\text{C}$  NMR (100 MHz,  $\text{CDCl}_3$ )  $\delta$  149.50, 136.84, 128.46, 124.99, 123.99, 123.90, 121.29, 119.22, 108.42, 100.92, 55.67, 30.19, 23.03, 21.79

**6 a**  $^1\text{H}$  NMR (300 MHz,  $\text{CDCl}_3$ )  $\delta$  8.24 (d,  $J = 9.0$ , 2H), 7.91 (d,  $J = 9.0$ , 2H), 7.56 (dd,  $J = 7.9$ , 1.6 Hz, 1H), 7.11 (td,  $J = 7.9$ , 1.7 Hz, 1H), 7.03 (s, 1H), 6.94 (td,  $J = 7.8$ , 1.3 Hz, 1H), 6.74 (dd,  $J = 8.2$ , 1.3 Hz, 1H), 3.62 (s, 3H).  $^{13}\text{C}$  NMR (101 MHz,  $\text{CDCl}_3$ )  $\delta$  150.26, 150.08, 145.00, 128.69, 126.78, 124.79, 124.07, 122.42, 121.45, 110.93, 55.76.

**6 b**  $^1\text{H}$  NMR (300 MHz,  $\text{CDCl}_3$ )  $\delta$  8.32 – 8.21 (m, 2H), 7.99 – 7.86 (m, 2H), 7.44 (d,  $J = 8.5$  Hz, 1H), 7.08 (dd,  $J = 8.6$ , 2.1 Hz, 1H), 6.96 (br s, 1H), 6.88 (d,  $J = 2.1$  Hz, 1H), 3.64 (s, 3H).  $^{13}\text{C}$  NMR (101 MHz,  $\text{CDCl}_3$ )  $\delta$  150.56, 150.42, 144.81, 128.68, 124.53, 124.27, 124.08, 123.37, 119.49, 114.66, 56.19.  $^{13}\text{C}$  NMR (101 MHz,  $\text{CDCl}_3$ )  $\delta$  155.93, 149.89, 146.24, 133.70, 130.65, 128.92, 125.77, 123.70, 121.11, 111.82, 72.63, 70.51, 69.21, 61.92, 54.94, 49.58.

***N*-(2-(2-(2-hydroxyethoxy)ethoxy)ethyl)-*N*-(2-methoxyphenyl)-4-nitrobenzenesulfonamide (7a), *N*-(4-bromo-2-methoxyphenyl)-*N*-(2-(2-(2-hydroxyethoxy)ethoxy)ethyl)-4-nitrobenzenesulfonamide (7 b)** :

**Compound 6 a** (20.0 g, 65 mmol), 2-(2-(2-chloroethoxy)ethoxy)ethan-1-ol (9.4 mL, 65 mmol), potassium carbonate (8.9 g, 65 mmol), and potassium iodide (43 g, 259 mmol) were suspended in dry DMF (80 mL) and heated to 70 °C while stirring under nitrogen. After 24 h, the reaction was poured into brine (700 mL), and the mixture was extracted with ethyl acetate (3 × 200 mL). The combined organic layers were dried over sodium sulfate, filtered, and concentrated via rotary evaporation. The crude residue was purified by column chromatography (silica gel, 30-100% EtOAc in hexanes) to afford **7 a** as a transparent, yellow oil (26.0 g, 50.0 mmol, 97%). **7 a** gave **2** as a light brown oil (37 g, 0.84 mmol, quantitative yield).  $^1\text{H}$  NMR (400 MHz,  $\text{CDCl}_3$ )  $\delta$  8.27 (d,  $J = 8.8$ , 2H), 7.85 (d,  $J = 8.8$ , 2H), 7.40 – 7.28 (m, 2H), 6.97 (td,  $J = 7.6$ , 1.3 Hz, 1H), 6.77 (dd,  $J = 8.3$ , 1.3 Hz, 1H), 3.71 (dq,  $J = 4.9$ , 1.6 Hz, 2H), 3.57 (ddd,  $J = 8.6$ , 4.9, 2.8 Hz, 10H), 3.34 (s, 3H).  $^{13}\text{C}$  NMR (100 MHz,  $\text{CDCl}_3$ ):  $\delta$  162.54, 156.13, 147.81, 134.03, 133.09, 132.92, 131.26, 130.56, 130.44, 125.12, 123.36, 120.78, 111.47, 72.45, 70.29, 70.08, 68.79, 61.72, 54.72, 53.43, 49.51, 36.49, 31.41.

**7 b**  $^1\text{H}$  NMR (400 MHz,  $\text{CDCl}_3$ ):  $\delta$  8.28 (d, 2H,  $J = 8.8$  Hz), 7.84 (d, 2H,  $J = 9.2$  Hz), 7.21 (d, 1H,  $J = 8.4$  Hz), 7.09 (dd, 1H,  $J = 8.4$ , 2.0 Hz), 6.91 (d, 1H,  $J = 2.0$  Hz), 3.71-3.66 (m, 3H), 3.56-3.51 (m, 8H), 3.35 (s, 3H).  $^{13}\text{C}$  NMR (101 MHz,  $\text{CDCl}_3$ ):  $\delta$  156.46, 149.93, 145.99, 134.71, 128.82, 125.07, 124.30, 123.97, 123.76, 115.57, 72.54, 70.42, 69.08, 61.84, 55.35, 49.43.

**2-(2-(2-(*N*-(2-methoxyphenyl)-4-nitrophenyl)sulfonamido)ethoxy)ethoxy)ethyl 4-methylbenzenesulfonate (8 a), 2-(2-(2-(*N*-(4-bromo-2-methoxyphenyl)-4-nitrophenyl)sulfonamido)ethoxy)ethoxy)ethyl 4-methylbenzenesulfonate (8 b) : Compound 7 (30 g, 68 mmol) and triethylamine (19 mL, 136 mmol) were dissolved in methylene chloride (200 mL) and cooled to 0 °C while stirring. Tosyl chloride (26 g, 136 mmol) was added, and the reaction was allowed to warm to ambient temperature while stirring. After 6 h, the reaction was concentrated via rotary evaporation, and the resulting residue was purified by column chromatography (silica gel, 25% EtOAc in hexanes to 10% MeOH in EtOAc) to afford **8 a** as a white solid (31 g, 75%). <sup>1</sup>H NMR (300 MHz, CDCl<sub>3</sub>) δ 8.26 (d, *J* = 8.8 Hz, 2H), 7.84 (d, *J* = 8.8 Hz, 2H), 7.78 (d, *J* = 8.3 Hz, 2H), 7.37 – 7.24 (m, 4H), 6.95 (td, *J* = 7.6, 1.3 Hz, 1H), 6.77 (dd, *J* = 8.8, 1.3 Hz, 1H), 4.17 – 4.08 (m, 2H), 3.67 – 3.59 (m, 2H), 3.55 – 3.41 (m, 8H), 3.34 (s, 3H), 2.43 (s, 3H). <sup>13</sup>C NMR (75 MHz, CDCl<sub>3</sub>) δ 155.97, 149.86, 146.31, 145.01, 133.63, 133.10, 130.62, 130.02, 128.92, 128.14, 125.82, 123.70, 121.10, 111.82, 70.83, 70.43, 69.41, 69.25, 68.91, 54.96, 49.61, 21.83.**

**8 b** <sup>1</sup>H NMR (400 MHz, CDCl<sub>3</sub>): δ 8.35 (d, 2H, *J* = 8.2 Hz), 7.91 (d, 2H, *J* = 6.8 Hz), 7.83 (d, 2H, *J* = 8.4 Hz), 7.46 (d, 2H, *J* = 8.0 Hz), 7.24 (d, 1H, *J* = 8.0 Hz), 7.17-7.13 (m, 2H), 4.15-4.17-4.14 (m, 2H), 3.62 (t, 2H, *J* = 4.4 Hz), 3.43-3.40 (m, 8H), 3.41 (s, 3H), 2.47 (s, 3H). <sup>13</sup>C NMR (101 MHz, CDCl<sub>3</sub>): δ 164.25, 157.24, 152.89, 152.51, 141.87, 139.99, 137.24, 135.91, 134.98, 132.44, 131.21, 130.74, 130.39, 124.57, 122.88, 67.21, 62.46, 56.49, 28.01, 20.85.

***N*-(4-(5,5-dimethyl-1,3-dioxan-2-yl)-2-methoxyphenyl)-*N*-(2-(2-(2-((*N*-(2-methoxyphenyl)-4-nitrophenyl)sulfonamido)ethoxy)ethoxy)ethyl)-4-nitrobenzenesulfonamide (9 a), *N*-(4-bromo-2-methoxyphenyl)-*N*-(2-(2-(2-((*N*-(2-methoxyphenyl)-4-nitrophenyl)sulfonamido)ethoxy)ethoxy)ethyl)-4-nitrobenzenesulfonamide (9 b) :** **Compound 8 a** (13 g, 21 mmol), **Compound 4** (8.2 g, 19 mmol), potassium carbonate (10.7 g, 74 mmol), and potassium iodide (3.2 g, 19 mmol) were suspended in dry DMF (100 mL) and heated to 70 °C while stirring under nitrogen. After 24 h, the reaction was poured into brine (600 mL), and the mixture was extracted with ethyl acetate (3 × 100 mL). The combined organic layers were dried over sodium sulfate, filtered, and concentrated via rotary evaporation. The crude residue was passed through a silica plug (100 g, 10% MeOH in EtOAc), filtered, and concentrated to afford **9 a** as a foamy yellow solid (9.0 g, 98%). <sup>1</sup>H NMR (400 MHz, CDCl<sub>3</sub>): δ 8.26-8.19 (m, 5H), 7.91-7.81 (m, 5H), 7.31 (m, 2H), 6.90-6.74 (m, 3H), 5.43 (s, 1H), 3.77-3.35 (m, 22H), 1.25-1.21 (m, 3H), 0.77 (s, 3H). <sup>13</sup>C NMR (100 MHz, CDCl<sub>3</sub>): δ 128.46, 124.36, 124.01, 121.23, 119.62, 108.06, 103.01, 69.03, 65.28, 60.38, 55.71, 21.03, 14.17

**9 b** <sup>1</sup>H NMR (400 MHz, CDCl<sub>3</sub>) δ 8.34 – 8.21 (m, 4H), 7.91 – 7.79 (m, 4H), 7.36 – 7.28 (m, 2H), 7.17 (d, *J* = 8.3 Hz, 1H), 7.07 (dd, *J* = 8.3, 2.1 Hz, 1H), 7.00 – 6.88 (m, 2H), 6.78 (d, 1H), 4.13 – 3.46 (m, 8H), 3.44 (s, 4H), 3.36 (s, 3H), 3.33 (s, 3H). <sup>13</sup>C NMR (101 MHz, CDCl<sub>3</sub>) δ 156.62, 155.98, 149.99, 149.89, 146.31, 146.14, 134.75, 133.70, 130.67, 128.94, 128.92, 125.81, 125.23, 124.35, 124.02, 123.84, 123.72, 121.13, 115.66, 111.85, 70.39, 70.36, 69.17, 55.46, 54.98, 49.60, 49.56.

**4-(5,5-dimethyl-1,3-dioxan-2-yl)-2-methoxy-*N*-(2-(2-(2-((2-methoxyphenyl)amino)ethoxy)ethoxy)ethyl)aniline (10 a) 4-bromo-2-methoxy-*N*-(2-(2-(2-((2-methoxyphenyl)amino)ethoxy)ethoxy)ethyl)aniline (10 b) :** **Compound 8 a** (10 g, 12 mmol), thiophenol (8.5 mL, 83 mmol, 7 equiv.), and potassium carbonate (16 g, 118 mmol) were suspended in DMF (100 mL) and stirred at room temperature. After 2 h, the reaction was poured

into brine (700 mL), and the mixture was extracted with ethyl acetate (3 × 100 mL). The combined organic layers were dried over sodium sulfate, filtered, and concentrated via rotary evaporation. The crude residue was purified by column chromatography (silica gel, 20-40% EtOAc in hexanes) to afford **10 a** as a transparent, amber oil (2.1 g, 3.8 mmol, 78%). <sup>1</sup>H NMR (400 MHz, CDCl<sub>3</sub>) δ 6.95-6.91 (m, 3H), 6.84 (t, *J* = 7.6 Hz, 1H), 6.74 (d, *J* = 7.2 Hz, 1H), 6.68-6.55 (m, 3H), 5.29 (s, 1H), 3.85-3.60 (m, 20H), 1.28 (s, 3H), 0.77 (s, 3H). <sup>13</sup>C NMR (100 MHz, CDCl<sub>3</sub>) δ 147.70, 147.12, 147.17, 142.37, 140.23, 139.90, 139.30, 126.73, 124.24, 115.78, 114.99, 114.78, 110.063, 103.49, 100.97, 73.39, 65.60, 54.86, 52.41, 30.12

**10 b** <sup>1</sup>H NMR (400 MHz, CDCl<sub>3</sub>) δ 6.95 (dd, *J* = 8.4, 2.1 Hz, 1H), 6.87 (td, *J* = 7.5, 1.6 Hz, 1H), 6.83 (d, *J* = 2.1 Hz, 1H), 6.76 (dd, *J* = 7.9, 1.5 Hz, 1H), 6.70 (dd, *J* = 7.4, 1.6 Hz, 1H), 6.67 – 6.59 (m, 1H), 6.45 (d, *J* = 8.4 Hz, 1H), 4.58 (s, 2H), 3.81 (s, 3H), 3.79 (s, 3H), 3.74 (q, *J* = 5.2 Hz, 4H), 3.67 (s, 4H), 3.33 (t, *J* = 5.4 Hz, 2H), 3.28 (t, *J* = 5.4 Hz, 2H). <sup>13</sup>C NMR (100 MHz, CDCl<sub>3</sub>) δ 147.70, 147.12, 138.10, 137.37, 123.73, 121.24, 116.78, 112.79, 110.78, 110.03, 109.49, 107.97, 70.39, 70.35, 69.83, 69.60, 55.66, 55.41, 43.32.

**7-(4-(5,5-dimethyl-1,3-dioxan-2-yl)-2-methoxyphenyl)-13-(2-methoxyphenyl)-1,4,10-trioxa-7,13-diazacyclopentadecane-8,12-dione (11 a), 7-(4-bromo-2-methoxyphenyl)-13-(2-methoxyphenyl)-1,4,10-trioxa-7,13-diazacyclopentadecane-8,12-dione (11 b) : Compound 10 a** (3.00 g, 6.32 mmol) and glycoyl chloride (0.83 mL, 6.76 mmol) were separately dissolved in anhydrous benzene (50 mL) under nitrogen. Using two syringe pumps (KDS-100, KD Scientific), the two solutions were added dropwise over 24 h (rate 2.0 mmL/h) to a stirring solution of anhydrous pyridine (5.15 mL, 63.2 mmol) and anhydrous benzene (2.0 L) in a flame-dried, three-neck round bottom flask under nitrogen. After completion of addition, the reaction was heated to reflux while stirring under nitrogen. After 12 h, the solvent was removed via rotary evaporation, and the crude residue was purified by column chromatography (basic alumina, 0-10% MeOH in CH<sub>2</sub>Cl<sub>2</sub>) to afford **11 a** as a foamy white solid (3.2 g, 53%). <sup>1</sup>H NMR (400 MHz, CDCl<sub>3</sub>) δ 7.67–6.62 (m, 7H), 5.06–2.65 (m, 22H). <sup>13</sup>C NMR (100 MHz, CDCl<sub>3</sub>): δ 169.59, 155.55, 130.16, 128.32, 118.10, 118.98, 108.45, 104.52, 71.20, 55.76, 55.49, 30.24, 29.93, 23.08, 21.84. HRMS-ESI calculated for C<sub>30</sub>H<sub>40</sub>N<sub>2</sub>O<sub>9</sub> [M + Na<sup>+</sup>]: 595.2632; found: 595.2622.

**11 b** <sup>1</sup>H NMR (400 MHz, CDCl<sub>3</sub>) δ 7.67 – 6.62 (m, 7H), 5.06 – 2.65 (m, 22H). HRMS-ESI calculated for C<sub>24</sub>H<sub>30</sub>O<sub>7</sub>N<sub>2</sub>Br (M+H<sup>+</sup>), 537.1231; found, 537.1231.

**7-(4-(5,5-dimethyl-1,3-dioxan-2-yl)-2-methoxyphenyl)-13-(2-methoxyphenyl)-1,4,10-trioxa-7,13-diazacyclopentadecanert-butyl-4-(13-(4-bromo-2-methoxyphenyl)-1,4,10-trioxa-7,13-diazacyclopentadecan-7-yl)-3-methoxybenzoate (12 a), 7-(4-bromo-2-methoxyphenyl)-13-(2-methoxyphenyl)-1,4,10-trioxa-7,13-diazacyclopentadecane (12 b) : Compound 11 a** (10 g, 22.7 mmol) was dissolved in anhydrous tetrahydrofuran (20 mL) in a flamed-dried, round bottom flask equipped with a reflux condenser. The resulting solution was cooled to 0 °C, and diborane (50 mL, 1.0 M in anhydrous tetrahydrofuran, 2.2 equiv.) was added dropwise. The reaction was heated to reflux under nitrogen for 2 h. The reaction was poured into water (20 mL) the solvent was removed via rotary evaporation. The crude residue was purified by column chromatography (basic alumina, 50% EtOAc in hexanes) to afford **12 a** as a transparent, pale yellow oil (6 g, 63%). <sup>1</sup>H NMR (400 MHz, MeOD): δ 8.13 (d, 2H, *J* = 7.6 Hz, 2H), 7.47 (d, 2H, *J* = 7.68 Hz, 2H), 6.92 (m, 3H), 4.87 (s, 1H), 3.81-3.29 (m, 24H), 2.81 (m, 3H), 0.84 (s, 3H) . <sup>13</sup>C NMR (100 MHz, MeOD): δ 48.47, 126.18, 123.48, 72.24, 69.98, 68.17, 60.87, 59.81, 54.52, 45.06, 40.72, 36.67, 33.76, 20.20.



**12 b** <sup>1</sup>H NMR (500 MHz, CDCl<sub>3</sub>) δ 7.03 (d, *J* = 7.8 Hz, 1H), 7.00 – 6.81 (m, 5H), 3.82 (s, 3H), 3.81 (s, 3H), 3.72 – 3.59 (m, 10H), 3.50 – 3.37 (m, 10H). <sup>13</sup>C NMR (100 MHz, CDCl<sub>3</sub>) δ 153.68, 153.12, 140.61, 139.80, 123.71, 122.49, 122.21, 121.18, 120.92, 115.28, 114.36, 111.98, 71.41, 71.18, 70.98, 70.81, 69.97, 69.80, 55.86, 55.58, 53.38, 53.26, 52.61. HRMS-ESI calculated for C<sub>24</sub>H<sub>33</sub>O<sub>5</sub>N<sub>2</sub>BrNa (M+Na<sup>+</sup>), 531.1465; found, 531.1469.

**3-methoxy-4-(13-(2-methoxyphenyl)-1,4,10-trioxa-7,13-diazacyclopentadecan-7-yl)benzaldehyde (13)** : **Compound 12 a** was added to TFA:CH<sub>2</sub>Cl<sub>2</sub> (1:1 v/v) mixture solution and heat up to 70 °C for overnight. Then sat. KHCO<sub>3</sub> solution and KOH pallet were used to adjust pH to 7 and extract with EtOAc and water to collect the organic layer. The combined layer was dried over MgSO<sub>4</sub> and purified by prep TLC (CH<sub>2</sub>Cl<sub>2</sub> : MeOH = 9:1) to give the 13 as brown oil. <sup>1</sup>H NMR (400 MHz, CDCl<sub>3</sub>) δ 9.77 (s, 1H), 7.33 (s, 2H), 6.94 (m, 4H), 6.84 (m, 3H), 3.85 – 3.81 (m, 12H), 3.63 – 3.41 (m, 12H). <sup>13</sup>C NMR (100 MHz, MeOD) δ 166.31, 150.12, 147.78, 135.36, 130.59, 129.41, 127.17, 126.87, 125.49, 125.36, 124.52, 124.05, 123.14, 123.06, 122.44, 121.90, 120.33, 119.33, 119.03, 118.58, 110.47, 109.36, 109.16, 74.75, 70.80, 68.38, 67.70, 66.58, 66.43, 66.90, 65.19, 53.99, 53.54, 53.13, 52.97, 51.98.

< BODIPY based fluorescent sodium sensor 15 a, b >

**7-(4-(2,8-diethyl-5,5-difluoro-1,3,7,9-tetramethyl-5H-4l4,5l4-dipyrrolo[1,2-c:2',1'-f][1,3,2]diazaborinin-10-yl)-2-methoxyphenyl)-13-(2-methoxyphenyl)-1,4,10-trioxa-7,13-diazacyclopentadecane (15)** : **Compound 13** (0.045 g, 0.098 mmol) was suspended in CH<sub>2</sub>Cl<sub>2</sub> and 2,4-dimethyl-1H-pyrrole (0.02 mL, 2.2 equiv.) were added dropwise into the solution. The reaction mixture stirred for 1 hour under an argon atmosphere and condensed under reduced pressure. (14 a and b) The crude products were used for the next step without further purification and poured into toluene (20 mL) and N,N-Diisopropylethylamine (0.06 mL, 4.5 equiv.) was added for 10 minutes and followed by adding Boron trifluoride diethyl etherate (0.14 mL, 10 equiv.) dropwise and heated up the reaction up to 90 °C. Water and CH<sub>2</sub>Cl<sub>2</sub> were added and the organic layer was separated and was dried over MgSO<sub>4</sub> to obtain **Compound 15** <sup>1</sup>H NMR (400 MHz, CDCl<sub>3</sub>) δ 7.62 (d, *J* = 10.2 Hz, 2H), 7.54 (m, 2H), 7.18 (d, *J* = 10.2 Hz, 2H), 7.02-6,71 (m, 4H), 3.62 (s, 3), 2.33 (s, 3H), 1.62 (m, 18H), 1.23 (m, 17H), 0.84 (m, 10H).

**7-(4-(5-fluoro-5-methoxy-1,3,7,9-tetramethyl-5H-4l4,5l4-dipyrrolo[1,2-c:2',1'-f][1,3,2]diazaborinin-10-yl)-2-methoxyphenyl)-13-(2-methoxyphenyl)-1,4,10-trioxa-7,13-diazacyclopentadecane** : followed the reported procedure.<sup>15-17</sup> **Compound 15** (0.045 g, 0.098 mmol) was treated with TMSOTf (2 equivalent) in CH<sub>2</sub>Cl<sub>2</sub> at 0 °C. Subsequently, MeOH and Et<sub>3</sub>N (2 equivalent each) were added dropwise into the solution at 0 °C. The reaction mixture stirred for 1 hour under an argon atmosphere and the solvent was then removed in vacuo and the residue dissolved in CH<sub>2</sub>Cl<sub>2</sub> and washed with distilled water. After drying over MgSO<sub>4</sub>, reduction of the volume followed in vacuo and the crude products were purified by silica gel column using CH<sub>2</sub>Cl<sub>2</sub> and MeOH gradation from 0 to 15% of MeOH. <sup>1</sup>H NMR (400 MHz, CDCl<sub>3</sub>) δ 7.62 (d, *J* = 10.2 Hz, 2H), 7.54 (m, 2H), 7.18 (d, *J* = 10.2 Hz, 2H), 7.02-6,71 (m, 4H), 3.62 (s, 3), 2.33 (s, 3H), 1.62 (m, 18H), 1.23 (m, 17H), 0.84 (m, 10H).

**N-(6-(dimethylamino)-9-(3-methoxy-4-(13-(2-methoxyphenyl)-1,4,10-trioxa-7,13-diazacyclopentadecan-7-yl)phenyl)-3H-xanthen-3-ylidene)-N-methylmethanaminium (19 a), 3-(acetoxymethoxy)-N-(3-(acetoxymethoxy)-3-oxopropyl)-N-(6-(bis(3-(acetoxymethoxy)-3-**

**oxopropyl)amino)-9-(3-methoxy-4-(13-(2-methoxyphenyl)-1,4,10-trioxa-7,13-diazacyclopentadecan-7-yl)phenyl)-3H-xanthen-3-ylidene)-3-oxopropan-1-aminium (19 b) :** **Compound 13** (0.1 g, 0.219 mmol), 3-dimethylaminophenol (130 mg, 2 equiv.), and p-TsOH•H<sub>2</sub>O (10 mg, 0.05 mmol) in propionic acid (10 mL) was stirred at 65 °C overnight. After cooling to room temperature, the mixture was poured into 3 M NaOAc (70 mL). The resulting suspension was extracted with CHCl<sub>3</sub> (70 mL × 3). The combined organic extracts were dried over MgSO<sub>4</sub> and evaporated. The residue was then dissolved in a mixture of MeOH (10 mL) and CHCl<sub>3</sub> (10 mL), followed by the addition of chloranil (35 mg, 0.5 equiv.). The mixture was vigorously stirred for 2 h and concentrated in vacuo. The resulting solid was purified by flash chromatography (CHCl<sub>3</sub>:MeOH, 9:1) three times to give a dark purple solid. This compound was then dissolved in water (50 mL) and KPF<sub>6</sub> (520 mg, 10 equiv.) was added to the solution. Precipitation thus formed was collected by filtration, rinsed with cold water, and dried in vacuo to give **19 a** (70 mg, 19 %) as a dark purple powder. <sup>1</sup>H NMR (400 MHz, CDCl<sub>3</sub>) δ 7.54-6.27 (m, 6H), 3.77-2.83 (m, 20H), 1.26-0.88 (m, 12H). <sup>13</sup>C NMR (100 MHz, MeOD) δ 132.26, 113.15, 95.69, 69.10, 55.18, 39.93, 39.33, 38.94, 29.92

**19 b** <sup>1</sup>H NMR (400 MHz, CDCl<sub>3</sub>) δ 7.27-6.84 (m, 7H), 3.87 (m, 3H), 3.72 (m, 4H), 3.50 (m, 10H), 3.18 (m, 3H), 1.67 (m, 12H). <sup>13</sup>C NMR (100 MHz, MeOD) δ 166.31, 150.12, 147.78, 135.36, 130.59, 129.41, 127.17, 126.87, 125.49, 125.36, 124.52, 124.05, 123.14, 123.06, 122.44, 121.90, 120.33, 119.33, 119.03, 118.58, 110.47, 109.36, 109.16, 74.75, 70.80, 68.38, 67.70, 66.58, 66.43, 66.90, 65.19, 53.99, 53.54, 53.13, 52.97, 51.98.

<Xanthene based fluorescent sodium sensor>

**6hydroxy-9(3-methoxy4(13(2-methoxyphenyl)-1,4,10-trioxa7,13-diazacyclopentadecan-7-yl)phenyl)-3H-xanthen-3-one (TG-Sodium).**

In the glovebox, **8** (0.102 g, 0.20 mmol, 3.0 equiv.) was dissolved in 1 mL THF and xanthone **9** (30 mg, 0.066 mmol, 1.0 equiv.) was dissolved in 5 mL THF. Both dissolved compounds were then brought out of the glove box. **8** in THF was cooled to -78 °C and 1.7M tert-butyl lithium in pentane (129 μL, 0.22 mmol, 3.3 equiv.) was then added to the cooled solution dropwise. The resulting mixture was stirred for 8 minutes at -78 °C. Xanthone **9** dissolved THF was then added to the reaction mixture dropwise at -78 °C. After addition has completed, the reaction mixture was warmed to room temperature and stirred for 30 minutes. 2M HCl (2 mL) was then added to the reaction mixture, which was allowed to stir for 1 hour at room temperature. The mixture was poured into a saturated solution of NaHCO<sub>3</sub> and extracted with ethyl acetate (2×). The combined organic layer was then washed with water (2×) and dried over Na<sub>2</sub>SO<sub>4</sub>. The solvent was removed by rotary evaporation to give a red film. Purification by column chromatography (basic alumina, 10-30% methanol in DCM) gave TG-Sodium as a red film (13 mg, 0.020 mmol, 31%). <sup>1</sup>H NMR (500 MHz, Acetonitrile-d<sub>3</sub> and 2 drops of Methanol-d<sub>4</sub>, 75°C) δ 7.47 (d, J = 8.1 Hz, 1H), 7.32 (d, J = 8.0 Hz, 1H), 7.20 (t, J = 8.0 Hz, 1H), 7.14 – 6.96 (m, 6H), 6.45 (dd, J = 9.7, 2.1 Hz, 2H), 6.37 (d, J = 2.2 Hz, 2H), 3.83 (s, 3H), 3.81 (s, 3H), 3.72 (q, J = 5.9 Hz, 4H), 3.63 (t, J = 5.0 Hz, 2H), 3.57 (t, J = 5.2 Hz, 2H), 3.52 (q, J = 6.1, 5.7 Hz, 4H), 3.32 (dt, J = 9.4, 4.6 Hz, 4H), 3.27 (br s, 1H), 3.25 (t, J = 4.9 Hz, 2H), .21 (t, J = 5.0 Hz, 2H). HRMS-ESI calculated for C<sub>37</sub>H<sub>41</sub>O<sub>8</sub>N<sub>2</sub> (M+H<sup>+</sup>), 641.2857; found, 641.2869.

**From resorcinol condensation** Aldehyde **2** (50 mg, 0.23 mmol) and resorcinol (55 mg, 0.51 mmol, 2.2 equiv) were combined with 4 mL TFA in a heavy-walled reaction tube. The reaction was sealed, heated at 110 °C for 12 h, and cooled to room temperature. After removing

the TFA solvent by rotary evaporation, the residue taken up in 10% methanol/dichloromethane and dry-loaded onto silica gel. Flash column chromatography (silica gel, 10% methanol/dichloromethane) furnished **compound 19** as a orange/yellow film (23 mg, 14% yield). <sup>1</sup>H NMR (CD<sub>3</sub>OD, 300 MHz): δ 8.90 (1H, s), 7.94 (2H, m), 7.27 (1H, m), 7.10 (2H, m), 6.99 (3H, m), 6.60 (2H, m).

**9-(3-methoxy-4-(13-(2-methoxyphenyl)-1,4,10-trioxa-7,13-diazacyclopentadecan-7-yl)phenyl)-3-oxo-3H-xanthen-6-yl trifluoromethanesulfonate** : Compound 19 was dissolved in DMF and N-Phenyl-bis(trifluoromethanesulfonimide) (3 equivalents) was added along with N,N-Diisopropylethylamine (3 equivalents) in DMF and stirring at room temperature for overnight. The solution was extracted with ethyl acetate (3 × 200 mL) with brine. The combined organic layers were dried over sodium sulfate, filtered, and concentrated via rotary evaporation. The crude residue was purified by column chromatography (silica gel, 0-20% MeOH in CH<sub>2</sub>Cl<sub>2</sub>) to afford **Compound xxa** as a red film

**tert-butyl (1-(9-(3-methoxy-4-(13-(2-methoxyphenyl)-1,4,10-trioxa-7,13-diazacyclopentadecan-7-yl)phenyl)-3-oxo-3H-xanthen-6-yl)piperidin-4-yl)carbamate** : **Compound 23** was dissolved in DMSO and tert-butyl piperidin-4-ylcarbamate (3 equivalents) was dropwisely added and stirring at room temperature for overnight. The solution was extracted with ethyl acetate (3 × 200 mL) with brine. The combined organic layers were dried over sodium sulfate, filtered, and concentrated via rotary evaporation. The crude residue was moved to the next step without further purification.

**6-(4-aminopiperidin-1-yl)-9-(3-methoxy-4-(13-(2-methoxyphenyl)-1,4,10-trioxa-7,13-diazacyclopentadecan-7-yl)phenyl)-3H-xanthen-3-one** : **Compound 24** was dissolved in TFA:CH<sub>2</sub>Cl<sub>2</sub> (1:1 v/v) and stirring at room temperature for overnight. The solution was extracted with ethyl acetate (3 × 200 mL) with NaHCO<sub>3</sub>. The combined organic layers were dried over sodium sulfate, filtered, and concentrated via rotary evaporation. The crude residue was purified by column chromatography (silica gel, 0-20% MeOH in CH<sub>2</sub>Cl<sub>2</sub>) to afford **Compound xxa** as a red film

**methyl 6-((1-(9-(3-methoxy-4-(13-(2-methoxyphenyl)-1,4,10-trioxa-7,13-diazacyclopentadecan-7-yl)phenyl)-3-oxo-3H-xanthen-6-yl)piperidin-4-yl)amino)-6-oxohexanoate** : **Compound 25** was dissolved in DMF. N-ethyl-N'-dimethylaminopropylcarbodiimide (EDCI) (3 equiv), 1-hydroxybenzotriazole (HOBt) (5 equiv), and trimethylamine (Et<sub>3</sub>N) (5 equiv) were added subsequently into the solution in DMF. <sup>1</sup>H NMR (CDCl<sub>3</sub>)

### 5.1.3. Result and discussion

#### 5.1.3.1. Design and Synthesis of Sodium Fluorescent Sensors.

Based on the desired properties, my project has focused on synthesizing fluorescent sodium sensors which have high turn-on, high selectivity toward sodium ion and show adequate trappability in live cells. New sodium sensors were derived from a sodium selective receptor, 1,4,10-trioxa-7,13-diazacyclopentadecane, which was developed by Minta *et al.*<sup>12</sup> The ring size of 1,4,10-trioxa-7,13-diazacyclopentadecane provides good selectivity for Na<sup>+</sup> over K<sup>+</sup>. This selective sodium receptor will be covalently linked to various fluorophores to construct molecular

probes. Herein, I focused on synthesizing two key sodium receptor derivatives, one which is functionalized with an aldehyde group and the other which is a bromo derivative.

The aldehyde group is a useful handle that can be used to condense with pyrrole, 3-aminophenol, and xanthone to generate BODIPY, rhodamine, and xanthene cores respectively. One of the biggest advantages of BODIPY sensors is their versatility in biological labeling and inherent resistance to photobleaching and chemical degradation.<sup>11</sup> The basic BODIPY fluorophores, composed of 3-ethyl-2,4-dimethyl-1H-pyrrole, were reported to have quantum yields as high 0.70.<sup>18</sup> I synthesized the aldehyde derivative from Li-halogen exchange of bromo derivatives, using *t*BuLi, or from Vilsmeier reaction using phosphoryl chloride on the parent crown ether. However, both methods involve flammable reagents, which can be dangerous on large scales. To avoid these hazards, I chose an alternate route, starting with 3-hydroxy-4-nitrobenzaldehyde which can be protected with 2,2-dimethylpropane-1,3-diol and subjected to macrocyclization to form the Na receptor. The acetal can then be deprotected using TFA, yielding the desired aldehyde derivative. The aldehyde-derivatized receptor was then reacted with two different kind of pyrroles and 3-aminophenol to form BODIPY sensors.

The aldehyde sodium receptor also can be used to make rhodamine-based fluorescent sensors. CoroNa-red (Molecular Probes, Invitrogen, Eugene, OR) is very lipophilic and allows direct bath-loading into cells due to the positive charge on the probe. The challenging point for rhodamine based sensors is that the  $K_d$  value has been reported as 200 mM, which is too high for even extracellular sodium ion levels (~100-150 mM).<sup>19</sup> **Compound 13** was condensed with 3-dimethylaminophenol and di-*tert*-butyl 3,3'-((3-hydroxyphenyl)azanediyl)dipropionate (**compound 18**) to make two rhodamine based fluorescent sensors, **compound 19 a and b**.

In the case of the bromo derivative, the key step was the formation of lithium adduct by adding *t*BuLi and reacting with xanthone to generate xanthenes. Xanthenes were chosen as the fluorophores for a number of reasons. First, they are relatively hydrophilic and photostable relative to many commonly used fluorophores. Secondly, their excitation energies can be readily tuned by changing the aryl substituents on the xanthone, either at the 2'- or 7'- positions or by an  $S_NAr$  reaction of the phenolic triflate. Finally, they were known to yield good turn-on levels and photostability in other small-molecule probes utilizing a chelation-based, photo-induced electron transfer (PET) mechanism.<sup>20,21</sup> Previously, several attempts were made to develop trappable xanthenes by conjugating the *tert*-butyl ester group at para position to sodium receptor and xanthone. However, though most literature suggests that *tert*-butyl esters are inert to *tert*-butyllithium, it seemed that some sort of side reactivity at the ester group may have occurred based on several trials.

Furthermore, several xanthenes based fluorescent sensors were synthesized by previous lab members using bromo-sodium receptors and xanthone. (Scheme 5.5). The fluorine substituents at the 2'- and 7'- positions substantially lowered the pKa of the xanthene phenol, approximately 4.9 versus 6.9 for unsubstituted Tokyo Green dyes, and increased photostability.<sup>13</sup> Previous graduate student, Spencer Knight prepared several series of sodium probes based on SP488 by introducing ester groups on xanthone. (Scheme 5.5) Both the apo and sodium-bound forms of SP488 and show reasonable dissociation constant ( $K_d$ ) of 31.4 mM, which is in the range of endogenous sodium levels within cells. SP488 shows a quantum yield as 0.0051 in 0 mM Na<sup>+</sup> and 0.1248 in the presence of 135 mM Na<sup>+</sup> showing the 24-fold fluorescence turn-on with high sodium selectivity over other biologically relevant metals (Figure 5.5). However, this successful *in vitro* result did not agree with the results from cellular experiments conducted in HEK293T cells. The sensor was permeable but not trappable in the cell. In order to improve SP488 by making it more trappable,

A series of sensors were synthesized by linking the AM-ether or ester moiety as shown in scheme 5.5. However, none of these sensors displayed the desired trappability, suggesting they cannot be applied to detect sodium influxes in monolayer cell culture model.

Based on this previous observation, I decided to introduce the trappable moieties such as tri AM-ether and positive charge to increase trappability in the cell. Also, I tried to develop the protocol to solve the low reaction yield of the lithiation which was reported as 3-5% previously. This optimization includes preparation of extremely dry THF and adjusting the appropriate concentration of the bromo-sodium receptor to prevent precipitation during cooling down in ice bath (-78 °C). Molecular sieve, 300 g and 150 g each in schlenk flask and were heated up to 200 °C under high vacuum for 3 days. THF was collected from solvent purification system. Second, THF was filtered through activated alumina with glass filter twice. Using extremely dry THF could support the consistent success of the lithiation reaction. Under this protocol, the yield of the lithiation was drastically increased up to 40%. However, attempt to use try solution could not solve the inconsistency of lithiation reaction. Therefore, I decided to make detour route with aldehyde sodium receptor, which can build up TG-sodium by resorcinol concentration. This route established consistent and stable reaction condition and through modification on one side of xanthene, ester moiety can be conjugate to increase the cell-retention (compound 26) which showed stable signal upon cell washing.

#### 5.1.3.2. Spectroscopic Properties and Response to Sodium

I synthesized several fluorescent sodium sensors from aldehyde receptors and measured their fluorescence turn-on responses *in vitro*. To mimic physiological conditions, Na<sup>+</sup> titrations were conducted in aqueous buffers with various Na<sup>+</sup> concentrations while maintaining the ionic strength at 135 mM with K<sup>+</sup>. I prepared 10 mM MOPs buffer at pH 7.4 with 0 mM Na<sup>+</sup> / 135 mM K<sup>+</sup> and 135 mM Na<sup>+</sup> / 0 mM K<sup>+</sup>.

In the case of BODIPYs, **Compound 15** showed 1.1-fold fluorescence turn on in response to sodium (Figure 5.1). This small turn-on might be the consequence of the high hydrophobicity of BODIPY fluorophores (logD value ~4), which has previously been determined.<sup>13</sup> This hydrophobicity could be reduced by conjugating carboxylate groups at the 3 position of the pyrrole, which would give the molecule an overall negative charge and improve the solubility of the dye in water.

To increase aqueous solubility and lipophilicity and to obtain a favorable logP, facile modification with functional groups was attempted.<sup>15</sup> The di-fluoro BODIPY was accessed by activated with excess trimethylsilyl trifluoromethane sulfonate (TMSOTf) to yield intermediate, followed by addition of a suitable alcohol to afford the desired monoalkoxy- BODIPY in moderate yield to give **Compound 15a** and **Compound 15b**. (Scheme 5.2.) This modification resulted in 13 fold-fluorescent turn-on in case of **Compound 15a** compared to silence fluorescent behavior of **Compound 15**. However, even though it showed fluorescent turn-on *in vitro*, it did not showed fluorescent turn-on by adding gramicidin *in vivo*. Moreover, it showed severe cell leaking upon cell washing from HEK293T cell culture along with fluorescence turn-off. (Figure 5.1.)

Rhodamine sensors were synthesized from condensation of the aldehyde receptor with aminophenol. Their physical properties were measured under the same conditions as previously described for the BODIPY-based sensors. **Compound 19a** showed 1.4-fold turn-on in the presence of 135 mM Na<sup>+</sup>. This small turn-on response might be caused by unfavorable electrostatic interactions between the positively charged rhodamine core and positively charged sodium ion. (Figure 5.4 a) and b)). This result was similar to that of CoroNa Red, which is reported to have a

$K_d$  value of 200 mM. To overcome this repulsion, balancing the negative charge on the rhodamine body with an AM-ether was attempted. The resulting sensor showed 11-fold fluorescence turn-on in 135 mM Na<sup>+</sup> MOPS buffer, pH 7.4. (Figure 5.4, c and d) This fluorescence enhancement in the future could be significantly improved by optimizing the synthesis work up, which involved several consecutive aqueous washes during the extraction step. The AM-ether is vulnerable to hydrolysis under aqueous condition, which resulted in some decomposition of the sensor. Another scale up synthesis of the AM-ether rhodamine sensor is on-going.

Lastly, xanthenes could be synthesized from two different pathways (Scheme 5.6.) **Compound 19**, which is designated TG-Sodium, was previously synthesized by another student via lithiation. TG-Sodium exhibited an absorption peak centered at 495 nm with a maximum fluorescence emission at 512 nm. The quantum yield ( $\Phi$ ) of the apo form is low ( $\Phi = 0.0037$ ) due to efficient photoinduced electron transfer (PeT). In the presence of 135 mM Na<sup>+</sup>, the quantum yield increases to 0.12, resulting in a 20-fold enhancement upon sodium binding.

I also tried to synthesize TG-sodium via an alternate synthetic route, using resorcinol condensation following reported method.<sup>22</sup> This condensation in strong acid detoured the way of t-butyl lithiation and in addition, it reveals the decent yield. However, the TG-sodium showed severe leaking out of the cell, which is not appropriate to obtain reliable information. To increase cell-retention, ester moiety (adipate ester) has been introduced through hydrophilic linker. (Figure 5.6) This adipate linked TG-sodium probe exhibited enhanced cell-trappability, which maintained cell-retention upon 3<sup>rd</sup> washing, furthermore, it showed fluorescent turn-on by Gramacidin addition, showing 2.2-fold fluorescent increase.

#### 5.1.4. Conclusion and Future Directions

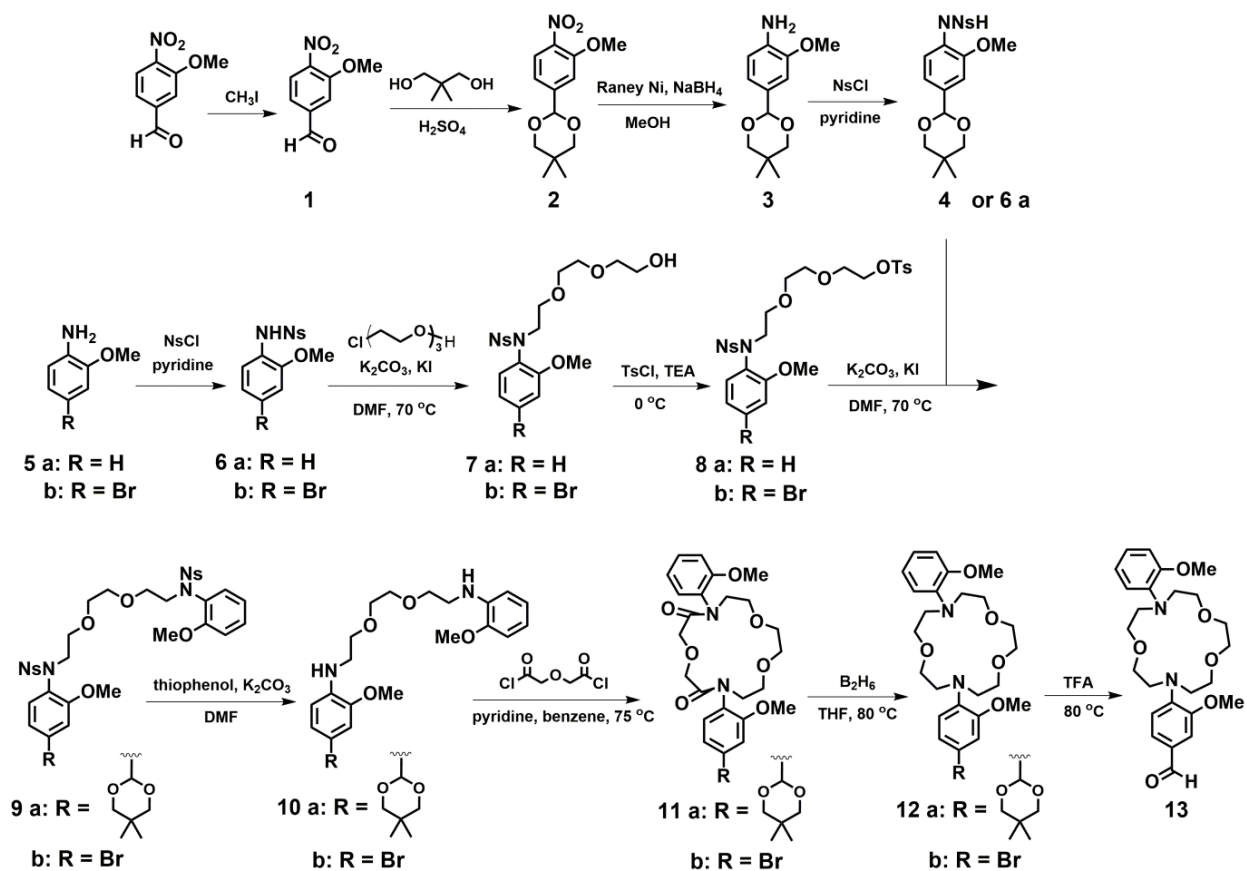
So far, we have presented the synthesis of two key molecules, **compound 13** and **compound 12 b**, and demonstrated successful condensations with various fluorophores to develop fluorescent sensors. The sensors showed typical responses to sodium ion in aqueous buffers at pH 7.4. Based on findings from previous research efforts, a primary goal for sodium sensor development is preparation of trappable dyes for use in mammalian cell lines.

To accomplish this goal, I attempted to introduce trappable moieties on the fluorophore such as AM-ethers or triphenyl phosphine to give reliable information about sodium influxes (scheme 5.8). I am now focused on making a series of trappable sensors based on xanthene and rhodamine derivatives. I am planning to access these dyes via lithiation of the bromo sodium receptor and addition to the boc-protected piperazine-substituted xanthenes. After synthesizing the piperazine xanthene **compound 23**, conjugating trappable moieties into xanthone is straightforward to generate the series of sensors shown in scheme 5.7. The same idea using boc-protected piperazine can be applied to the rhodamine, condensing aldehyde sodium receptor with tert-butyl 4-(3-hydroxyphenyl)piperazine-1-carboxylate results in the boc-protected piperazine rhodamine. Various trappable moieties can be incorporated into these rhodamine dyes as well in scheme 5.8.

Once the dyes are synthesized, they will be tested in a model cell line such as HEK 293T. Previously, SP488 and TG-Sodium were successfully applied to see the intracellular sodium ion without washing in HEK293T cells. Preliminary optimization experiments have helped us identify conditions that work well for sodium sensor calibration experiments in cells. Cells were stained by incubating a 10  $\mu$ M solution of sodium sensor in HEPES buffer, pH 7.3 for 30 min. After detecting the dye's fluorescence in the cell, the HEPES media was exchanged for HEPES buffer

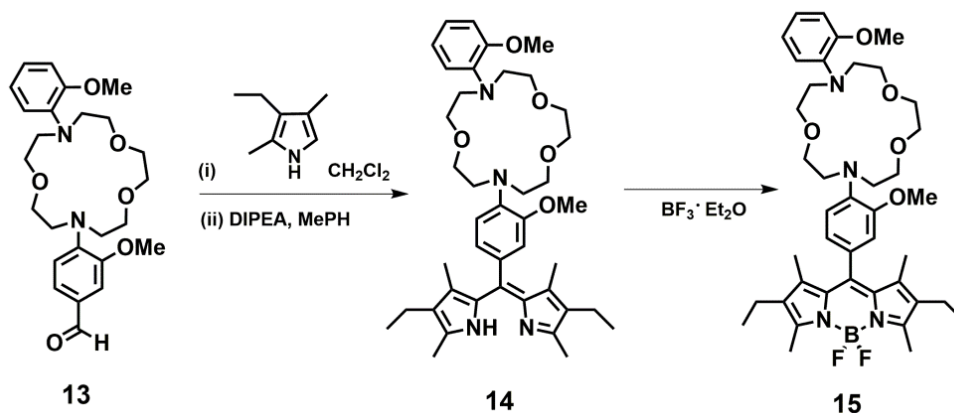
containing 2-10 M gramicidin (Invitrogen). Gramicidin is a pore-forming antibiotic that allows equilibration of  $\text{Na}^+$  inside and outside cells. The cells were allowed to equilibrate in the new media for 5 min prior to imaging. In the same way, quabain, which is a poisonous cardiac glycoside, can be used as the inhibitor of  $\text{Na}^+/\text{K}^+$  ATPase to increase the intracellular sodium influx. After exchanging HEPES media containing 2-10 M 10 uM quabain (Invitrogen), more than 10 min is needed to equilibrate in the new media prior to imaging. The increased fluorescent signal in living cells equilibrated with gramicidin or quabain in HEK293T cells demonstrates that these sodium sensors can reliably report  $\text{Na}^+$  levels in a concentration-dependent manner in living cells.

## Figures



**Scheme 5.1.** Synthesis of the two key molecules, bromo sodium receptor, **compound 12b** and aldehyde sodium receptor, **compound 13**.





**Scheme 5.2.** Fluorescent sodium sensor based on BODIPY, **compound 15**.

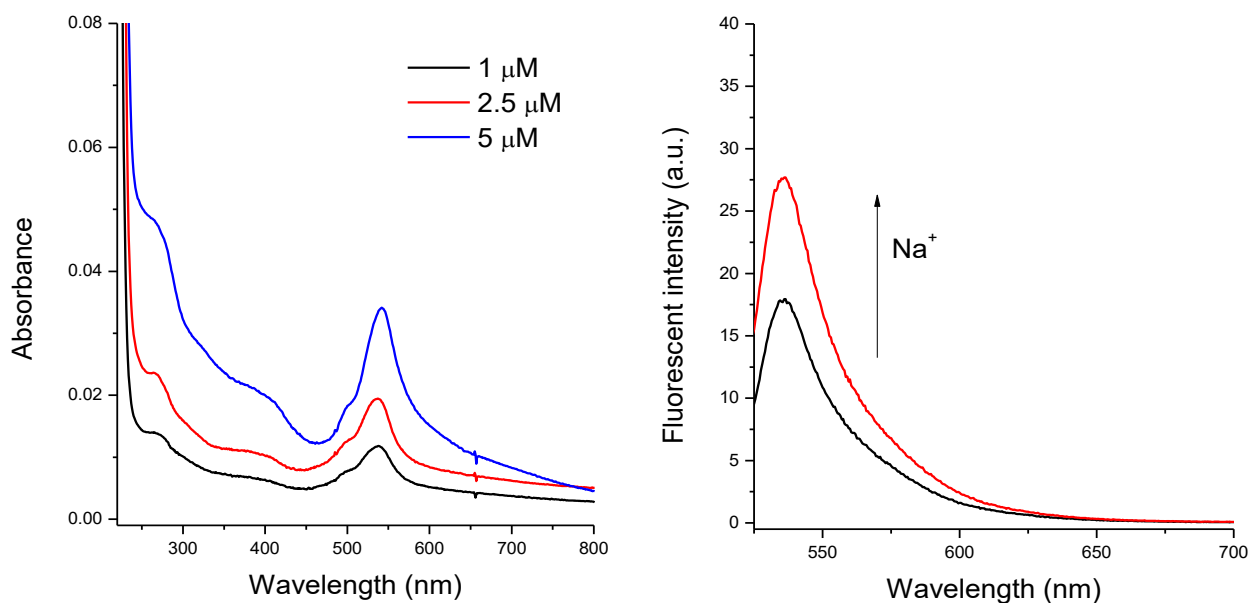
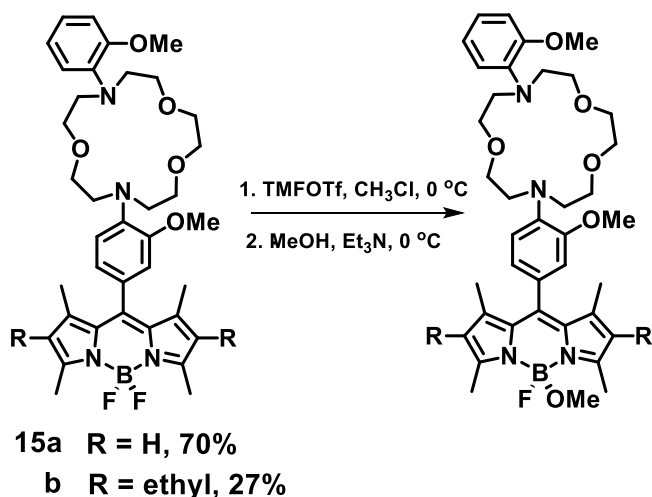


**Figure 5.1.** BODIPY based fluorescent sensor, **compound 15** a) UV-vis absorption of various concentration from 1 μ to 5 μN in 135 mM K<sup>+</sup> in 10 mM MOPS buffer, pH 7.4 b) Fluorescent intensity of 5 μM **compound 15** black: 0 mM Na<sup>+</sup> / 135 mM K<sup>+</sup> red: 0 mM K<sup>+</sup> / 135 mM Na<sup>+</sup> in 10 mM MOPS, pH 7.4  $\lambda_{ex}$  = 514 nm  $\lambda_{em}$  = 535 nm.



**Scheme 5.3.** Fluorescent sodium sensor based on BODIPY substitution of F to OMe, **Compound 15a** and **Compound 15b**.

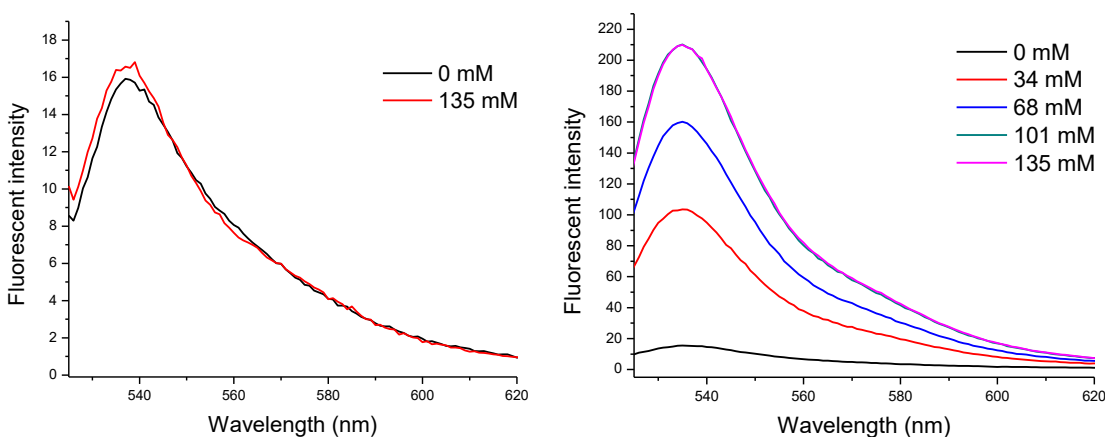


**Figure 5.2.** a) BODIPY based fluorescent sensor, 5  $\mu$ M **Compound 15** of fluorescent intensity black: 0 mM Na<sup>+</sup> / 135 mM K<sup>+</sup> red: 135 mM Na<sup>+</sup> / 0 mM K<sup>+</sup> in 10 mM MOPS, pH 7.4 b) BODIPY based fluorescent sensor, 5  $\mu$ M **Compound 15b** of fluorescent intensity black: 0 mM Na<sup>+</sup> / 135 mM K<sup>+</sup>, red: 34 mM Na<sup>+</sup> / 100 mM K<sup>+</sup> blue 68 mM Na<sup>+</sup> / 67 mM K<sup>+</sup>, purple 101 mM Na<sup>+</sup> / 35 mM K<sup>+</sup>, magenta: 135 mM Na<sup>+</sup> / 0 mM K<sup>+</sup> in 10 mM MOPS, pH 7.4  $\lambda_{\text{ex}} = 514$  nm  $\lambda_{\text{em}} = 535$  nm.

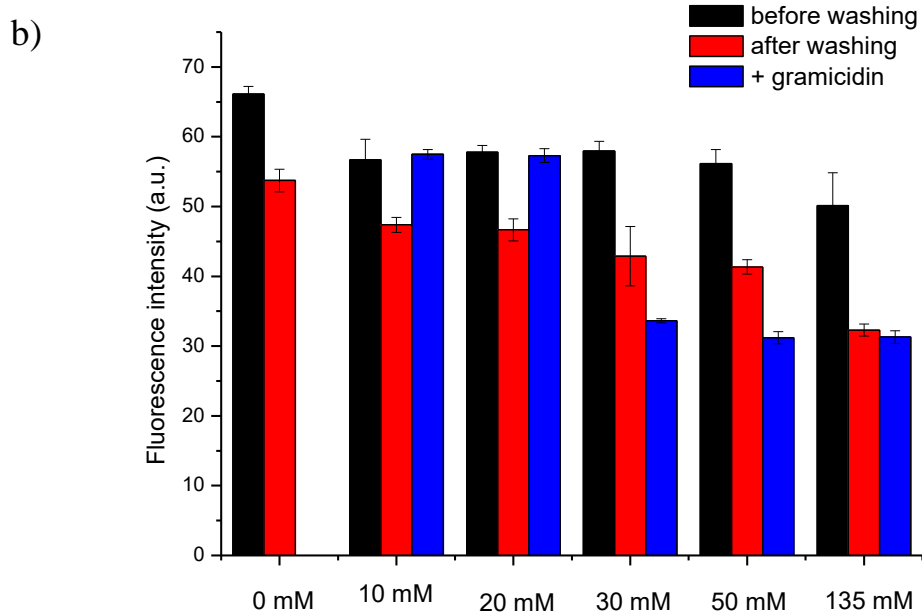
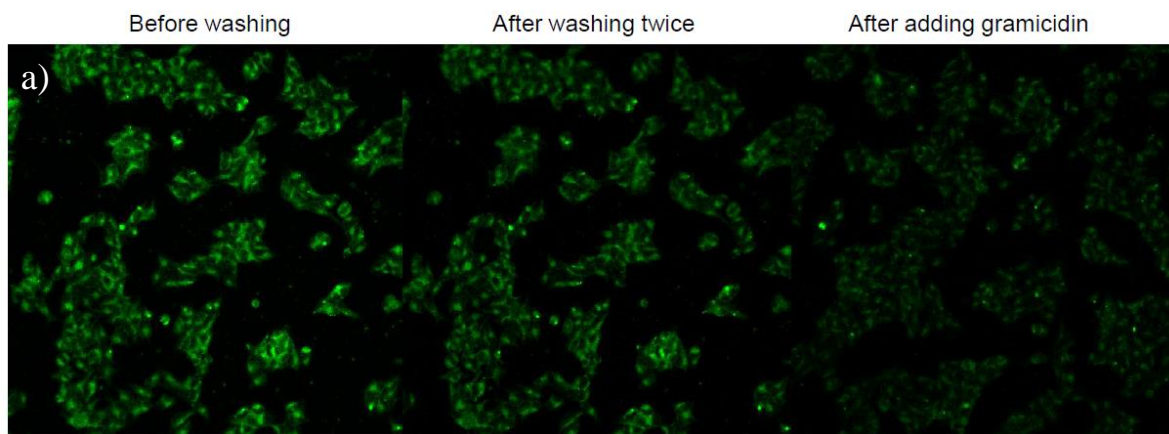
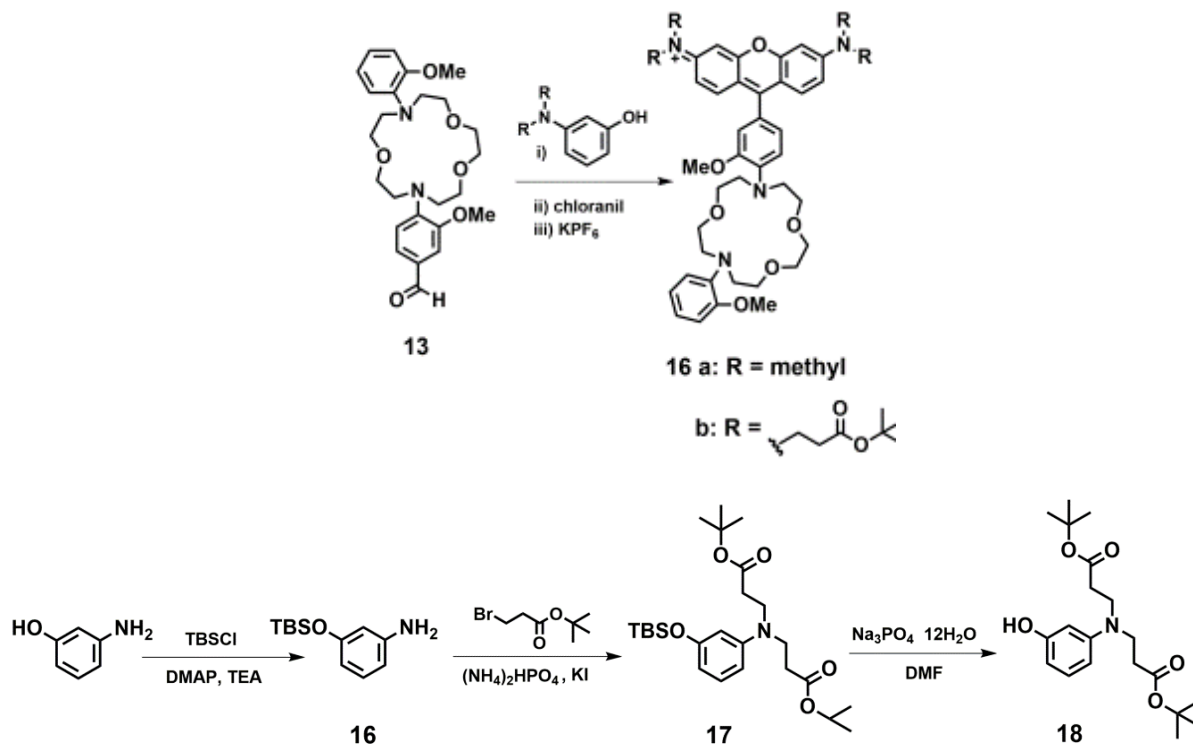


**Figure 5.3.** a) Cell imaging of 10  $\mu\text{M}$  **Compound 15a** in 10 mM HEPES buffer pH 7.4 before washing the cell after incubation compared with washing twice and after the addition of gramicidin. b) The integrated fluorescent intensity depending on sodium concentration from 0, 10, 20, 30, 50, 135 mM  $[\text{Na}^+ + \text{K}^+]_t = 135$  mM  $\lambda_{\text{ex}} = 488$  nm  $\lambda_{\text{em}} = 525$  nm.



**Scheme 5.4.** Fluorescent sodium sensor based on rhodamine **compound 16 a** and **16 b**

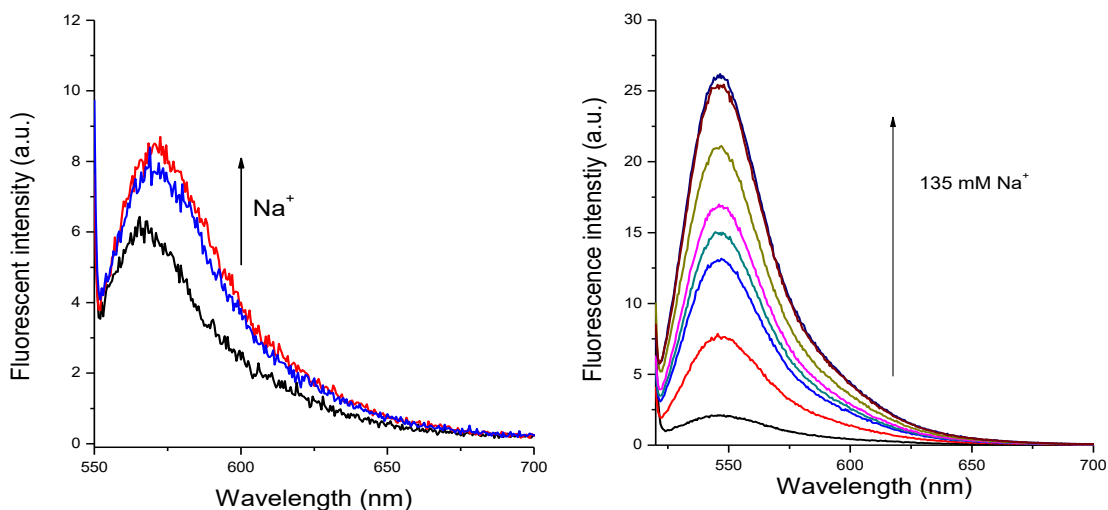
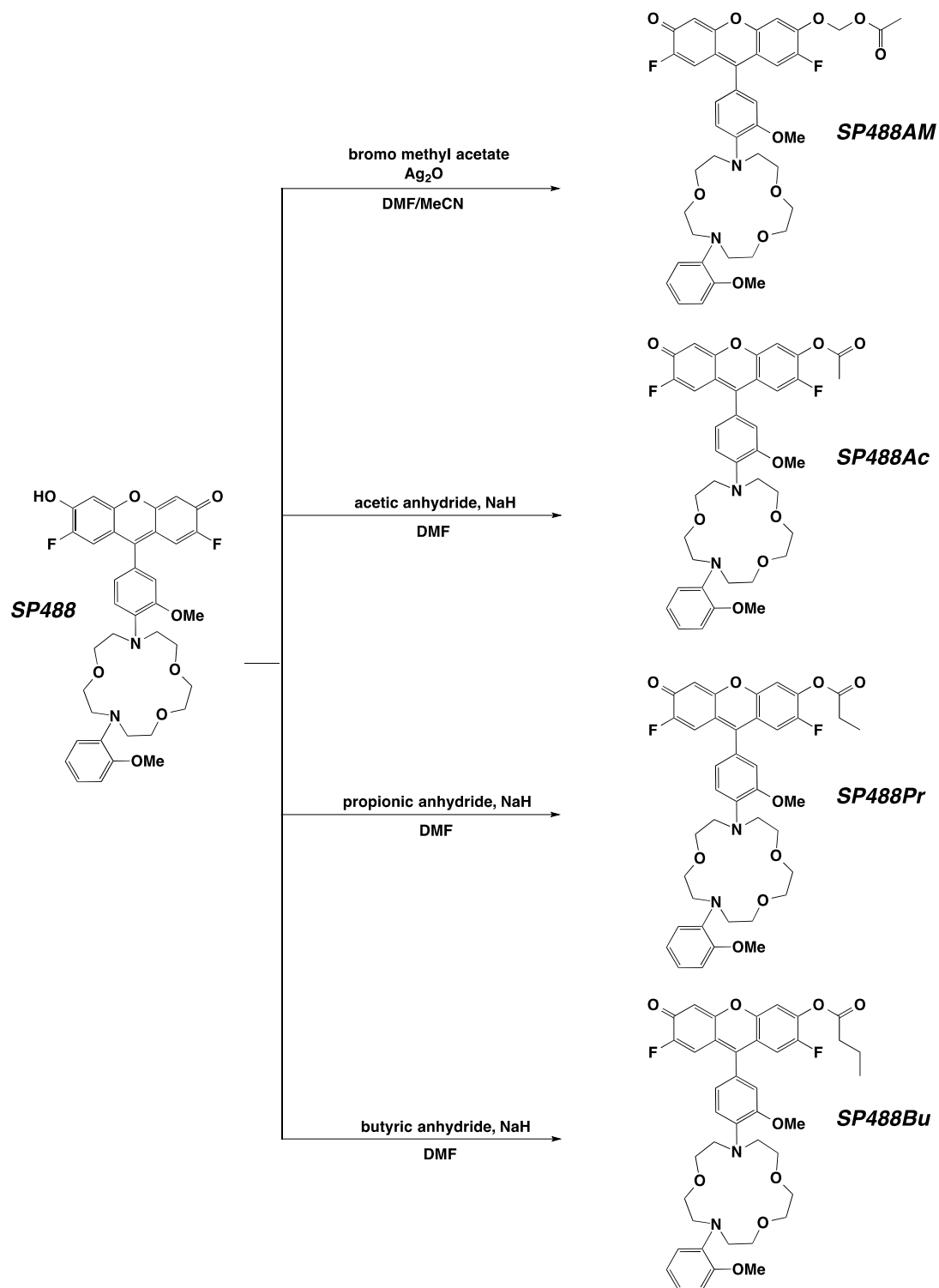
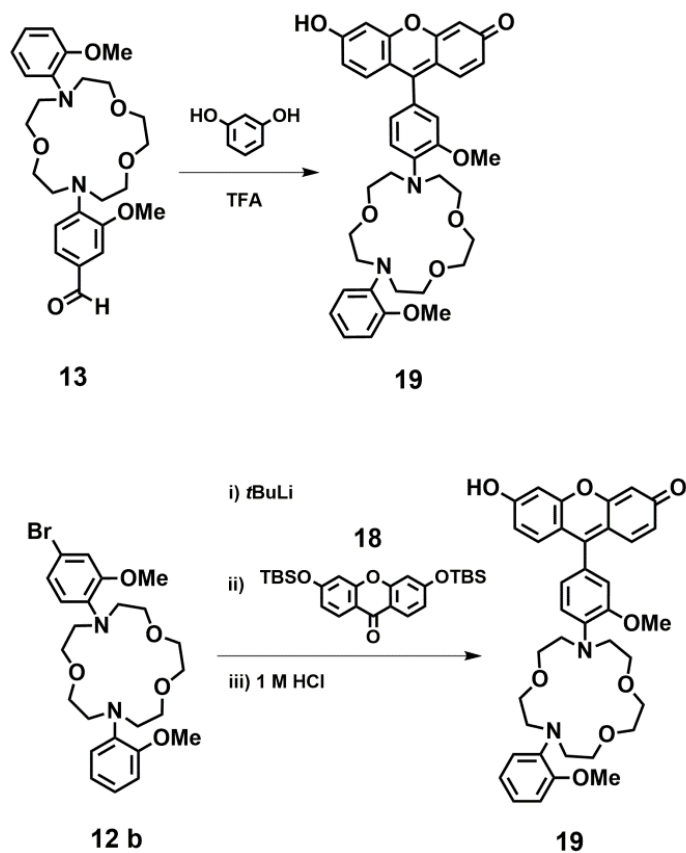


**Figure 5.4.** a) Rhodamine based fluorescent sensor, 5  $\mu\text{M}$  **Compound 16a** of fluorescent intensity black: 0 mM  $\text{Na}^+$  / 135 mM  $\text{K}^+$  red: 0 mM  $\text{K}^+$  / 135 mM  $\text{Na}^+$  in 10 mM MOPS, pH 7.4 b) Rhodamine based fluorescent sensor, 5  $\mu\text{M}$  **Compound 16b** of fluorescent intensity black: 0 mM  $\text{Na}^+$  / 135 mM  $\text{K}^+$ , red: 20 mM  $\text{Na}^+$  / 115 mM  $\text{K}^+$ , blue 40 mM  $\text{Na}^+$  / 95 mM  $\text{K}^+$ , green 60 mM  $\text{Na}^+$  / 55 mM  $\text{K}^+$ , magenta: 75 mM  $\text{Na}^+$  / 60 mM  $\text{K}^+$ , olive: 90 mM  $\text{Na}^+$  / 45 mM  $\text{K}^+$ , wine: 101 mM  $\text{Na}^+$  / 35 mM  $\text{K}^+$ , navy: 135 mM  $\text{Na}^+$  / 0 mM  $\text{K}^+$  in 10 mM MOPS, pH 7.4  $\lambda_{\text{ex}} = 514 \text{ nm}$   $\lambda_{\text{em}} = 535 \text{ nm}$ .



**Scheme 5.5.** Synthesis of SP488 derivatives by linking trappable moieties.



**Scheme 5.6.** Two different pathways to synthesize **compound 19**. The top was resorcinol condensation using aldehyde sodium receptor in trifluoroacetic acid and the bottom is through lithiation using bromo receptor and TBS-protected xanthone in tetrahydrofuran

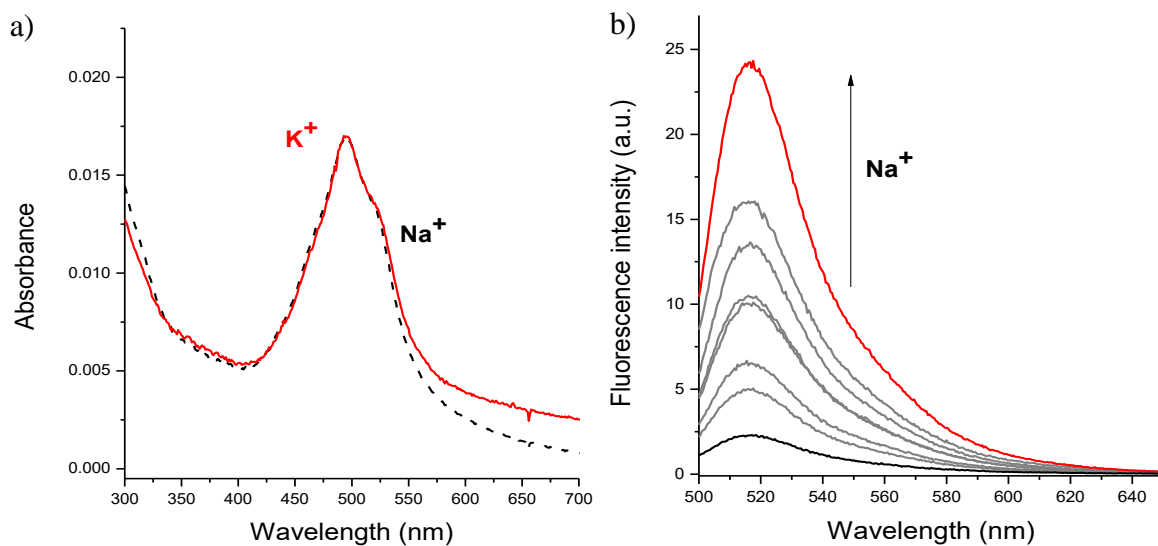
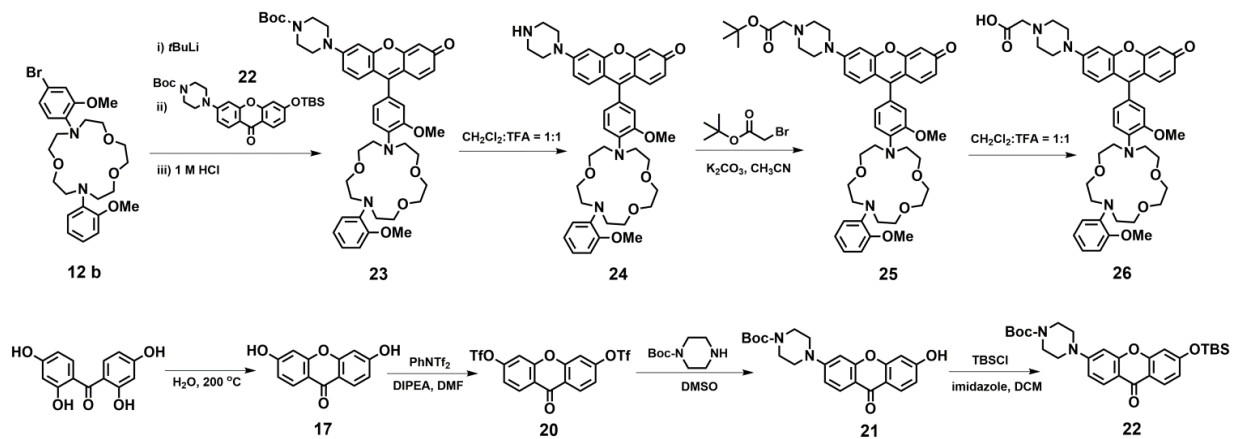
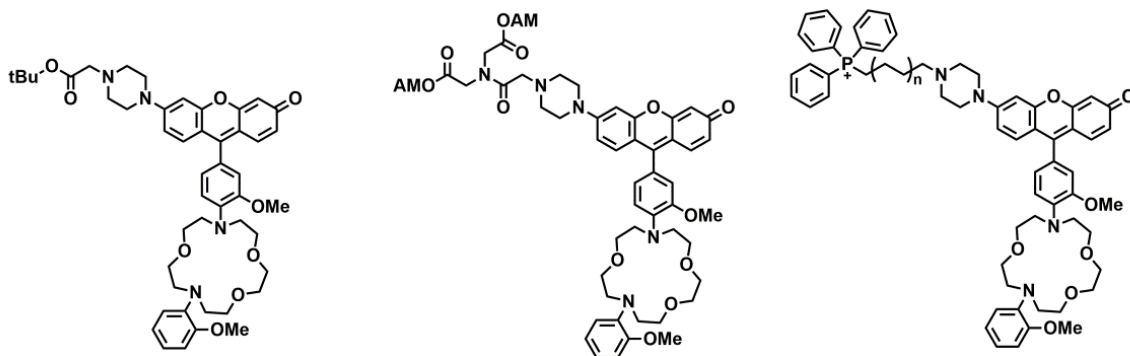


**Figure 5.5.** Compound **19** synthesized from resorcinol condensation. 1  $\mu\text{M}$  in 10 mM MOPS pH 7.4 a) UV-visible spectrum of in the absence (red) and presence (black) of  $\text{Na}^+$  135 mM, respectively b) Fluorescent spectra with increase of the  $\text{Na}^+$  concentration up to 135 mM in total metal concentration of 135 mM ( $\text{M} = \text{K}^+$  or  $\text{Na}^+$ ) in MOPS buffer, pH 7.4.



**Scheme 5.7.** Synthesis of key intermediate, **compound 23**, from lithiation using box-protected piperazine xanthone bromo-sodium receptor



**Scheme 5.8.** Trappable fluorescent sodium sensor based on piperazine xanthene



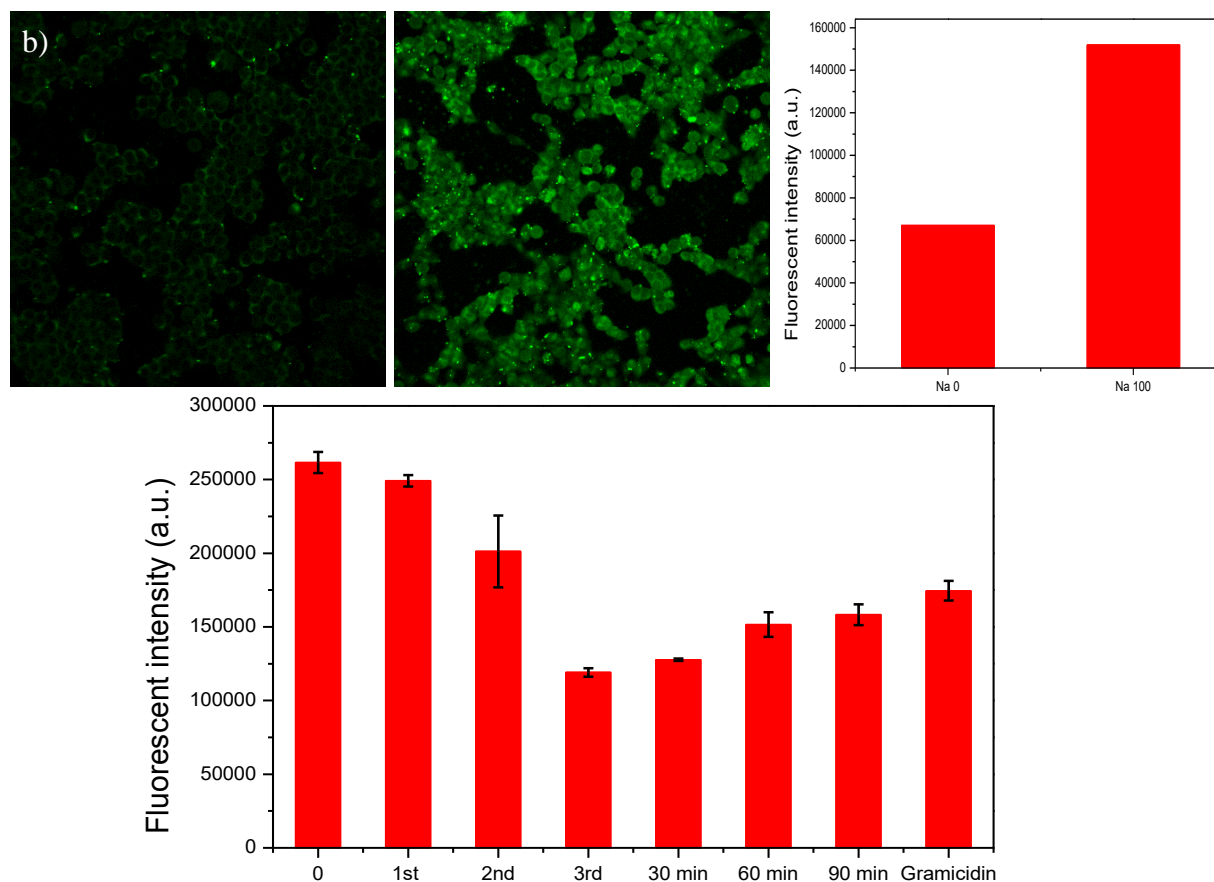
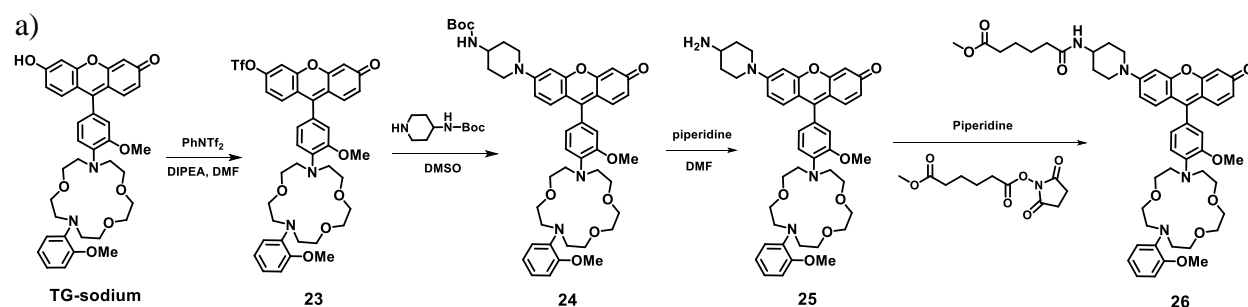


**Figure 5.6.** a) Synthetic route to make **Compound 26** from TG-sodium b) Cell images of 1  $\mu\text{M}$  compound 26 treated with  $\text{Na}^+$  0 mM and 135 mM ( $[\text{Na}^+] + [\text{K}^+] = 135 \text{ mM}$  in 10 mM MOPS pH 6.7) c) Integrated fluorescent intensity in case of treated with  $\text{Na}^+$  0 mM and upto third washing and observed fluorescent intensity upto 90 min after third washing. Fluorescent does not increased after the addition of gramicidin in  $\text{Na}^+$  0 mM condition in 10 mM MOPS pH 6.7.

## References

- (1) Rose, C. R.; Ransom, B. R. Gap Junctions Equalize Intracellular Na<sup>+</sup> Concentration in Astrocytes. *Glia* **1997**, *20* (4), 299–307.
- (2) Rose C R; Ransom B R. Regulation of Intracellular Sodium in Cultured Rat Hippocampal Neurones. *J. Physiol.* **1997**, *499* (3), 573–587.
- (3) Sodium in Health and Disease <https://www.crcpress.com/Sodium-in-Health-and-Disease/Burnier/p/book/9780849339783> (accessed Apr 28, 2018).
- (4) Murphy, E.; Eisner, D. A. Regulation of Intracellular and Mitochondrial Sodium in Health and Disease. *Circ. Res.* **2009**, *104* (3), 292–303.
- (5) Bers, D. M.; Barry, W. H.; Despa, S. Intracellular Na<sup>+</sup> Regulation in Cardiac Myocytes. *Cardiovasc. Res.* **2003**, *57* (4), 897–912.
- (6) Obach, R. S. Prediction of Human Clearance of Twenty-Nine Drugs from Hepatic Microsomal Intrinsic Clearance Data: An Examination of In Vitro Half-Life Approach and Nonspecific Binding to Microsomes. *Drug Metab. Dispos.* **1999**, *27* (11), 1350–1359.
- (7) Coleman, M. Axon Degeneration Mechanisms: Commonality amid Diversity. *Nat. Rev. Neurosci.* **2005**, *6* (11), 889–898.
- (8) Mark, R. J.; Hensley, K.; Butterfield, D. A.; Mattson, M. P. Amyloid Beta-Peptide Impairs Ion-Motive ATPase Activities: Evidence for a Role in Loss of Neuronal Ca<sup>2+</sup> Homeostasis and Cell Death. *J. Neurosci.* **1995**, *15* (9), 6239–6249.
- (9) Burdette, S. C.; Lippard, S. J. Meeting of the Minds: Metalloneurochemistry. *Proc. Natl. Acad. Sci.* **2003**, *100* (7), 3605–3610.
- (10) Goldin, A. L. Resurgence of Sodium Channel Research. *Annu. Rev. Physiol.* **2001**, *63* (1), 871–894.
- (11) Liu, Y.; Li, B.; Cheng, D.; Duan, X. Simple and Sensitive Fluorescence Sensor for Detection of Potassium Ion in the Presence of High Concentration of Sodium Ion Using berberine–G-Quadruplex Complex as Sensing Element. *Microchem. J.* **2011**, *99* (2), 503–507.
- (12) Götz, M. E.; König, G.; Riederer, P.; Youdim, M. B. H. Oxidative Stress: Free Radical Production in Neural Degeneration. *Pharmacol. Ther.* **1994**, *63* (1), 37–122.
- (13) Minta, A.; Tsien, R. Y. Fluorescent Indicators for Cytosolic Sodium. *J. Biol. Chem.* **1989**, *264* (32), 19449–19457.
- (14) Gyles, P. A.; Miller, A. Occurrence and Characteristics of Inorganic Ions and Microorganisms in Potable Water from Jamaica. *Environ. Earth Sci.* **2011**, *62* (7), 1431–1435.
- (15) Courtis, A. M.; Santos, S. A.; Guan, Y.; Hendricks, J. A.; Ghosh, B.; Szantai-Kis, D. M.; Reis, S. A.; Shah, J. V.; Mazitschek, R. Monoalkoxy BODIPYs—A Fluorophore Class for Bioimaging. *Bioconjug. Chem.* **2014**, *25* (6), 1043–1051.
- (16) Gabe, Y.; Ueno, T.; Urano, Y.; Kojima, H.; Nagano, T. Tunable Design Strategy for Fluorescence Probes Based on 4-Substituted BODIPY Chromophore: Improvement of Highly Sensitive Fluorescence Probe for Nitric Oxide. *Anal. Bioanal. Chem.* **2006**, *386* (3), 621–626.
- (17) Tahtaoui, C.; Thomas, C.; Rohmer, F.; Klotz, P.; Duportail, G.; Mély, Y.; Bonnet, D.; Hibert, M. Convenient Method To Access New 4,4-Dialkoxy- and 4,4-Diaryloxy-Diaza-S-Indacene Dyes: Synthesis and Spectroscopic Evaluation. *J. Org. Chem.* **2007**, *72* (1), 269–272.
- (18) Boens, N.; Leen, V.; Dehaen, W. Fluorescent Indicators Based on BODIPY. *Chem. Soc. Rev.* **2012**, *41* (3), 1130–1172.
- (19) Kamkaew, A.; Lim, S. H.; Lee, H. B.; Kiew, L. V.; Chung, L. Y.; Burgess, K. BODIPY Dyes in Photodynamic Therapy. *Chem. Soc. Rev.* **2012**, *42* (1), 77–88.

- (20) Pinto, M. E. S. and M. M. M. Synthesis of Xanthenes: An Overview <http://www.eurekaselect.com/61220/article> (accessed Apr 28, 2018).
- (21) Yoshida, Y.; Shimakawa, S.; Itoh, N.; Niki, E. Action of DCFH and BODIPY as a Probe for Radical Oxidation in Hydrophilic and Lipophilic Domain. *Free Radic. Res.* **2003**, *37* (8), 861–872.
- (22) Miller, E. W.; Bian, S. X.; Chang, C. J. A Fluorescent Sensor for Imaging Reversible Redox Cycles in Living Cells. *J. Am. Chem. Soc.* **2007**, *129* (12), 3458–3459.

# Appendix 1.

## **Functionalized Porous Aromatic Framework (PAFs)**

Portions of this work were performed in collaboration with the following persons:

Dr. Jun Xu in Prof. Jeffrey Reimer group in UC Berkeley measured the solid-state  $^{13}\text{C}$  NMR.  
Dr. Gokhan Barin in Prof. Jeff Long in UC Berkeley performed surface area measurement

## A1.1. Introduction

Last few decades, enormous examples are reported in inorganic–organic hybrid polymers. Porous polymer compounds with infinite structures have been intensively studied and the natural and/or artificial zeolites which have been representative for their elaborate functions such as molecular storage, recognition, separation and catalytic activity. To improve its application availability, chemist have developed porous organic–inorganic hybrids and organic frameworks, supramolecules, and oligomers with a controlled functional pore to be suitable for application such as molecular separation, clean energy storage, photoelectric materials, molecular motors, and catalysis. As another direction of artificial porous polymer, compounds with backbones constructed from metal ions as connectors and ligands as linkers has been introduced so-called coordination polymers or Metal Organic Frameworks (MOFs). ‘Coordination polymer’ was first used by Y. Shibata in 1916 and the area was first reviewed in 1964<sup>1</sup>. Since the coordination polymer has introduced, covalent organic frameworks (COFs), polymers of intrinsic microporosity (PIMs), conjugated microporous polymers (CMPs), hyper-crosslinked polymers (HCPs) In 2009, T. Ben, S. Qiu, S. Zhu groups developed a method to synthesize the first long range ordered porous aromatic framework (PAF) based on diamond-topology, PAF-1. The original idea for the synthesis of PAF-1 comes from the structure and properties of diamond, in which each carbon atom is tetrahedrally connected to four neighboring atoms by covalent bonds. Breaking the C–C covalent bond of diamond and inserting rigid phenyl rings should allow sufficient exposure of the faces and edges of phenyl rings with the expectation of increasing the internal surface areas via a nickel(0)-catalyzed Yamamoto-type Ullmann cross-coupling.<sup>2</sup> PAF-1 had a record surface area as BET = 5640 m<sup>2</sup> g<sup>-1</sup> and exceptional physicochemical stability stable in acidic and basic condition and high temperature (> 400 °C). Based on this high surface area, PAF-1 exhibited very high uptake of carbon dioxide (1.3 g g<sup>-1</sup> at 40 bar, 298 K). Besides the high uptake of carbon dioxide, the significant progress in the development of PAF has been reported, which particularly focus on the relationship between structure design, synthesis method and properties. Most PAFs do not dissolve in organic solvents and the structure is maintained in boiling water and cold acid or base solution. Based on this stability, the application of PAFs has extended to gas separation, storage, and heterogeneous catalysis. I would like to apply the porous aromatic framework (PAF) as backbone for detecting copper and iron ions selectively and efficiently.

I have developed new platforms for detecting metal ions which can be applied in living systems and environment system.<sup>3</sup> Expanding the solid-state framework to detect metal ions could lead to efficient uptake based on the advantages of high surface area, well-defined porosity<sup>2,4,5</sup>, easy processability<sup>6</sup>, and the diversity of synthetic routes for functionality<sup>2,7–11</sup>. The functional porous polymers have been reported to demonstrate efficient uptake used in heavy metal ions uptake such as mercury<sup>12</sup>, lanthanide ions<sup>13</sup>. Inspired by this examples, new platforms of functionalized PAFs would be designed to visualize copper and iron through corporation of colorimetric assay as biological and environmental application.

## A1. 2. Methods

### A1.2.1. Synthesis of functionalized PAFs

Anhydrous 1,5-cyclooctadiene (cod, 1.05 mL, 8.32 mmol, Aldrich) was added to a solution of bis(1,5-cyclooctadiene)nickel(0) (2.25 g, 8.18 mmol, Aldrich) and dried 2,2'-bipyridyl (1.28 g, 8.18 mmol, Aldrich) in distilled DMF (100 mL, Aldrich) in a dry box. The mixture was heated at

80 °C for 1 h. Tetrakis(4-bromophenyl)methane (1.00 g, 1.57 mmol) was added to the purple solution and the mixture was stirred at 80 °C overnight to obtain a deep purple suspension. After cooling to room temperature, concentrated HCl was added to the mixture. The residue was filtered with washing with warm THF (100 mL), H<sub>2</sub>O (100 mL), ethanol (100 mL), and CH<sub>3</sub>Cl (100 mL) respectively, and dried in a vacuum oven at 170 °C to give PAF-1 as an off white powder. For PAF-1, % calc. for C<sub>24.5</sub>H<sub>16</sub>: C 94.80, H 5.20; observed. A pressure flask was charged with PAF-1 (0.20 g), paraformaldehyde (1.0 g), glacial AcOH (6.0 ml), H<sub>3</sub>PO<sub>4</sub> (3.0 ml), and conc. HCl (20.0 ml). The flask was sealed and heated to 90 °C for 3 days. The resulting solid was filtered and washed with H<sub>2</sub>O (500 mL), THF (100 mL), ethanol (100 mL), and CH<sub>3</sub>Cl (100 mL) to give PAF-1-CH<sub>2</sub>Cl PAF-1-CH<sub>2</sub>Cl.

Subsequently, PAF-1-CH<sub>2</sub>Cl was substituted 2-(methylthio)ethane-1-thiol (3 equiv) in ethanol at 90 °C for 3 days to produce PAF-1-SSMe.

PAF-1-CH<sub>2</sub>Cl were transferred to different ligands as different ligand under refluxing for three days. The ligand was 2-methoxyethane-1-thiol (3 equiv) with cesium carbonate (3 equiv) in ethanol, 2-(methylthio)ethan-1-ol (3 equiv) with sodium hydride (3 equiv) in toluene, methyl 3-mercaptopropanoate (3 equiv) in ethanol and this methyl 3-mercaptopropanoate was esterased using LiOH in methanol. Methyl glycinate (3 equiv) with trimethylamine (3 equiv) in ethanol and it was esterased with LiOH in methanol. Also this PAFs were further modified by adding hydroxylamine followed by 1M HCl. PAF-1-CH<sub>2</sub>Cl were substituted with hydrazinecarbothioamide (3 equiv) with trimethylamine (3 equiv) in ethanol, and hydrazine (3 equiv) in ethanol. The structures are shown in Scheme 1.2 and numbered from 1 to 9.

The ether functionalized PAFs, PAF-1-CH<sub>2</sub>Cl were substituted with series of ether<sup>14-16</sup> sodium methoxide (3 equiv) in presence of sodium hydride (3 equiv), 2-methoxyethan-1-ol (3 equiv) with sodium hydride (3 equiv), 2-(2-methoxyethoxy)ethan-1-ol (3 equiv) with sodium hydride (3 equiv) in toluene. And the solution is under reflux for 3 days. The structure of ether functionalized PAFs were shown in Scheme 1.3.

The resulting solid was collected, washed with H<sub>2</sub>O (100 mL), THF (100 mL), ethanol (100 mL), and CH<sub>3</sub>Cl (100 mL), and then dried under vacuum oven (150 °C) to produce functionalized PAFs as yellowish white powder. The functionalized PAFs were checked with FT-IR and elemental analysis of Cl and S for calculating the efficiency of functionalization.

. Elemental analysis found for PAF-1.CH<sub>2</sub>Cl, % calc. for C<sub>26.5</sub>H<sub>20</sub>Cl<sub>2</sub>: C 77.76, H 4.92, Cl 17.32; observed C 75.88, H 4.63, Cl 13.6. Dried in vacuum oven at 150 °C to produce pale yellow solid of

#### A1.2.2. Structural characterization

*Infrared spectra* were obtained on a Perkin-Elmer Spectrum 100 Optica FTIR spectrometer furnished with an attenuated total reflectance accessory.

*Carbon, hydrogen, nitrogen, and sulfur elemental analyses* were obtained from the Microanalytical Laboratory at the University of California, Berkeley. Elemental analysis for chlorine was performed at Galbraith Laboratories.

*Solid state NMR spectra* <sup>1</sup>H-<sup>13</sup>C cross-polarization (CP) spectra were collected on a 7.05 Tesla magnet at <sup>13</sup>C frequency of 75.5 MHz under 10 kHz magic-angle spinning (MAS) condition. A Chemagnetics 4 mm H/X probe and a Tecmag Discovery spectrometer were used. The Hartmann-Hahn condition for CP experiments was obtained on solid adamantane, which is also a secondary reference of <sup>13</sup>C chemical shift (the methylene signal of adamantane was set to 38.48 ppm relative to TMS). Two pulse phase modulation (TPPM) proton decoupling scheme was used.

The TPPM angle was 15 degree and the decoupling field strength was ~60 kHz. A contact time of 10 ms and a pulse delay of 4 s were used in CP experiments.

*Inductively coupled plasma-mass spectrometry (ICP-MS)* was performed on samples that had been diluted into 2% nitric acid (made freshly from concentrated nitric acid (BDH Aristar Ultra) and MilliQ water) containing 20 ppb Ga internal standard (Inorganic Ventures, Christiansburg, VA). The samples were analyzed on a ThermoFisher iCAP-Qc ICP-MS in Kinetic Energy Discrimination (KED) mode against a calibration curve of known metal concentrations (made from CMS-5, Inorganic Ventures, Christiansburg, VA).

*Conductivity measurement* The ether functionalized PAFs (20 to 200 mg) was added to salt solutions (NaCl 12 mL) and sodium uptake has been analyzed by conductivity meter (Hanna Instruments, HI-8733N). Rejection ( $R_i$ ) of the ions was calculated by;

$$R_i = (C_{ir} - C_{ip}) * 100\% / C_{ir}$$

where  $C_{ir}$  and  $C_{ip}$  represent the ion concentrations in the retentate and permeate solutions, respectively.<sup>17</sup>

### A1.2.3. Metal uptake in aqueous samples

Functionalized PAFs (2 mg) were added in different metal stock solutions in 10 mM HEPES pH = 7.0. The metal stock was prepared using ZnCl<sub>2</sub>, CuCl<sub>2</sub>, CaCl<sub>2</sub>, MgCl<sub>2</sub>, NiCl<sub>2</sub>, CoCl<sub>2</sub>, MnCl<sub>2</sub>, NH<sub>4</sub>Fe(SO<sub>4</sub>)<sub>2</sub>·12H<sub>2</sub>O, FeCl<sub>3</sub> with 1 equiv of citric acid (10 ppm each in 100 mM HEPES buffer, pH 6.7). The functionalized PAFs have been stored in metal solutions equipped with shaker for overnight at room temperature. The next day, the supernatant was filtered through a 0.45 mm membrane filter and measured ICP-MS by the filtered supernatant. The amount of metals uptake was calculated by subtracting the stock solutions with filtered supernatant.

For ether functionalized PAFs were added in different metal stock solutions in 10 mM HEPES pH = 7.0. The metal stock was prepared using NaCl or KCl make 20 g/L and dilute the stock solution to 4 g/L.

## A1.3. Result and Discussion

The parent material PAF-1 was synthesized following a procedure reported in the literature,<sup>14</sup> and chloromethylation of the phenyl rings of PAF-1<sup>16</sup> followed by treatment with different ligands afforded the final PAFs products (Scheme A1.1, 1.2 and 1.3). The first generation for the biological application purpose was copper detection based on thioether ligand. Therefore the methyl thioether was functionalized as PAF-1-SMe (Chapter 2) and the elongated linkers (2-(methylthio)ethane-1-thiol) are prepared following the same procedure. (Scheme A1.1) Elemental analysis also revealed a decrease in chlorine content from 13.6% in PAF-1-CH<sub>2</sub>Cl to 36-50% SCH<sub>3</sub> group in PAF-1-SMe and 8.52 wt% corresponding to 27% SSMe group. The PAF-1-SSMe showed comparable copper uptake with PAF-1-SMe along with metal selectivity and uptake kinetics and biological application in Wilson's disease model rodent's urine samples. Even though there are more sulfur which provides copper binding sites, the post modification efficiency is lower than that of PAF-1-SMe, therefore, the overall copper uptake does not surpass compared with PAF-1-SMe. (Figure A1.1) Even though this elongated linker did not show the better copper uptake, this examples gives us a valuable point of expanding functionalized porous aromatic frameworks.

Inspired by the fact that thioether group is solely responsible for copper uptake, other linkers have been substituted with PAF-1-CH<sub>2</sub>Cl to screen out the responsibility of the linkers and metal selectivity. The linkers have been varied by inserting oxygen or nitrogen or glycine or urea groups.

After substitution reaction with PAF-1-CH<sub>2</sub>Cl, functionalization efficiency was calculated by the elemental analysis and based on the content of sulfur, the functionalization efficiency was calculated.

Elemental analysis revealed that 4.3% in the 2-methoxyethane-1-thiol (compound 1), to 1.95% in the 2-(methylthio)ethan-1-ol (compound 2), to 1.2% in the methyl 3-mercaptopropanoate (compound 3), to 1.7% in the methyl glycinate (compound 5), to 9.8% in the hydrazinecarbothioamide (compound 8), and to 1.1% in the hydrazine (compound 9) substituted PAFs. Further modified PAFs such as esterated one and hydroxyl amine attached ones showed comparable Cl elemental analysis. Especially, hydrazinecarbothioamide showed significantly low post-modification yield.

The sulfur content in 2-(methylthio)ethan-1-ol (compound 2) was determined to be  $4.3 \pm 1.3\%$  which is 35% modification and sulfur content in the methyl 3-mercaptopropanoate (compound 3) to be 6.1% which is 65% modification via elemental analysis, providing further evidence for efficient thioether formation from the chloromethyl starting material. Infrared spectroscopy revealed the successful formation of functionalized PAFs, as evidenced by the disappearance of the peak corresponding to the C–H wagging mode of the –CH<sub>2</sub>Cl group at 1270 cm<sup>-1</sup> in PAF-1-CH<sub>2</sub>Cl (Figure A1.2 and zoom in plot is Figure A1.3). In case of low post modification such as compound 8, residual wagging band –CH<sub>2</sub>Cl group still detected. Finally, solid-state <sup>1</sup>H–<sup>13</sup>C cross-polarization magic angle spinning (CP/MAS) NMR spectroscopy (Figure 1.4) monitored distinct <sup>13</sup>C chemical shifts associated with the functionalized PAFs.

After confirming the structural integrity of functionalized PAFs, we assessed its capacity for metal capture from aqueous solution in wide range of metal levels (The metal stock was prepared using ZnCl<sub>2</sub>, CuCl<sub>2</sub>, CaCl<sub>2</sub>, MgCl<sub>2</sub>, NiCl<sub>2</sub>, CoCl<sub>2</sub>, MnCl<sub>2</sub>, NH<sub>4</sub>Fe(SO<sub>4</sub>)<sub>2</sub>·12H<sub>2</sub>O, FeCl<sub>3</sub> with 1 equiv of citric acid; the concentration of metal were 0.3 ppm, 2 ppm, and 20 ppm, Figure 1.5). Each mixture was capped and stored in a shaker at room temperature overnight, and then filtered separately through a 0.45 mm membrane filter. The filtrates were analyzed by ICP-MS to determine the remaining metal content. The amount of metal adsorbed by functionalized PAFs was calculated by subtracting the residual metal concentration from the initial metal concentration. And the compound 2 and compound 4 showed distinct iron(II) and iron(III) uptake. Especially, compound 2 showed the different uptake compared with compound 1 which has reverse opposition with oxygen and sulfur.

In case of ether functionalized PAFs, the conductivity was checked with 20 mg of PAFs. In case of PAF-1-OMe, the conductivity changed from 3.50 to 3.30 g/L and the conductivity changed from 3.50 to 3.24 g/L in case of PAF-1-OH, it changed from 3.50 to 3.02 g/L of PAF-1-methyl glycol, and changed from 3.50 to 3.30 g/L of PAF-1-glycol, changed from 3.20 to 3.16 g/L of PAF-1- 2-(2-methoxyethoxy)ethan-1-ol. All of these case did not show significant decrease in the conductivity, the amount of PAFs have been increased from 20 to 200 mg and then, in case of PAF-1-OMe and PAF-1-glycol showed noticeable decrease from 3.97 to 3.32 g/L and 3.97 to 2.39 g/L. However, at the same time, we observed pH dropped might derived from coordinated proton is exchanged with sodium.

#### A1.4. Conclusion

In conclusion, we have modified the thioether-functionalized porous aromatic framework PAF-1-SMe to ether-thioether group, carboxylic acid group, glycine, hydrazinecarbothioamide, hydrazine, urea, and thiourea group through the same procedure. Compound 2 and compound 4



revealed that metal selectivity of ether-thioether functionalized PAFs (compound 2) and carboxylic acid functionalized PAFs (compound 4) shifted from copper(II) to both iron(II) and iron(III). The application of compound 2 as environmental iron indicator in drinking water was described in the Chapter 3. In case of ether functionalized PAFs, different length of ether linkers were substituted with PAF-1-CH<sub>2</sub>Cl and those ether PAFs were further demethylated with BBr<sub>3</sub> to give alcohol groups at the end. Those ether functionalized PAFs and alcohol functionalized PAFs were applied in saline water to check its sodium uptake by conductivity change. When the dose increased up to 200 mg, it showed meaningful results around 40% uptake in case of PAF-1-glycol. However we observed this sodium uptake happened by exchanged coordinated proton, resulting in significant drop in pH. Further modification can be made by adding buffer anion ligand to take released sodium ion to resolve this pH drop phenomenon.

## Figures

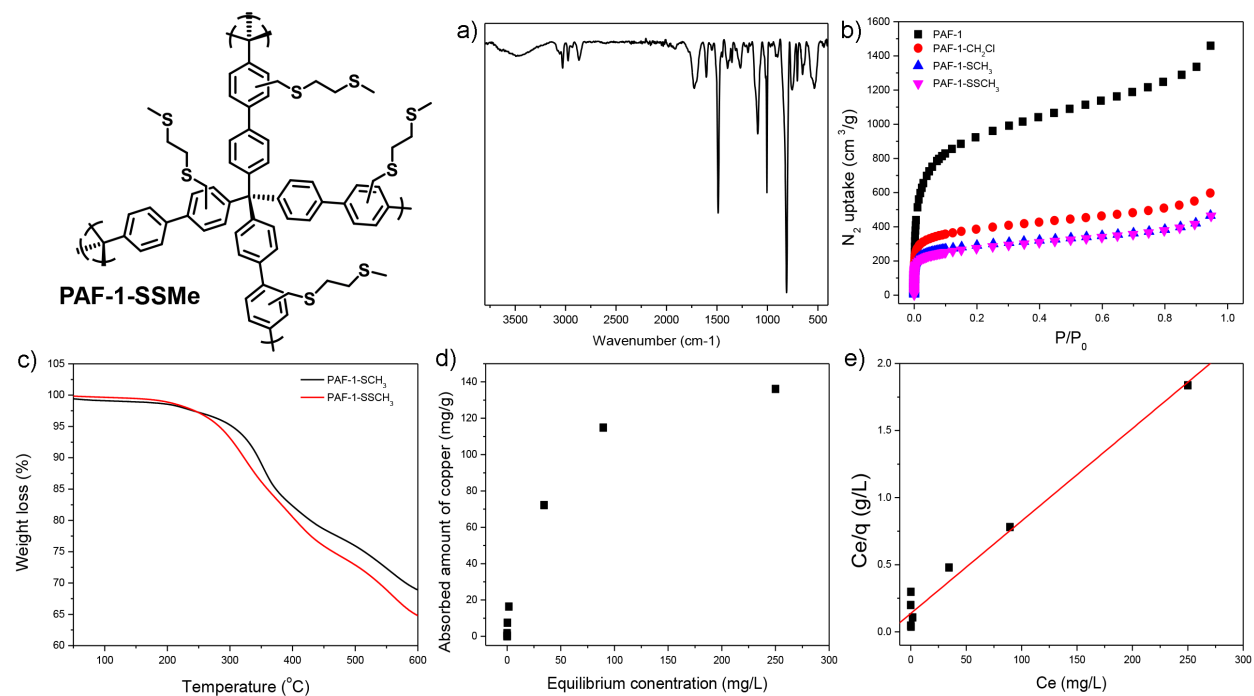


**Figure A1.** The structures of PAF-1-SSMe. a) FT-IR b) surface area measurement of PAF-1, PAF-1-CH<sub>2</sub>Cl, PAF-1-SMe, and PAF-1-SSMe. c) TGA of PAF-1-SMe and PAF-1-SSMe, d) copper absorption of PAF-1-SSMe e) the saturation uptake  $q_e$  of PAF-1-SSMe.

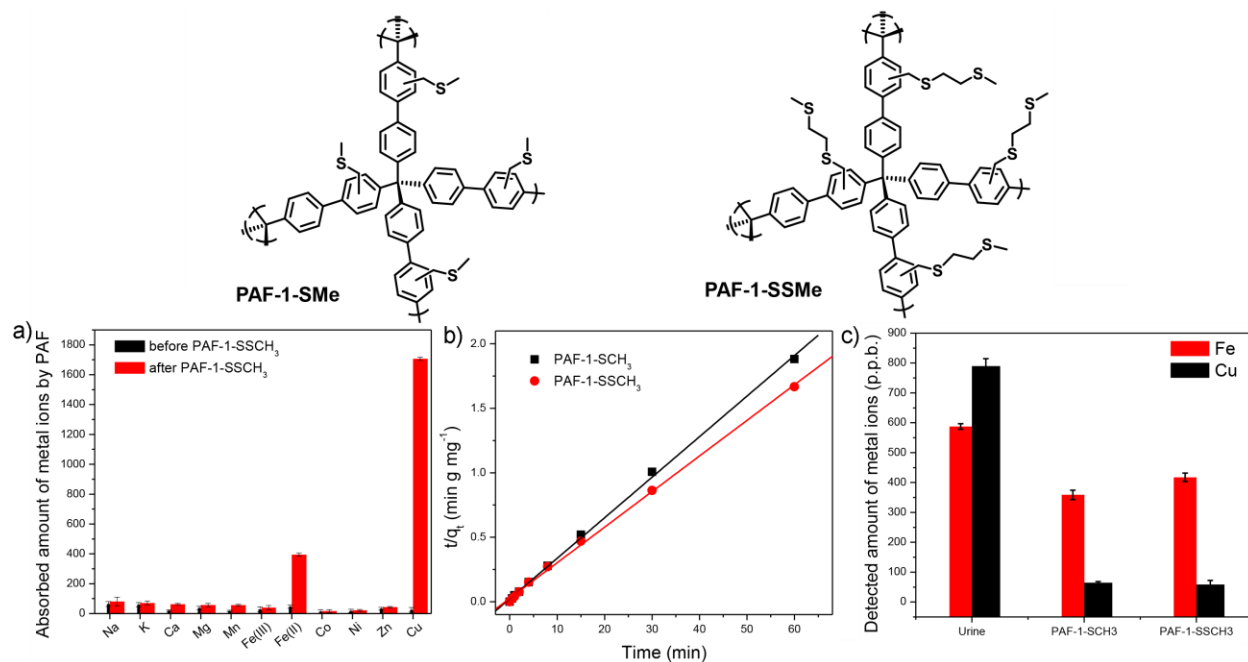
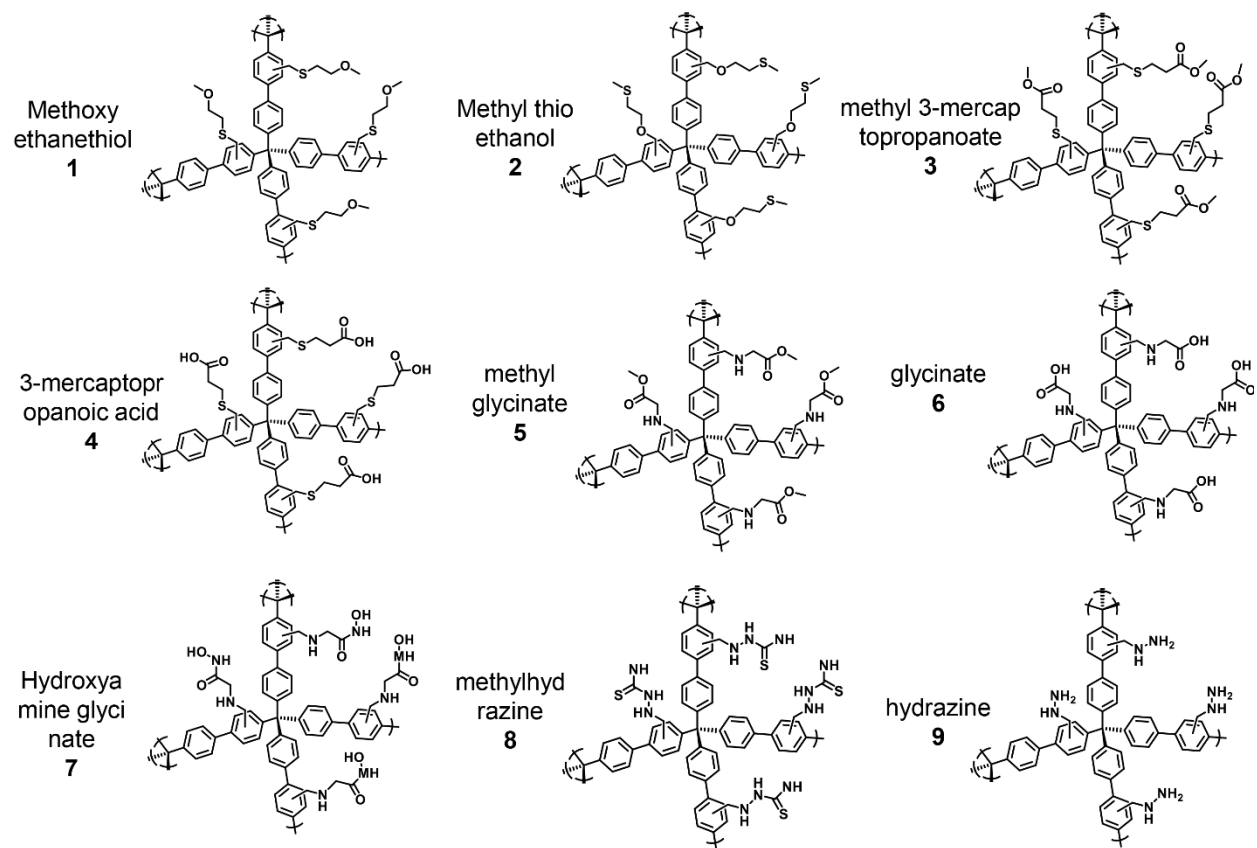
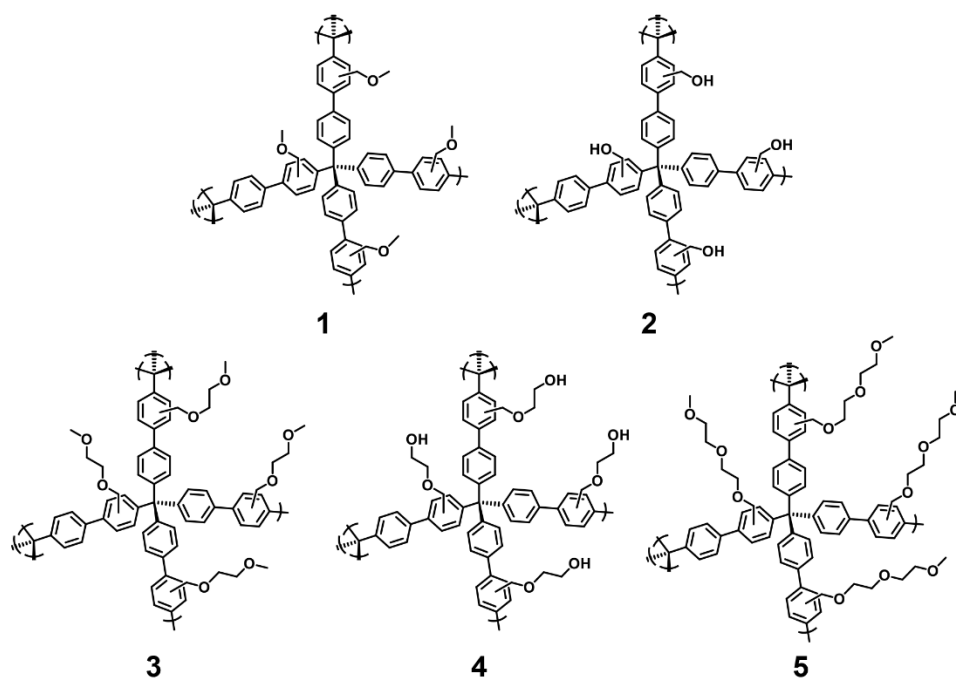


**Figure A2.** Structures of PAF-1-SMe and PAF-1-SSMe. a) metal selectivity of both PAFs showing good selectivity for copper and affinity to ferrous ions. b) Copper absorption kinetics of both PAFs which is calculated as The rate of Fe(II) of PAF-1-SCH<sub>3</sub> is calculated as 0.71 (g mg<sup>-1</sup> min<sup>-1</sup>) The rate of PAF-1-SSCH<sub>3</sub> is calculated as 0.44 (g mg<sup>-1</sup> min<sup>-1</sup>) c) Copper uptake in urine samples showing 725 ppb for PAF-1-SMe and 733 ppb for PAF-1-SSMe.



**Scheme A1.** The structures of functionalized PAFs.



**Scheme A2.** The structures of ether functionalized PAFs.

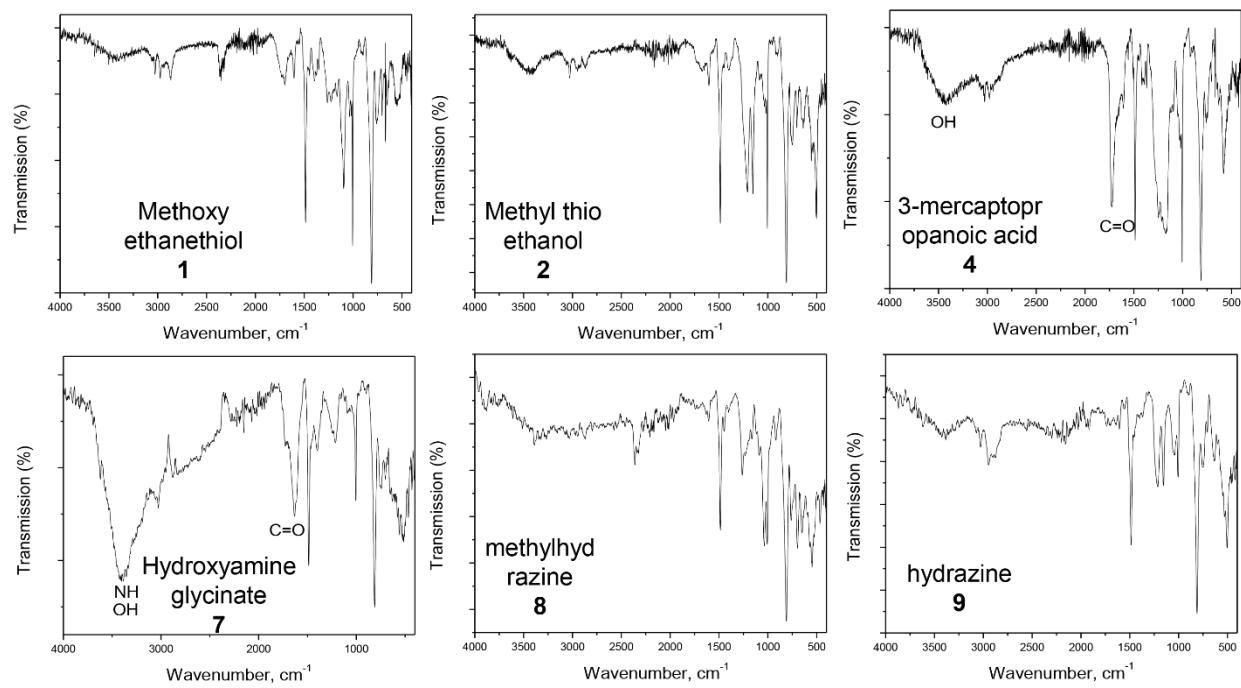


**Figure A3.** FI-IR of functionalized PAFs range from 4000 to 400  $\text{cm}^{-1}$ .

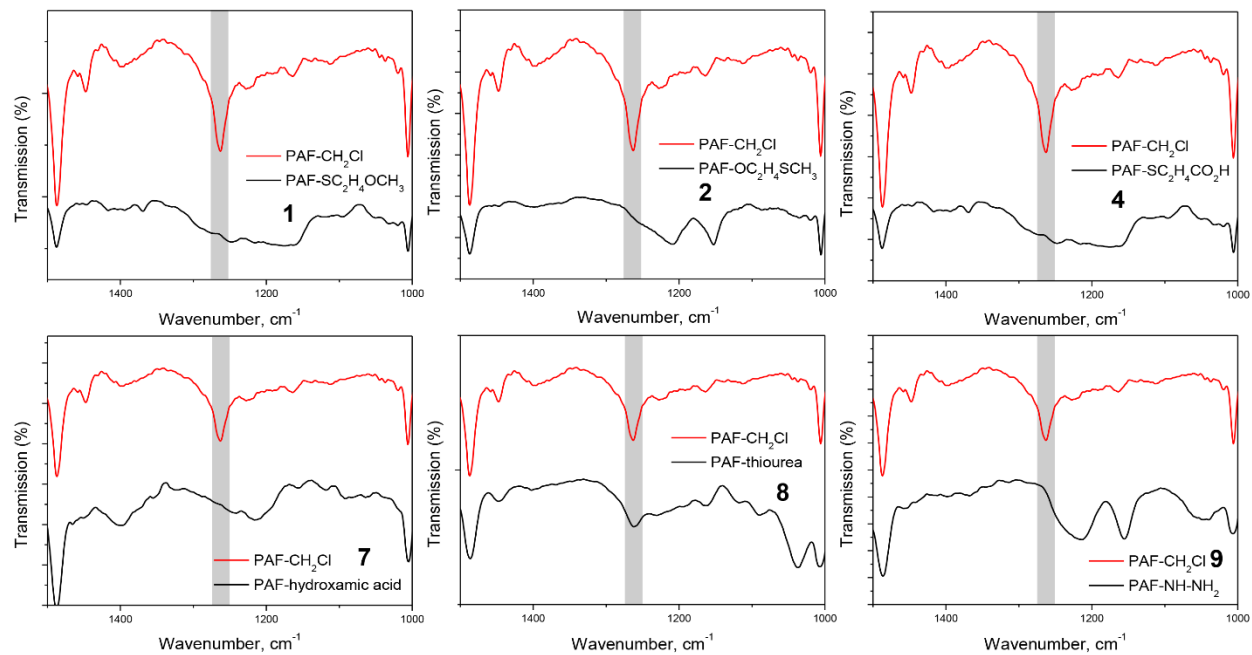


**Figure A4.** FI-IR of functionalized PAFs with comparison of PAF-1-CH<sub>2</sub>Cl range from 1500 to 1000 cm<sup>-1</sup>.

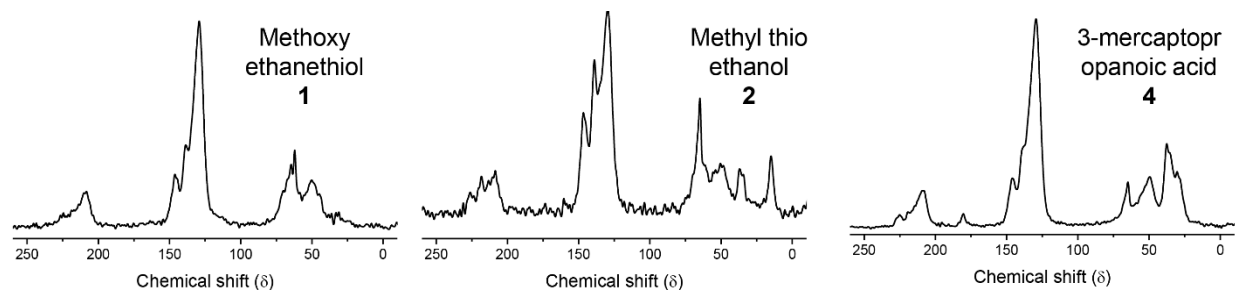


**Figure A5.**  $^{13}\text{C}$  NMR of functionalized PAFs.



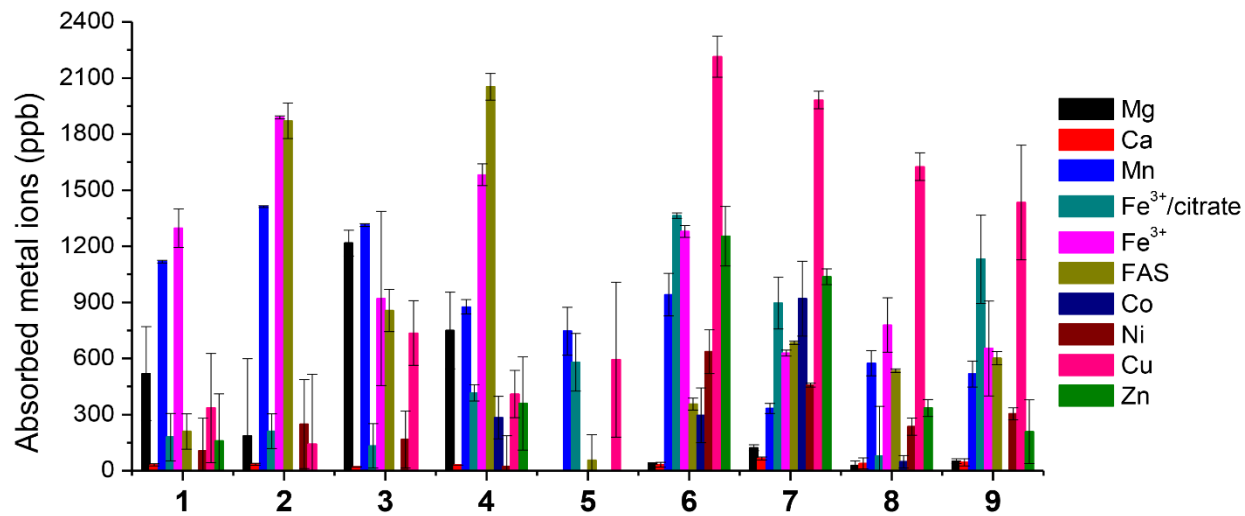


**Figure A6.** Adsorbed metal uptake of functionalized PAFs 1.5 mg in metal solution (1 ppm) in 1 mL HEPES buffer (100 mM, pH = 6.7)

#### A1.4. References

- (1) Jolly, W. L. *Preparative Inorganic Reactions*; Interscience Publishers: New York, 1964.
- (2) Ben, T.; Ren, H.; Ma, S.; Cao, D.; Lan, J.; Jing, X.; Wang, W.; Xu, J.; Deng, F.; Simmons, J. M.; et al. Targeted Synthesis of a Porous Aromatic Framework with High Stability and Exceptionally High Surface Area. *Angew. Chem. Int. Ed.* **2009**, *48* (50), 9457–9460.
- (3) Lee, S.; Barin, G.; Ackerman, C. M.; Muchenditsi, A.; Xu, J.; Reimer, J. A.; Lutsenko, S.; Long, J. R.; Chang, C. J. Copper Capture in a Thioether-Functionalized Porous Polymer Applied to the Detection of Wilson’s Disease. *J. Am. Chem. Soc.* **2016**, *138* (24), 7603–7609.
- (4) Jiang, J.-X.; Trewin, A.; Su, F.; Wood, C. D.; Niu, H.; Jones, J. T. A.; Khimyak, Y. Z.; Cooper, A. I. Microporous Poly(tri(4-Ethynylphenyl)amine) Networks: Synthesis, Properties, and Atomistic Simulation. *Macromolecules* **2009**, *42* (7), 2658–2666.
- (5) El-Kaderi, H. M.; Hunt, J. R.; Mendoza-Cortés, J. L.; Côté, A. P.; Taylor, R. E.; O’Keeffe, M.; Yaghi, O. M. Designed Synthesis of 3D Covalent Organic Frameworks. *Science* **2007**, *316* (5822), 268–272.
- (6) Budd, P. M.; Ghanem, B. S.; Makhseed, S.; McKeown, N. B.; Msayib, K. J.; Tattershall, C. E. Polymers of Intrinsic Microporosity (PIMs): Robust, Solution-Processable, Organic Nanoporous Materials. *Chem. Commun.* **2004**, *0* (2), 230–231.
- (7) Sumida, K.; Rogow, D. L.; Mason, J. A.; McDonald, T. M.; Bloch, E. D.; Herm, Z. R.; Bae, T.-H.; Long, J. R. Carbon Dioxide Capture in Metal–Organic Frameworks. *Chem. Rev.* **2012**, *112* (2), 724–781.
- (8) Ding, S.-Y.; Wang, W. Covalent Organic Frameworks (COFs): From Design to Applications. *Chem. Soc. Rev.* **2013**, *42* (2), 548–568.
- (9) Feng, X.; Ding, X.; Jiang, D. Covalent Organic Frameworks. *Chem. Soc. Rev.* **2012**, *41* (18), 6010–6022.
- (10) Zhou, H.-C. “Joe”; Kitagawa, S. Metal–Organic Frameworks (MOFs). *Chem. Soc. Rev.* **2014**, *43* (16), 5415–5418.
- (11) Ben, T.; Qiu, S. Porous Aromatic Frameworks: Synthesis, Structure and Functions. *CrystEngComm* **2012**, *15* (1), 17–26.
- (12) Li, B.; Zhang, Y.; Ma, D.; Shi, Z.; Ma, S. Mercury Nano-Trap for Effective and Efficient Removal of mercury(II) from Aqueous Solution. *Nat. Commun.* **2014**, *5*, 5537.
- (13) Demir, S.; Brune, N. K.; Van Humbeck, J. F.; Mason, J. A.; Plakhova, T. V.; Wang, S.; Tian, G.; Minasian, S. G.; Tyliszczak, T.; Yaita, T.; et al. Extraction of Lanthanide and Actinide Ions from Aqueous Mixtures Using a Carboxylic Acid-Functionalized Porous Aromatic Framework. *ACS Cent. Sci.* **2016**, *2* (4), 253–265.
- (14) King, K. A.; Spellane, P. J.; Watts, R. J. Excited-State Properties of a Triply Ortho-Metalated iridium(III) Complex. *J. Am. Chem. Soc.* **1985**, *107* (5), 1431–1432.
- (15) Harootunian, A. T.; Kao, J. P.; Eckert, B. K.; Tsien, R. Y. Fluorescence Ratio Imaging of Cytosolic Free Na<sup>+</sup> in Individual Fibroblasts and Lymphocytes. *J. Biol. Chem.* **1989**, *264* (32), 19458–19467.
- (16) Minta, A.; Tsien, R. Y. Fluorescent Indicators for Cytosolic Sodium. *J. Biol. Chem.* **1989**, *264* (32), 19449–19457.
- (17) Liu, X.; Demir, N. K.; Wu, Z.; Li, K. Highly Water-Stable Zirconium Metal–Organic Framework UiO-66 Membranes Supported on Alumina Hollow Fibers for Desalination. *J. Am. Chem. Soc.* **2015**, *137* (22), 6999–7002.

## Appendix 2

### **Modifying Electron Density of Tris(2-methylpyridine)amine (TPA)**

## A2.1. Introduction

The first Tris(2-pyridylmethyl)amine (TPA)-based copper probe was reported by Taki and Yamamoto in 2010.<sup>1</sup> Upon Cu<sup>+</sup> binding to the probe FluTPA1, oxidative C–O bond cleavage separates the TPA fragment from the fluorophore and releases the fluorescent dye with a 100-fold turn-on. FluTPA1 and its membrane-permeable FluTPA2 analogue, based on Tokyo Green,<sup>2</sup> show good selectivity to copper over other metal cations, as well as biological oxidants, including hydrogen peroxide, hypochlorite, and hydroxyl radical. FluTPA2 exhibits a notable fluorescence turn-on in HeLa cells after treatment with copper.<sup>1</sup> Based on these examples, various TPA-ligand has subsequently been used to cage 2-(2'-hydroxyphenyl) benzothiazole,<sup>3</sup> coumarin,<sup>4</sup> xanthone,<sup>5</sup> resorufin,<sup>6</sup> cyanine-quinone,<sup>7</sup> and imino-coumarin<sup>8</sup> (Figure A2.1), although only the latter three have been applied to cells. Additionally, a mitochondrially targeted reaction-based Cu<sup>+</sup> probe, RdlTPA-TPP (Figure A2.1), has been developed using the TPA ligand, circumventing the localization problem associated with this probe.<sup>9</sup> In addition, Chris Chang lab have recently utilized the TPA trigger to develop the first bioluminescent probe for Cu<sup>+</sup>, Copper Caged Luciferin-1 (CCL-1), which enables the imaging of labile copper levels in cells and living animals.<sup>10</sup>

Here, we noticed the possibility of tuning the TPA-ligand scaffold to improve turn-on kinetics and increase the signal-to-noise ratio fluorescent probes. The proposed mechanism indicated that Cu<sup>+</sup> catalyzed oxidative cleavage of the benzylic C–O bond of coumarine-TPA in the presence of O<sub>2</sub>. From ESI-MS traces, the complex between the probe with Cu<sup>+</sup> coordination with water is then oxidized by O<sub>2</sub> resulting in cleavage of the C–O bond and formation of a stabilized Cu<sup>2+</sup>–TPA complex.<sup>4</sup> Based on this proposed mechanism, the electron density of C–O bond could play an important role in between Cu<sup>+</sup> and C–O bond interaction. (Figure A2.2) To modify electron density on TPA, electron deficient groups or electron donating group would be linked to *p*-position toward pyridine. (Figure A2.2 b). Such structure-activity studies will allow Cu<sup>+</sup> coordinated to TPA moiety whether the kinetics of the formation of putative Cu<sup>2+</sup> intermediate would be affected. Maintaining TPA is important because previously TPA was replaced by pyridine, resulting in that Cu<sup>+</sup> could not effectively bind to the probe, and the C–O bond of the ether could not be broken. This control experiment revealed that the benzylic ether (C–O) linkage is cleaved only after Cu<sup>+</sup> selectivity coordinates with the tetradentate moiety of fluorescent probes.<sup>4</sup>

We would electron donating group may facilitate the Cu-induced C–O bond cleavage verse electron withdrawing group may retard the cleavage. Karlin, Zuberbühler, and coworkers found that increasing the electron donating character in such 4-pyridyl scaffolds increases the thermodynamic stability of their Cu<sup>2+</sup> complexes.<sup>11</sup> The strategy will allow us to identify what the important, rate-limiting steps are in the copper-induced receptor cleavage pathway towards developing an optimized luminescent copper probe.

## A2.2. Materials and methods

### A2.2.1 Materials and physical methods.

All reactions utilizing air- or moisture-sensitive reagents were performed in flame-dried glassware under a dry N<sub>2</sub> atmosphere. All other reagents were purchased from Aldrich, Oakwood, AK Scientific, or Fisher Scientific and used as received without further purification. Silica gel P60 (SiliCycle) and Brockmann basic aluminum oxide (Sigma-Aldrich) were used for column chromatography. <sup>1</sup>H and <sup>13</sup>C NMR spectra of new compounds were collected in either CDCl<sub>3</sub> or

CD<sub>3</sub>OD (Cambridge Isotope Laboratories) at 25 °C at the reported frequency at the College of Chemistry NMR Facility at the University of California, Berkeley unless otherwise specified. All chemical shifts were referenced to the residual solvent peak from chloroform at 7.26 ppm. Preparatory HPLC purification was performed on an Agilent 1260 Infinity HPLC with an Agilent Zorbax-Extend C18 column (particle size 5 μm, 5 mm × 250 mm) and a flow rate of 10 mL/min. UV spectra were acquired using a Cary Bio50 spectrophotometer (Varian).

#### A2.2.2. Synthesis

**Compound 1** (dimethyl 4-methoxypyridine-2,6-dicarboxylate): dimethyl 4-hydroxypyridine-2,6-dicarboxylate (0.5 g, 2.4 mmol) is dissolved in acetonitrile and K<sub>2</sub>CO<sub>3</sub> (1.5 equiv) and methyl iodide (1.5 equiv) were added into the mixture and heat upto reflux for 18 hours. After cooling to the room temperature, water was added and extracted with ethyl acetate. Purification with silica gel column with eluent (dimethyl chloride/methanol from 1% to 10%). The yield is 22%. <sup>1</sup>H NMR (CD<sub>3</sub>OD, 400 MHz): δ 7.84 (2H, s), 4.90 (6H, s), 4.03 (3H, S)

**Compound 2** (4-methoxy-2,6-bis(methoxymethyl)pyridine): Compound 1 is dissolved in methanol and NaBH<sub>4</sub> (4 equiv) was added in three portions. The product was used without further purification. <sup>1</sup>H NMR (CDCl<sub>3</sub>, 400 MHz): δ 6.96 (2H, s), 4.89 (2H, s), 4.60 (4H, S), 3.88 (3H, S)

**Compound 3** (2,6-bis(chloromethyl)-4-methoxypyridine): Compound 2 was added into SOCl<sub>2</sub> (5 mL) at 0 °C and warm up to room temperature and stir for 1 hour. Heat up the mixture to reflux for 2 hours. After cooling to the room temperature, the mixture was concentrated and sat. NaHCO<sub>3</sub> was added and filter to collect the precipitate. and extracted with ethyl acetate. Purification with silica gel column with eluent (dimethyl chloride/methanol from 1% to 10%). The yield is 56%. <sup>1</sup>H NMR (CDCl<sub>3</sub>, 400 MHz): δ 7.11 (2H, s), 4.71 (4H, s), 3.86 (3H, S), 3.33 (4H, S)

**Compound 4** (1-(6-(chloromethyl)-4-methoxypyridin-2-yl)-N,N-bis(pyridin-2-ylmethyl)methanamine) : Compound 3 (1 equiv), 2,2'-Dipyridylamine (1.1 equiv), and DIPEA (6 equiv) were added into distilled THF. The mixture was stirring at room temperature for a week. The color changed from pale yellow to dark orange and formed precipitate. After one week, collect the precipitate through filtration. <sup>1</sup>H NMR (CDCl<sub>3</sub>, 400 MHz): δ 7.45 (1H, s), 7.30 (1H, S), 7.15 (2H, d), 7.10 (2H, d), 7.01 (2H, d), 6.84 (2H, s), 4.27 (2H, d), 3.86 (6H, S), 3.81 (3H, S).

**Compound 5** (methyl 2,6-bis(hydroxymethyl)isonicotinate) : methyl isonicotinate (1 g, 7.3 mmol), ammonium persulfate (10 equiv), and Ferrous chloride tetrahydrate (0.25 equiv) were added into methanol:water (1:1 v/v) mixture. The mixture was heat up to 50 °C for 17 hour. After cooling down, the mixture was concentrated and filter the crude product which is used for the next step without purification.

**Compound 6** (methyl 2,6-bis(chloromethyl)isonicotinate) : Compound 5 (0.2 g, 1.01 mmol) was added in dry DCM. TEA (2 equiv) and methanesulfonyl chloride (2.1 equiv) were added through syringe. The mixture was heat up to reflux for 15 hours. The crude compound is purified by silica gel column using CH<sub>2</sub>Cl<sub>2</sub> and MeOH gradation from 0 to 15% of MeOH. <sup>1</sup>H NMR (CDCl<sub>3</sub>, 400 MHz): δ 8.5 (2H, s), 7.30 (1H, S), 3.69 (3H, s), 3.15 (4H, s).

**Compound 7** (methyl 2-((bis(pyridin-2-ylmethyl)amino)methyl)-6-(chloromethyl)isonicotinate) : Compound 6 (1 equiv), 2,2'-Dipyridylamine (1.1 equiv), and DIPEA (6 equiv) were added into distilled THF. The mixture was stirring at room temperature for a week. The color changed from pale yellow to dark orange and formed precipitate. After one week, collect the precipitate through filtration. <sup>1</sup>H NMR (CDCl<sub>3</sub>, 400 MHz): δ 8.35 (2H, d),

8.04-8.01 (5H, multiple), 7.98 (2H, s), 7.96 (1H, s), 7.01 (2H, d), 4.87 (2H, t), 4.48 (4H, t), 4.15 (2H, t), 3.31 (3H, S).

**Resorufin-ED** (7-((6-((bis(pyridin-2-ylmethyl)amino)methyl)-4-methoxypyridin-2-yl)methoxy)-3H-phenoxazin-3-one) : Compound 4 (1.2 equiv), resorufin (1 equiv), and  $K_2CO_3$  (1.5 equiv) were dissolve in DMF. The mixture was heat up to 90 °C for overnight. The mixture was extracted with  $H_2O$ /ethyl acetate three times. The organic layers were collected and dried with  $MgSO_4$  and purified by column chromatography (basic alumina, 10-30% methanol in DCM).  $^1H$  NMR ( $CD_3OD$ , 400 MHz):  $\delta$  8.55 (2H, d), 7.77-7.41 (6H, m), 7.28-7.07 (6H, m), 6.04 (2H, s), 4.90 (2H, s), 3.82 (3H, d), 4.15 (6H, t). LC-MS calculated for  $C_{32}H_{27}N_5O_4$  ( $M+H^+$ ), 546.2; found, 547.0.

**Resorufin-EW** (methyl 2-((bis(pyridin-2-ylmethyl)amino)methyl)-6-(((3-oxo-3H-phenoxazin-7-yl)oxy)methyl)isonicotinate) : Compound 7 (1.2 equiv), resorufin (1 equiv), and  $K_2CO_3$  (1.5 equiv) were dissolve in DMF. The mixture was heat up to 90 °C for overnight. The mixture was extracted with  $H_2O$ /ethyl acetate three times. The organic layers were collected and dried with  $MgSO_4$  and purified by column chromatography (basic alumina, 10-30% methanol in DCM).  $^1H$  NMR ( $CD_3OD$ , 400 MHz):  $\delta$  8.53 (24H, s), 7.69-7.17 (12H, m), 4.55 (2H, s), 4.28 (6H, d), 3.08 (3H, s).

### A2.3. Results and Discussion

I prepared two functionalized TPA by starting with methoxy group linked on *p*-position at of 2,6-bis(chloromethyl)pyridine as electron donating moiety or methyl ester group as electron withdrawing moiety. Two modified TPA molecules were successfully coupled with resorufin. In case of methoxy verified resorufin called as Resorufin-ED was characterized by  $^1H$  NMR and mass spectroscopy. After confirmed its structure, I checked its fluorescent behavior toward copper coordination. Resorufin-ED showed concentration dependent absorption increases checked by UV-spectroscopy, however, it showed slightly decrease fluorescenc in presence of 2 equiv of copper over 3 hours in 25 mM HEPES buffer pH 6.7 for 3 hours. (Figure A2.5) This behavior can be compared parallel with the reported fluorescent response of ResCu which is constructed with resorufin fluorophore and TPA cleavage moiety (The structure is shown in Figure A2.1).<sup>6</sup> Previous reported data showed that copper-induced cleavage of TPA caused 7-fold fluorescent turn on by adding 2 equiv of copper within 2 h. We could not figure it out why the fluorescent of Resorufin-ED showed slightly decrease in addition of  $Cu^+$  even though it was expected to show faster kinetics based on Karlin and Zuberbühler group's study about increasing the electron donating character increases the thermodynamic stability of their  $Cu^{2+}$  complexes<sup>11</sup>.

As pair of Resorufin-ED, I synthesized the Resorufin-EW, functionalized with methyl ester as electron withdrawing group, but did not fully characterize and its fluorescent behavior toward copper was not checked out. Beside of methoxy and methyl ester functionalization on TPA ligand, dimethyl amine, methyl, and trifluoromethane groups were designed, however, those synthesis was challenge so was not successful to prepare TPA groups.

### A2.4. Conclusion

Copper-mediated oxidative cleavage of TPA has been utilized in numerous fluorescent probes, showing selective cleavage toward copper. However the mechanism of this copper-induced C-O cleavage has not been clearly understood even though the presence of radical species on phenol is the crucial intermediates. To elucidate the mechanism of the copper-induced cleavage

of TPA, we attempted to vary the electron density of TPA by introducing electron donating group and electron withdrawing group on *p*-position of TPA binding pocket. Methoxy group linked TPA was successfully conjugated with resorufin to give Resorufin-ED and the probe was characterized by  $^1\text{H}$  NMR, mass, and UV-spectroscopy. However, the reaction toward copper showed slightly decreased fluorescence over 3 hr in presence of 2 equiv of  $\text{Cu}^+$ . By considering the reported resorufin-TPA fluorescent probe (ResCu) which showed about 7-fold fluorescent increase under similar condition, Resorufin-ED did not exhibit faster kinetics but slight decrease. We did not go further to make other TPA with different functional groups, however, it would be promising to check out other functional groups, especially, electron withdrawing group to compare its reaction toward copper with ResCu and Resorufin-ED.

## Figures

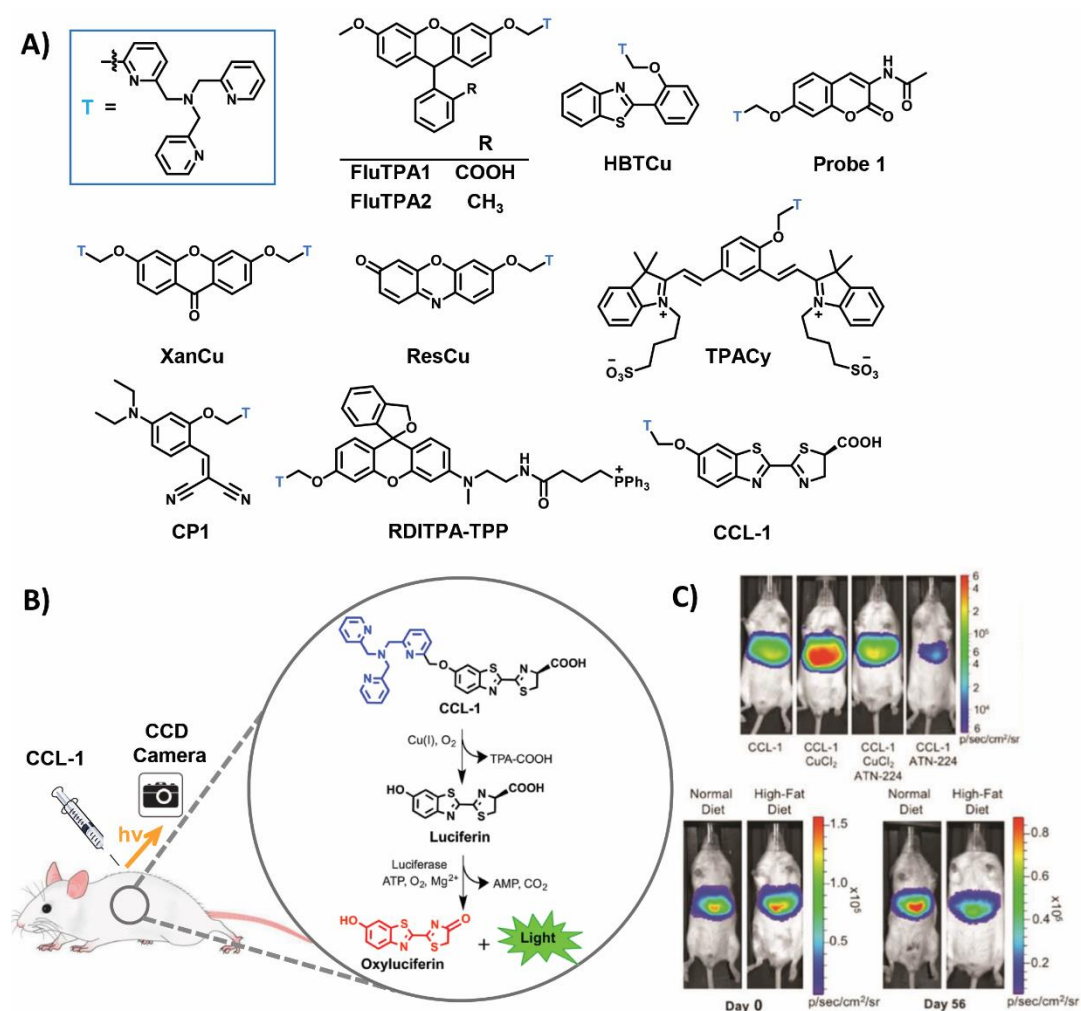


**Figure A2.1.** Structures and representative data from reaction-based indicators for  $\text{Cu}^+$ . (A) All reaction-based triggers for  $\text{Cu}^+$  are based on the TPA trigger (designated “T”, in blue). This trigger has been appended to many small molecule reporters, including fluorescein (FluTPA1), Tokyo Green (FluTPA2), cyanine-quinone (TPACy), an imino-coumarin precursor (CP1), benzothiazole (HBTCu), coumarin (Probe 1), xanthone (XanCu), resorufin (ResCu), rhodol with a mitochondrial tag (RdITPA-TPP), and, most recently, luciferin (CCL-1). (B) The use and mechanism-of-action of CCL-1 for imaging  $\text{Cu}^+$  in live animals is illustrated. (C) In mice expressing liver-specific luciferase, CCL-1 signal is observed only in the liver and is dependent on copper levels (top panel); its signal increases in response to copper supplementation with copper chloride and decreases in response to copper chelation with ATN-224, a derivative of tetrathiomolybdate. (C, Bottom panel) After 8 weeks of a high-fat diet, mice have lower CCL-1 liver signal than mice fed a control diet for 8 weeks, even though both groups of mice began the study with the same CCL-1 liver signal.



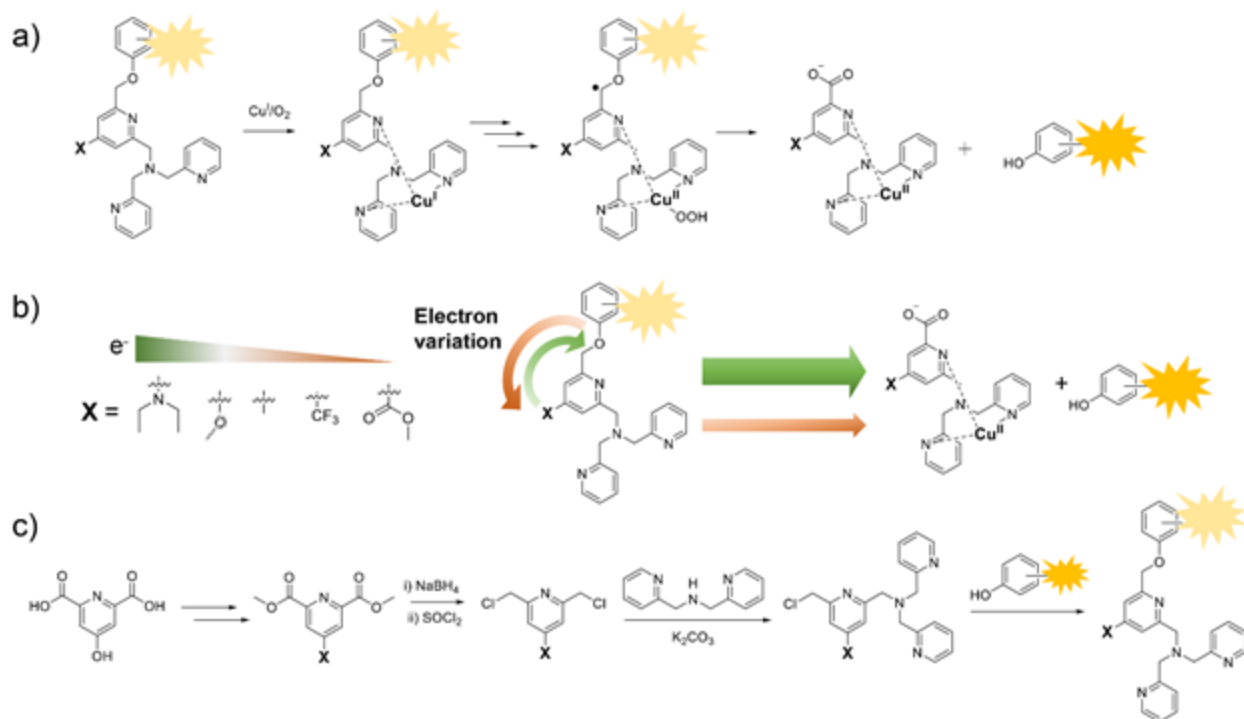


**Figure A2.2.** a) Proposed mechanism for copper-induced cleavage of the TPA moiety b) Strategies for improving cleavage kinetics by tuning tripodal ligand structure by linking electron donating groups or electron withdrawing groups c) General strategy for the synthetic scheme for electron-varied TPA

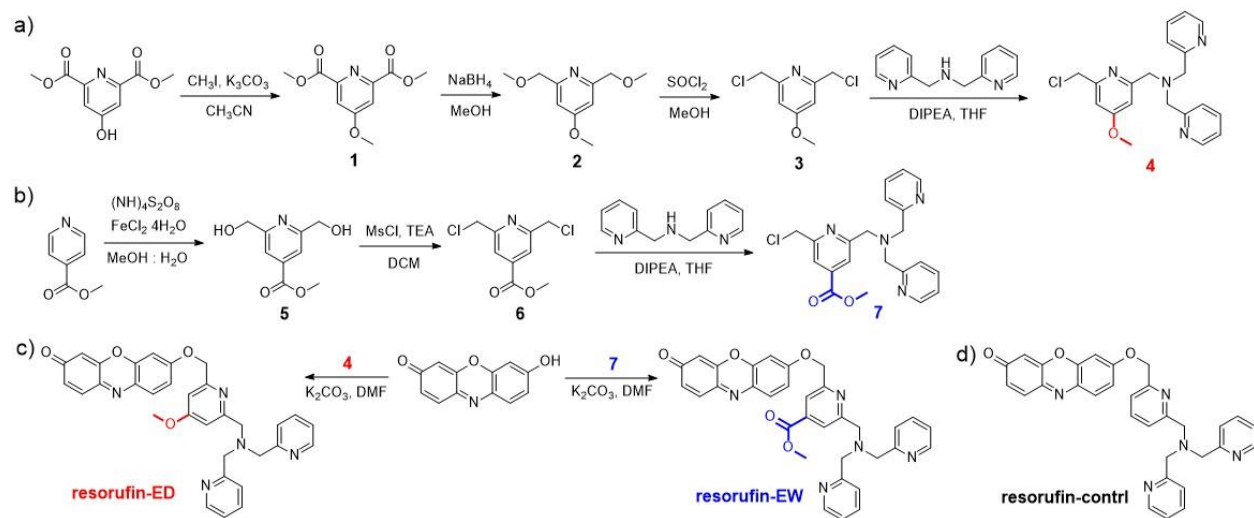


**Figure A2.3.** Schematic for a) methoxy-linked TPA b) ester-linked TPA c) Conjugation with resorufin with compound 4 and 7. For control, non-electron modified TPA was linked to give resorufin-control.

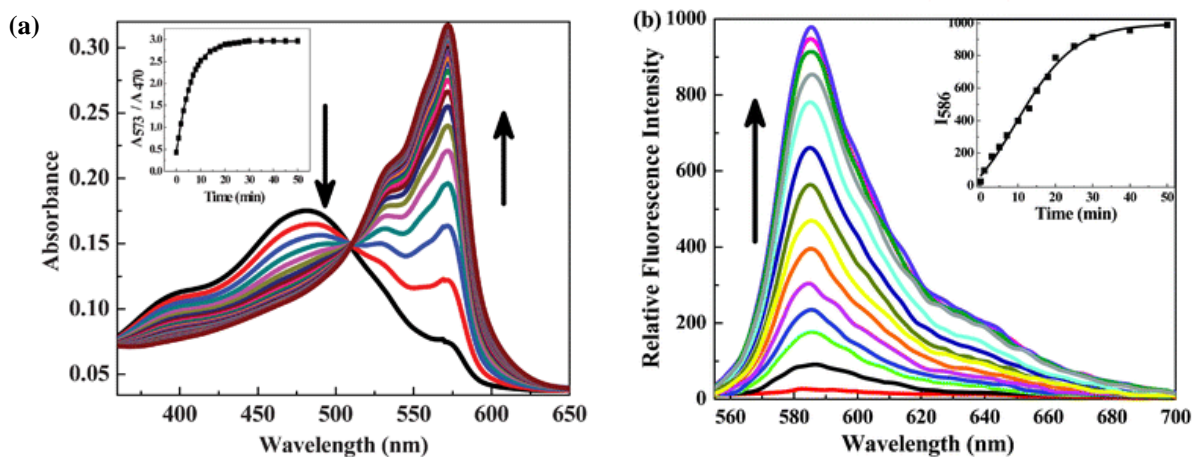


**Figure A2.4.** (a) Time dependent absorption spectra of ResCu (10.0  $\mu\text{M}$ ) after addition of 20.0  $\mu\text{M}$  of  $\text{Cu}^+$  in aqueous solution (50 mM HEPES, pH 7.2, 2 mM GSH) (isobestic point = 510 nm). fluorometer data. (b) ResCu (1.0 mM) after addition of 20.0 mM of  $\text{Cu}^+$  in aqueous solution (50 mM HEPES, pH 7.2, 2 mM GSH) ( $\lambda_{\text{ex}}$  = 540 nm). *Figures are cited from RSC Adv., 2013, 3, 16788–16794*

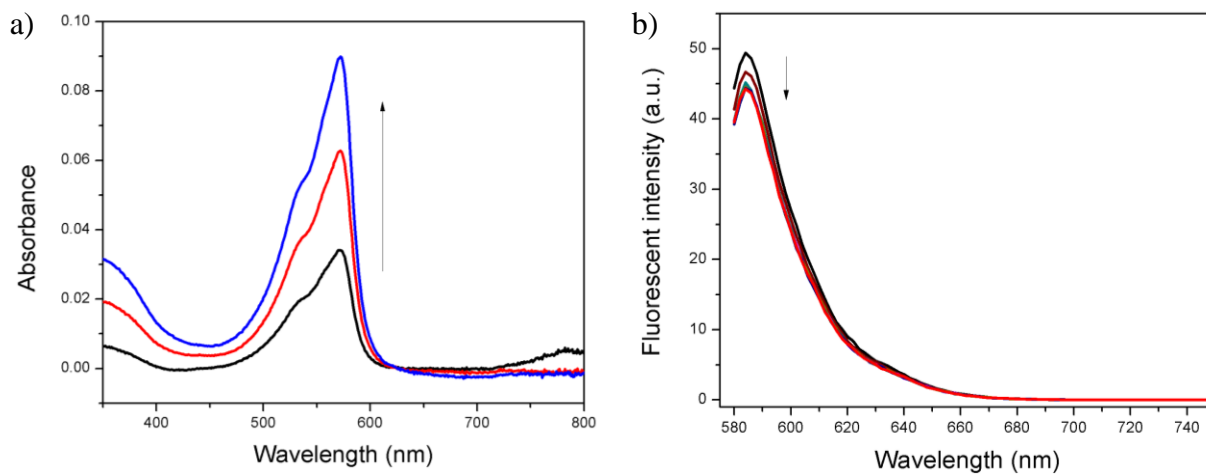


**Figure A2.5.** a) Absorption spectra of Resorufin-ED (10.0  $\mu\text{M}$  ; black, 20.0  $\mu\text{M}$  ; red, 10.0  $\mu\text{M}$  ; blue) in aqueous solution (25 mM HEPES, pH 6.7, 2 mM GSH) and fluorescent spectra b) Resorufin-ED (10  $\mu\text{M}$ ) after addition of 20.0  $\mu\text{M}$  of  $\text{Cu}^+$  in aqueous solution (25 mM HEPES, pH 7.2, 2 mM GSH) ( $\lambda_{\text{ex}} = 540 \text{ nm}$ ). Figures are cited from *RSC Adv.*, **2013**, 3, 16788–16794

## A2.5. References

1. Krishnamoorthy, L.; Cotruvo, J. A. J.; Chan, J.; Kaluarachchi, H.; Muchenditsi, A.; Pendyala, V. S.; Jia, S.; Aron, A. T.; Ackerman, C. M.; Vander Wal, M. N.; Guan, T.; Smaga, L. P.; Farhi, S. L.; New, E. J.; Lutsenko, S.; Chang, C. J., Copper regulates cyclic-AMP-dependent lipolysis. *Nat. Chem. Biol.* **2016**, *12*, 586-592.
2. Turski, M. L.; Brady, D. C.; Kim, H. J.; Kim, B.-E.; Nose, Y.; Counter, C. M.; Winge, D. R.; Thiele, D. J., A Novel Role for Copper in Ras/Mitogen-Activated Protein Kinase Signaling. *Mol Cell Biol* **2012**, *32* (7), 1284-1295.
3. Brady, D. C.; Crowe, M. S.; Turski, M. L.; Hobbs, G. A.; Yao, X.; Chaikuad, A.; Knapp, S.; Xiao, K.; Campbell, S. L.; Thiele, D. J.; Counter, C. M., Copper is required for oncogenic BRAF signalling and tumorigenesis. *Nature* **2014**, *509*, 492-496.
4. Andreini, C.; Bertini, I.; Rosato, A., Metalloproteomes: A Bioinformatic Approach. *Acc. Chem. Res.* **2009**, *42* (10), 1471-1479.
5. Cvetkovic, A.; Menon, A. L.; Thorgersen, M. P.; Scott, J. W.; Poole, F. L. I.; Jenney, F. E. J.; Lancaster, W. A.; Praissman, J. L.; Shanmukh, S.; Vaccaro, B. J.; Trauger, S. A.; Kalisiak, E.; Apon, J. V.; Siuzdak, G.; Yannone, S. M.; Tainer, J. A.; Adams, M. W. W., Microbial metalloproteomes are largely uncharacterized. *Nature* **2010**, *466*, 779-782.
6. Song, Y.; Zhang, H.; Chen, C.; Wang, G.; Zhuang, K.; Cui, J.; Shen, Z., Proteomic analysis of copper-binding proteins in excess copper-stressed rice roots by immobilized metal affinity chromatography and two-dimensional electrophoresis. *BioMetals* **2014**, *27*, 265-276.
7. Pace, N. J.; Weerapana, E., A Competitive Chemical-Proteomic Platform to Identify Zinc-Binding Cysteines. *ACS Chem. Biol.* **2014**, *9* (1), 258-265.
8. Weerapana, E.; Wang, C.; Simon, G. M.; Richter, F.; Khare, S.; Dillon, M. B. D.; Bachovchin, D. A.; Mowen, K.; Baker, D.; Cravatt, B. F., Quantitative reactivity profiling predicts functional cysteines in proteomes. *Nature* **2010**, *468*, 790-795.
9. Lippard, S. J.; Berg, J. M., *Principles of Bioinorganic Chemistry*. University Science Books: Mill Valley, CA.; Mill Valley, CA, 1994.
10. Yatsunyk, L. A.; Rosenzweig, A. C., Cu<sup>+</sup> Binding and Transfer by the N Terminus of the Wilson Disease Protein. *J. Biol. Chem.* **2007**, *282*, 8622-8631.
11. Guan, R.; Ho, M. C.; Brenowitz, M.; Tyler, P. C.; Evans, G. B.; Almo, S. C.; Schramm, V. L., Entropy-driven binding of picomolar transition state analogue inhibitors to human 5'-methylthioadenosine phosphorylase. *Biochemistry* **2011**, *50* (47), 10408 - 10417.
12. Hecquet, L.; Bolte, J.; Demuyne, C., New Assays for Transketolase. *Bioscience, Biotechnology, and Biochemistry*, **1993**, *57*, 2174-2176.
13. Constantin, C. Catching Metalloproteins: Reactive Cysteine Profiling and Metal-targeted Photocrosslinking Probes. Master of Science, Ecole Polytechnique Federale de Lausanne, Lausanne, 2015.
14. Birringer, M. S.; Perozzo, R.; Kut, E.; Stillhart, C.; Surber, W.; Scapozza, L.; Folkers, G., High-level expression and purification of human thymidine kinase 1: quaternary structure, stability, and kinetics. *Protein Expr Purif* **2006**, *47* (2), 506-515.
15. Ackerman, C. M. Detecting, Measuring and Manipulating Copper in Biological Systems. University of California at Berkeley, Berkeley, CA, 2017.
16. Doñate, F.; Juarez, J. C.; Burnett, M. E.; Manuia, M. M.; Guan, X.; Shaw, D. E.; Smith, E. L. P.; Timucin, C.; Braunstein, M. J.; Batuman, O. A.; Mazar, A. P., Identification of

biomarkers for the antiangiogenic and antitumour activity of the superoxide dismutase 1 (SOD1) inhibitor tetrathiomolybdate (ATN-224). *Br J Cancer* **2008**, *98*, 776 - 783.

## Appendix 3

### **Identifying Active Methionine under Oxidative Stress**

The procedure of protein labeling was developed by Dr. Shixian Lin

### A3.1. Introduction

Methods to label amino acid have been focused on electrophilic reagents which convert methionine to sulfonium salts at low pH. Methionine is the most hydrophobic amino acid and the second rarest amino acid, and the majority of methionine residues are found within interior protein cores. The surface-accessible methionines are limited but this methionines offer a potentially valuable handle for highly selective protein modification. In addition, post-translational modifications of methionine, including by oxidation and/or metal binding, are emerging as critical nodes in signaling pathways that control important biological signaling and pathways. For example, reversible oxidation of specific methionine residues within actin can control its assembly and disassembly to serve as a navigational signal, and the antioxidant function of methionine sulfoxide reductase has been linked to regulation of life span. In addition, recent work suggests that methionine oxidation can also increase binding interactions with aromatic residues within proteins. A major chemical challenge in developing a selective methionine modification reaction under pH-neutral physiological conditions is its relatively weak nucleophilicity, which precludes the traditional approach of identifying an appropriate methionine-specific electrophilic partner for its acid-base bioconjugation in the presence of competing, more nucleophilic amino acids such as cysteine, lysine, tyrosine, or serine. As such, we sought to pursue redox reactivity as an alternative strategy for methionine ligation and now report a method, termed redox-activated chemical tagging, that enables chemoselective methionine bioconjugation in proteins and proteomes.

Inspired by observations of facile autoxidation of methionine residues to methionine sulfoxides during mass spectrometry analyses, an oxidative sulfur imidation reaction might serve as an attractive starting point for the ReACT strategy, owing to the flexibility of introducing various functionalities on the nitrogen pendant. Chris Chang group initiated the study by screening a variety of sulfur imidation reactions with methionine derivative S1 as a model substrate in 1:1 CD<sub>3</sub>OD/D<sub>2</sub>O solvent using proton nuclear magnetic resonance (<sup>1</sup>H NMR) analysis of substrate conversion and reaction selectivity between the desired N-transfer product (NTP, sulfimide) and unwanted O-transfer product (OTP, sulfoxide) (Figure. A1 B). Surveys of various transition metal-catalyzed sulfur imidation reactions were unfruitful, resulting in either no conversion or formation of sulfoxide as the only product. However, a strain-driven sulfur imidation of methionine using oxaziridine 1 (Ox1) as the sulfur imidation reagent afforded 95% conversion of S1 within 2.5 min without additional catalyst with a NTP:OTP ratio of 5:1 (Figure. A1 B). On the basis of previous reports that oxaziridines substituted with an electron-withdrawing group (EWG) favored formation of the OTP (30), a carbamate substituted with a weak EWG was initially examined (Figure. A1C). From this starting point, altering the linkage of the probe from carbamate to a weaker electron withdrawing urea (Ox2) resulted in enhanced selectivity (NTP:OTP = 12:1) with comparable conversion. Further attempts to tune electronic effects by substitution of the benzylic hydrogen of Ox2 with an electron withdrawing CF<sub>3</sub> group (Ox3) resulted in much lower selectivity (NTP:OTP = 2:1) and reaction conversion (58%), likely as a result of increased steric hindrance. We observed a marked improvement in NTP:OTP selectivity from 6:1 to 18:1 by increasing the percentage of water in the solvent medium from 0 to 95% (Figure. A1 B). In accord with previously posited hypotheses, this improvement likely results from increased stabilization of the transition state leading to intermediate A, which should be improved by solvation and hydrogen bonding to the developing alkoxy anion (Fig. A1 C). Together, these data presage the utility of this ligation reaction in biological environments.



Cysteine is also a major ligand for copper in cells,<sup>9</sup> so we believed that an isoTOP-ABPP approach would allow us to identify novel cuproproteins in the human proteome. While free cysteine residues are nucleophilic, we hypothesized that copper-cysteine complexation would diminish cysteine nucleophilicity. A decrease in nucleophilicity should minimize interaction with a cysteine-reactive, alkyne-containing probe, resulting in decreased labeling. Subsequent Click chemistry can be used to append a fluorophore for in-gel fluorescence visualization on an SDS-PAGE gel or a cleavable biotin tag for identification by mass spectrometry analysis, which can be used to elucidate Cu-binding cysteine residues. As such, mass spectrometry data can be read out as a ratio of light- to heavy- labeled peptide to generate a list of potential copper-binding proteins. This chapter details our efforts towards using this strategy to profile the copper-binding proteome. The optimization of cellular treatments and efforts towards validation of potential targets are described herein.

## **A3.2. Materials and methods**

### *A3.3.1. Preparation of human cell line proteome*

Cells were maintained by the UC Berkeley Tissue Culture Facility. HEK 293T cells were maintained as a monolayer in exponential growth at 37 °C in a 5% CO<sub>2</sub> atmosphere in Dulbecco's Modified Eagle Medium (DMEM, Gibco) supplemented with 10% fetal bovine serum (FBS, Hyclone), and glutamax (Gibco). One day before harvesting, HEK 293T cells were passaged and plated in DMEM.

### *A3.4.2. Procedures for click reactions.*

Oxaziridine labeled protein or proteome samples carrying alkyne handles at the concentration 1 mg/mL in PBS were labeled with the CuAAC reaction. The reactions were performed by addition of 1 mM CuSO<sub>4</sub> (100x stock in water), 100 μM Tris(benzyltriazolylmethyl)amine (TBTA, 100x stock in DMSO), 100 μM azide-PEG3-biotin or azide-Cy3 (100x stock in DMSO, Click Chemistry Tools) and 2 mM sodium ascorbate (100x stock in water). The reactions were then agitated for 1 hour at room temperature before quenching with 5 mM disodium bathocuproine disulfonate (BCS, 100x stock in water). Protein samples carrying azide handles at the concentration 1 mg/mL in PBS were labeled with dibenzocyclooctyne (DBCO) containing compounds using copper-free click reaction. The reactions were performed by addition of 2-10 equivalents of DBCO-Biotin, DBCO-Cy3, DBCOPEG-10kDa or DBCO-MMAE and reacted for 8 hour at room temperature before quenching by protein desalting.

### *A3.5.3. Reactive methionine profiling*

HeLa cell lysates at the concentration 1 mg/mL in RIPA buffer (1 mL each) were labeled with 10 μM (low dose, 200x stock in DMF), 50 μM (medium dose, 200x stock in DMF) or 250 μM (high dose, 200x stock in DMF) Ox4 probe. The rationales behind these chosen concentrations is: the reaction was close to be saturated with 250 μM probe by In-gel fluorescent imaging assay (Fig. S12). So we chose 250 μM as high dose group; previous literature applied 10 μM probe for the hyper-reactive cysteine profiling. So we used 10 μM probe as our low dose group. The ReACT labeling reactions were performed at room temperature for 10 min and quenched by desalting twice to remove free oxaziridine probes. The CuAAC reactions were performed on the labeled protein with aforementioned method using 200 μM acid-cleavable biotin azide probe (200x stock in

DMSO).(40, 41) Samples were precipitated and washed with 7 cold methanol and dissolved in 250  $\mu$ L of 2% SDS/PBS. The solutions were diluted to 5 mL with 1% triton X-100/PBS. The solutions were then added with 2 mg of streptavidin-coated magnetic beads (Promega Corporation) overnight at 4 °C with agitation. The magnetic beads were washed with 1% triton X-100/PBS (5 mL), PBS (5 mL), 6 M urea (5 mL) and PBS (5 mL). The washed beads were then reduced with 5 mM TCEP at 65 °C for 15 min and alkylated with 10 mM iodoacetamide (IAA) at 37 °C for 30 min. On-beads trypsin (2  $\mu$ g each sample) digestion were performed at 37 °C for 16 hour. The beads were then pelleted and washed with PBS (2 x 2mL), water (2 x 2mL). Modified peptides on the magnetic beads were cleaved using 1% formic acid/water (2 x 500  $\mu$ L) at room temperature for 30 min and subsequently cleaved with 1% formic acid + 50% acetonitrile/water (2 x 500  $\mu$ L) with agitation for 30 min. The eluents were combined and concentrated with a vacuum concentrator. Peptide samples were desalted by Pierce™ C18 Spin Columns (Thermo Fisher Scientific) and kept at – 20 °C until analysis.

#### A3.6.4. *Synthesis of Ox2*

N-ethyl-3-phenyl-1,2-oxaziridine-2-carboxamide (Ox2) To a solution of benzaldehyde (1.21 mL, 12 mmol) and urea (880 mg, 10 mmol) in THF (20 mL) was added Ti(OiPr)<sub>4</sub> (3.2 mL, 11 mL) at r.t. After stirring overnight, the mixture was concentrated under vacuum to afford a residue. To a mixture solution of satd. K<sub>2</sub>CO<sub>3</sub> (30 mL) and DCM (30 mL) was added metachloroperoxybenzoic acid (mCPBA, 6.9 g, 76% purity, 30 mmol) at r.t. After stirring for 10 min, a solution of the above residue in DCM (30 mL) was added slowly into the mixture at r.t. After stirring for another 6 h, water (100 mL) was added and the mixture was extracted with DCM for three times. The combined organic layer was then washed with brine, dried over Na<sub>2</sub>SO<sub>4</sub>, filtered and concentrated under vacuum to give a residue, which was purified by column chromatography (DCM/Et<sub>2</sub>O, 100 : 1) to afford the Ox2 as a white solid (802 mg, 42%). <sup>1</sup>H NMR (400 MHz, CDCl<sub>3</sub>)  $\delta$  7.52 – 7.37 (m, 5H), 6.14 (brs, 1H), 4.99 (s, 1H), 3.40 – 3.23 (m, 2H), 1.19 (t, J = 7.3 Hz, 3H). <sup>13</sup>C NMR (101 MHz, CDCl<sub>3</sub>)  $\delta$  162.23, 132.48, 131.06, 128.69, 128.03, 79.42, 35.45, 14.79. (Figure S16) m/z HRMS (ESI) found [M+H]<sup>+</sup> 193.0972, C<sub>10</sub>H<sub>13</sub>O<sub>2</sub>N<sub>2</sub> + requires 193.0972.

#### A3.7.5. *Protocol for gel analysis*

We then evaluated ReACT as a method for site-selective methionine conjugation of proteins. Starting with bovine serum albumin (BSA) as a model protein using a two-step labeling protocol, BSA at a concentration of 15  $\mu$ M was first treated with 100  $\mu$ M oxaziridine probe Ox4 bearing a bioorthogonal alkyne group and then subsequently coupled to Cy3-azide through a copper-catalyzed azide-alkyne cycloaddition (CuAAC) reaction. The resulting redox conjugation yield to BSA was analyzed by in-gel fluorescence imaging. ReACT proceeds rapidly and can be completed with a yield > 95% within 1 to 2 min, with 50% of labeling occurring within the first 5 s after the addition of Ox4 to the protein under standard reaction conditions (Figure. A3.3). Moreover, the measured second-order rate constant for reaction of methionine (at 5- to 40-fold excess) with Ox2 in phosphate-buffered saline is  $18.0 \pm 0.6 \text{ M}^{-1} \text{ s}^{-1}$ , which is comparable to what is observed for the CuAAC reaction. We then moved on to apply ReACT to modification of calmodulin (CaM) as a model protein with redox-sensitive methionine. CaM carries nine redox-active methionine residues, and upon pretreatment with increasing concentrations of hydrogen peroxide, we observed the expected dose-dependent decrease in Ox4 labeling as these residues were oxidized from methionine to methionine sulfoxide, the latter of which is insensitive to ReACT. Only methionine residues were identified carrying the desired modification by LC-

MS/MS analysis of Ox4-labeled calmodulin, with no probe-generated conjugation modification observed on any other amino acids. The results presage the potential application of ReACT to probe redox-sensitive methionines by distinguishing them from their oxidized forms.

Initially, we turned our attention to the use of ReACT as a methionine-targeted warhead for chemoproteomics applications, owing to its high specificity and reactivity, as well as the small warhead size of the oxaziridine group (e.g., the molecular weight of Ox4 is 202 Da) that allows access to a broad range of proteins. To this end, we applied ReACT to probe reactive methionines in the proteome through tandem orthogonal proteolysis–activity–based protein profiling (TOP-ABPP). Through dose-dependent treatment of cells with low, medium, and high levels of ReACT probe Ox4 (Fig. A3.3), we sought to identify hyperreactive methionines that should be enriched with low-dose labeling along with less-reactive methionine sites. By performing parallel TOP-ABPP ( $n = 2$  for all three groups) in HeLa cell lysates, we were able to identify 116 (low dose), 458 (medium dose), and 1111 (high dose) peptides that carry the desired ReACT methionine modification (Fig. 4, A and B, and Data S2). Compilation of the hyperreactive methionine-containing target proteins identified in the low-dose ReACT-treated group spanned many protein classes, including enzymes, chaperones, and nucleoproteins, as well as many structural proteins. In general, only surface-accessible methionine residues were identified even with the high-dose probe, indicating that ReACT does not disrupt or denature proteins under these labeling conditions (Fig. A3C).

With these data in hand, we envisioned that ReACT could enable installation of various payloads onto a protein of interest at defined methionine sites, serving as a method for functionalization using naturally occurring amino acids (Fig. 2A). To this end, we evaluated the reactivity of various alkyne- and azide-containing oxaziridine probes (1 mM) with a 100- $\mu$ M CaM model protein (Fig. A2B). LC-MS/MS results showed that ReACT enabled near quantitative installation of these bioorthogonal handles on all nine native methionine residues within 10 min of labeling time at room temperature, with a 25:1 selectivity over the only other observed minor CaM product bearing eight sulfimide modifications (NTP) and one sulfoxide modification (OTP) (Fig. A2B). Further functionalizations with biotin, fluorophore, and polyethylene glycol (PEG) payloads proceeded smoothly. The high methionine reactivity and specificity of ReACT coupled with the ready availability of click reaction partners provides a straightforward method for precise protein functionalization based on this naturally occurring amino acid (Fig. A2A).

Cell lysate were prepared as 2 mg/mL and MrsA (cytosol) : 20  $\mu$ M, Trx (500  $\mu$ g) : 1 mM stock with Tris buffer (50 mM pH 7.4) TCEP: 400 mM stock with milliQ

- 1) Labeled with Ox2 (1 mM) for 1 hr
- 2) Desalting column
- 3) Reduction by MsrA (0.2  $\mu$ M), Trx (2  $\mu$ M), TCEP (20  $\mu$ M) at 37 oC for 2 hrs
- 4) Desalting
- 5) Label with Ox4 (100  $\mu$ M) for 30 min to 1 hr
- 6) Click with cy3 or biotin / TBTA/ CuSO<sub>4</sub> / Ascorbic acid for 1 hr
- 7) Stop the click by adding BCS (5 equiv)
- 8) Run protein gel

- Control showed good staining, however, H<sub>2</sub>O<sub>2</sub> (10 mM for 2 hr incubation at 37 oC) did not show same pattern staining.
- Repeated H<sub>2</sub>O<sub>2</sub> experiment but it was same
- Control protein lysate were measured 10, 20, 30 min and 1, 2, 4, 6, 12 hr time interval and 2 hr incubation showed the brightest – after 2hr it might precipitate

### **A3.8. Results and Discussion**

The surface-accessible methionines are limited but this methionines offer a potentially valuable handle for highly selective protein modification. Previously, Ox2 reagent was prepared and through protein labeling experiment, it showed that only methionine gave a ligated product. Cysteine as well as selenocysteine were oxidized to their cystine forms, with no NTP formation observed, attesting to the high selectivity of the ReACT reagent for methionine functionalization over its sulfur congener. As a further demonstration of the high selectivity of ReACT for methionine conjugation, we next identified sites of probe labeling within a whole proteome using liquid chromatography–tandem mass spectrometry (LC-MS/MS) analysis. HeLa cell lysates were treated with Ox4, trypsin digested, and then analyzed by LC-MS/MS for probe modification on all nucleophilic amino acids using the Tandem program. We observed labeling of 235 methionine residues and a single lysine residue, with no other modifications detected on cysteine side chains or other nucleophilic amino acids (Fig. 1D and Data S1). These experiments demonstrate the fast kinetics of the ReACT strategy as well as near-perfect selectivity for methionine residues from the single-protein to whole-proteome level under mild biocompatible conditions.

The lysate incubated with hydrogen peroxide will be oxidize sepcific methionine involved in oxidative stress in the cell, however non-active methionine stays intact. This non-active methionine is masked with Ox3 and then oxidized methionine is reduced using MsrA and a strong protein disulfide reducing agent such as tris(2-carboxyethyl)phosphine (TCEP) along with Trx. Once oxidized methionine is reduced to free methionine, it can be labeled with Ox2, followed by click chemistry to labeled with fluorescent probe to show the labeled band visualization or by biotin to pull down all methionine with Ox2 alkyne. In control protein lysate from HEK 293T cell, I was able to check the fluorescent from the lane treated with MsrA/TCEP/Trx but not anywhere else. The repeated experiment confirmed that active methionine involved in oxidative stress can be labeled with the strategy. Time dependent incubation of hydrogen peroxide showed that 120 min was the brightest and after 120 min, it might cause precipitation of proteins in presence of the hydrogen peroxide. However the protein lysate treated with hydrogen peroxide 2 mM or 10 mM for 1 hour at room temperature did not show the proper labeling even in the repeated experiment.

### **A3.9. Conclusion**

We attempted to label methionine which is involved in oxidative stress by using ReACT reagents. Reactive methionine can be selectively labeled with Ox2 after masking non-reactive methionine with Ox3, followed by reduction of reactive methionine with MsrA/Trx/TCEP. Free methionine reduced is finally labeled with Ox2 for click chemistry. This strategy was able to stain active methionine in non-hydrogene peroxide treated protein lysate, however, hydrogen peroxide treated lysate did not show any labeling. Increase the concentration of hydrogen peroxide did not solve the issue, further the incubation time of hydrogen peroxide also did not show the expected result neither. There are several conditions can be tried such as using different oxidation rather

than hydrogen peroxide. Also control lysate stained with Ox2 and biotin can measured with LC-MS/MS to identify what kind of protein were involved in oxidative stress.

## Figures

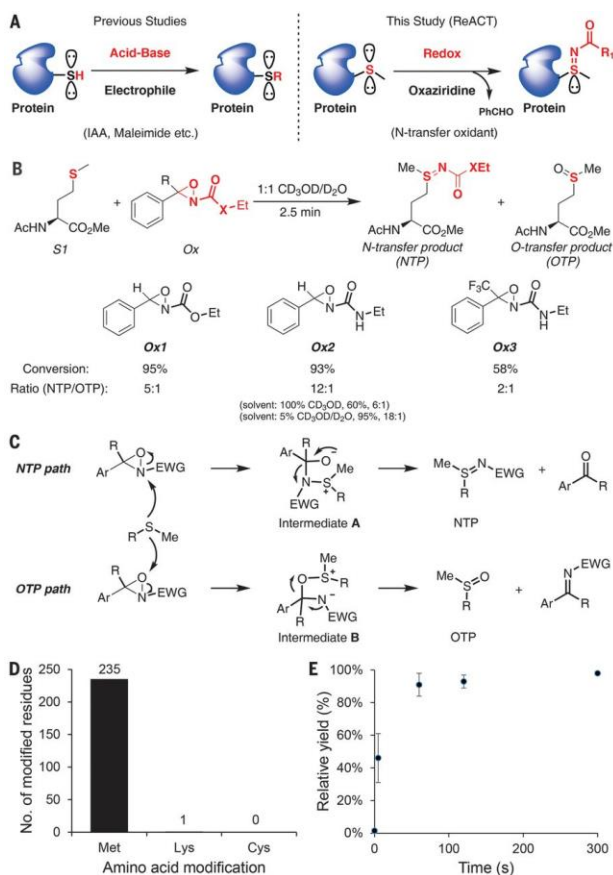


**Figure A3.1.** Fig. 1. The ReACT strategy for chemoselective methionine bioconjugation. (A) (Left) Acid-base conjugation strategies for cysteine-based protein functionalization. Iodoacetamide (IAA) and maleimide reagents are representative electrophiles for selective cysteine bioconjugation. (Right) ReACT strategies for methionine-based protein functionalization. Oxaziridine (Ox) compounds serve as oxidant-mediated reagents for direct functionalization by converting methionine to the corresponding sulfimide conjugation product. During this redox process, the Ox ReACT reagents are reduced to benzaldehyde. (B) Model redox conjugation reaction with 25 mM of N-acetyl-L-methionine methyl ester (S1) and 27.5 mM of various oxaziridine compounds as substrates in cosolvent (CD<sub>3</sub>OD/D<sub>2</sub>O = 1:1). The reactions were monitored by detecting the chemical shift of the methionine methyl group with <sup>1</sup>H NMR (fig. S1). The reaction time was 10 min in 100% CD<sub>3</sub>OD solution due to slow reaction rate and 20 min in 5% CD<sub>3</sub>OD/D<sub>2</sub>O solution due to poor solubility of substrate in aqueous solution. (C) The proposed reaction mechanism between methionine and oxaziridine compound proceeds by nucleophilic attack of sulfide at N atom or O atom of oxaziridine ring, followed by N–O bond cleavage to generate reaction intermediate A or B, respectively. The NTP or OTP is generated, along with the corresponding aldehyde or imine as side product, through an intramolecular rearrangement. (D) Number of unique ReACT-sensitive Met, Lys, and Cys residues detected in HeLa cell lysates when treated with 1 mM Ox4 for 10 min. (E) Yield of conjugation reaction was performed with 15 mM of BSA carrying four methionines per protein and 100 mM Ox4 at the indicated time point as measured by in-gel fluorescence imaging. Error bars, mean ± SD from three independent experiments. Cited from *Science* 2017, 355, 597-602.

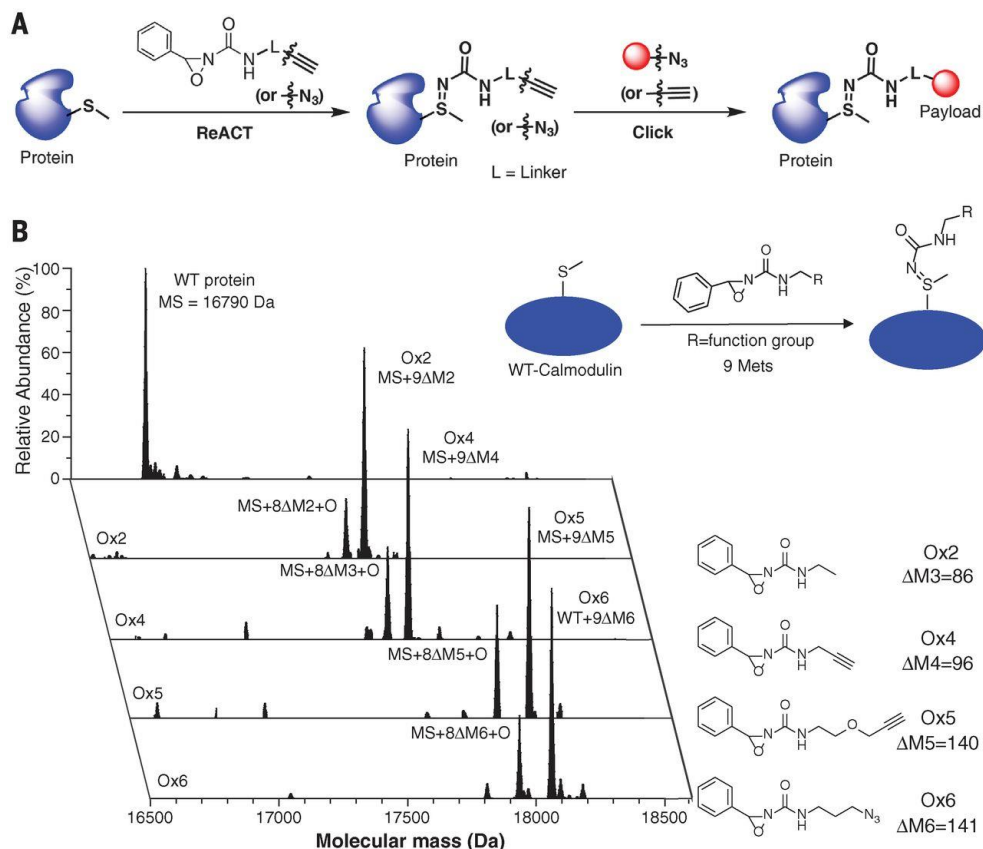


**Figure A3.2.** (A) General two-step procedure for methionine-specific protein functionalization is a combination of ReACT and click reactions. Various payloads (red sphere) can be installed through methionine conjugation at a directed position on a given protein. (B) Redox conjugation of a CaM model protein (100  $\mu\text{M}$ ) with various Ox compounds (1 mM). The chemical structures of oxaziridine probes are shown with molecular weight changes ( $\Delta M$ ) listed for the corresponding modifications. The deconvoluted MS data of full protein peaks are plotted in the same figure. The major peaks correspond to CaM protein carrying nine sulfimide modifications ( $\Delta M$ ). For Ox2-labeled protein: expected mass 17,564 Da, found 17,565 Da; Ox4-labeled protein: expected mass 17,654 Da, found 17,654 Da; Ox5-labeled protein: expected mass 18,050 Da, found 18,051 Da; Ox6-labeled protein: expected mass 18,059 Da, found 18,060 Da. The minor peaks correspond to CaM protein bearing eight sulfimide modifications ( $\Delta M$ ) and one sulfoxide modification (O). *Cited from Science 2017, 355, 597-602*

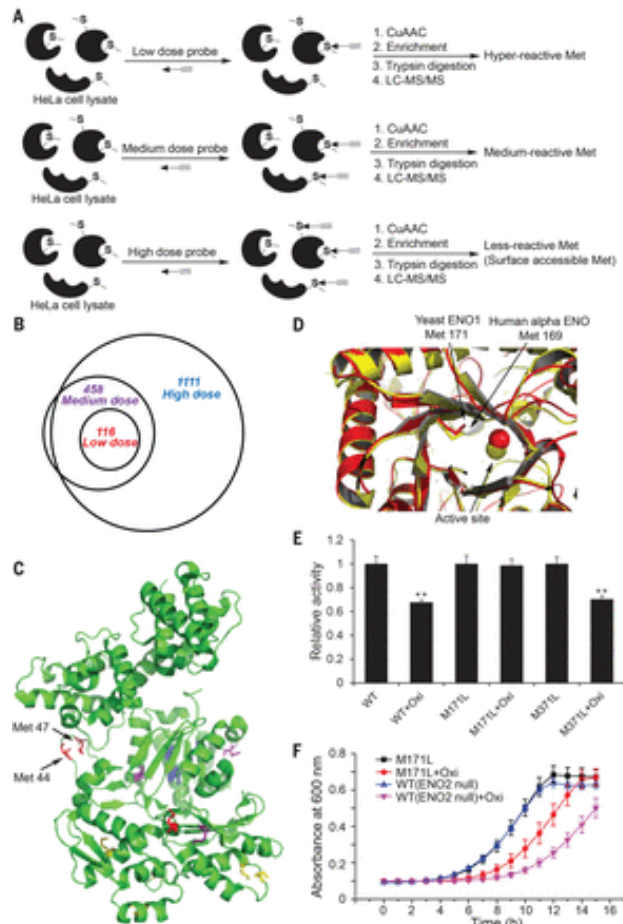


**Figure A3.3.** (A) Reactive methionine profiling with ReACT involves treatment of proteomes with low, medium, and high doses of Ox4 probe, followed by CuAAC-based installation of acid cleavable biotin-azide tag, enrichment with streptavidin magnetic beads, and sequential on-bead trypsin digestions to afford probe-labeled peptides for LC-MS/MS analysis. (B) The number of peptides carrying the desired ReACT modification on methionine and appearing in two independent runs from the low-, medium-, and high-dose groups is shown. (C) Reactive methionine map on actin (PDB 3byh), with hyperreactive methionines colored in red, including Met44 and Met47; medium-reactive methionines colored in purple; and less-reactive methionines colored in blue. The methionines colored in yellow represent residues identified by LC-MS/MS that do not carry redox modification. The domains carrying these yellow-colored methionines are involved in actin polymerization. Because of this activity, no desired modification is detected on these residues even when these are surface accessible on the protein x-ray crystal structure. (D) Protein structure alignment of human alpha enolase (yellow; PDB 2psn) and yeast enolase 1 (red; PDB 2AL1), with conserved methionine residues shown in stick representation. (E) The relative activity of yeast enolase 1 variants with or without treatment of NaClO (100  $\mu$ M). Error bars, mean  $\pm$  SD from four independent experiments. P values indicated in the figure represent results of an unpaired t test. (F) Growth curve of wild-type (WT) (ENO2 null) and ENO1-M171L (ENO2 null) strains, with or without treatment of NaClO (100  $\mu$ M). Knockout and mutation strains were generated by clustered regularly interspaced short palindromic repeats (CRISPR)–Cas9–mediated genome editing. Error bars, mean  $\pm$  SD from three independent experiments. *Cited from Science 2017, 355, 597-602*



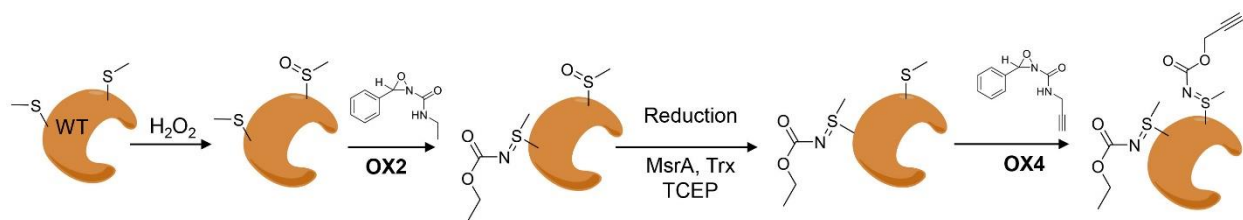


**Figure A3.4.** Work flow to label methionine involved in oxidation under hydrogen peroxide. Masking non-active methionine with ethyl oxaziridine (ethyl-Ox) and reduce oxidized methionine with MsrA/Trx/TCEP and label with ethylene oxaziridine (Ox2) for click chemistry to identify redox active methionine.

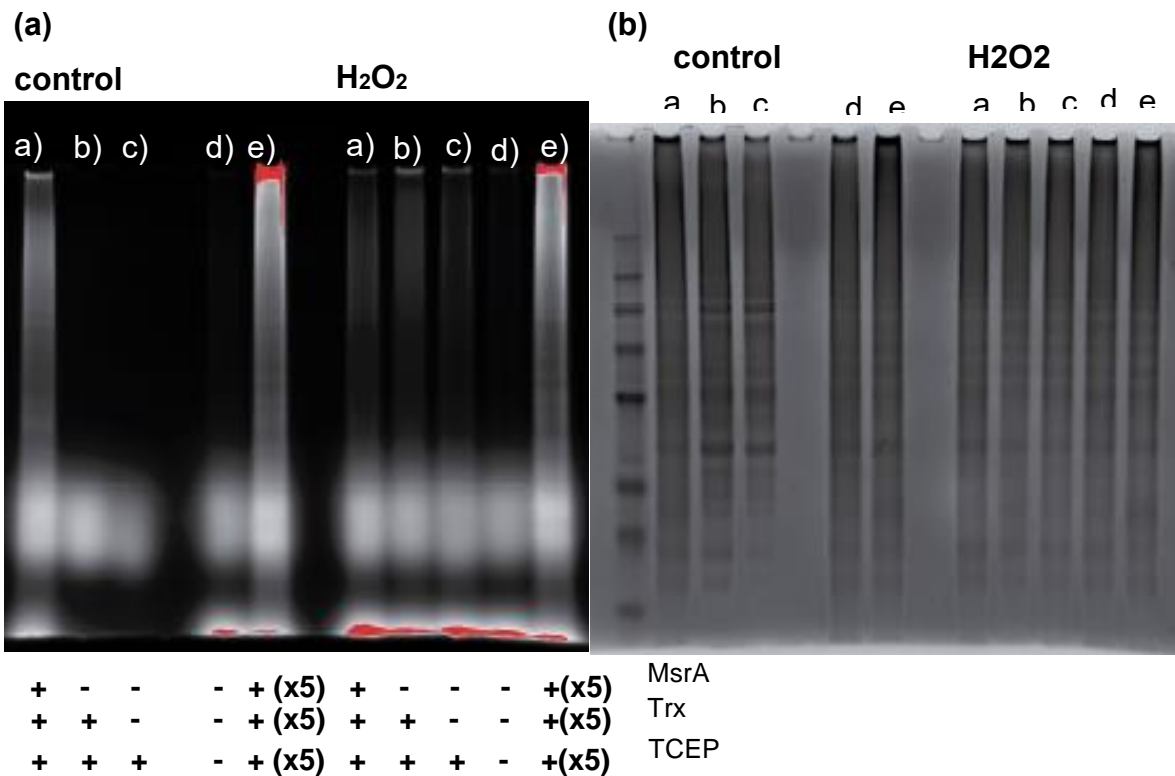


**Figure A3.5.** (a) Fluorescent labeling of HEK 293T cell lysates (1 mg/mL) treated with 2 mM H<sub>2</sub>O<sub>2</sub> for 1 hr at room temperature and non-H<sub>2</sub>O<sub>2</sub> treated cells (control). Lanes a) is incubated with MsrA/Trx/TCEP, lanes b) is without MsrA, lane c) is without Trx and TCEP, lane d) is control, and lane e) is five times of reagents of lane a) to confirm its reduction ability. (b) is coomassie staining of (a).

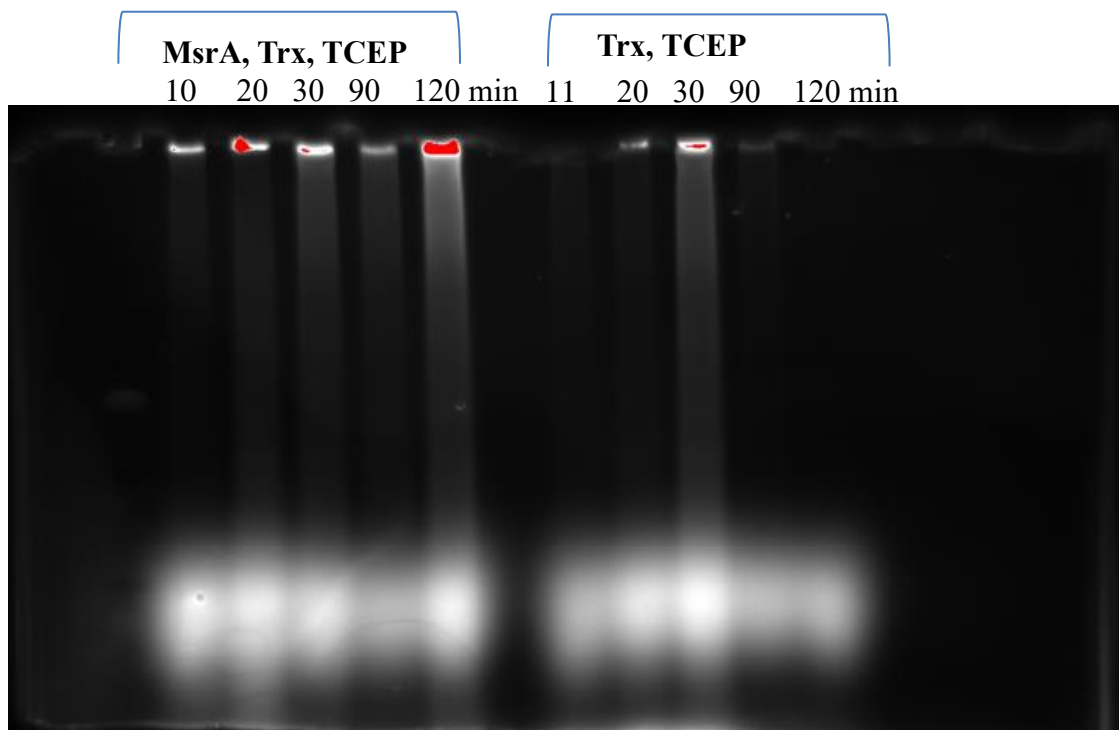


**Figure A3.5.** Time dependence of redox activity of MsrA/Trx/TCEP in non-H<sub>2</sub>O<sub>2</sub> treated HEK 293T cell lysates (1 mg/mL).

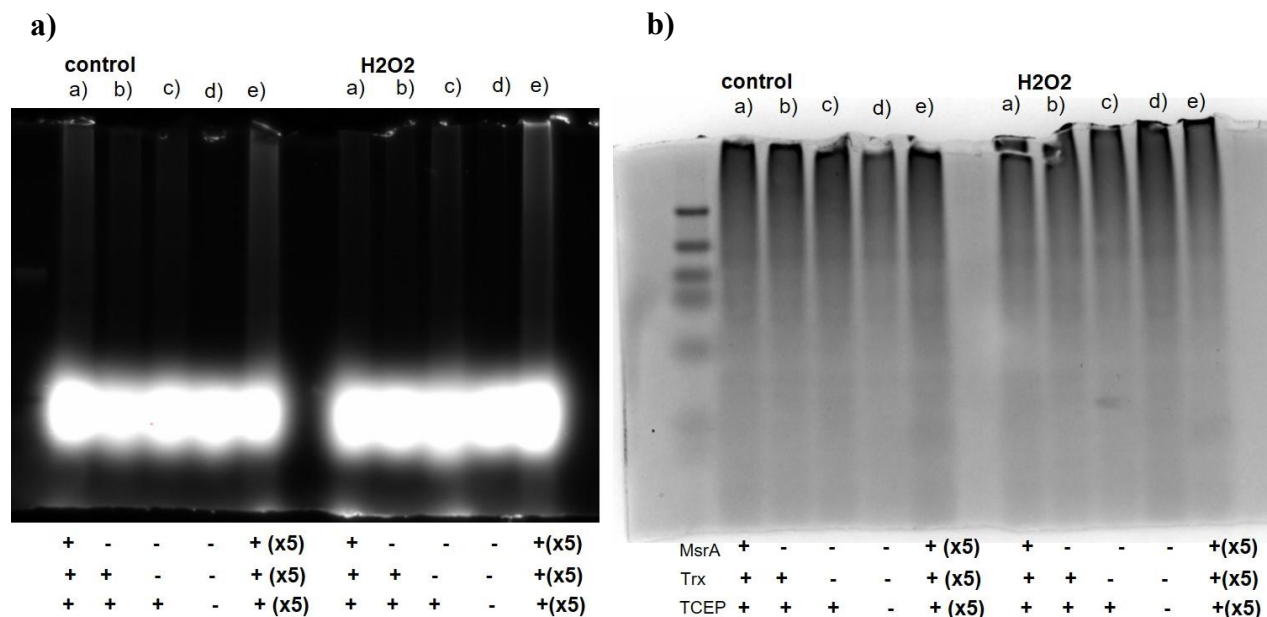


**Figure A3.6.** Repeated experiment of Figure A3.4 a) Fluorescent labeling of HEK 293T cell lysates (1 mg/mL) treated with 10 mM H<sub>2</sub>O<sub>2</sub> for 1 hr at room temperature and non-H<sub>2</sub>O<sub>2</sub> treated cells (control). Lanes a) is incubated with MsrA/Trx/TCEP, lanes b) is without MsrA, lane c) is without Trx and TECP, lane d) is control, and lane e) is five times of reagents of lane a) to confirm its reduction ability. (b) is coomassie staining of (a).

## 2.10. References

1. Krishnamoorthy, L.; Cotruvo, J. A. J.; Chan, J.; Kaluarachchi, H.; Muchenditsi, A.; Pendyala, V. S.; Jia, S.; Aron, A. T.; Ackerman, C. M.; Vander Wal, M. N.; Guan, T.; Smaga, L. P.; Farhi, S. L.; New, E. J.; Lutsenko, S.; Chang, C. J., Copper regulates cyclic-AMP-dependent lipolysis. *Nat. Chem. Biol.* **2016**, *12*, 586-592.
2. Turski, M. L.; Brady, D. C.; Kim, H. J.; Kim, B.-E.; Nose, Y.; Counter, C. M.; Winge, D. R.; Thiele, D. J., A Novel Role for Copper in Ras/Mitogen-Activated Protein Kinase Signaling. *Mol Cell Biol* **2012**, *32* (7), 1284-1295.
3. Brady, D. C.; Crowe, M. S.; Turski, M. L.; Hobbs, G. A.; Yao, X.; Chaikuad, A.; Knapp, S.; Xiao, K.; Campbell, S. L.; Thiele, D. J.; Counter, C. M., Copper is required for oncogenic BRAF signalling and tumorigenesis. *Nature* **2014**, *509*, 492-496.
4. Andreini, C.; Bertini, I.; Rosato, A., Metalloproteomes: A Bioinformatic Approach. *Acc. Chem. Res.* **2009**, *42* (10), 1471-1479.
5. Cvetkovic, A.; Menon, A. L.; Thorgersen, M. P.; Scott, J. W.; Poole, F. L. I.; Jenney, F. E. J.; Lancaster, W. A.; Praissman, J. L.; Shanmukh, S.; Vaccaro, B. J.; Trauger, S. A.; Kalisiak, E.; Apon, J. V.; Siuzdak, G.; Yannone, S. M.; Tainer, J. A.; Adams, M. W. W., Microbial metalloproteomes are largely uncharacterized. *Nature* **2010**, *466*, 779-782.
6. Song, Y.; Zhang, H.; Chen, C.; Wang, G.; Zhuang, K.; Cui, J.; Shen, Z., Proteomic analysis of copper-binding proteins in excess copper-stressed rice roots by immobilized metal affinity chromatography and two-dimensional electrophoresis. *BioMetals* **2014**, *27*, 265-276.
7. Pace, N. J.; Weerapana, E., A Competitive Chemical-Proteomic Platform to Identify Zinc-Binding Cysteines. *ACS Chem. Biol.* **2014**, *9* (1), 258-265.
8. Weerapana, E.; Wang, C.; Simon, G. M.; Richter, F.; Khare, S.; Dillon, M. B. D.; Bachovchin, D. A.; Mowen, K.; Baker, D.; Cravatt, B. F., Quantitative reactivity profiling predicts functional cysteines in proteomes. *Nature* **2010**, *468*, 790-795.
9. Lippard, S. J.; Berg, J. M., *Principles of Bioinorganic Chemistry*. University Science Books: Mill Valley, CA.; Mill Valley, CA, 1994.
10. Yatsunyk, L. A.; Rosenzweig, A. C., Cu+ Binding and Transfer by the N Terminus of the Wilson Disease Protein. *J. Biol. Chem.* **2007**, *282*, 8622-8631.
11. Guan, R.; Ho, M. C.; Brenowitz, M.; Tyler, P. C.; Evans, G. B.; Almo, S. C.; Schramm, V. L., Entropy-driven binding of picomolar transition state analogue inhibitors to human 5'-methylthioadenosine phosphorylase. *Biochemistry* **2011**, *50* (47), 10408 - 10417.
12. Hecquet, L.; Bolte, J.; Demuynck, C., New Assays for Transketolase. *Bioscience, Biotechnology, and Biochemistry*, **1993**, *57*, 2174-2176.
13. Constantin, C. Catching Metalloproteins: Reactive Cysteine Profiling and Metal-targeted Photocrosslinking Probes. Master of Science, Ecole Polytechnique Federale de Lausanne, Lausanne, 2015.
14. Birringer, M. S.; Perozzo, R.; Kut, E.; Stillhart, C.; Surber, W.; Scapozza, L.; Folkers, G., High-level expression and purification of human thymidine kinase 1: quaternary structure, stability, and kinetics. *Protein Expr Purif* **2006**, *47* (2), 506-515.
15. Ackerman, C. M. Detecting, Measuring and Manipulating Copper in Biological Systems. University of California at Berkeley, Berkeley, CA, 2017.
16. Doñate, F.; Juarez, J. C.; Burnett, M. E.; Manuia, M. M.; Guan, X.; Shaw, D. E.; Smith, E. L. P.; Timucin, C.; Braunstein, M. J.; Batuman, O. A.; Mazar, A. P., Identification of biomarkers

for the antiangiogenic and antitumour activity of the superoxide dismutase 1 (SOD1) inhibitor tetrathiomolybdate (ATN-224). *Br J Cancer* **2008**, 98, 776 - 783.

## Appendix 4

### **Metalloproteomic Study with Episulfide Alkyne Probes**

Portions of this work were performed in collaboration with the following persons:

Yuki Nishikawa at Kyoto University synthesized three alkyne probes and did preliminary gel analysis of those probes

## A2.1. Introduction

Metal elements represent some of the most fundamental chemical building blocks of life and are required to sustain the growth, development, and sustenance of all living organisms and ecosystems across the planet.<sup>1</sup> Across all species, proteins compose of about 50% of the cell mass and reaches 2~4 million proteins per cubic micrometer.<sup>2</sup> The extensive proteomics of the cell adapts dynamically to external or internal perturbations and thereby defines the cell's functions and reveals its phenotype.<sup>3,4</sup> Having an insight of complete and quantitative proteomics as well as understanding intact structure is ultimate goal of biology. Traditionally, specific proteins are isolated and analyzed their functions and structure through the established methods. However, it becomes to run large-scale measurement of proteomes to have information based on the computational datasets.<sup>3</sup> This proteomes approaches have been transformed by development of mass-spectroscopy-based methods. This technique can identify and localization of amino acids as well as determine the composition, stoichiometry and topology of the subunits of protein complexes and even useful to establishing their structures. Its estimated that metalloproteins are about one third to one half of the proteome.<sup>5</sup> However, discovering new metal-binding proteins is challenging. It is hard to predict metal-binding proteins through computational methods, as there is no conserved consensus sequence for metal-coordination so far. The high-throughput mass-spectroscopy methods are emerging for characterizing novel metalloproteins.<sup>6</sup> However, those method often requires specialized equipment and laborious procedures. One of methods using mass-spectroscopy is an isoTOP-ABPP (isotopic tandem orthogonal proteolysis–activity-based protein profiling) which has been developed for profiling cysteine residues that bind copper.<sup>7</sup> (Figure 1) This appendix describes an alternative strategy for profiling metalloproteins using ABPP especially using episulfide for metal coordination, activating nucleophilic reaction from amino acid near to metal site. Instead of profiling amino acid reactivity as an indirect readout of metal-binding, the strategy described in this appendix attempts tag metalloproteins based on interactions between metal center and probe headgroup such as acyl-imidazole and episulfide groups. We envisioned developing a probe that would contain a metal-chelating headgroup, a photocrosslinking group, and a pull-down handle for protein identification. We envisioned the metal-chelating would provide specificity, the photocrosslinking group would covalently link probe to protein, and the pull-down handle would enable protein identification.

## A4.2 Materials and Methods

### A4.2.1. General synthetic methods

Reactions using moisture- or air-sensitive reagents were carried out in flame-dried glassware under an inert atmosphere of N<sub>2</sub>. Solvent was passed over activated alumina and stored over activated 3Å molecular sieves before use when dry solvent was required. All other commercially purchased chemicals were used as received (without further purification). SiliCycle 60 F254 silica gel (pre-coated sheets, 0.25 mm thick) were used for analytical thin layer chromatography and visualized by fluorescence quenching under UV light. Silica gel P60 (SiliCycle) was used for column chromatography. <sup>1</sup>H and <sup>13</sup>C NMR spectra were collected at 298 K in CDCl<sub>3</sub> or CD<sub>3</sub>OD (Cambridge Isotope Laboratories, Cambridge, MA) at 25 °C on Bruker AVQ-400, AVB-400, AV-500, or AV-600 at the College of Chemistry NMR Facility at the University of California, Berkeley or on Bruker 900 at the QB3 Central California 900 MHz NMR Facility. All chemical shifts are reported in the standard notation of  $\delta$  parts per million



relative to residual solvent peak at 7.26 (CDCl<sub>3</sub>) or 3.31 (CD<sub>3</sub>OD) for <sup>1</sup>H and 77.16 (CDCl<sub>3</sub>) or 49.00 (CD<sub>3</sub>OD) for <sup>13</sup>C as an internal reference. Splitting patterns are indicated as follows: br, broad; s, singlet; d, doublet; t, triplet; m, multiplet; dd, doublet of doublets. Low-resolution electrospray mass spectral analyses were carried out using a LC-MS (Agilent Technology 6130, Quadrupole LC/MS and Advion expression-L Compact Mass Spectrometer). High-resolution mass spectral analyses (ESI-MS) were carried out at the College of Chemistry Mass Spectrometry Facility at the University of California, Berkeley.

## A2.3. Materials and methods

### A4.3.1. Synthesis of acyl-imidazole, epoxy-alkyne, and episulfide-alkyne

2-((prop-2-yn-1-yloxy)methyl)oxirane (epoxy-alkyne) : 2-(chloromethyl)oxirane (0.5 g) was added in benzene:50% NaOH (1:1 v/v) at 0 °C. To this mixture, prop-2-yn-1-ol (1.2 equiv) and tetrabutylammonium bromide (0.5 equiv) were added and warm up to room temperature and stir vigorously for 2 days. Extract with water and ethyl acetate and organic layers were combined and dried with Mg<sub>2</sub>SO<sub>4</sub>. The crude produce was purified with hexane and ethyl acetate from 5% to 50%. The TLC was stained with potassium permanganate. <sup>1</sup>H NMR (400 MHz, CDCl<sub>3</sub>) 4.21(2H,s) 4.03 (1H, s), 3.66-3.58 (2H, m), 2.46 (1H, s), 2.18-1.98 (2H,m).

2-((prop-2-yn-1-yloxy)methyl)thiirane (episulfide-alkyne) : In a round-bottomed flask (10 mL) equipped with a magnetic stirrer and condenser, a solution of the epoxy-alkyne (1 mmol) and thiourea (0.152 g, 2 mmol) in MeOH (3 mL) was prepared. Molecular sieve 4Å (0.1 g) was then added to the resulting solution and the reaction mixture was stirred magnetically under reflux condition for 12-25 min. The progress of the reaction was monitored by TLC. After completion of the reaction, MeOH was evaporated and diethyl ether (5 mL) was added to the reaction mixture followed by stirring for 5 min. The mixture was filtered and the organic solvent was evaporated to give crude thiirane for further purification by a short-column chromatography over silica gel. Yield 97%. <sup>1</sup>H NMR (400 MHz, CDCl<sub>3</sub>) 4.21(2H,s) 3.66-3.58 (2H, m), 3.10 (1H, s), 2.36 (1H, s), 2.08-1.78 (2H,m).

### A4.3.2 Preparation of cell lysate

Cells were maintained by the UC Berkeley Tissue Culture Facility. HEK 293T cells were maintained as a monolayer in exponential growth at 37 °C in a 5% CO<sub>2</sub> atmosphere in Dulbecco's Modified Eagle Medium (DMEM, Gibco) supplemented with 10% fetal bovine serum (FBS, Hyclone), and glutamax (Gibco). One day before harvesting, HEK 293T cells were passaged and plated in DMEM.

### A4.3.3. Preparation of apo-carbonic anhydrase

Dissolve CA 1 mg in 1 mL in 25 mM HEPES pH 7.4 buffer with 0.05 M dipicolinic acid (hard to make stock solution of dipicolinic acid so dissolve it together with CA). Keep the solution at room temperature for 3~4 hr in 3K ultrafiltration (10K is also fine. How it works is it filtered below 3 K) filled up 10 mL and centrifuge at 5000 g for 100 min. discard the filtrate and fill 10 mL again. Exchange buffer to 25 mM HEPES pH 8.5 and make sure the final concentration of dipicolinic acid is below 5 μM. Check the concentration of the protein and store at -80 °C.

### A4.2.3. Protocol for preparation of mass-spectroscopy sampling

### Pre- Day-1

1. Scrape plates separately, such that 6 150mm dishes are combined to make one sample – there should be 4 samples total (these will be split into 4 BCS-treated and 4 Control). Then take up cells from the 5 dishes combined in ~50 mL cold PBS (aspirate, scrape into 8 mL PBS, then wash each plate with 2 mL). Wash 2x more times with 20 mL cold PBS, spinning down at 1.4G for 5 mins between each wash.
2. Then pellet samples and bring each sample into the glovebox as a pellet.
3. Once in the glovebox, reconstitute each sample in 1.4 mL and sonicate each sample in the glovebox – 5 sec on, 10 sec off x 6 – check by looking at under the microscope.
4. Then quantify protein (using Bradford – each sample is ~8 mg/mL). Dilute desired proteome to 2 mg/ml solution in PBS (total volume = 2.5 mL or 2 mL)
5. Treat 4 samples with 10 uM CuCl in MOPS (prepared from concentrated stock in 0.1 M HCl, 50 mM stock) for 1.0 hr. Treat 4 control samples with the same volume of acid + MOPS only. While this is labeling, bring in IA-alkyne.
6. Add fresh made IA-alkyne probe stock (10mM in DMSO) to each sample to get final concentration of 100uM (this is 25 uL in 2.5 mL samples or 20 uL in 2.0 mL samples). After addition of the probe, vortex and incubate the reaction in RT for one hour.
7. Then run each of the 8 samples through a PD-10 column – load 2.5 mL, then elute in 3.5 mL.
8. Collect in 500 uL aliquots (~8 drops) then find protein by running a Bradford assay. Protein was in fractions 3-6 (collecting FT, then subsequent fractions 1-8). Dilute to 2 mg/mL (500 uL x 4)
9. Prepare a fresh solution of 50mM TCEP in water (14.4mg/ml), chill MeOH in -20 freezer.
10. To each control eppie, add 10ul of the 5mM Light Tev-biotin tag (9.24mg/ml), to each treated/disease sample add 10ul of 5mM-Heavy Tev-biotin tag (9.27mg/ml) and vortex
11. Vortex the TEV tag stock thoroughly before adding to the sample
12. If you see particles floating in the Azo tag stock, sonicate the stock to re-solubilize
13. Add 10ul of fresh 50mM TCEP solution without vortexing
14. Add 30ul of TBTA “ligand” solution and vortex (0.9mg/ml in DMSO:*t*-butanol=1:4)
15. Add 10ul of 50mM Copper (II) Sulfate (12.5mg/ml in water) and vortex
16. Incubate the reaction at RT for one hour with vortexing every 15min. At this stage, the proteins will start to precipitate and the solution will turn cloudy.
17. Combine the tubes pairwise (Heavy+Light) and centrifuge for 4min at 6500g. A protein pellet will form.
18. Use 100ul or 200ul pipet for all the transfer steps to minimize the sample loss
19. Save the pipet tip and re-use later for transferring the same sample
20. Step 11-13 should be done at 4°C or on ice
21. Remove the supernatant, add 500 uL cold methanol (pre-chilled at -20°C) to each tube and sonicate for several seconds till pellet goes into solution completely.

22. Centrifuge tubes for 4 min at 6500g in the cold room
23. Remove the supernatant and repeat the wash (steps 11 and 12) with 500ul cold methanol
24. Remove the supernatant, add 1ml 1.2% SDS/PBS (w/v), sonicate for several seconds till the solution turns clear and heat to 80-90°C for 5min. Then, centrifuge for 5 min at 6500g.
25. Take out the streptavidin agarose beads slurry from 4°C fridge and resuspend the slurry by rotating the bottle. Aliquot 170 ul slurry per sample, up to 6 samples per column.
26. Wash beads in the vacuum manifold with 1 ml PBS three times, then resuspend beads in the original volume taken from the avidin-agarose bottle (including beads).
27. Using a 200 ul pipette tip with ~1 cm cut off, transfer 170ul washed beads into 15mL conicals containing 5mL PBS
28. Transfer the 1ml sample to the 15ml conical tube which already contains 5ml PBS and beads. The final concentration of SDS in the sample is 0.2%.
29. Incubate the labeled proteome sample with the beads in 15ml conical tube on a rotator at 4°C (cold room) over-night

#### Day-2 (4-5h)

1. Incubate the labeled proteome sample with the beads on a rotator at RT for couple hours to re-solubilize the SDS.
2. Centrifuge the conical tubes at 1400g for 3 min and remove the supernatant.
3. Wash the beads by adding 5ml of 0.2%SDS/PBS (w/v), place on a rotator for 10min, then spin at 1400g for 3min and remove the supernatant
4. Transfer beads to Micro Bio-Spin column using two washes of 500 ul PBS
5. Wash beads on vacuum manifold using three 1 ml washes of PBS
6. Wash beads on vacuum manifold using three 1 ml washes with water
7. Transfer the washed beads to screw-capped eppi tubes using two 250 ul washes of **fresh** 6M Urea/PBS (1.8g/5ml)
8. Add 25ul fresh-made DTT solution (30mg/ml in water) to each tube
9. Incubate the tube at 65°C for 20 min resuspending every 10 min (avoid vortexing)
10. Cool the tube for several seconds and add 25ul fresh-made 400mM IA solution (74mg/ml in water) to each tube. Incubate with agitation at 37°C for 30min.
11. Dilute the reaction by adding 950ul PBS to each tube, centrifuge at 1400g for 2min and remove the supernatant.
12. Add a pre-mixed solution of 200ul of 2M Urea/PBS, 2ul of 100mM Calcium Chloride (14.7mg/ml) in water and 4ul of Trypsin solution (20ug lyophilized powder reconstituted in 40ul Trypsin Buffer) to each tube.
13. Incubate the reaction at 37°C over-night in the shaking incubator

#### Day-3 (1h)

1. Transfer the supernatant and beads to a Bio-Spin column
  - a. If saving the tryptic peptides elute into a low adhesion tube by centrifugation (1,000g)

- b. Add 16uL formic acid and store at -80C.
2. Wash the beads with 3X 500ul PBS and then 3X 500ul water.
3. Transfer the beads to screw top epi tubes with 2X 500ul water
4. Spin down the beads and remove the supernatant
5. Wash the beads with 1 x TEV buffer (140 ul water, 7.5 ul of 20x TEV buffer, 1.5 ul of 100 uM DTT).
6. To the beads, add a premixed solution of TEV buffer as above, containing 5 ul of Ac-TEV protease.
7. Leave the reaction in a 29°C incubator overnight with mild agitation.

#### Day-4 (1h)

8. Transfer the supernatant and beads to a Bio-Spin column and elute into a low adhesion eppie tube
9. Wash the beads with 2 x 75 ul of water and combine the water washings with the eluent
10. Add 16 ul of formic acid to the sample and store TEV samples at -80°C until mass spectrometric analysis.

## **A2.4. Results and Discussion**

We performed our initial chemoproteomics experiment (Figure A4.1) comparing HEK 293T cells treated *in situ* with 2mM with BCS, EDTA, DFO, TETA, and TTM for one hour to vehicle-treated HEK 293T cells. Cells were incubated with acyl-imidazole alkyne probe and episulfide-alkyne probes for another one hour in the biobox, followed by click chemistry, and subsequent processing steps were performed aerobically.<sup>15</sup> The fluorescent intensity revealed that acyl imidazole does not show any difference between control and chelator incubated cases. However in case of episulfide-alkyne probe exhibited distinct fluorescent decrease in presence of all chelator incubated cases, indicating that the metal activation is the key step for metalloprotein labeling with those probes. This results was confirmed by several repeated experiments. To identify the protein labeled with episulfide-alkyne, mass spectroscopy samples were prepared for control/EDTA and control/TETA cases. Each cases were prepared in triplet. For mass spectroscopy samples, isoTOP-ABPP strategy were utilized by treating control lysate linked with light-TEV and chelator treated incubated with heavy-TEV.

Seeking to validate targets identified on the generated list, the following criteria were considered for validation - (1) Light/Heavy ratio > 3 (2) n > 2 (3) protein has an established activity/functional assay *in vitro* and *in situ* (4) protein has a known metal sites. To demonstrate the probe's ability to detect metalloproteins, carbonic anhydrase was chosen as model protein and apo-carbonic anhydrase was prepared for comparing the presence of zinc and EDTA affects the labeling of episulfide-alkyne probe. Furthermore, one of Chang group's postdoc, Byungsun, prepared another series of episulfide probes with different linker length and with rigid benzene ring. 2-(4-ethynylphenyl)oxirane and 2-(4-ethynylphenyl)thiirane where are linked to benzene ring did not show any chelator effect upon BCS, EDTA, DFO, TETA, and TTM. Also longer linker with amide bond in the middle, N-(hex-5-yn-1-yl)-4-(thiiran-2-yl)butanamide and N-(hex-5-yn-1-yl)-4-(thiiran-2-yl)butanamide also did not difference in presence and absence of chelator. Those imply that the length and rigidity is important for designing the metalloprotein especially, be able to reach metal center where usually buried deep on the protein surface.

## A2.5. Conclusion

We developed a chemoproteomic strategy for identifying novel metalloproteins with new probes. This strategy was based on the hypothesis that probes are activated with metal coordination, triggering nucleophilic attack from amino acids on protein surfaces which is near to the metal coordination sites. The probes are based on episulfide with alkyne-containing probe for tag labeling. For control probe, epoxide probes have been prepared to decrease nucleophilicity, resulting in decreased labeling. Furthermore, the episulfide probes have been prepared by differentiating the length of the carbon chain or introducing the aryl group to increase the rigidity of the probes. The epoxide probes showed decreased staining compared with episulfide probes, confirming that nucleophilicity is an important factor for staining. Among those probes, the episulfide1 showed significant decrease staining in presence of chelator (EDTA, BCS, DFO, TTM, and TETA). The protein polysates from HEK293T cell were labeled with episulfide in presence and absence of EDTA and TETA. Through mass-spectroscopy, we attempted to identify a number proteins. Additionally, carbonic anhydrase proteins were selected to demonstrate the episulfide-alkyne probes can be active by the presence of zinc and not activated in absence of zinc (incubated with excess EDTA). So far apo-carbonic anhydrase was prepared and will test with episulfide-alkyne probe.

## Figures

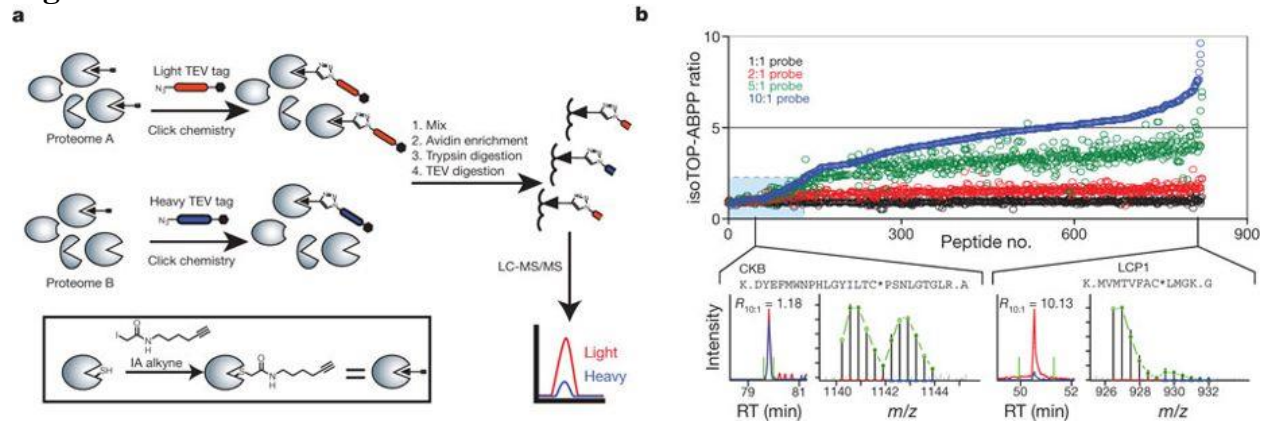


**Figure A2.1.** a) isoTOP-ABPP involves proteome labelling, click-chemistry-based incorporation of isotopically labelled cleavable tags, and sequential on-bead protease digestions to provide probe-labelled peptides for MS analysis. The IA probe is shown in the inset. LC-MS/MS, liquid-chromatography-MS/MS. B) Measured isoTOP-ABPP ratios for peptides from MCF7 cells labelled with four pairwise IA probe concentration. *Cited from Nature, 2010, 468, 790–795.*

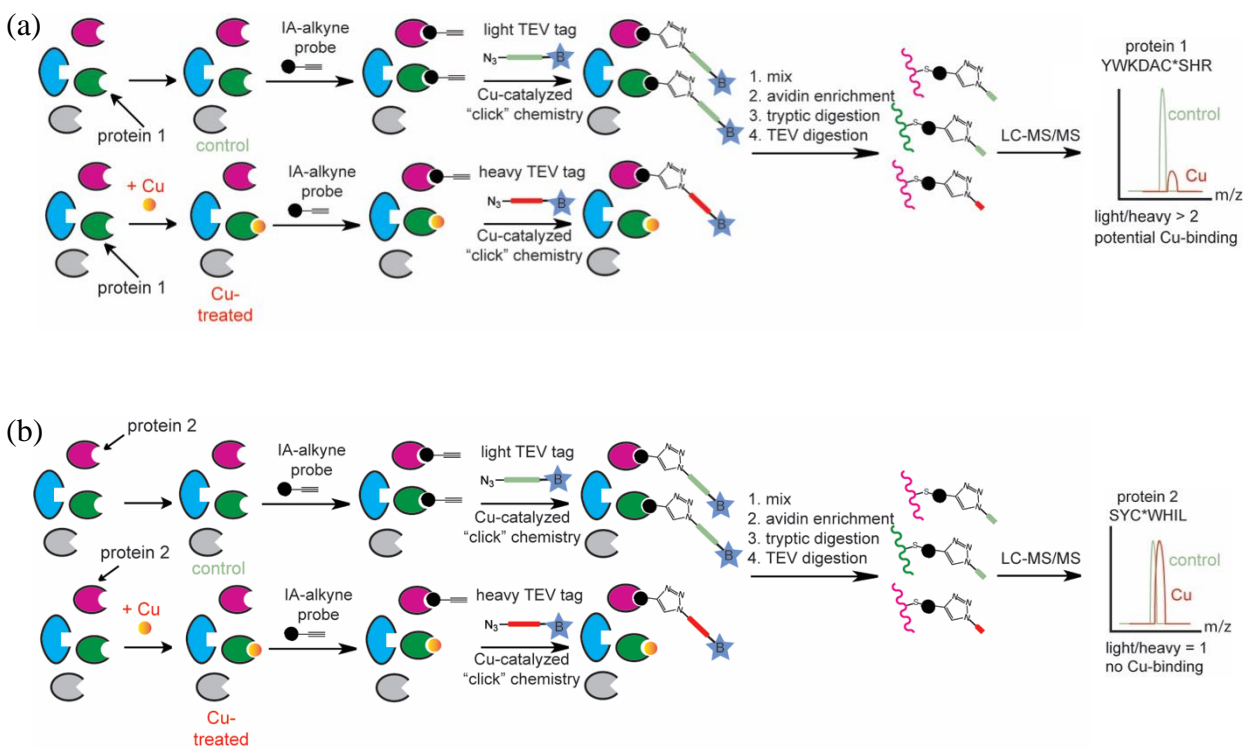


**Figure A2.2.** (a) A Cu-binding protein, such as the protein depicted in green, will exhibit a light/heavy ratio  $> 2$  while (b) a control protein, such as the protein depicted in pink, will exhibit a light/heavy ratio  $= 1$  in an isoTOP-ABPP experiment.

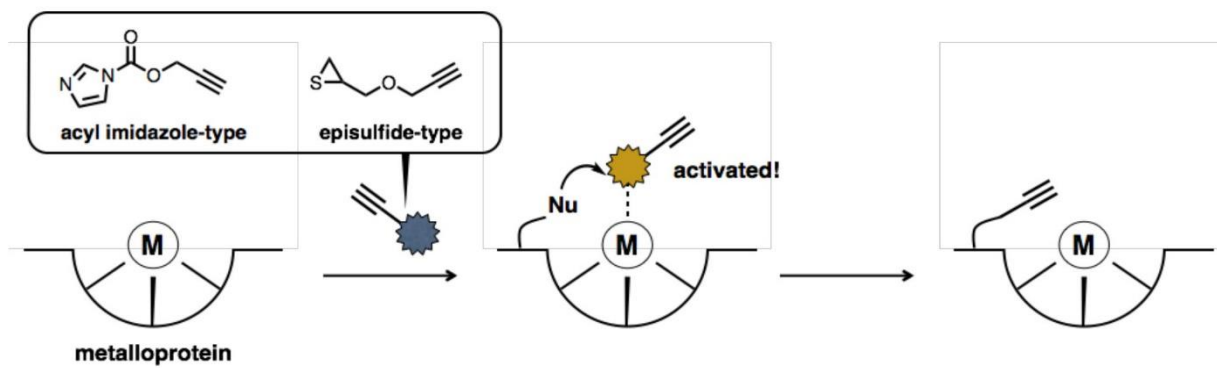


**Figure A4.3.** The structures of acyl-imidazole-alkyne and episulfide-alkyne probes and the illustration of how the probe works in the cells.



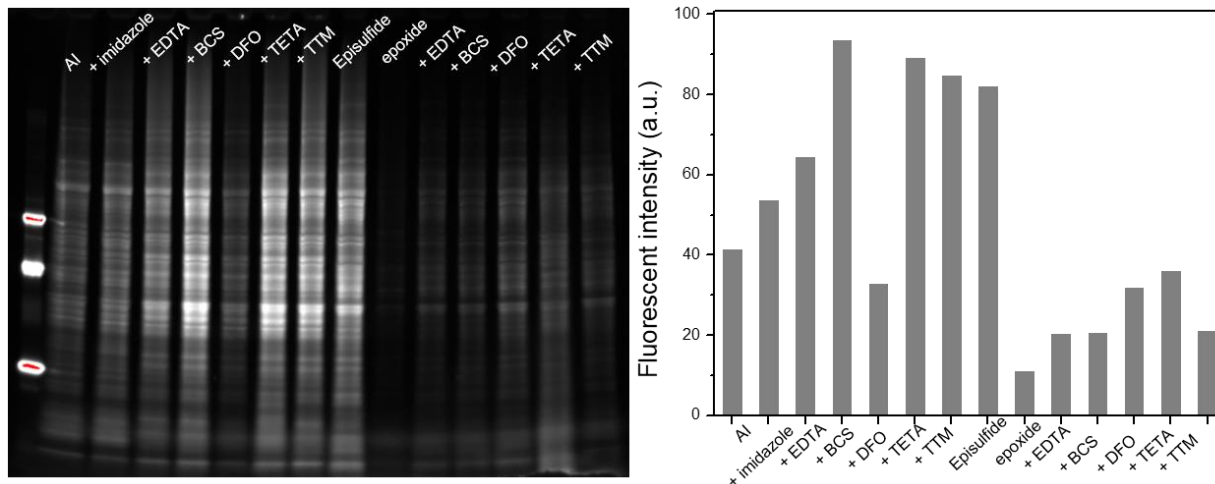


**Figure A4.4** Acyl-imidazole (50  $\mu\text{M}$ ) and the labeling in presence of 100 equiv of imidazole for competitive binding. The rest of half left side is protein lysate (1 mg/mL) incubated with indicated chelator (2 mM) for 15 min, followed by incubation of acyl imidazole-alkyne for 1 hour at room temperature. The episulfide-alkyne showed the brightest among the protein lysates, however the epoxy-alkyne shows really dim. The rest of half right side is protein lysate (1 mg/mL) incubated with indicated chelator (2 mM) for 15 min, followed by incubation of episulfide-alkyne for 1 hour at room temperature. The plot is integrated fluorescent intensity in each lane.

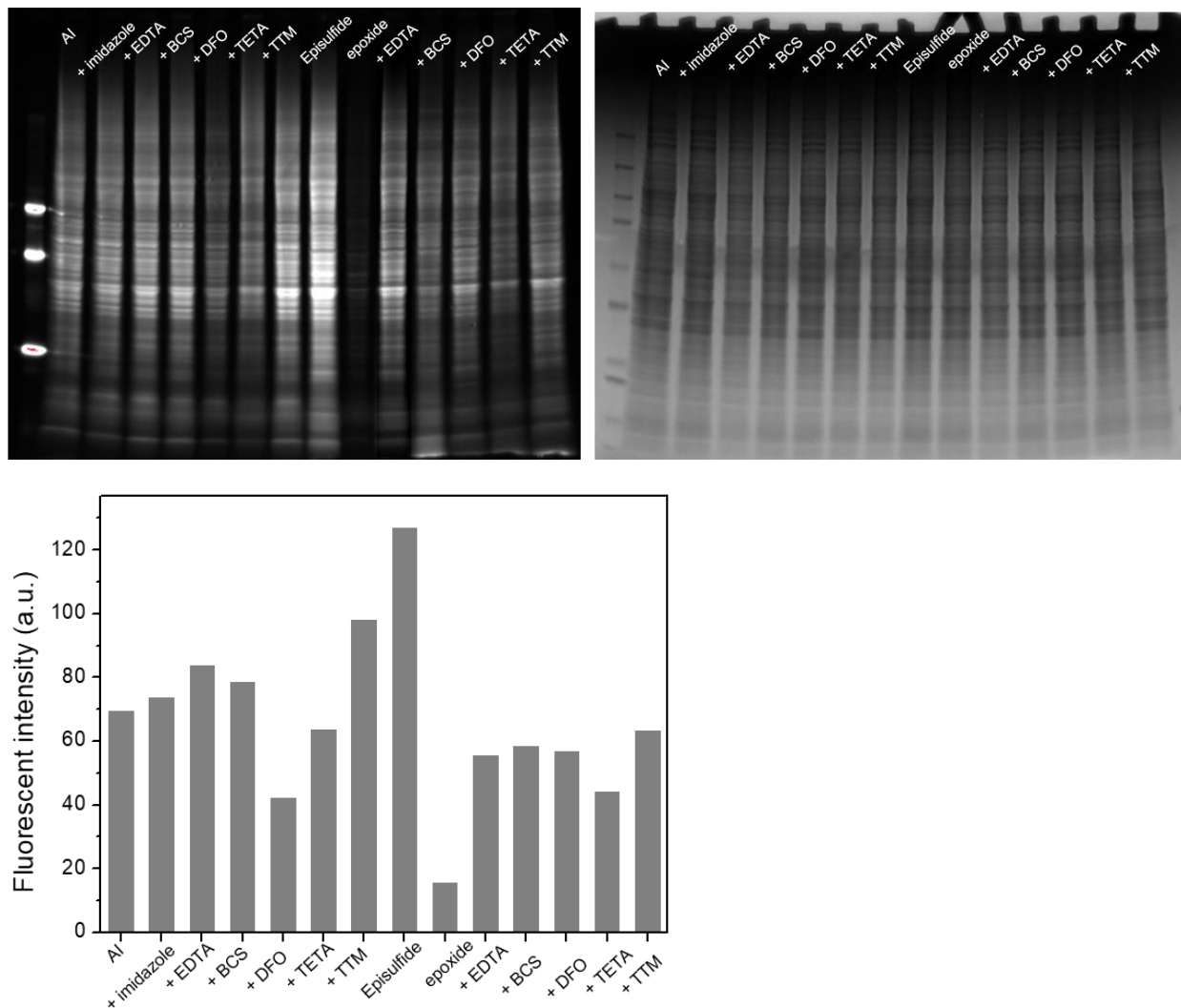


**Figure A4.5.** Acyl-imidazole (100  $\mu\text{M}$ ) and the labeling in presence of 100 equiv of imidazole for competitive binding. The rest of half left side is protein lysate (1 mg/mL) incubated with indicated chelator (2 mM) for 15 min, followed by incubation of acyl imidazole-alkyne for 1 hour at room temperature. The episulfide-alkyne (100  $\mu\text{M}$ ) showed the brightest among the protein lysate, however the epoxy-alkyne (100  $\mu\text{M}$ ) shows really dim. The rest of half right side is protein lysate (1 mg/mL) incubated with indicated chelator (2 mM) for 15 min, followed by incubation of episulfide-alkyne for 1 hour at room temperature. The plot is integrated fluorescent intensity in each lane.

## A2.6. References

1. Krishnamoorthy, L.; Cotruvo, J. A. J.; Chan, J.; Kaluarachchi, H.; Muchenditsi, A.; Pendyala, V. S.; Jia, S.; Aron, A. T.; Ackerman, C. M.; Vander Wal, M. N.; Guan, T.; Smaga, L. P.; Farhi, S. L.; New, E. J.; Lutsenko, S.; Chang, C. J., Copper regulates cyclic-AMP-dependent lipolysis. *Nat. Chem. Biol.* **2016**, *12*, 586-592.
2. Turski, M. L.; Brady, D. C.; Kim, H. J.; Kim, B.-E.; Nose, Y.; Counter, C. M.; Winge, D. R.; Thiele, D. J., A Novel Role for Copper in Ras/Mitogen-Activated Protein Kinase Signaling. *Mol Cell Biol* **2012**, *32* (7), 1284-1295.
3. Brady, D. C.; Crowe, M. S.; Turski, M. L.; Hobbs, G. A.; Yao, X.; Chaikuad, A.; Knapp, S.; Xiao, K.; Campbell, S. L.; Thiele, D. J.; Counter, C. M., Copper is required for oncogenic BRAF signalling and tumorigenesis. *Nature* **2014**, *509*, 492-496.
4. Andreini, C.; Bertini, I.; Rosato, A., Metalloproteomes: A Bioinformatic Approach. *Acc. Chem. Res.* **2009**, *42* (10), 1471-1479.
5. Cvetkovic, A.; Menon, A. L.; Thorgersen, M. P.; Scott, J. W.; Poole, F. L. I.; Jenney, F. E. J.; Lancaster, W. A.; Praissman, J. L.; Shanmukh, S.; Vaccaro, B. J.; Trauger, S. A.; Kalisiak, E.; Apon, J. V.; Siuzdak, G.; Yannone, S. M.; Tainer, J. A.; Adams, M. W. W., Microbial metalloproteomes are largely uncharacterized. *Nature* **2010**, *466*, 779-782.
6. Song, Y.; Zhang, H.; Chen, C.; Wang, G.; Zhuang, K.; Cui, J.; Shen, Z., Proteomic analysis of copper-binding proteins in excess copper-stressed rice roots by immobilized metal affinity chromatography and two-dimensional electrophoresis. *BioMetals* **2014**, *27*, 265-276.
7. Pace, N. J.; Weerapana, E., A Competitive Chemical-Proteomic Platform to Identify Zinc-Binding Cysteines. *ACS Chem. Biol.* **2014**, *9* (1), 258-265.
8. Weerapana, E.; Wang, C.; Simon, G. M.; Richter, F.; Khare, S.; Dillon, M. B. D.; Bachovchin, D. A.; Mowen, K.; Baker, D.; Cravatt, B. F., Quantitative reactivity profiling predicts functional cysteines in proteomes. *Nature* **2010**, *468*, 790-795.
9. Lippard, S. J.; Berg, J. M., *Principles of Bioinorganic Chemistry*. University Science Books: Mill Valley, CA.; Mill Valley, CA, 1994.
10. Yatsunyk, L. A.; Rosenzweig, A. C., Cu<sup>+</sup> Binding and Transfer by the N Terminus of the Wilson Disease Protein. *J. Biol. Chem.* **2007**, *282*, 8622-8631.
11. Guan, R.; Ho, M. C.; Brenowitz, M.; Tyler, P. C.; Evans, G. B.; Almo, S. C.; Schramm, V. L., Entropy-driven binding of picomolar transition state analogue inhibitors to human 5'-methylthioadenosine phosphorylase. *Biochemistry* **2011**, *50* (47), 10408 - 10417.
12. Hecquet, L.; Bolte, J.; Demuynck, C., New Assays for Transketolase. *Bioscience, Biotechnology, and Biochemistry*, **1993**, *57*, 2174-2176.
13. Constantin, C. Catching Metalloproteins: Reactive Cysteine Profiling and Metal-targeted Photocrosslinking Probes. Master of Science, Ecole Polytechnique Federale de Lausanne, Lausanne, 2015.
14. Birringer, M. S.; Perozzo, R.; Kut, E.; Stillhart, C.; Surber, W.; Scapozza, L.; Folkers, G., High-level expression and purification of human thymidine kinase 1: quaternary structure, stability, and kinetics. *Protein Expr Purif* **2006**, *47* (2), 506-515.
15. Ackerman, C. M. Detecting, Measuring and Manipulating Copper in Biological Systems. University of California at Berkeley, Berkeley, CA, 2017.
16. Doñate, F.; Juarez, J. C.; Burnett, M. E.; Manuia, M. M.; Guan, X.; Shaw, D. E.; Smith, E. L. P.; Timucin, C.; Braunstein, M. J.; Batuman, O. A.; Mazar, A. P., Identification of biomarkers

for the antiangiogenic and antitumour activity of the superoxide dismutase 1 (SOD1) inhibitor tetrathiomolybdate (ATN-224). *Br J Cancer* **2008**, 98, 776 - 783.